Design and Characterisation of Calibration Systems for Small-Sized Telescope Cameras in the Cherenkov Telescope Array.

NAYAK, AMRIT,PRITTAM

Design and Characterisation of Calibration Systems for Small-Sized Telescope Cameras in the Cherenkov Telescope Array

Amrit Nayak

A Thesis presented for the degree of
Doctor of Philosophy

Department of Physics
Durham University
United Kingdom
September 2025

Design and Characterisation of Calibration Systems for Small-Sized Telescope Cameras in the Cherenkov Telescope Array

Amrit Prittam Nayak

Submitted for the degree of Doctor of Philosophy
September 2025

Abstract

The Cherenkov Telescope Array Observatory (CTAO) represents the next generation in very-high-energy gamma-ray astronomy, promising an order-of-magnitude improvement in sensitivity over existing instruments. With a diverse array of telescopes, including the Small-Sized Telescopes (SSTs) optimized for the highest energies, CTAO will open new windows on the gamma-ray sky in the 20 GeV–300 TeV regime and beyond. A critical component enabling this scientific performance is the stability and reliability of the telescope cameras, which rely on fast photo sensors. For example - Silicon Photomultiplier (SiPM) in SST Camera. Since SiPM characteristics can drift due to temperature variations, aging, or operational conditions, a robust calibration system is essential to ensure data quality and long-term stability.

This thesis presents the design, testing, and integration of the calibration system developed for the SST camera (SSTCAM). Beginning with a review of calibration strategies employed in current-generation gamma-ray telescopes, the work identifies the performance requirements imposed by CTAO and adapts them for the SSTCAM. The development process is described across successive design iterations, including hardware prototypes and firmware implementations. Extensive performance studies of the calibration device are reported, covering dynamic range, operating condition dependencies, and beam profile characterization. Results demonstrate compliance with CTAO specifications while also revealing areas for improvement.

Building on these findings, the thesis explores the transition from a single-channel device to a multi-channel calibration unit capable of supporting diverse activities such as flat-fielding, pixel linearity monitoring, and single photo-electron calibration. The final design integrates lessons learned from earlier versions and outlines a pathway toward full incorporation within the SSTCAM. In parallel, simulation studies are conducted to assess the feasibility of applying the calibration procedures in practice, offering guidance for future system integration.

By providing a dedicated, flexible, and high-performance calibration solution, this work contributes a key technological element to the success of the CTAO's SST program.

Supervisors: Prof. Anthony M. Brown and Prof. Paula M. Chadwick

Declaration

The work in this thesis is based on research carried out at the Department of Physics, Durham University, United Kingdom. No part of this thesis has been submitted elsewhere for any other degree or qualification and it is all my own work unless referenced to the contrary in the text.

Acknowledgements

Jay Jagannath!

First and foremost, I bow my head in gratitude to Lord Jagannath for showing me the path and placing me where I was truly meant to be. "Tuma bina gati nahi, prabhu!" Without Your guidance, I would be wandering aimlessly, but with Your grace, I found light even in the darkest corridors of research life.

Next, I would like to express my deepest thanks to my supervisors, Prof. Anthony Brown and Prof. Paula Chadwick. From the very beginning, you both have been my compass, ensuring that I never strayed too far from the track (even when I occasionally took scenic detours). The lively and enriching discussions we had always left me feeling inspired, ready to chase the next idea. And of course, I cannot even begin to measure the patience and time you invested in reading, re-reading, editing, and polishing this thesis—it is no exaggeration to say this thesis carries your fingerprints on every page.

I also owe a heartfelt thanks to Dr. Richard White for opening the door to the Cherenkov Telescope Array and introducing me to the wonderful world of the SST camera collaboration. Our Thursday meetings during the turbulent days of Covid weren't just about science—they gave me direction, hope, and something meaningful to hold onto when the world outside felt uncertain. Your support during my research visit to the Max Planck Institute of Nuclear Physics was beyond anything I could have expected, and I remain truly grateful. I would also like to thank Dr. Davide Depaoli, who became my steady anchor during my time at MPIK. Not only did you help me sharpen my lab skills, but your words of encouragement—always delivered at just the right moment—were the cherry on top of an unforgettable experience.

To my office mates—Cameron, Ieva, and Sheridan—you made office life so much more than just equations and data. Whether it was a spirited scientific debate or a random chat about movies, those conversations kept me balanced (and probably kept me from talking to my computer too much).

I extend my gratitude to everyone at CfAI. The pizza talks were not only a treat for the stomach but also a feast for the mind—often opening my eyes to new ideas

or connections I hadn't thought of before. The seminars, too, were little sparks of curiosity that kept science exciting and alive.

A massive shout-out to my big family, who never failed to celebrate my smallest victories as if they were grand milestones. You are my constant cheerleaders, and I could never ask for more. And to my second family here in Durham—my support system through thick and thin—thank you for making these years so memorable. From knee-cracking badminton matches to fun socials, every moment with you has been priceless. Jamie, Beyza, Diana, Julio, Kate, Buthayna, Neel, Sheersh, Ujjwal, Ashqar, Afthab, Houtan, David and Libby— thank you for being incredible friends whose encouragement, laughter, unforgettable parties, delicious potlucks, chaotic game nights, and countless birthday celebrations brought joy, balance, and sanity to this PhD journey. Vinay, special thanks to you for being not just a great housemate but also an even greater friend. I wish you all the success in your journey ahead—you deserve nothing less.

This journey would not have been possible without my parents. Thank you for teaching me to dream big and to keep striving, no matter how difficult the road may get. Your sacrifices and unwavering faith in me are the foundation upon which this thesis stands. I am forever indebted to your love and support.

And finally, to Ellie—thank you for giving this thesis its final polish. Thank you for painstakingly proofreading, for making sure my arguments (and my brackets) had enough space to breathe, and for reminding me every day that I was capable of finishing this journey. Your patience, encouragement, and good humour made the long hours of writing far less daunting.

To everyone who, in ways big or small, helped shape this work and made it better—thank you from the bottom of my heart.

Contents

Abstract **i**

Declaration **iii**

Acknowledgements **iv**

List of Figures **xi**

List of Tables **xvi**

Abbreviation **xviii**

Introduction **xxi**

1 Gamma Ray Astronomy **1**

1.1 Cosmic Rays 1

1.2 Gamma Rays 4

1.3 Gamma ray Production Mechanism 5

1.3.1 Electromagnetic Process 6

1.3.2 Hadronic Process 9

1.4 Gamma ray Interaction 10

1.5 Gamma ray Detection 11

1.5.1 Direct Detection 12
1.5.2 Indirect Detection 14
1.6 Air Showers 15
1.6.1 Electromagnetic Air Shower 15
1.6.2 Hadronic Air Shower 17
1.7 Cherenkov Radiation 18
1.8 Imaging Atmospheric Cherenkov Technique 20
1.9 Cherenkov Telescope Array 24
1.9.1 Performance 24
1.9.2 CTA Telescopes 25
1.9.3 Location 30
1.9.4 Science Goals 32

2 Small-Sized Telescope Camera (SSTCAM) 35
2.1 Initial Prototypes 35
2.2 SSTCAM 37
2.2.1 Photosensor: SiPM 38
2.2.2 Data Acquisition: TARGET 42
2.3 Photosensor Calibration 45
2.3.1 Flat Fielding 45
2.3.2 Single Photoelectron Calibration 46
2.3.3 Linearity 47
2.4 On Telescope Calibration Devices 48
2.4.1 VERITAS 48
2.4.2 MAGIC 48
2.4.3 H.E.S.S 49
2.4.4 LST 49
2.4.5 MST 50
2.4.6 LHAASO WFCTA 51
2.5 CTAO Requirement 52
2.6 Conclusion 53

3 Flasher Calibration System **54**

3.1 Design Description 55

3.1.1 Timing Block 55

3.1.2 Intensity block 59

3.1.3 Output Block 59

3.1.4 Power Block 60

3.1.5 Control Block 61

3.1.6 Communication Block 63

3.1.7 Additional Block 63

3.2 Previous prototypes 64

3.3 Firmware Description 66

3.4 Concept of Operation 70

3.5 Characterisation Test setup 70

3.5.1 Silicon Photomultiplier (SiPM) 70

3.5.2 Power Supply 71

3.5.3 Arbitrary Waveform Generator (AWG) 72

3.5.4 Oscilloscope 72

3.5.5 Climate Chamber 72

3.5.6 Lab Computer 73

3.6 Data Acquisition Software 75

3.7 Characterisation Test Results 75

3.7.1 Visual check 77

3.7.2 Intensity Stability 79

3.7.3 Dynamic Range 79

3.7.4 Temperature dependence 83

3.7.5 Frequency dependence 86

3.7.6 Beam Uniformity 87

3.7.7 Timing Characteristics 89

3.7.8 Long term test 92

3.8 Conclusion 93

4 Towards the Next Generation Flasher **98**

4.1 Flasher-Fibre system . . . 100

4.1.1 Under-lid fibre: Profile Tests . . . 101

4.1.2 Under-lid fibre: Response across camera . . . 106

4.1.3 Fibre for flat fielding: Profile Tests . . . 117

4.1.4 Fibre for flat fielding: Illumination Pattern . . . 120

4.1.5 Lessons from Flasher-fibre work . . . 121

4.2 Flasher-Coaxial Cable System . . . 122

4.2.1 Optical Signal Test . . . 122

4.2.2 Coaxial Cable Noise Test . . . 124

4.2.3 Lessons from Flasher-coaxial cable work . . . 125

4.3 Conclusion . . . 125

5 Flasher Version 4 Calibration System **127**

5.1 Design Description . . . 128

5.1.1 Power Block . . . 131

5.1.2 Control Block . . . 131

5.1.3 Channel Selector and Trigger Selector . . . 132

5.2 Concept of Operation . . . 133

5.3 Firmware Description . . . 135

5.4 Benchmarking Tests Description . . . 138

5.5 Integration into SSTCAM . . . 140

5.5.1 M2 Flasher Integration . . . 141

5.5.2 Corner Flasher Integration . . . 141

5.5.3 Flasher Fibre Integration . . . 146

5.6 Conclusion . . . 147

6 Application of the Flasher Systems in SSTCAM **151**

6.1 Functional checks . . . 152

6.2 Pixel Linearity . . . 153

6.3 Flat Fielding . . . 155

6.3.1 Case 1: Uniform Illumination . . . 157

6.3.2 Case 2: Gaussian Illumination 158
6.3.3 Case 3: Gaussian Illumination + Diffuser 162
6.4 Single Photoelectron Calibration 166
6.4.1 Dark Count Photons 168
6.4.2 Underlid Flasher 176
6.5 Conclusion 178

7 Summary and Future Work **181**

Appendix **187**

A Dark count vs Flasher - Which is Faster? **187**

Bibliography **189**

List of Figures

1.1 All particle cosmic ray spectrum 3
1.2 Fermi all sky map of gamma rays 5
1.3 Electromagnetic process producing gamma-rays 8
1.4 Pair production by interaction of gamma ray with matter 11
1.5 Earth opacity to electromagnetic radiation 12
1.6 Space based gamma ray telescopes 13
1.7 Production mechanism of electromagnetic shower 16
1.8 Production mechanism of hadronic shower 17
1.9 Dipole moment creation due to passage of charged particle 18
1.10 Wavefront generation in cherenkov radiation 19
1.11 Cherenkov light pool 21
1.12 Cherenkov real image 21
1.13 Air shower to camera image 22
1.14 Stereoscopic observation with IACT 23
1.15 Comparison of differential sensitivity 25
1.16 Comparison of angular resolution. 26
1.17 Different types of Telescopes for CTA 27
1.18 Proposed alpha configuration array 30
1.19 Computer rendering of CTA sites 31

2.1 Annotated picture of CHEC camera prototypes 36
2.2 CAD model of SSTCAM 37
2.3 Simplified representation of a SiPM pixel 39
2.4 Comparison of Cherenkov spectrum and PDE of SiPM 40
2.5 Different types of optical crosstalk in SiPM array 41
2.6 Performance characterisation of SiPM for SSTCAM 43
2.7 Annotated picture of the TARGET module 44
2.8 Comparision of SPE spectrum between SiPM and PMT 47
2.9 VERITAS calibration system 49
2.10 LST calibration system 50
2.11 MST calibration system 51

3.1 Operational block diagram of calibration system 56
3.2 Timing block component connection 57
3.3 Timing diagram showing the setup of DS1023 58
3.4 Photo relays manipulating the brightness of Light Emitting Diode (LED) Flasher 61
3.5 Pinout diagram of the microcontroller 62
3.6 Block diagram of the Ethernet driver 63
3.7 Choice between internal and external trigger 65
3.8 Pictures of V1, V2 and V3 Flasher board 66
3.9 CAD model of the version 3 baord 67
3.10 Description of the version 3 firmware 69
3.11 SiPM evaluation board 71
3.12 Characteristic Flasher signal observed by an SiPM detector. 73
3.13 Lab test setup 74
3.14 Plot to indicate time take by Flasher to reach stable operation 80
3.15 Pulse-to-pulse intensity variation of Flasher 81
3.16 30 minutes intensity stability of Flasher 82
3.17 Dynamic range study of the Flasher system. 83
3.18 Temperature stabilisation of the Flasher board 84
3.19 Linear fit to temperature stability 85

3.20 Flasher intensity dependence on temperature 86
3.21 Application of the temperature correction 87
3.22 Frequency dependence of Flasher Intensity 88
3.23 Robot arm setup used to scan the beam 89
3.24 Measured beam profile of the Flasher LED 90
3.25 Representation of the timing parameters tested in V3 test 91
3.26 Pulse width distribution of the Flasher 92
3.27 Event time distribution of the Flasher 93
3.28 Rise time and fall time distribution of the Flasher 94
3.29 Long term test results of the Flasher 95

4.1 Test setup to perform line scans of fibre 102
4.2 Line scans of scintillating fibre 104
4.3 Line scans of light diffusing fibre 105
4.4 Preparation for the test to find the illumination pattern by scintillating fibre 107
4.5 Illumination pattern with the scintillating fibre 109
4.6 Time profile across all pixels with the scintillating fibre and the light diffusing fibre 110
4.7 Preparation for the detailed test to find the illumination pattern by scintillating fibre 114
4.8 Sheets of material tested for their reflectivity 115
4.9 Sheet of material reflectivity curve 116
4.10 Illumination pattern for scintillating fibre recorded with TARGET module 117
4.11 Variation of illumination across each quarter 118
4.12 FWHM distribution across all the pixel 118
4.13 Coupling mechanism of LED and fibre 119
4.14 Illumination pattern by the M93L01 fibre 120
4.15 Coax cable connection to the Flasher board 123
4.16 Test setup for noise test of coaxial cable 124
4.17 Average baseline amplitude value with and without coaxial cable . . . 125

5.1 Potential location of the Flasher V4 board 129
5.2 Block diagram of V4 Flasher 130
5.3 Pinout and staged output of SIPO 132
5.4 CAD model of V4 Flasher 134
5.5 Concept of operation for V4 Flasher 136
5.6 Bit transfer example for setting up Flasher V4 137
5.7 Location of Flasher within camera 142
5.8 Corner Flasher assembly 143
5.9 Attachment of M2 Flasher assembly to telescope structure 144
5.10 Illumination pattern observed by CHEC M 145
5.11 Corner Flasher assembly 146
5.12 Fibre placement in the CAD model 147
5.13 Fibre placement in the CAD model 148
5.14 Coupling of the LED to the fibre 148
5.15 CAD model of the Flasher V4 placed inside camera 149
5.16 Image of the Flasher V4 after production 150

6.1 Plot showing the linearity of the pixels for SiPM module 154
6.2 Plot showing the linearity of the pixels for SiPM module 154
6.3 Gaussian distribution of baseline noise 156
6.4 Camera response to uniform illumination 158
6.5 Amplitude dependence of the flat field correction for uniform illumination 159
6.6 Flat field result simulation with uniform illumination source 159
6.7 Camera response to Gaussian Illumination 160
6.8 Amplitude dependence of the flat field correction for Gaussian illumination 161
6.9 Spatial uniformity dependence of the flat field correction for Gaussian illumination 162
6.10 Flat field result simulation with Gaussian illumination source 163
6.11 Comparison between Gaussian illumination and Gaussian-plus-diffuser illumination 164

6.12 Camera response to Gaussian-plus-diffuser illumination 164
6.13 Amplitude dependence of the flat field correction for Gaussian-plus-diffuser illumination 165
6.14 Spatial Uniformity dependence of the flat field correction for Gaussian-plus-diffuser illumination 166
6.15 Flat field result simulation with Gaussian-plus-diffuser illumination source 167
6.16 Python classes and methods in the SSTCAM simulation software . . 169
6.17 Method to recover the charge from the signal waveform using template pulse 171
6.18 Reference pulse used for charge extraction from event waveform . . . 171
6.19 Plot between charge extraction efficiency, noise level and optical crosstalk173
6.20 SPE spectrum for simulation data 174
6.21 Gain error vs noise level and optical crosstalk from simulation data . 175
6.22 Best fit SPE spectra for experimental data at different NSB level . . . 177
6.23 Relationship between gain and NSB level for experimental data . . . 178
6.24 SPE calibration using underlid Flasher channel 179

7.1 Trinity and QCAM 186

List of Tables

1.1 LST main design parameters 27
1.2 MST main design parameters 29
1.3 SST main design parameters 29

2.1 Main Parameters of LVR3 SiPM technology 42
2.2 Requirements of the calibration device set by CTAO 53

3.1 Truth table for LMG1025 56
3.2 Effective resistance for different current settings 60
3.3 Basic methods for Flasher operation 68
3.4 Basic methods to operate the power supply 75
3.5 Basic methods to operate the Arbitrary Waveform Generator (AWG) 75
3.6 Basic methods to operate the temperature chamber 76
3.7 Basic methods to operate the oscilloscope 76
3.8 Visual checks and startup tests for the Flasher 78
3.9 Requirement vs Measured parameters for calibration system 97

4.1 Requirements for the next Flasher version. 99
4.2 Candidate materials for the rear-side of the door 113
4.3 Door material reflectivity results 113

4.4 Fibres tested for flat fielding 119
4.5 Optical properties with and without coaxial cable 123

5.1 Envisioned test procedures for the version 4 Flasher 140

6.1 Simulated illumination pattern for flat fielding tests 156

7.1 Requirement vs measured parameters for calibration system 183

Abbreviations

CTA Cherenkov Telescope Array

CTAO Cherenkov Telescope Array Observatory

SWGO Southern Wide-field Gamma-ray Observatory

SST Small Sized Telescope

IACT Imaging Atmospheric Cherenkov Telescopes

CHEC Compact High Energy Camera

SiPM Silicon Photomultiplier

NSB Night Sky Background

NSB Dark Count Rate

PMT Photomultiplier Tubes

PDE Photon Detection Efficiency

DAQ Data Acquisition System

UV Ultraviolet

IC Inverse Compton

LED Light Emitting Diode

SPE Single Photoelectron

RMS Root Mean Square

DCR Dark Count Rate

QCAM Quarter Camera

MCAM Mechanical Camera

FET Field Effect Transistor

DL Data Level

TIR Total Internal Reflection

PMMA Polymethyl Methacrylate

SPI Serial Peripheral Interface

PCB Printed Circuit Board

SIPO Serial In Parallel Out

TARGET TeV Array Readout Electronics with GSa/s sampling and Event Trigger

SMA SubMiniature version A

UV Ultra Violet

CR Cosmic rays

VHE Very High Energy

EAS Extensive Air Shower

CAD Computer Aided Design

ND Neutral Density

Introduction

Cherenkov Telescope Array Observatory (CTAO) is the next generation gamma ray experiment that is envisioned to offer at least an order of magnitude enhancement in the sensitivity compared to current generation telescopes. With a varied range of telescopes, Cherenkov Telescope Array (CTA) will offer an unprecedented view of the gamma ray sky in the energy range of 20 GeV - 10 TeV and beyond. This thesis presents the design, testing and integration of the calibration system for the Small Sized Telescope's camera.

Chapter 1 introduces the astrophysical origin of gamma rays in the Universe. Alongside discussing the gamma ray production mechanism, it also mentions the absorption and attenuation processes that shape gamma ray observations. With a short discussion about the space-based and ground-based detection principles, the process of Cherenkov radiation generation in the atmosphere and the ways Imaging Atmospheric Cherenkov Technique are used to observe these nanosecond scale radiation is outlined. The chapter concludes with an overview of the CTAO, its motivations, specifications, possible array layouts, and the key science projects it is designed to address.

Chapter 2 shifts the focus from the science case to the enabling technology. It

presents a detailed overview of the camera developed for the Small-Sized Telescope of CTA, with particular emphasis on the chosen photosensors (SiPM) and the associated data acquisition system. Since the quality of scientific observations is directly tied to the stability of the photosensors, whose performance may drift due to their intrinsic properties or environmental factors, a dedicated calibration system is essential. Such a system ensures that any degradation in performance is tracked and corrected during online operation or offline analysis. The chapter systematically reviews calibration systems currently employed in existing gamma ray telescopes and concludes by outlining the specific performance requirements defined by CTA for the Small Sized Telescope (SST) camera calibration unit.

Chapter 3 introduces the design principles underlying the development of the calibration device for SSTCAM. It describes the progression of design prototypes, the implementation of the latest firmware, and the overall concept of operation. The chapter then presents a detailed performance study of the version 3 of the device, benchmarked against CTAO requirements. Test procedures and results are reported for key aspects such as dynamic range, dependence on operating conditions, timing characteristics, and beam profile. The chapter concludes with a comparison between the specified requirements and the achieved performance.

Chapter 4 establishes the motivation for developing a new version of the calibration system. It explores two possible extension pathways and presents focused tests to evaluate their feasibility. The lessons learned from these studies informed the decision to employ multiple illumination channels, each tailored to support different calibration activities within the SSTCAM camera.

Chapter 5 builds on the lessons learned from the focused studies in Chapter 4 and introduces the design evolution of the new calibration system. It details the component choices, the revised concept of operation, and the improvements introduced over earlier versions. The chapter also outlines the planned procedure for integrating this upgraded system into the SSTCAM camera.

As the SSTCAM camera is still under development and the full system is not yet available, Chapter 6 presents simulation studies designed to assess the feasibility of different calibration activities using the dedicated calibration unit. In particular, three key tasks are examined in detail: pixel linearity monitoring, single photo-electron calibration, and flat-fielding.

Chapter 7 presents the thesis conclusion. It discusses the characterisation result of the version 3 of the Flasher and mentions how it compares with the requirements set by CTAO. It discusses the advantages and drawbacks of using fibre system and coaxial cable systems for a multi-channel Flasher. It also discusses the simulated result of different application of the Flasher. Towards the end, it mentions about the improvements that can be done to enhance the dynamic range and intensity of the Flasher. The chapter ends with discussion about the Flasher application outside of SSTCAM.

CHAPTER 1

Gamma Ray Astronomy

This chapter provides an overview of very high-energy gamma ray astronomy, beginning with a discussion of cosmic rays, gamma rays, and the fundamental interactions responsible for gamma ray production. Where relevant, theoretical models describing these mechanisms are introduced, accompanied by examples of astrophysical sources in the universe that are believed to emit gamma rays. The chapter then examines the detection techniques and observational strategies employed by current instruments, with particular emphasis on Imaging Atmospheric Cherenkov Telescopes (IACT). Finally, the next-generation ground-based observatory, the CTA, is introduced, highlighting its anticipated performance and key scientific objectives.

1.1 Cosmic Rays

The study of very high-energy phenomena in the Universe is intimately linked to the discovery of cosmic rays. The existence of this radiation was first demonstrated by Victor Hess in 1912 during a series of balloon flights, for which he was later awarded the Nobel Prize in Physics (1936) [1]. Hess observed that the ionization levels in the atmosphere increased with altitude, contradicting the expectation that

radiation from the Earth's crust would decrease with height. His daring experiment, conducted up to altitudes of about 5 km, revealed that highly penetrating radiation of extraterrestrial origin continuously bombards our planet. This marked the beginning of cosmic-ray physics and, in a broader sense, high-energy astrophysics.

Cosmic rays are predominantly composed of charged particles. About 90% of them are protons (hydrogen nuclei), 9% are helium nuclei, and roughly 1% are heavier nuclei extending up to iron and beyond [2]. A small fraction consists of electrons, positrons, and other subatomic particles. Their energies span an extraordinary range, from a few MeV up to beyond PeV energy range, far exceeding the energies achievable in human-made accelerators. At Earth, the cosmic-ray flux is steeply falling with energy. Figure 1.1 shows the cosmic ray spectrum which suggests that roughly one particle per square centimetre per second strikes the upper atmosphere at GeV energies, while at PeV energies the flux drops to about one particle per square meter per year [3]. At the extreme end, ultra-high-energy cosmic rays are so rare that only about one particle per square kilometre per century reaches Earth. The spectrum also indicates two distinctive spectral feature, called the 'knee' and the 'ankle'. At the knee region the power law spectral index changes from 2.7 to 3. One possible interpretation of the knee in the cosmic-ray spectrum is that it marks the energy at which a particle's gyro-radius becomes comparable to, or larger than, the characteristic scale of the Galactic magnetic field. At this point, the particles can no longer be efficiently confined within the Milky Way, leading to their escape into inter-Galactic space. This loss of confinement naturally explains the observed steepening, or falloff, in the cosmic-ray spectrum [4]. On the other hand, the ankle region signifies the transition of the major contribution from Galactic to extragalactic cosmic rays [4].

During their travel from the cosmic accelerators to earth, the direction information of the cosmic rays is lost due to their interaction with the Galactic and interplanetary magnetic field. Even a century after Hess's cosmic ray discovery, the origin, acceleration mechanism and propagation of cosmic rays continue to be central open questions in modern astrophysics. Thus, there is a major push towards observation of gamma rays which are also the by-product of particle acceleration.

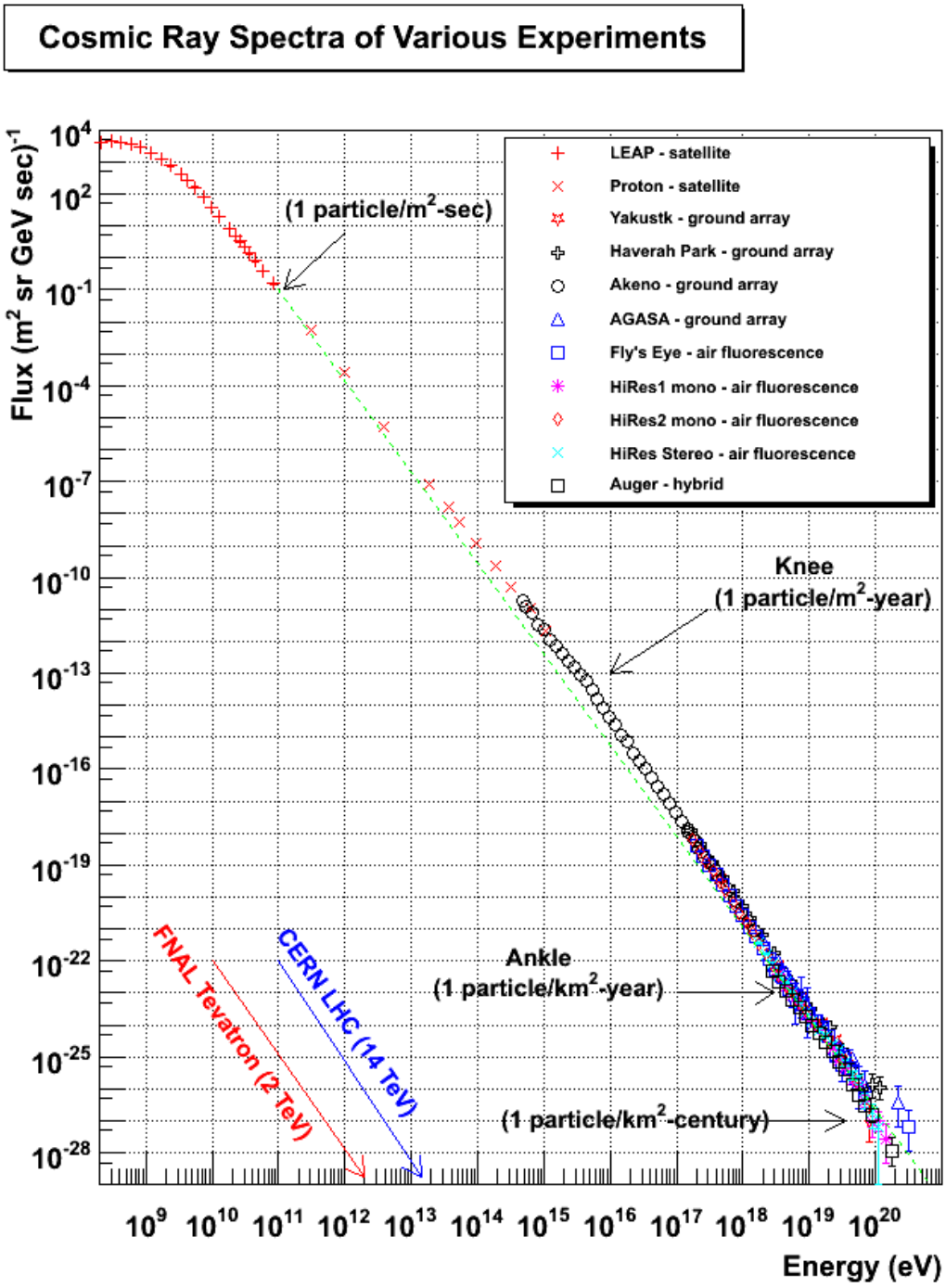

Figure 1.1: Cosmic-ray energy spectrum spanning from 10^8 eV to 10^{20} eV. The spectrum follows a broken power-law, with the spectral index steepening from 2.7 to 3 at the so-called knee. This feature marks the energy at which the particle gyro-radius exceeds the confinement capability of the Galactic magnetic field. The region between the knee and the ankle is dominated by Galactic sources, while the ankle indicates the transition to an extragalactic origin of cosmic rays [4].

Like any other electromagnetic radiation, their propagation is not influenced by the magnetic field, thus providing a direct insight into the acceleration sites. Hence, gamma ray astronomy plays a vital role in modern day astronomy in unravelling some of these long standing mysteries.

1.2 Gamma Rays

Gamma rays are the most energetic photons in the electromagnetic spectrum, extending from 511 keV to beyond tens of TeV. Such high energy photons cannot be thermally generated, rather they are radiated via electrodynamical processes that occur in the most violent particle accelerators that can be found in the universe. Figure 1.2 shows the *Fermi*-Gamma ray Space Telescope(*Fermi*) all-sky survey with 13 years of observation data (2008 - 2021). The diffuse glow along the Galactic plane arises from interactions of cosmic rays with interstellar gas and radiation fields. It also shows numerous point-like and extended sources like pulsars, supernova remnants, active galactic nuclei, and gamma ray bursts — objects that represent the most extreme environments in the universe.

Gamma rays are commonly divided according to their energy as follows.

- Low Energy (HE): 0.5 MeV $\leq$ E $\leq$ 3 MeV
- Medium Energy (HE): few MeV energy range
- High Energy (HE): 10 MeV $\leq$ E $\leq$ 100 GeV
- Very High Energy (VHE): 100 GeV $\leq$ E $\leq$ 100 TeV
- Ultra High Energy (UHE): 100 TeV $\leq$ E $\leq$ 100 PeV
- Extreme High Energy (EHE): E $\geq$ 100 PeV

The distinction of gamma rays into these energy bands are approximate and are largely based on the detection technique used to observe them. The motivation for gamma ray astronomy lies not only in identifying and characterizing these sources but also in addressing fundamental questions about the origin and acceleration of

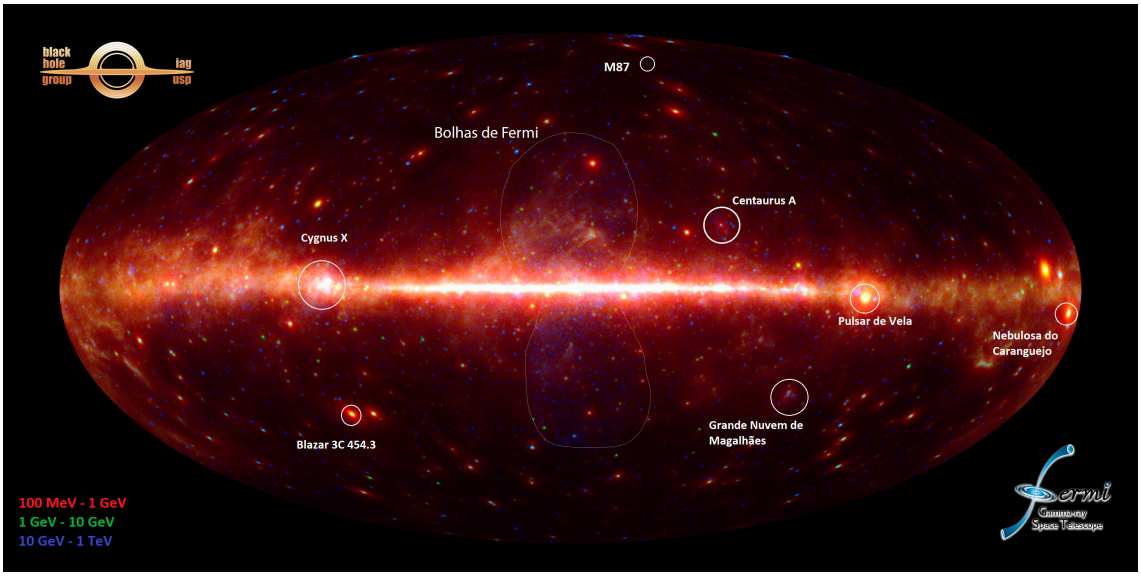

Figure 1.2: The all-sky image of gamma rays observed by the *Fermi* Gamma ray Telescope after 13 years of operation. The color bands indicate different energy ranges. The diffuse glow of gamma-rays produced from interaction of cosmic rays as well as many discrete gamma ray sources close and far from the galactic plane are visible [5].

cosmic rays, the behaviour of matter under extreme conditions, the nature of dark matter and even physics beyond the standard model. First of all, it is important to understand the production mechanism of gamma rays.

1.3 Gamma ray Production Mechanism

Gamma rays originate from non-thermal interactions involving highly energetic particles. Whenever relativistic particles, such as electrons, protons, or heavier nuclei, encounter matter, magnetic fields, or radiation fields, they can transfer part of their energy into high-energy photons. Broadly, these mechanisms are categorized into two classes: electromagnetic processes, where energetic electrons produce gamma rays through interactions with fields and photons, and hadronic processes, where collisions of high-energy nuclei lead to the creation and subsequent decay of secondary particles that emit gamma rays. The specific processes are discussed in Section 1.3.1 and 1.3.2.

1.3.1 Electromagnetic Process

Bremsstrahlung

Bremsstrahlung, or "braking radiation", occurs when a charged particle—typically a relativistic electron or proton—is deflected by the Coulomb field of an atomic nucleus, emitting part of its kinetic energy as a photon. The radiation power is inversely proportional to the mass of the accelerating particle. Since an electron is about 1836 times lighter than a proton, it emits significantly more radiation than a proton. In astrophysical environments, this process becomes an efficient gamma ray production channel in regions with high densities of ambient matter. For instance, in the solar atmosphere, energetic electrons accelerated during solar flares undergo Coulomb interactions with ions in the dense chromosphere, producing Bremsstrahlung photons observable from X-ray to gamma ray energies [6]. A representation of the Bremsstrahlung process is shown in Figure 1.3 (*top*).

Inverse Compton Scattering

Compton scattering results from the interaction of a high energy photon with unbound electrons (unlike the photoelectric effect in which photons interact with bound electrons). The change in the energy of the re-emitted photon is given by:

$$\Delta \mathrm{E} = \frac{\mathrm{E}_i \mathrm{E}_f}{\mathrm{m}_e \mathrm{c}^2}(1 - \cos\theta) \tag{1.1}$$

where E_i and E_f are the energy of incoming and scattered photon respectively, m_e is the mass of electron, c is the speed of light and θ is the angle of scattering.

On the contrary, when high-energy electrons transfer part of their energy to low-energy photons, the photon is up scattered to higher energies producing the Inverse Compton (IC) emission. It is exact opposite of the classic Compton scattering. In the rest frame of the electron, the scattered energy is given by

$$\mathrm{E}_{scattered} \approx \gamma \mathrm{E}_{primary}(1 + \beta\cos\theta) \tag{1.2}$$

where γ is the Lorentz factor, $\beta = \frac{\mathbf{v}}{\mathbf{c}}$, and $\mathrm{E}_{scattered}$ and $\mathrm{E}_{primary}$ are the scattered

photon and initial photon energy. Transforming it to the observer frame, this results in $E_{scattered} \sim \gamma^2 E_{scattered}$.

In astrophysical environments, IC is an important mechanism wherever relativistic electrons coexist with intense radiation fields. A striking example is the gamma ray halo around the Sun, observed with *Fermi*-LAT, where cosmic-ray electrons scatter off the solar photon field, producing a diffuse gamma ray glow extending several degrees around the solar disc [7]. Figure 1.3 (*middle*) explains the process of Compton scattering and inverse Compton scattering.

Synchrotron Radiation and Curvature Radiation

Synchrotron radiation is produced when relativistic electrons travel in spiral paths around the magnetic field. The radiation is emitted in form of a beamed cone (shown in Figure 1.3 (*bottom*)). This is different to curvature radiation where the high energy particle curves its path in the presence of a strong magnetic field and emits radiation due to deceleration. Curvature radiation is a special case of synchrotron radiation. The non-relativistic counterpart of this type of radiation is known as cyclotron radiation. Synchrotron radiation is particularly relevant in highly magnetized environments such as pulsar wind nebulae, where electrons accelerated by the pulsar's wind interact with strong magnetic fields, producing broad-band non-thermal emission from radio to gamma rays [8].

In addition to electrons, relativistic protons can also emit synchrotron radiation, although at much higher energies due to their larger mass. Proton synchrotron radiation is considered in extreme astrophysical sources such as active galactic nuclei jets and gamma ray bursts, where ultra-high-energy protons spiral in intense magnetic fields, potentially contributing to observed very-high-energy gamma ray emission. For instance, in the case of the blazar Mkn 501, proton synchrotron radiation has been considered as a potential source of high-energy emission, particularly in the TeV range [9].

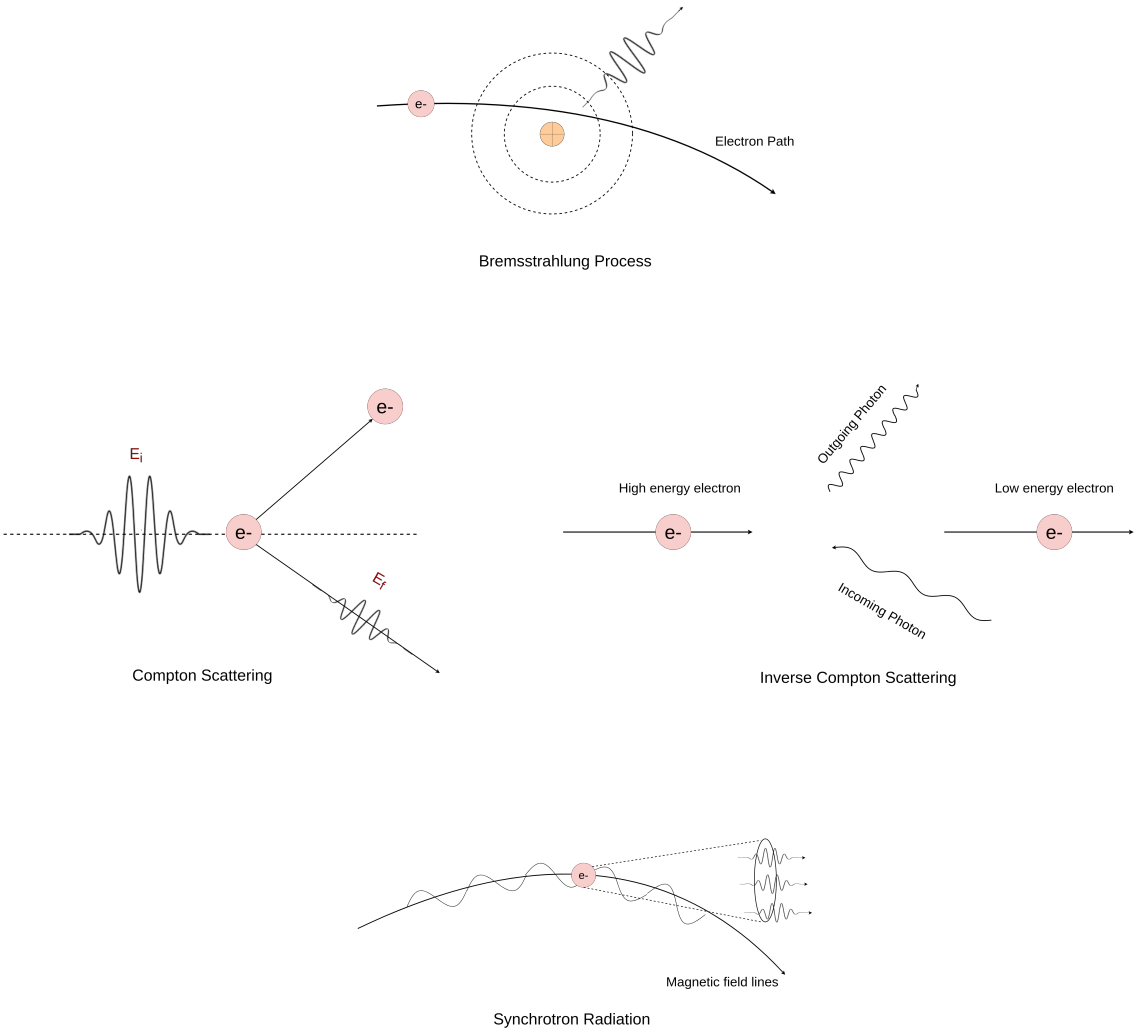

Figure 1.3: Illustration of electromagnetic processes producing gamma rays. (*top*) Bremsstrahlung: gamma rays emitted as an electron is decelerated in the Coulomb field of an atomic nucleus. (*middle*) Compton and inverse Compton scattering: gamma rays generated when electrons transfer energy to photons during collisions. (*bottom*) Synchrotron radiation: gamma rays produced by relativistic charged particles spiralling in a magnetic field.

1.3.2 Hadronic Process

Pion Production

When a high energy particle collides with surrounding matter, the collision produces huge number of secondary particles. The most favourable hadronic interaction is the proton-proton interaction which produces charged pions (π^+, π^-) and neutral pions (π^0) in equal abundance. The neutral pions have the shortest lifetimes, decaying on a timescale of 8.4×10^{-17} s into gamma ray photons, muons and muon neutrinos [10].

$$\pi^0 \rightarrow \gamma\gamma \ , \qquad \pi^+ \rightarrow \mu^+ + \nu_\mu \ , \qquad \pi^- \rightarrow \mu^- + \bar{\nu}_\mu \tag{1.3}$$

The detection of gamma rays with spectra characteristic of pion decay provides direct evidence for the presence of high-energy protons. Additionally, the neutrinos produced offer a unique window for neutrino astronomy [11]. A well-known example of gamma ray production via pion decay occurs when Cosmic rays (CR)s interact with the solar atmosphere. The intensity of the resulting gamma ray emission depends on the penetration of CRs, which varies with the solar cycle, leading to a correlation between gamma ray flux and solar activity [7].

Nuclear process

Processes such as photo-ionization or inelastic collisions can excite atomic nuclei to higher energy states. The subsequent de-excitation produces photons with energies characteristic of the nuclear transitions, typically in the MeV range, and thus observable in the low gamma ray regime. A well-studied example is the 1.809 MeV gamma ray line from the decay of radioactive aluminium-26 (half life of 7.2M years), which is produced in massive stars and supernovae. This line emission has been detected from supernova remnants and across the Galactic plane, providing key evidence for ongoing nucleosynthesis in the Milky Way [12].

1.4 Gamma ray Interaction

Understanding the interactions of gamma rays with matter and radiation is essential for both interpreting astrophysical observations and designing detectors. High-energy photons can be absorbed, scattered, or converted into particle-antiparticle pairs, affecting their propagation through space and their detectability. The following section discusses how gamma-rays are absorbed or attenuated.

Pair production with photon

On the collision of two photons with total energy greater than the rest mass energy of two electrons (1.02 MeV), they produce an electron positron pair, thus eliminating the gamma ray photon. The excess energy of the photons is transferred into the kinetic energy of the produced pairs. This is a common attenuation process of gamma rays emanating from distant astrophysical sources. They get attenuated in the photon field of Extragalactic Background Light (EBL), which is believed to originate from the first generation of stars in the early universe. This raises an important cosmological question about the density of the EBL, which can be constrained by examining the optical depth of Very High Energy (VHE) photons as a function of redshift and its resulting imprint on the high-energy spectra of distant sources [10].

Pair production with matter

A gamma ray photon can also interact with the Coulomb field of an atomic nucleus to produce electron positron pair. A illustration of the process is shown in Figure 1.4. The process is given by

$$\gamma + \mathrm{Z} \rightarrow \mathbf{e}^{+} + \mathbf{e}^{-} + \mathrm{Z} \tag{1.4}$$

where Z is the atomic number of the material with which the interaction happens.

Such interactions are especially significant when high-energy photons enter Earth's atmosphere. Here, gamma rays interact with nitrogen and oxygen nuclei, generating high-energy electrons and positrons. These secondary particles subsequently anni-

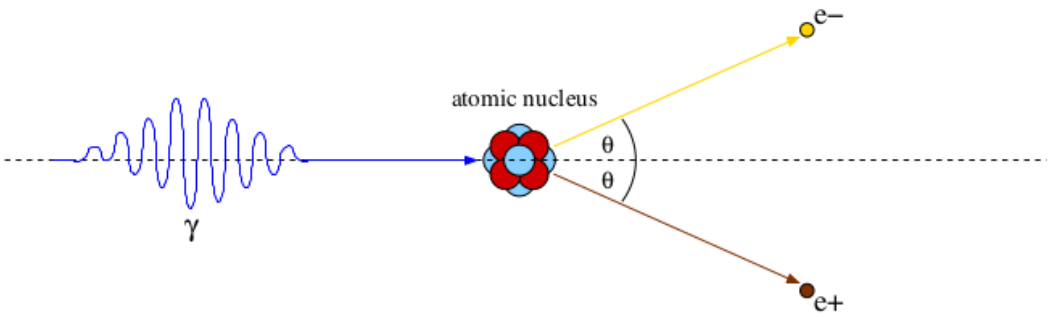

Figure 1.4: Pair production by interaction of Gamma rays with atomic nuclei leading to it's attenuation. Such interaction with the earth's atmospheric nuclei leads to the gamma ray attenuation making their direct detection on earth highly unlikely [13].

hilate, producing new gamma rays and initiating an electromagnetic cascade that yields a large number of high-energy particles. The detection of these particles and their associated radiation forms the basis of ground-based gamma ray astronomy (discussed further in Section 1.6).

This same attenuation mechanism is also fundamental to space-based instruments such as the Fermi Gamma ray Space Telescope, which uses pair production to detect incoming gamma rays. By tracking the trajectories of the produced electrons and positrons, Fermi reconstructs both the direction and the energy of the primary gamma ray (discussed further in Section 1.5.1).

1.5 Gamma ray Detection

The method for detecting gamma rays is directly tied to their energy. While the flux of low-energy gamma rays is high, allowing for their detection by small-area detectors (from centimetres to a metre), the flux of high-energy gamma rays (E≥50 MeV) diminishes significantly. This necessitates the use of very large detectors, ranging from a square meter to a square kilometre in size, which has led to the development of both direct and indirect detection methods.

1.5.1 Direct Detection

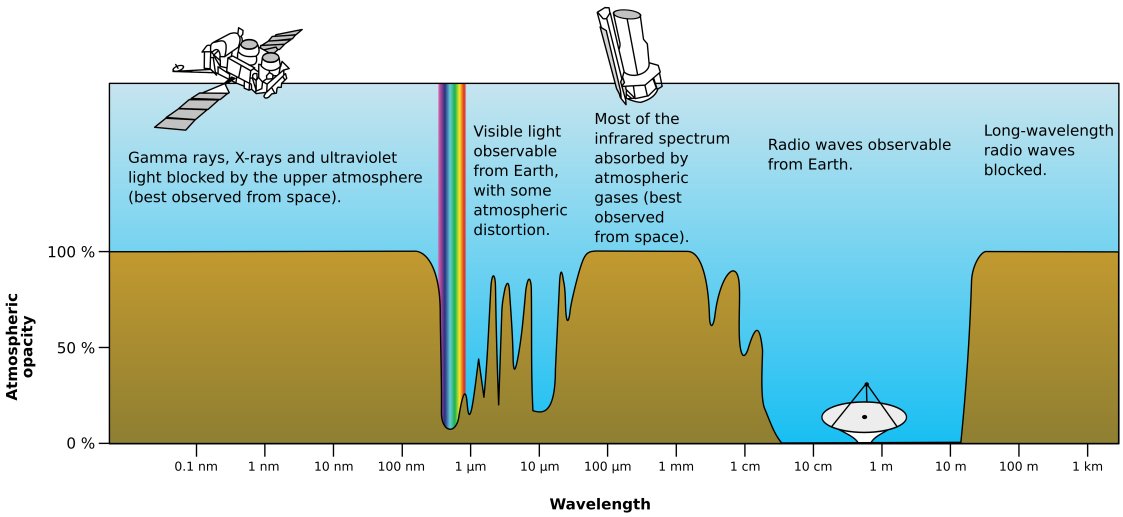

Figure 1.5: Earth's opacity to electromagnetic waves. Gamma rays are completely blocked by earth's atmosphere making their direct detection from ground completely impossible. Space based instrument are favourable for direct detection and indirect methods are used for observation from ground based teelscopes.

Figure 1.5 shows that Earth's atmosphere is completely opaque to high-energy gamma rays. This means direct observation is only possible through space-based telescopes equipped with appropriate detectors. Before the advent of satellite missions, cosmic-ray and gamma ray studies were carried out using high-altitude balloon experiments. A typical space based mission includes a high Z material that enhances the pair production probability, a tracker to reconstruct the direction information and a calorimeter to infer the energy. The first dedicated space-based gamma ray instrument was Explorer XI, launched in 1961, which detected fewer than 100 photons but provided the first evidence of the cosmic gamma ray background [14]. This was followed by COS-B, launched in 1975, which carried a spark-chamber detector and produced the first gamma ray sky map, identifying several sources including the Vela pulsar [15]. The next major step came with the Compton Gamma Ray Observatory (CGRO), launched on April 5, 1991, which hosted multiple instruments. Among them, the Energetic Gamma Ray Experiment Telescope (EGRET) was designed for the 20 MeV to 30 GeV range. EGRET used a spark chamber tracker with a calorimeter to measure the energy and direction of incident gamma rays, while an

anti-coincidence dome suppressed charged-particle backgrounds. This experiment was highly successful, producing a detailed catalog of gamma ray sources and firmly establishing space-based gamma ray astronomy [16].

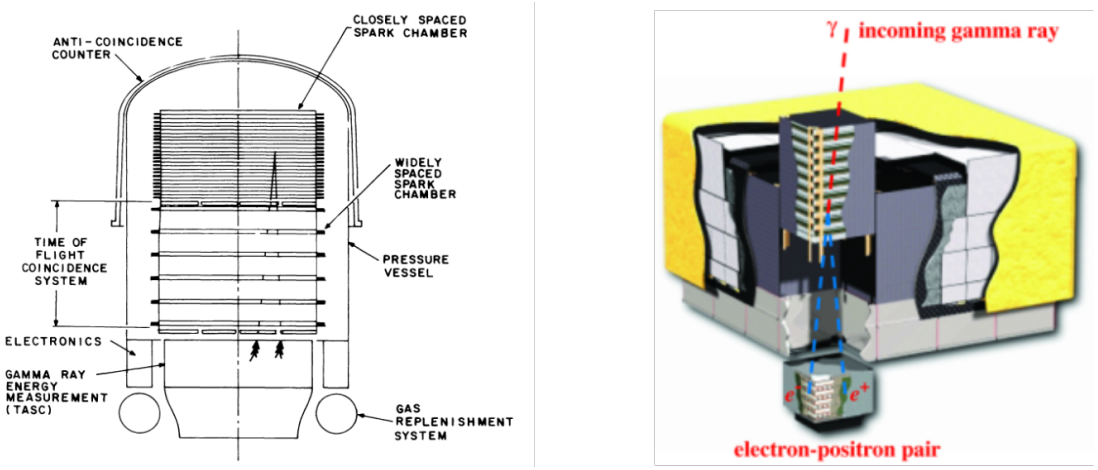

Figure 1.6: (*left*) Energetic Gamma Ray Experiment Telescope (EGRET) on board Compton Gamma Ray Observatory (CGRO) [16] and a cross-section of the *Fermi*-telescope(*right*) showing the silicon trackers and the calorimeter at the base [17].

The success of CGRO has motivated many space mission including SWIFT [18], AGILE [19] and INTEGRAL [20]. The only operational Gamma ray telescope as of today (September 2025) is NASA's *Fermi* telescope (launched on June 2008). It has two instruments- Large Area Telescope (LAT) and Gamma ray Burst Monitor (GBM). *Fermi*-LAT utilizes a series of tungsten foils interleaved between silicon strips. The electron-positron pair produced by the interaction of gamma ray with tungsten are tracked by the silicon stripes (offering directional reconstruction) and ultimately absorbed by a calorimeter (made up of scintillator and PMT) to provide energy information. The GBM comprising of NaI and BGO detectors monitor the count rates to provide information about Gamma ray Bursts (GRBs). Together with the LAT and GBM, *Fermi* telescope offers an excellent window into gamma ray observation from 8 keV to 300 GeV. A cross section of the detector is shown in Figure 1.6 (*right*).

1.5.2 Indirect Detection

As the energy of primary gamma rays increase, progressively larger calorimeters—and thus larger detectors—are required to contain all the particles created in the shower. For example, detecting 1 TeV gamma rays would demand a detector covering an area equivalent to approximately 30 football fields. Constructing such enormous telescopes in space is both logistically and financially unfeasible. Consequently, ground-based observatories remain the only practical option for studying high-energy gamma rays. However, due to the Earth's opacity to gamma rays (Figure 1.5), these observations must be carried out indirectly.

The Earth's ∼100 km atmospheric depth is analogous to the high Z material of space-based telescope. The pair production process in earth's atmosphere leads to a large shower of energetic particles known as an Extensive Air Shower (EAS), discussed later in Section 1.6. The EAS creates particles that are travelling faster than the phase velocity of light in air, thus they emit Cherenkov radiation (discussed later in Section 1.7). Also, depending on the energy of the particles in a shower, they travel deeper in the atmosphere before their first interaction. This makes them accessible at higher altitudes. Depending on what is being observed (particles or Cherenkov radiation), there are two classes of ground based instruments, namely Imaging telescope and particle detector. The imaging type telescope relies on Cherenkov shower rings to reconstruct the direction of primary gamma ray photon (discussed further in Section 1.8) whereas particle detectors rely on the time-of-arrival information to reconstruct the direction [21].

The first type are the particle detectors that directly detect the high energy particles in an air shower through scintillator arrays coupled to Photomultiplier Tubes (PMT)s (GRAPES 3 [22], TUNKA-Grande [23] and KASKADE [24]) or with Resistive Plate Chambers(RPC) [25] as used in ARGO-YBJ [26]. RPCs detect charged particles by amplifying their ionization in a gas gap under a high electric field, with the signal read out via induced charges on external electrodes. The second method of observing high energy particle showers is by using water Cherenkov detectors. Here, the air showers that survive at higher altitudes generate Cherenkov light on passing through large water tanks. These signals are picked up by fast

PMT modules inside the water tank; the time-of-flight information eventually provides the directional reconstruction of the air shower [21]. High Altitude Water Cherenkov (HAWC) [27] and the upcoming Southern Wide field Gamma ray Observatory (SWGO) [28] are two classic examples of water Cherenkov experiments.

In summary, surviving air showers at high altitudes are directly detected using scintillators coupled with photo sensors or RPCs. Likewise, local Cherenkov radiation produced by charged particles in water is measured with water-Cherenkov detectors. Finally, atmospheric Cherenkov radiation generated higher in the atmosphere is observed using imaging air-shower telescopes. However, in this thesis I will concentrate on Imaging Atmospheric Cherenkov Telescope (IACT). Thus, the discussion moves into introducing air showers and how the particle in the air showers create Cherenkov radiation.

1.6 Air Showers

1.6.1 Electromagnetic Air Shower

A primary gamma ray photon entering the Earth's atmosphere initiates an electromagnetic cascade by producing an electron-positron pair via pair production. These secondary particles, in turn, emit photons through Bremsstrahlung as they are deflected by atomic nuclei. Each newly produced photon can then generate another electron-positron pair and each scattered particle (electron and positron) can further undergo Bremsstrahlung process to generate more photons. This cycle repeats forming an electromagnetic air shower which continues until the energy of the particles falls below the critical energy (typically 80 MeV for electrons in air). A simplified representation of this process, based on the Bethe-Heitler model, is illustrated in Figure 1.7. This is based on two assumption that energy is divided equally between each particle at every stage and the radiation length and conversion length are equal(X_0). The shower maximum (t_{max}) can be estimated as

$$t_{max} = n_{max} \times X_0 = \frac{E_0/E_c}{\ln 2} X_0 \tag{1.5}$$

Considering the critical energy as E_c, n_{max} as the maximum number of radiation radiation length after which the energy of the primary particle is attenuated and referring to Heitler model in Figure 1.7,

$$E_c = \frac{E_0}{2^{n_{max}}} \tag{1.6}$$

$$n_{max} = \frac{E_0/E_c}{\ln 2} \tag{1.7}$$

Plugging the value of n_{max} into Eq 1.5, we get

$$t_{max} = \frac{E_0/E_c}{\ln 2} X_0 \tag{1.8}$$

where E_0 is the energy of the primary gamma ray initiating the air shower, E_c is the critical energy where further particle generation stops and X_0 is the radiation length. EAS initiated by gamma-rays occur at altitudes of between 8 km to 12 km depending on the initial photon energy.

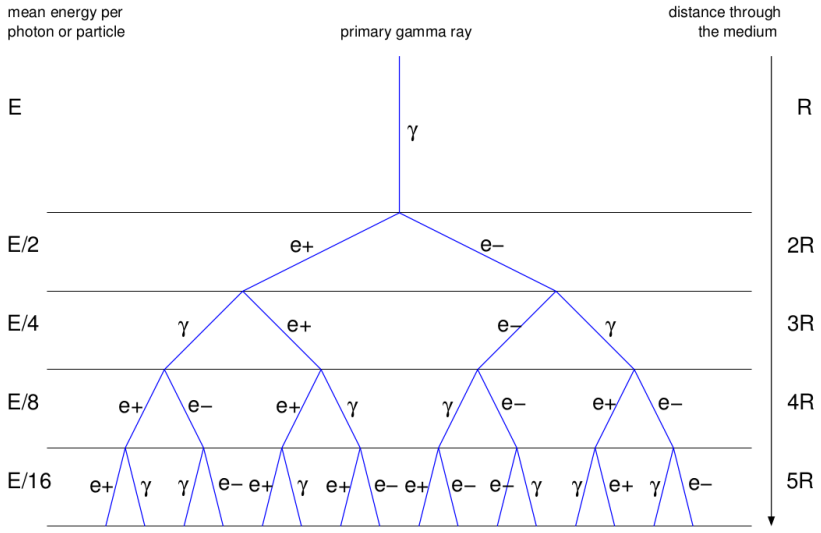

Figure 1.7: Gamma ray induced electromagnetic shower showcasing the energy loss process at each radiation length via pair production. This is a simple model adapted from Longair [29].

1.6.2 Hadronic Air Shower

As discussed in Section 1.3.2, inelastic scattering of hadrons near an atomic nucleus produces unstable mesons (charged and neutral pions). The neutral pions decays into gamma rays which further annihilate into electron-positron pair. The pair produce gamma-rays through Bremsstrahlung radiation and the electromagnetic shower continues from here. Similarly the muons produced from the charged pions decay into electrons and positrons that further produce electromagnetic showers. There is a nucleonic component (protons and neutrons) of the shower that feed both to the electronic and muonic component of the shower. A simplistic representation of the process has been shown in Figure 1.8. The neutrinos produced in the air shower carries the signature that the shower is hadron initiated. Hadronic air showers outnumber the electromagnetic air showers 10^3 to 1, forming a huge background. Since Cosmic rays are primarily high energy protons, they initiate a hadronic air shower in the Earth's atmosphere creating a huge background from Gamma ray observation.

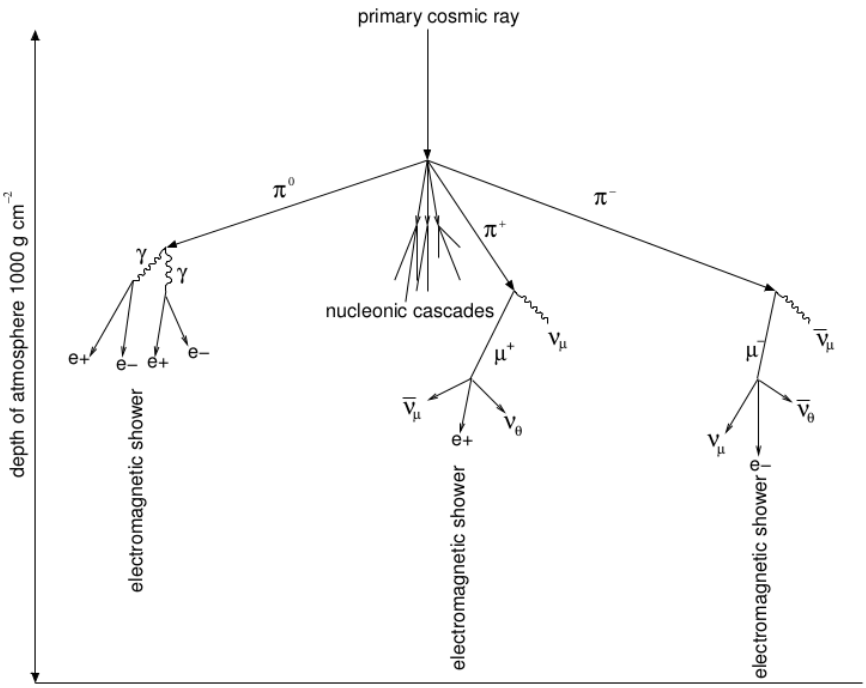

Figure 1.8: Cosmic ray induced hadronic shower showcasing the production of secondary particles through different processes [13]. The neutral and charged pions further produce gamma rays that initiate secondary electromagnetic showers.

1.7 Cherenkov Radiation

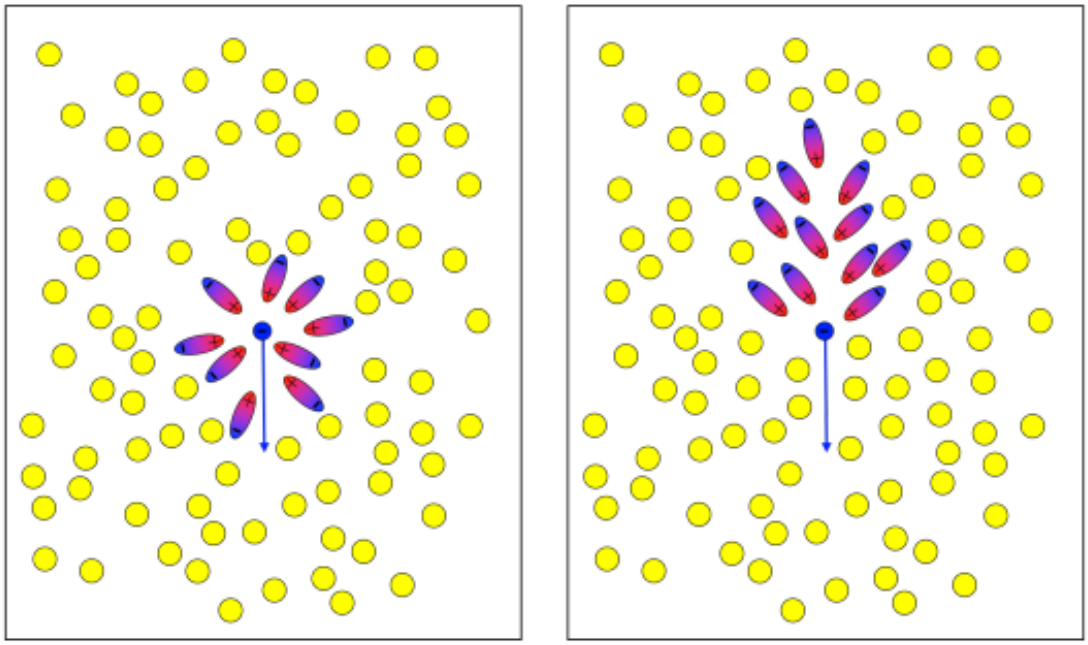

Figure 1.9: Polarisation of the dielectric medium due to passage of charge particle through dielectric medium at non-relativistic speeds (*left*) and at relativistic speeds (*right*) [30].

The charged particles generated in the air showers ionize the medium while travelling through it. At non-relativistic speeds, the overall ionization around the charged particle is symmetric. However, at relativistic speeds, the ionization is asymmetric in the direction of the motion of the particle, creating a net dipole moment (shown in Figure 1.9). This polarised medium releases a burst of electromagnetic radiation, most of which interferes destructively except in the direction of the particle's trajectory. This is known as Cherenkov radiation which was studied in depth by then PhD student Pavel Cherenkov in 1934 [31], and is analogous to generation of sonic boom in sound waves. A simplified geometrical representation of the generation of Cherenkov radiation is shown in Figure 1.10. In the case of air showers, it is mostly UV range dominated.

As seen in Figure 1.10, the opening angle (θ) is given by:

$$\cos\theta = \frac{1}{\beta \mathrm{n}} \tag{1.9}$$

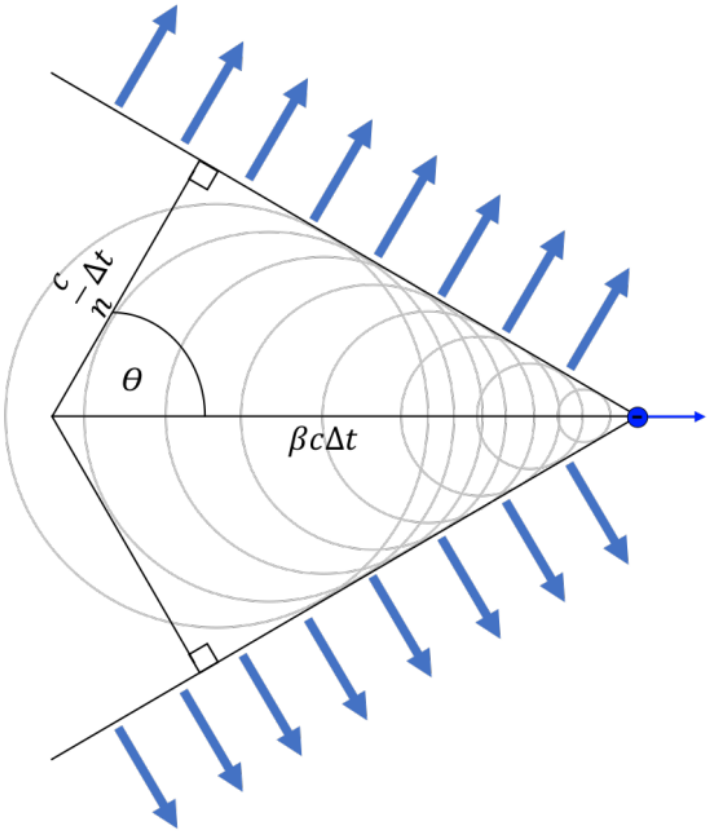

Figure 1.10: Cherenkov light generation when a charged particle travels faster than the speed of light in a dielectric medium.

where $\beta = \mathrm{v/c}$ and n is the refractive index. The spectrum of Cherenkov radiation is given by the Frank and Tamm [2] relation as:

$$\frac{\mathrm{d^2N}}{\mathrm{dxd}\lambda} = \frac{2\pi\alpha \mathrm{z}^2}{\lambda^2}\sin^2\theta \tag{1.10}$$

where α is the fine structure constant and λ is the wavelength at which Cherenkov radiation is emitted per unit path length dx. From the relation in equation 1.10, the total number of Cherenkov photons in an air shower per unit path length dx and between two wavelengths λ_1 and λ_2 can be calculated as the integral:

$$\frac{\mathrm{dN}}{\mathrm{dx}} = 2\pi\alpha \mathrm{z}^2 \int_{\lambda 1}^{\lambda 2} (1 - (\frac{\mathrm{c}}{\mathrm{vn}(\lambda)})^2 \frac{1}{\lambda^2})\mathrm{d}\lambda \tag{1.11}$$

where $\alpha \simeq \frac{1}{137}$ is the fine structure, z is the charge of the particle, $\mathrm{n}(\lambda)$ is the wavelength dependent refractive index of the medium and c is the speed of light. Thus, the Cherenkov photon emission depends on the refractive index of the medium in which it is generated.

As we go deeper into atmosphere, the refractive index increases, changing the opening angle of the Cherenkov radiation leading to the focussing effect of the Cherenkov radiation in a light pool around the trajectory of the charged particle (see Figure 1.11). Typically the opening angle is less than 1.4° leading to a radius of $\sim$ 120 m [10]. Since the distribution of charged particles generated in a hadronic air shower is non-uniform, overlapping Cherenkov rings are observed. This is in contrast to concentric Cherenkov rings which are observed in the case of an electromagnetic air shower (Figure 1.12). In some cases, muons while passing closer to the telescope produce a collimated light cone of Cherenkov light that are focussed by the telescope's mirror into the camera system. These rings looks identical to the one shown in Figure 1.12 (left).

1.8 Imaging Atmospheric Cherenkov Technique

Now it is well understood what to expect from an observation point of view when a primary gamma ray enters into Earth's atmosphere. We are hunting for the

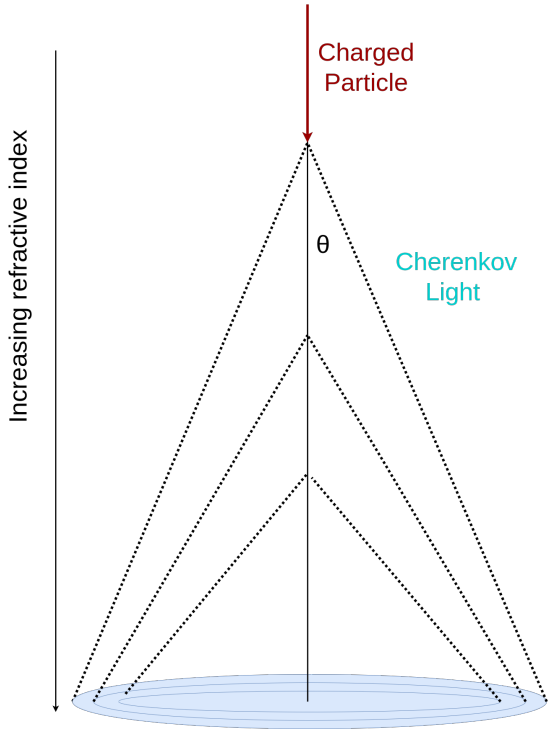

Figure 1.11: The Cherenkov light pool generation due to the change in the refractive index of the atmosphere. As the particle goes deeper in atmosphere, it encounters higher refractive index increasing the Cherenkov opening angle according to equation 1.9, creating concentric rings of light pool.

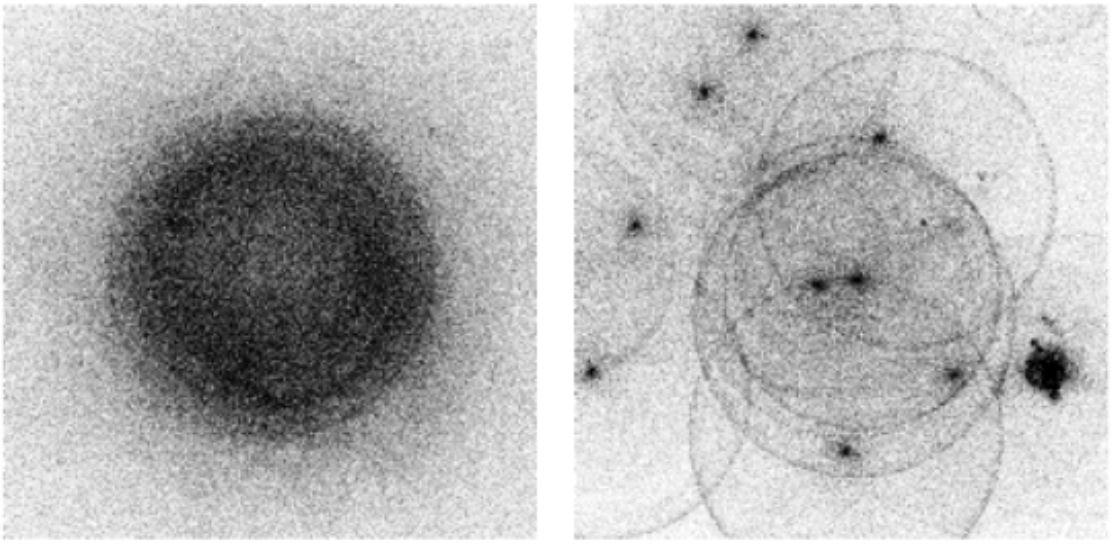

Figure 1.12: Ground distribution of Cherenkov light from a 300 GeV gamma ray (left) and a 1 TeV proton (right), simulated by K. Bernlöhr at MPIK Heidelberg. The hadronic air shower shows a more complex pattern, with contributions from hadronic sub-cores, secondary electromagnetic cascades, and characteristic muon rings [10].

Cherenkov radiation created by gamma rays to infer about it's direction and energy. These radiation exists in the atmosphere on nanosecond timescales (5-100 ns) and contains about 10^2 - 10^5 Cherenkov photons [32]. Thus, with the help of mirrors, they need to be focussed into a fast photo sensor which can create nanosecond snapshots. This is the basic principal of operation for an IACT.

The recorded image typically appears as an elongated, elliptical pattern, with its major axis oriented toward the direction of the primary gamma ray source (represented in Figure 1.13). The angular extent of such images usually spans between 1° - 5°. While a single telescope can be used to estimate the arrival direction of a gamma ray, employing a stereoscopic view significantly enhances the reconstruction accuracy.

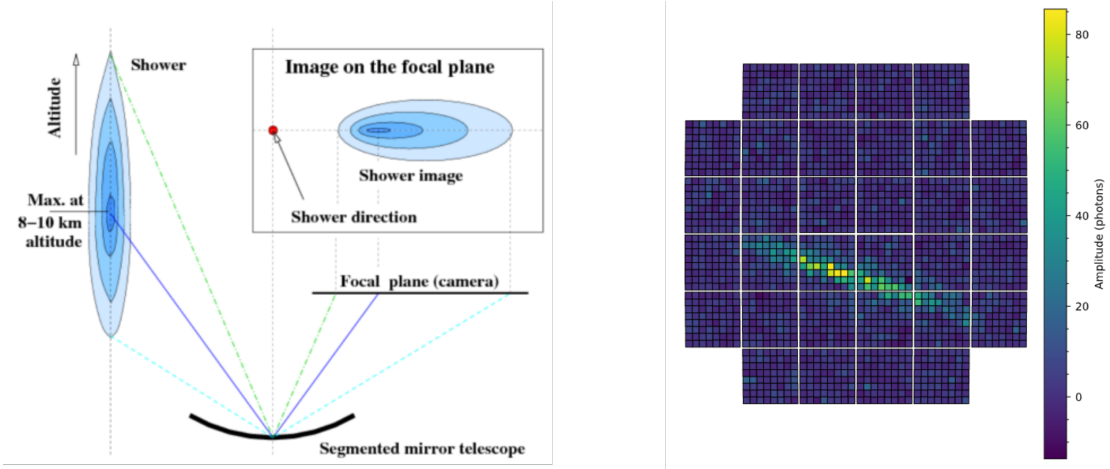

Figure 1.13: (*left*) The representation of the cherenkov image on the camera focal plane [33]. Cherenkov light emitted from the lateral distribution of the shower appears as an elongated ellipse on the focal plane with the major axis pointing towards the direction of the primary gamma ray. (*right*) Observation of a cherenkov image on the CHEC-S camera during a observation campaign.

With multiple telescopes observing the same air shower from different angles, both the position of the shower core (the point where the shower axis intersects the ground) and the arrival direction of the primary particle (its sky coordinates) can be determined with much greater precision. Achieving stereoscopy requires observations with at least two telescopes. An IACT event observed with the CHEC-S (discussed later in Section 2.1) camera of SST and a representative stereoscopic reconstruction is shown in Figure 1.14. Combining the information about the distance

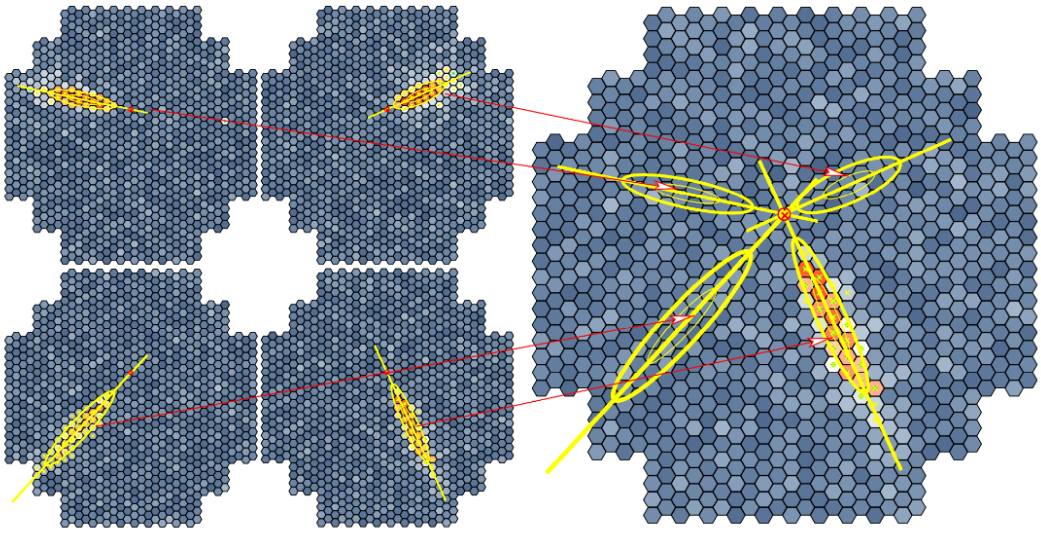

Figure 1.14: A method of locating the direction of primary gamma ray (shower core) using stereoscopic observation from four telescope images [33].

of telescope from the reconstructed shower core and image size (the total amount of integrated signal obtained from the Cherenkov shower), allows the primary particle energy to be inferred. The detailed procedures for air shower reconstruction through Hillas parametrisation [34] or relatively new deep learning methods in IACT data analysis [35] is beyond the scope of this thesis; more detail can be found in [10, 13, 36–38].

Several ground-based facilities have implemented the stereoscopic technique to explore the very-high-energy gamma ray sky. The first operational system, the Whipple Observatory, pioneered the technique and led to the first clear detection of a TeV gamma ray source in 1989 [39]. Subsequent arrays such as HEGRA [40] in La Palma demonstrated the advantages of stereoscopic observations. Today, leading IACT observatories include H.E.S.S. [41] in Namibia, MAGIC [42] in the Canary Islands, and VERITAS [43] in Arizona, LHAASO IACT in China, each contribute significantly to the catalogue of TeV sources and advancing our understanding of cosmic accelerators. More than 300 VHE gamma ray sources have been identified (as of August 2025) [44]. Looking ahead, the CTA, currently under construction, will provide the next generation of IACT observations with unprecedented sensitivity and sky coverage.

1.9 Cherenkov Telescope Array

CTA is the next-generation ground-based observatory for VHE gamma ray astronomy, designed to significantly expand our ability to probe the non-thermal universe. CTA will build on the successes of current IACT and move the field forward by operating as an open observatory[1] [45]. With an unprecedented energy coverage from 20 GeV to 300 TeV, CTA promises to both broaden and deepen our understanding of extreme astrophysical phenomena. Its ambitious performance benchmarks (Section 1.9.1), diverse suite of telescopes (Section 1.9.2) and carefully chosen sites (Section 1.9.3) together form the foundation for meeting its wide-ranging scientific objectives (Section 1.9.4).

1.9.1 Performance

CTA is designed to explore gamma ray energies from a few tens of GeV up to several hundred TeV with unprecedented sensitivity, representing a major leap beyond the capabilities of current experiments. The expected performance, derived from detailed Monte Carlo simulations [45] with 'Alpha' configuration[2], is illustrated in Figure 1.15. The differential sensitivity is defined as the minimum flux needed for a 5σ detection of a point-like source in 50 hours of observation. At lower energies, the sensitivity is primarily constrained by background noise, while at the highest energies it is limited by the intrinsic scarcity of gamma ray photons. For comparison, the sensitivities of the three current IACT facilities (MAGIC, VERITAS, and H.E.S.S.), along with the 10-year Fermi-LAT, 1-year LHAASO, 5-year HAWC, ASTRI 50 hour and SWGO results, are also shown. CTA is projected to achieve up to an order-of-magnitude improvement in sensitivity over existing IACTs in the core 20 GeV - 10 TeV energy range and explore the region above 10 TeV with unprecedented sensitivity for an IACT.

In addition to improved sensitivity, CTA will deliver a significant enhancement in angular resolution (Figure 1.16), defined as the angular radius containing 68% of

[1] An open observatory is a facility where observing time and data are accessible to the wider scientific community, rather than being limited to members of a closed collaboration.

[2] A simulated configuration of the postion of telescopes at the site for optimal performance

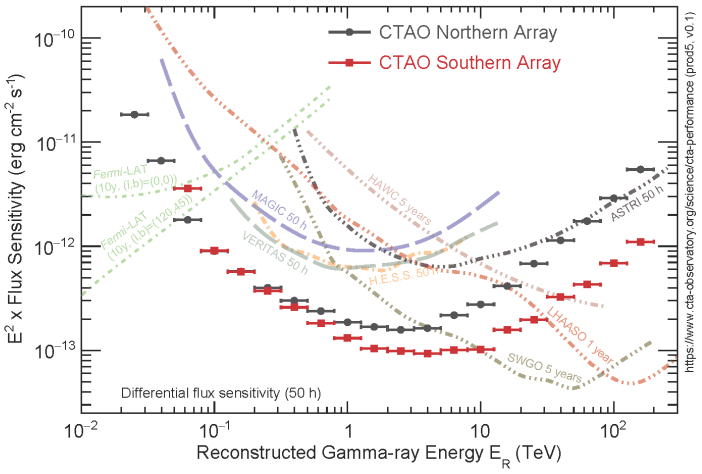

Figure 1.15: Sensitivity plot for different Gamma ray experiments compared to the CTA-North and CTA-South. This plot is from the latest Monte Carlo simulation(prod 5, Alpha configuration) of the CTA performance. There will be an order or magnitude increase in sensitivity compared to current generation telescopes. [46]

reconstructed gamma rays relative to their true direction. This improved resolution will allow more accurate source localization and morphological studies, opening new opportunities for disentangling complex astrophysical regions and reducing source confusion. This provides a concrete proof how CTAO with it's workforce of telescopes occupies a significant spot in wider multi-messenger astronomy network. The alerts from other experiments like SWIFT or ICECUBE could be responded immediately and the event could be studied in immense detail.

1.9.2 CTA Telescopes

CTA will consist of three distinct types of IACTs, each optimized for a different part of the gamma ray energy spectrum. These are the Large Size Telescopes (LSTs), Medium Size Telescopes (MSTs), and Small Size Telescopes (SSTs), illustrated in Figure 1.17.

The need for three telescope classes arises from the physics of Cherenkov light production and the variation of gamma ray flux with energy. At low energies (tens of GeV), the flux of gamma rays is quite high but due to low energy, they produce smaller Cherenkov light pools. Thus, large mirror are necessary to increased light collection efficiency. Thus, small number of large sized telescopes (LSTs) are

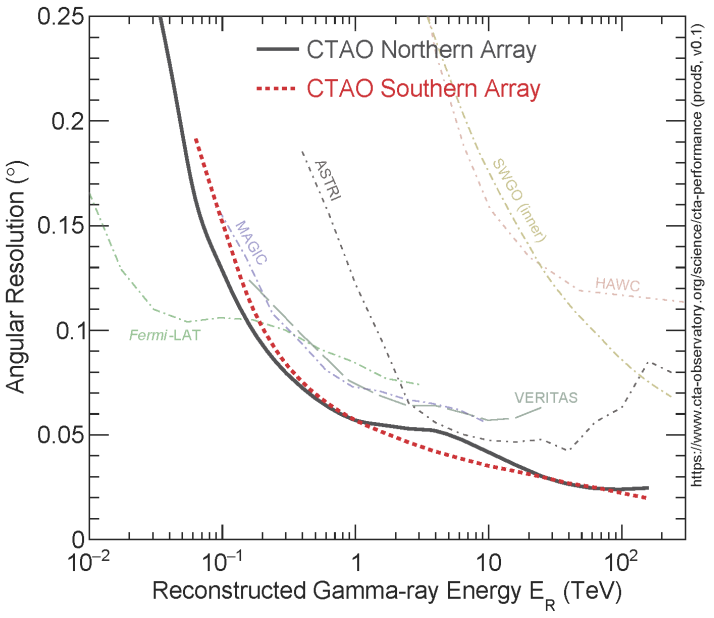

Figure 1.16: Angular resolution plot of CTA-north and CTA-south compared to other gamma ray experiments [46].

sufficient to cater to the low energy range of gamma rays. On contrary, the flux of gamma rays in the high energy regime (tens to hundreds of TeV) is sufficiently low but due to high energy of gamma rays, the Cherenkov light pool is quite big. Thus, there is a need of large number of small sized telescopes (SSTs) spread over an larger area to collect all the Cherenkov lights. Finally, the intermediate range is covered by medium sized telescopes (MST) that offer a balance between the light collection efficiency, cost and sensitivity. Together, they form a complementary system that enables CTA to probe a wide energy range from tens of GeV to hundreds of TeV. The performance matrix and their properties are discussed in the respective sections.

Large Sized Telescope(LST)

The LST is the most powerful low-energy component of the Cherenkov Telescope Array (CTA), designed to access the faintest gamma ray photons in the 20–150 GeV energy band. It features a 23 m-diameter parabolic mirror (approximately 400 m^2 reflective area), built from segmented facets on a lightweight structure using carbon-fibre and steel, allowing a low overall mass (∼100–114 tonnes) [47] [48]. Thanks to

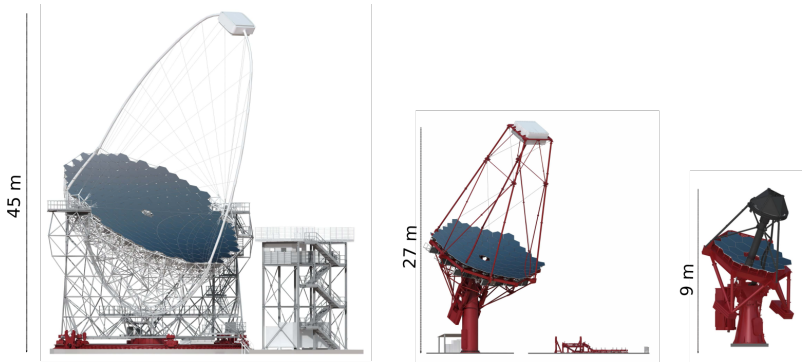

Figure 1.17: Computer rendering of the CTA Large Size Telescope (1*eft*), Medium Size Telescope (*middle*) and Small Size Telescope (*right*). The diagram is not to scale.

its lightweight design, the LST can slew to any point in the sky within 20 seconds, a critical capability for rapidly responding to transient gamma ray events such as gamma ray bursts and active Galactic nuclei flares.

The focal-plane camera of the LST is equally advanced: it weighs less than two tonnes and comprises 1,855 high-quantum-efficiency PMTs, arranged in modules to provide a field of view of roughly 4.5°, with pixel sizes of approximately 0.1°. Each PMT module incorporates light concentrators and onboard readout systems, enabling fast signal capture and online coincidence triggering across telescopes [47]. The essential telescope properties are shown in Table 1.1.

LST main parameters	
Optical Parameters	
Optical design	1-mirror, parabolic
Primary reflector diameter	23 m
Effective mirror area	370 m^2
Operational energy range	20 GeV – 150 GeV
Camera Parameters	
Pixel size	0.1°
Number of pixels	1855
Field of view	4.3°
Mechanical Parameters	
Total weight	103 t
Repositioning time	30 s

Table 1.1: LST main design parameters [48]

Medium Size Telescope(MST)

The Medium-Sized Telescope (MST) constitutes the CTA's core observational workhorse, optimized for mid-energy gamma rays in the 150 GeV to 5 TeV range. This energy regime represents a balance between photon abundance and detectability in the atmosphere. [48]. The MST employs a modified Davies-Cotton design [49] with reflector size about 12 m in diameter. The dish comprises 86 hexagonal mirror facets arranged on a spherical surface with a 19.2 m radius [50]. The MST supports two interchangeable camera systems:

- NectarCAM, deployed at the CTA-North site, comprises 265 removable modules, each housing seven PMTs with high-speed analog CMOS ("Nectar") readout at gigasample-per-second rates. [51]
- FlashCam, used at CTA-South, follows a fully digital readout approach—its detector plane groups 12 PMTs per module, with continuous digitization by 12-bit Flash-ADCs at 250 MS/s and digital triggering via Ethernet-based data transmission. [52]

Both cameras deliver a wide field of view (7.5°/7.7°) with pixel scales of approximately 0.17°, and offer near-identical performance between northern and southern configurations [48]. The basic telescope properties are shown in Table 1.2.

Small Sized Telescope(SST)

The Small-Sized Telescopes (SSTs) are specialized for very-high-energy gamma rays, particularly in the few TeV to beyond 100 TeV domain [48]. They form the largest sub-array (up to 70 units) deployed across several square kilometers at the southern site to capture the rare but bright Cherenkov showers at these energies. SSTs utilize a dual-mirror Schwarzschild-Couder optical design [53], ensuring excellent spatial resolution across a wide field of view (∼9°), while enabling a compact and cost-efficient configuration. The primary mirror measures ∼4.3 m in diameter and is paired with a monolithic 1.8 m-diameter secondary mirror, which concentrates light onto the camera. [54]. The highlights of the telescope properties are shown in Table 1.3.

MST main parameters	
Optical Parameters	
Optical design	Modified Davies-Cotton single-mirror
Primary reflector diameter	∼12 m
Effective mirror area	88 m^2
Operational energy range	150 GeV – 5 TeV
Camera Parameters	
Pixel size	∼0.17°
Number of pixels	1855(NectarCAM), 1764(FlashCam)
Field of view	≈8°
Mechanical Parameters	
Total weight	∼89 t
Repositioning time	< 90 s

Table 1.2: MST main design parameters [48]

SST main parameters	
Optical Parameters	
Optical design	Dual-mirror Schwarzschild–Couder
Primary reflector diameter	∼4 m
Effective mirror area	5 m^2
Operational energy range	∼1 TeV – >100 TeV
Camera Parameters	
Pixel size	0.16°
Number of pixels	2048 SiPM pixels
Field of view	∼9°
Mechanical Parameters	
Total weight	∼7.5 t
Repositioning time	<60 s

Table 1.3: SST main design parameters [48]

The SST's camera (SSTCAM) is particularly notable. It houses 2,048 SiPM pixels, contained in a compact structure (50–60 cm across weighing ≤100 kg) with full-waveform readout at 1 GS/s (giga-sample per second) [55]. Prototype implementations such as the ASTRI-Horn telescope structure and CHEC-S camera have already validated the SST concept both structurally and electronically [56]. SSTCAM is discussed in detail in Section 2.

1.9.3 Location

The CTA observatory will consist of two separate array sites to ensure coverage of both the northern and southern hemispheres. This dual-site approach not only guarantees full-sky coverage and maximizes detection efficiency but also provides an excellent opportunity to study a wider range of gamma ray sources and rare events, such as very-high-energy gamma ray bursts (VHE-GRBs) and supernova explosions [57].

- **CTA North:** Located at Roque de los Muchachos on La Palma Island, this site currently hosts the MAGIC experiment.
- **CTA South:** Situated in Chile's Atacama Desert, approximately 10 km southeast of the European Southern Observatory's Paranal Observatory.

The initial telescope layout, known as the 'Alpha' configuration, for both the northern and southern arrays is shown in Figure 1.18. In this configuration, CTA North will feature 13 telescopes (4 LSTs and 9 MSTs) distributed across an area of 0.5 km^2 [48], while CTA South will comprise 14 MSTs and 37 SSTs [48]. Artistic renderings of both sites are presented in Figure 1.19. The first prototype of the LST telescope was completed in 2018 at CTA North and has been operational since then. Construction of three additional LSTs and the base structures for MSTs at CTA North is currently underway. In contrast, CTA South is still in the site development phase.

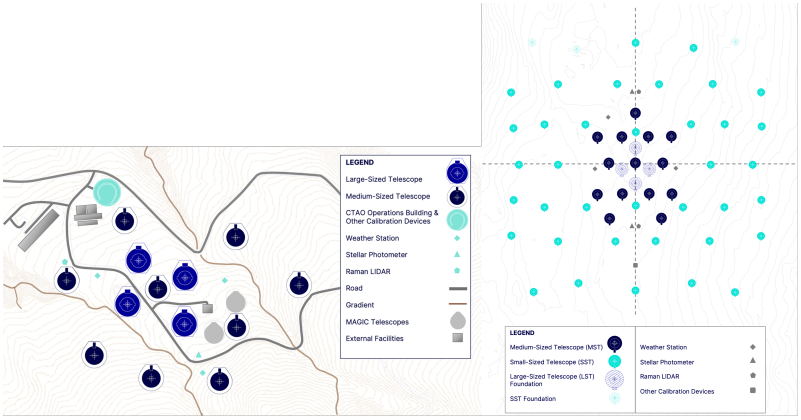

Figure 1.18: Proposed 'Alpha' configuration in CTAO-North (*left*) with 4 LSTs and 9 MSTs and CTAO-South (*right*) with 14 MSTs and 37 SSTs.

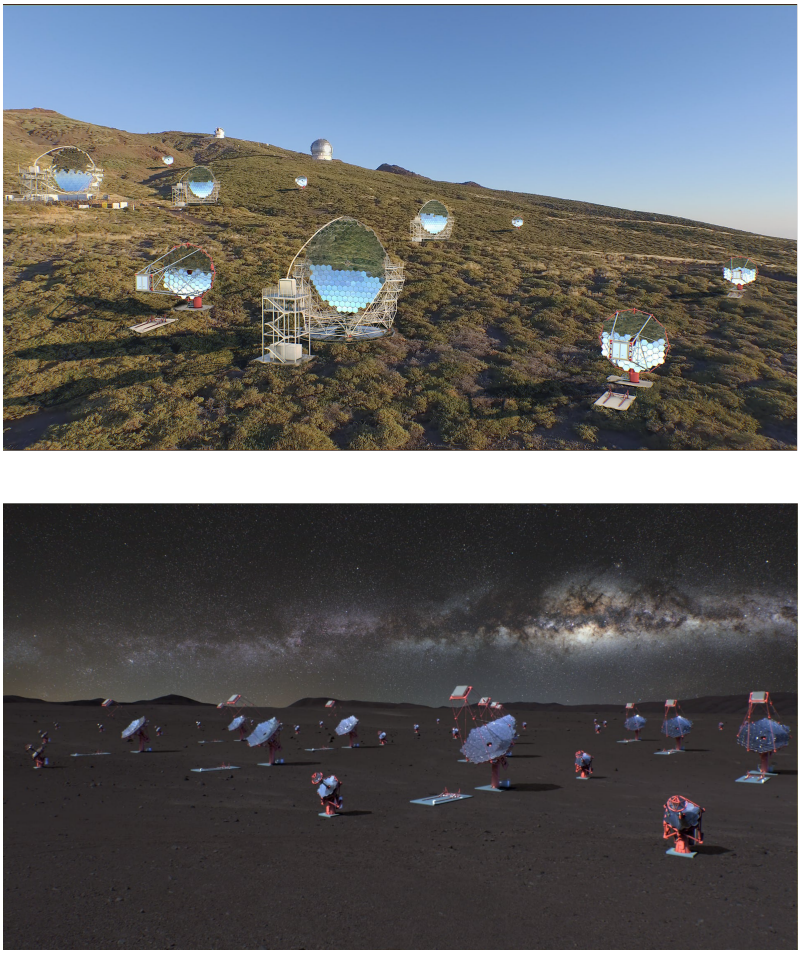

Figure 1.19: Artistic impression of CTA-North (*top*) and CTA-South (*bottom*) [48].

1.9.4 Science Goals

VHE gamma rays are of particular interest to cosmic-ray physicists, astrophysicists, cosmologists, and particle physicists because, unlike charged particles, they are not deflected by galactic or intergalactic magnetic fields. As a result, they travel in straight lines from their sources, carrying direct and unaltered information about extreme astrophysical environments. The CTAO Key Science Projects (KSPs) span a wide range of goals, including deep surveys of the Galactic Plane and extragalactic sky to uncover cosmic accelerators, targeted searches for dark matter signatures, rapid-response observations of transient phenomena like gamma-ray bursts, detailed studies of active galactic nuclei, and investigations of star-forming systems and galaxy clusters to probe cosmic-ray feedback and large-scale structures, all leveraging CTAO's broad energy coverage from 20 GeV to 300 TeV.

Some of the KSP that have a higher relevance for CTA's SST are discussed below.

- **Dark matter KSP**
  - Indirect detection of dark matter by searching for gamma ray signatures from annihilation or decay of Weakly Interacting Massive Particles (WIMPs) in dense regions like the Galactic Centre halo, dwarf spheroidal galaxies, the Large Magellanic Cloud, and galaxy clusters. With a 500-hour deep observation of the Galactic Centre halo, CTA will reach a sensitivity surpassing the benchmark relic cross-section across a broad range of WIMP masses, extending up to the multi-TeV scale [45]. In addition, CTA's enhanced angular and energy resolution, dramatically boosts its ability to detect dark matter spectral features or lines [58, 59].
- **Transient KSP**
  - Rapid follow-up observations of explosive events like gamma ray bursts (GRBs), gravitational-wave counterparts, AGN flares, Galactic transients, and neutrino alerts.Thanks to its large collection area and high signal-to-noise ratio, CTA offers exceptional instantaneous sensitivity across a

wide energy range. This provides a clear advantage over *Fermi*-LAT at lower energies and HAWC at higher energies. On transient timescales of a day or less, CTA is several orders of magnitude more sensitive than Fermi-LAT [60]. Transient KSP provides the evidence for the pivotal role of CTAO within the multi-messenger astronomy network.

  - The Cherenkov Telescope Array Observatory (CTAO) will be capable of discovering new Galactic transients with only mild sensitivity reduction (upto ∼15%) in crowded regions. It can detect variability: sources with photon fluxes below $\simeq 1 \times 10^{-13}$ ph cm^{-2} s^{-1} need over 10 hours of observation, while brighter sources ($\geq 3 \times 10^{-12}$ ph cm^{-2} s^{-1}) can show detectable flux fluctuations in just 0.5–1 hour [61].

- **Galactic Plane Survey (GPS) Cosmic-Ray PeVatron KSP**

  - Large-scale survey of the Galactic plane to map out very-high-energy gamma ray sources (such as pulsar wind nebulae, supernova remnants, binaries), complemented by deep follow-up of candidate PeVatron sources capable of accelerating hadrons to ∼PeV energies. The GPS KSP will devote 1600 hours of observations to map the entire Galactic plane, placing particular emphasis on key regions in both the southern and northern hemispheres [60].

  - The GPS could increase the current number of known Galactic VHE emitters by up to a factor of five and the GPS data will enable follow-up observations of these classes of these sources [62].

- **Extragalactic Survey KSP**

  - Wide-area survey of the extragalactic sky to study AGN populations, uncover new VHE-emitting source classes (e.g., Seyferts, Ultra Luminous Infrared Galaxies), and detect prompt-phase GRBs. The survey aims at reaching sensitivity of milli-Crab flux level, enabling the study of AGN luminosity functions and opening the exploration of faint and unexpected extragalactic VHE sources [60].

– Simulations suggest that CTA could more than double the number of known non-flaring AGNs at high energies and extend the gamma ray horizon out to at least redshift z$\simeq$2, expanding our observational reach into the distant universe [63].

In summary, this chapter outlined the fundamentals of very high-energy gamma ray astronomy, the role of IACT in advancing this field, and the transformative potential of the Cherenkov Telescope Array through its Key Science Projects (KSPs). Having established this scientific and instrumental context, the focus of the next chapter shifts toward one of the critical components of CTA: the Small Size Telescopes (SSTs) and, in particular, their camera system, SSTCAM. It oulines the design philosophy, photosensor technology, and readout architecture of SSTCAM, providing the foundation for understanding its calibration requirements and performance goals within the broader framework of CTA.

CHAPTER 2

Small-Sized Telescope Camera (SSTCAM)

This chapter presents the design of the SSTCAM, with particular emphasis on its photosensor and readout system. The discussion begins with an overview of the initial prototype camera (Section 2.1), highlighting the key lessons learned from its observing campaigns. Section 2.2 then focuses on the current SST camera, known as SSTCAM, describing the choice of photosensor, the factors influencing its performance, and the operating principles of the readout system. This section also outlines the expected data products and the processing chain that transforms raw data into science-ready results. Building on this, Section 2.3 underscores the importance of calibration in ensuring the accuracy and reliability of the science data. Subsequently, Section 2.4 reviews calibration systems employed in other IACT experiments. The chapter concludes with a discussion of the requirements defined by the CTAO for a dedicated calibration device tailored to SSTCAM.

2.1 Initial Prototypes

The final design of the camera unit and choice of photosensor for the camera was the product of a long process of camera prototyping, commissioning, and testing of two

prototypes, CHEC-M and CHEC-S. The Compact High Energy Camera (CHEC) was the first prototype of the camera for SST with Multi Anode Photomultiplier (MAPMTs) as the photosensor (hence CHEC-M). The extensive lab tests and on-telescope tests with the Gamma-Ray Telescope (GCT) prototype in Meudon, France, served as the proof of concept for the digitisation, trigger, control and readout systems of the camera and the images recorded by the camera were the first Cherenkov images seen by a CTA prototype. The lessons learned from extensive lab tests and the observing campaign in November 2015 [64] and spring 2018 [65] led to the design changes and development of the next prototype, CHEC-S.

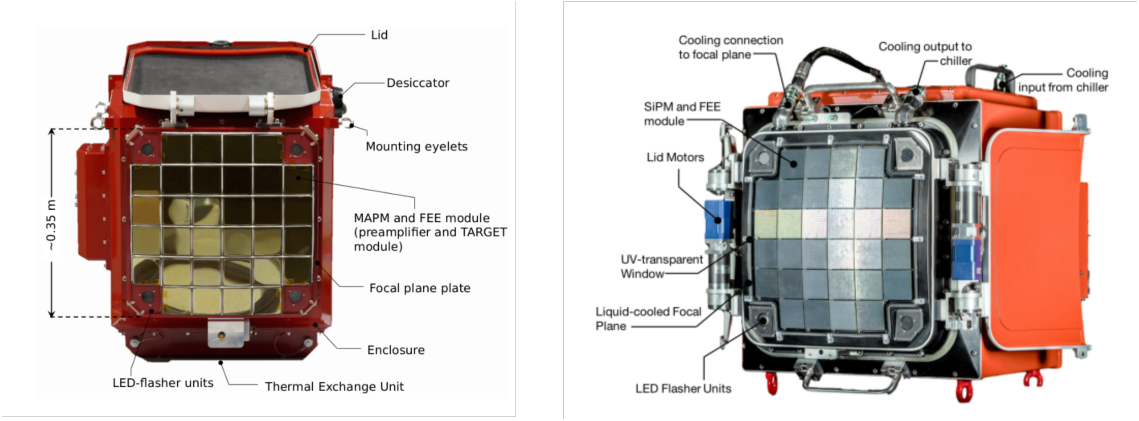

Figure 2.1: CHEC camera with MAPM photosensors CHEC-M (*left*) [65] and SiPM sensors, CHEC-S (*right*) [30].

Improved photon detection efficiency, lower operational voltage (tens of volts rather than thousands of volts), a higher fill factor (reducing dead space), enhanced photoelectron counting resolution, greater robustness to bright light, extended lifetime, and individual pixel gain manipulation compared to MAPMTs were the major drivers towards the usage of SiPM in the CHEC-S camera. CHEC-S underwent extensive lab tests and a dedicated observing campaign in 2019 on the ASTRI telescope on Mt Etna, Sicily. The majority of components used in the CHEC-S prototype formed the final version of CHEC design (now SSTCAM) with the exception of the final choice of SiPM model [66] (discussed further in Section 2.2.1). An annotated picture of CHEC-M and CHEC-S is shown in Figure 2.1.

2.2 SSTCAM

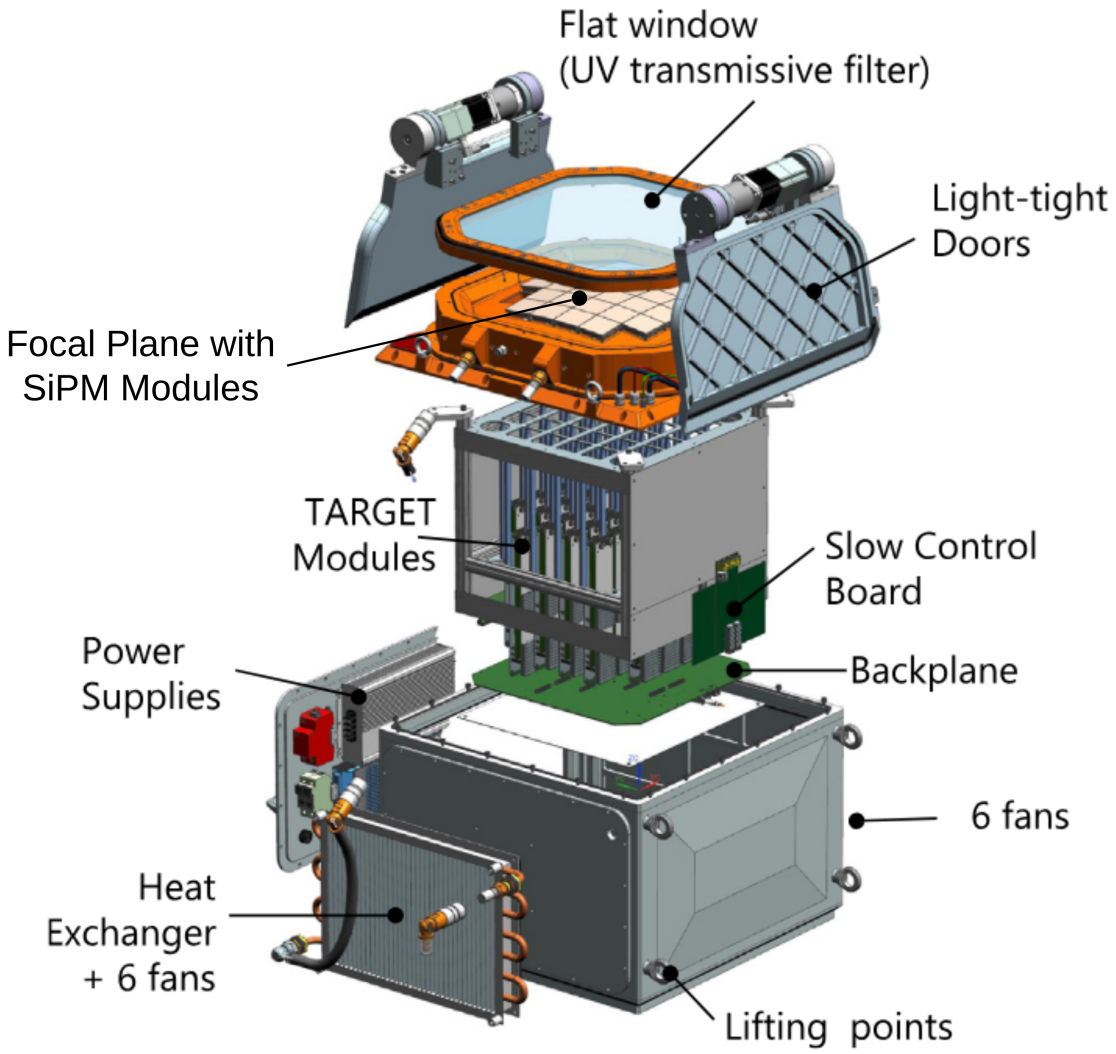

Figure 2.2: CAD model of SSTCAM camera [67]. The overall dimensions of the camera are 570 mm × 570 mm × 500 mm and it weighs approximately 90 kg.

SSTCAM is the recent version of the camera that has been chosen by CTAO to be commissioned on the ASTRI telescopes for SST [68]. With 2048 SiPM pixels arranged into 32 modules (64 pixel each arranged in 8×8 array), SSTCAM offers an effective field of view of 8.8°.

A SiPM with high photon detection efficiency (PDE) and low optical crosstalk is important for the SSTCAM (discussed further in Section 2.2.1). The signal from the SiPM is digitized using a custom ASIC known as TeV Array Readout Electronics

with GSa/s sampling and Event Trigger (TARGET) Application Specific Integrated Circuit (ASIC) [69]. An exploded CAD view of the SSTCAM with components annotated is shown in Figure 2.2. In the context of this thesis, the discussion is restricted to the photosensor (SiPM) and the data acquisition system (TARGET), as it is essential for understanding the subsequent calibration of the SSTCAM.

2.2.1 Photosensor: SiPM

A Silicon Photomultiplier (SiPM) is a solid-state photon detector composed of an array of tiny microcells (50μm for SSTCAM SiPM). Each microcell consist of Avalanche Photodiodes (APDs) operated in Geiger mode. A photodiode is in Geiger mode when the p-n junction in the photodiode is biased at a voltage higher than its breakdown voltage. In this state, a single photon can trigger a self-sustaining avalanche of charge carriers (due to photoelectric effect) which translates into equivalent current. The process continues until the junction capacitance discharges to bring the voltage below the breakdown voltage. The junction capacitor has to be recharged to prepare it for next photon detection. The rate at which it is recharged is controlled by a series resistor known as quenching resistor. The quenching resistor prevents accidental re-triggering due to trapped charges. Thus, the overall current from all the APDs in a single SiPM pixel provide an overall signal that is a multiplicity of the number of detected photons [32]. The equivalent circuit for a single SiPM pixel is shown in Figure 2.3.

The parameters that benchmark the performance of an SiPM are discussed as follows.

Overvoltage

The electrical characteristics of the SiPM depend on its overvoltage, which is the difference between the bias voltage and breakdown voltage of the APDs. The multiplicity (or gain) of the SiPM has a linear dependence on overvoltage. As temperature increases, the ionization rates of charge carriers decrease, requiring a higher electric field to initiate impact ionization. Consequently, the breakdown voltage exhibits an approximately linear increase with temperature, making the SiPM gain strongly

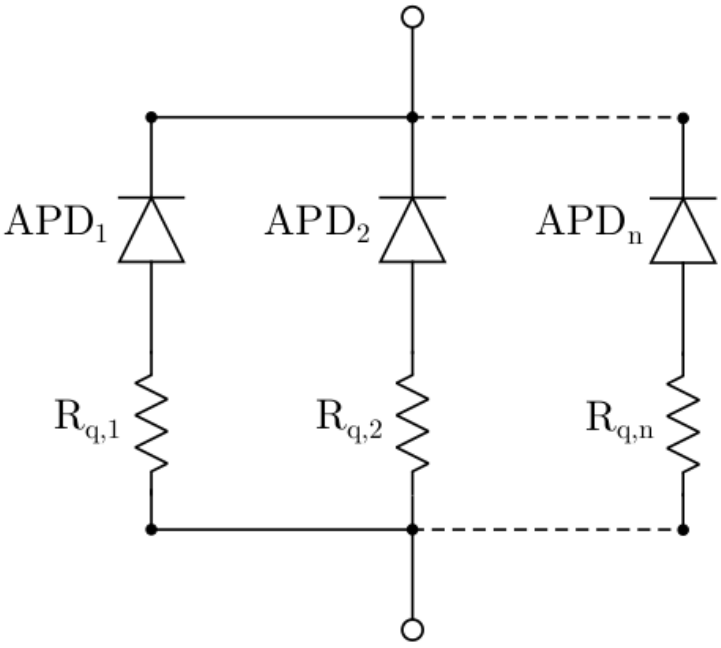

Figure 2.3: The equivalent circuit representation of an SiPM pixel. It consists of large number of Geiger mode APDs (microcells) and each of them is connected to a quenching resistor. The total current from all the microcells upon photon detection registers signal in the SiPM pixel [32].

temperature dependent. Therefore, by monitoring the temperature and the breakdown voltage, the bias voltage (and the overvoltage) can be manipulated to keep the gain fluctuation within acceptable range [32].

Photon Detection Efficiency (PDE)

This parameter quantifies the overall conversion efficiency from incident photons to detectable photoelectrons [70]. It is expressed as

$$\mathrm{PDE} = \mathrm{QE} \times \mathrm{FF} \times P_{\mathrm{avalanche}} \tag{2.1}$$

where QE (quantum efficiency) denotes the probability that a photon striking the APD generates an electron–hole pair, FF (fill factor) is the ratio of the photosensitive area to the total pixel area, and $P_{\mathrm{avalanche}}$ is the probability of initiating a Geiger-mode avalanche. The PDE values are typically specified by the manufacturer and can be tailored to specific applications. Figure 2.4 shows the comparison of the

Cherenkov spectrum with the PDE of the SiPM. It can be noted that the SiPM used in the camera has a higher PDE in the peak region of the Cherenkov spectrum.

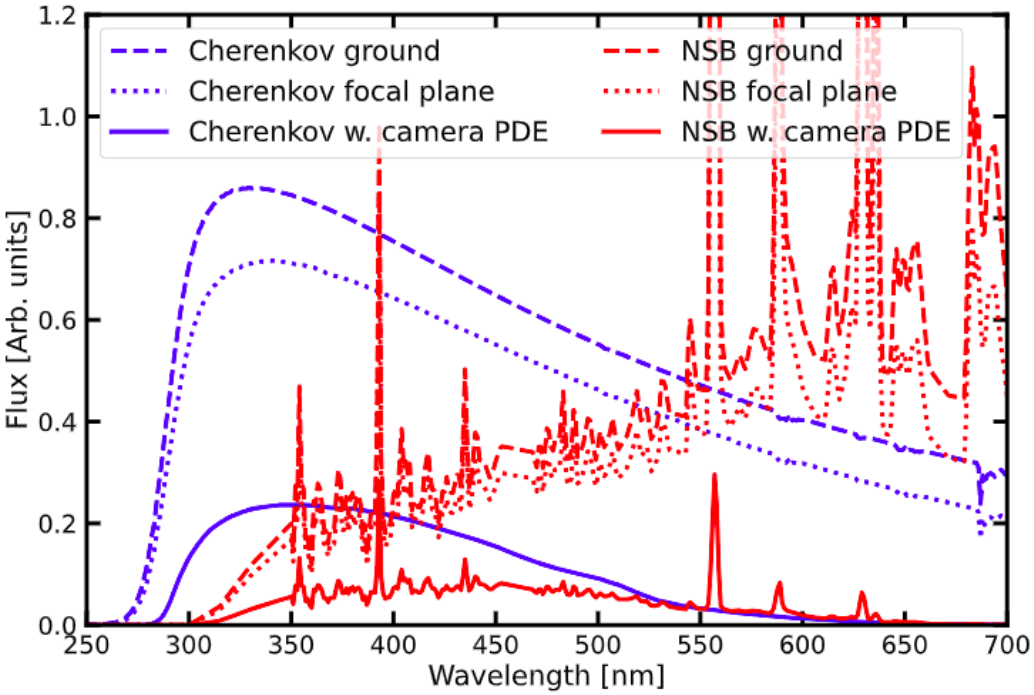

Figure 2.4: The Cherenkov spectrum has a peak in the UV range. The simulated performance of the camera by the convolution of the Cherenkov spectrum with PDE and window transmissivity is shown for comparison. It can be noted that the camera can capture the peak wavelength of the Cherenkov spectrum. The curves in red shows the night sky background whose contribution can be cutout by using specialized window material. This curve was generated by Simone Steinmassel for an internal report to SSTCAM.

Dark Count Rate (DCR)

Thermal agitation can generate an electron-hole pair that can further trigger an avalanche in the SiPM. This signal is completely indistinguishable from the one produced by an actual photon. The pseudo-photon detection triggered by thermal energy are referred to as dark counts and the DCR is represented as

$$\mathrm{DCT} = \frac{\mathrm{N}_{DC}}{t} \tag{2.2}$$

where N_{DC} counts occur in time t in a completely dark environment. As the dark count increases with temperature, it is a major source of noise in the SiPM. The dark counts are more prominent in SiPM compared to traditional PMTs [30].

Optical Crosstalk (OCT)

During the avalanche process in the microcells, infrared photons may be emitted. These secondary photons can trigger avalanches in neighbouring cells, producing signals indistinguishable from those generated by primary photons. This effect is referred to as optical crosstalk (OCT). Multiple pathways exist through which secondary photons can induce such avalanches, as illustrated in Figure 2.5.

Optical crosstalk represents a significant drawback of SiPM technology. In the context of Imaging Atmospheric Cherenkov Telescopes (IACTs), it leads to signal overestimation, thereby biasing energy reconstruction, and can also contribute to accidental triggers in the camera [71]. For these reasons, understanding and minimizing OCT is a critical aspect of SiPM selection for practical applications.

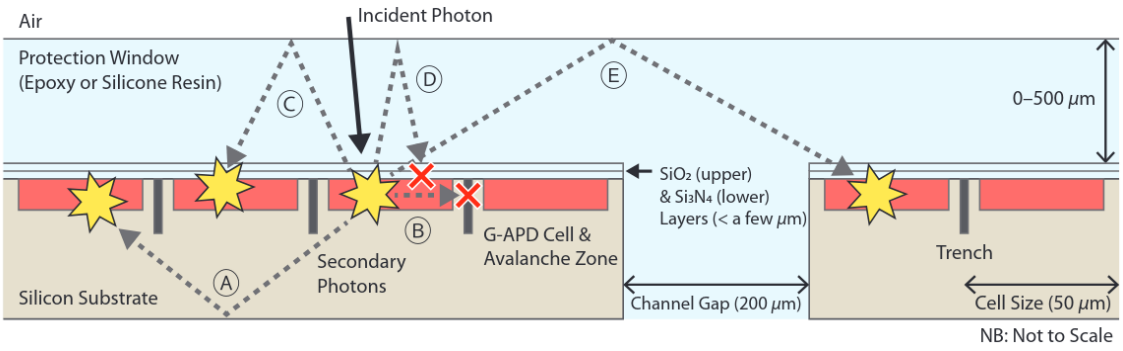

Figure 2.5: A schematic diagram of possible OCT photon paths inside a multichannel SiPM.After the avalanche process is triggered by the first incident photon (solid-line arrow), secondary photons may propagate and be detected by surrounding cells via several paths. Path A is due to Fresnel reflection at the boundary between the silicon substrate and the air (classified as prompt or delayed crosstalk depending if time delay is less or more than 8 ns). Path B is a direct path to an adjacent G-APD cell but mostly blocked by a trench (prompt crosstalk). Path C is by Fresnel reflection at the boundary between the protection window and the air (prompt crosstalk). Path D is similar to Path C, but the photon is reflected back to the first G-APD cell, which is already saturated. Path E is also similar to Path C, but it may be detected by neighbouring channels in the case of multichannel SiPMs (Reflected crosstalk) [71].

Afterpulsing

Some portion of the charge carriers get trapped in the defects in silicon and released later. This is not an issue if the release happens during the microcell recovery time as it has lower amplitude and can be discriminated against, but if it causes an avalanche after the recovery time, it can register as an independent event, completely indistinguishable single photoelectron pulse. Modern SiPM have reduced this effect [30].

Taking into consideration these parameters, multiple SiPMs were tested to identify the best performing SiPM technology. The SiPMs tested were Hamamatsu LCT5 with cell size 75 μm and 50 μm and Hamamatsu LVR3 with cell size 75 μm and 50 μm. They were tested both with and without protective coating, which increases the optical crosstalk by offering an optical path. The extensive lab tests result indicated that 50 μm LVR3 outperformed all other counterparts in all aspects of performance matrix. The optical crosstalk and photon detection efficiency of the candidate SiPMs are depicted in Figure 2.6. The main parameter of the selected SiPM is mentioned in Table 2.1.

Parameter	**Value**
Pixel area	6.0 mm × 6.0 mm
Microcell size	50 μm
Spectral response range	220 nm to 900 nm
Peak PDE	58 %
Breakdown voltage (V_{bd})	(38 ± 3) V
Operating overvoltage	5.9 V
Prompt OCT probability	3 %
Pixel Fill factor	74 %
V_{bd} Temperature Dependence	34 mV/°C

Table 2.1: Main parameters of LVR3 technology SiPM selected for SSTCAM (Hamamatsu S14521-1720) [67]

2.2.2 Data Acquisition: TARGET

The SiPM is attached to the focal plane electronics consisting of a pre-amplifier which eliminates the long SiPM fall time and a bias board to manipulate the gain of individual SiPM pixel by controlling their bias voltage. Further, the signal from the

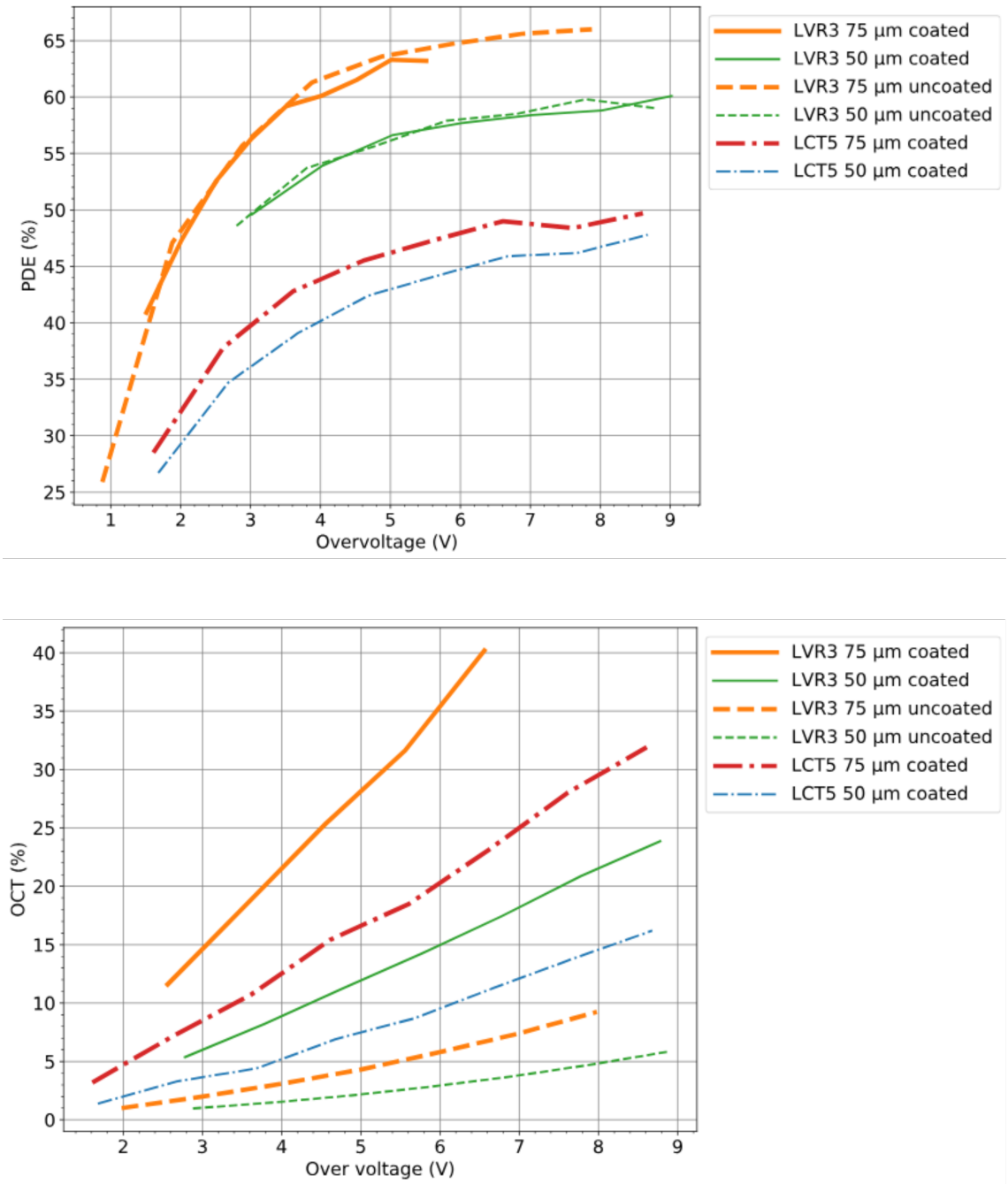

Figure 2.6: Photondetection efficiency (*top*) and optical crosstalk percentage (*bottom*) for different SiPM tested as candidate for SSTCAM. LVR3 75 μm uncoated has a higher PDE but its performance is limited by higher optical crosstalk values, whereas, LVR3 50 μm has slightly lower PDE but has much smaller OCT values. Thus, the latter was selected as the photosensor for SSTCAM [67].

64-pixel CTA module enters into the data acquisition system called the TARGET (TeV Array Readout Electronics with GSa/s sampling and Event Trigger) module [69]. The TARGET system performs five major tasks: analogue shaping, sampling, digitisation, trigger, and readout. The analogue signal is sampled and shaped by the amplifier and shaper circuit present on the TARGET module. The first level trigger (the analogue sum of 4 consecutive pixels is above a settable threshold) is prepared by the Application Specific Integrated Circuit (ASIC) and forwarded to the backplane for camera level trigger logic generation. There are 4 ASICs handling 16 pixels each on a TARGET module. Simultaneously, the sampled data (at 1GSa/s) is stored in a 16384-switched capacitor array (SCA). Upon receiving the camera level trigger and sampling from the backplane, 128 samples from the SCA are digitized using a Wilkinson 12-bit Analogue-to-Digital Converter (ADC) [72]. At the end of the camera level trigger, each TARGET module provides 64 digitized waveforms (corresponding to 64 pixels). These digitized waveforms are timestamped and stored for further analysis. Figure 2.7 shows an annotated picture of the TARGET module.

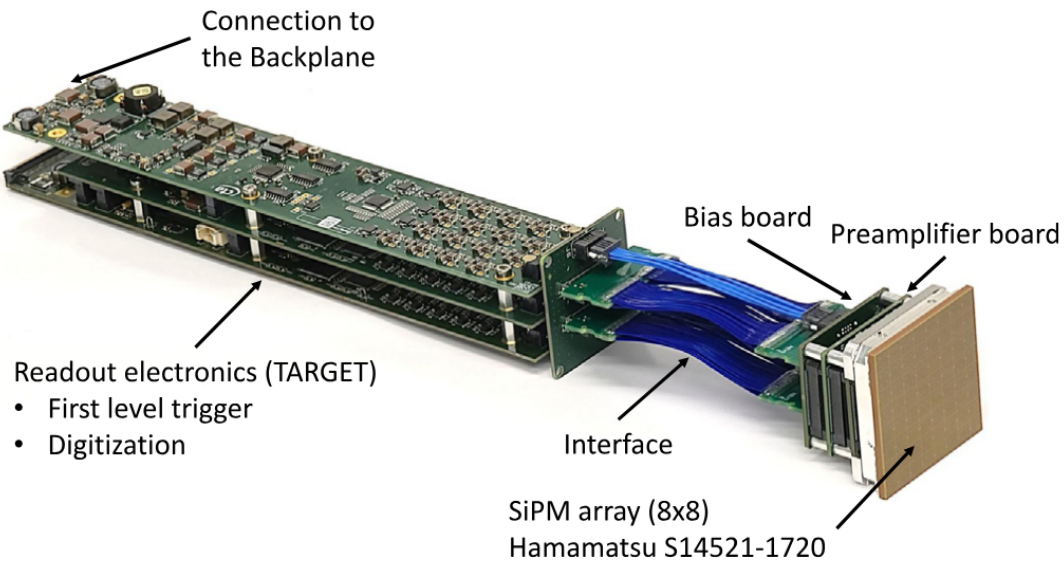

Figure 2.7: TARGET module with the SiPM pixel array attached to it. Preamplifier amplifies the SiPM signal and sends it to TARGET ASIC for sampling into switched capacitor array (SCA), analogue pulse shaping and first level trigger generation. Upon receiving the camera level trigger from backplane, the stored charges in the SCA are digitized into 128 samples long waveforms [32].

TARGET-level calibrations are first applied to the raw waveform data (R0), with the resulting calibrated waveforms stored as DL0 data. From each waveform, the charge (expressed in units of photoelectrons, p.e.) is extracted, and Hillas parameters are derived to produce the DL1 data. Subsequent processing of DL1 includes shower parameter reconstruction (direction and energy), particle-type identification, skymap and light-curve generation, and source catalogue creation—together forming the DL1 to DL5 data products [30]. This workflow bridges the detection of Cherenkov photons to the comprehensive study of gamma-ray astronomy with IACTs.

2.3 Photosensor Calibration

From Section 2.2.1, it is evident that the performance of any photosensor is affected by its intrinsic parameters such as optical crosstalk, photon detection efficiency, afterpulsing, dark count rate, and external operating conditions like bias voltage, temperature and night sky background. The raw signals obtained by the combination of the photosensor and the data acquisition module later translate into science level data products. However, the accuracy of this conversion critically depends on precise calibration of the photosensors. Calibration serves as the essential step that corrects for sensor-to-sensor variations, compensates for environmental effects, and ensures a uniform and stable detector response. Without such procedures, the systematic uncertainties introduced at the sensor level would propagate through the reconstruction pipeline, degrading the reliability of the final science results.

Since photosensors are widely used across many types of experiments, their calibration procedures are already well established within the academic community. Primarily, flat fielding, single photoelectron response and pixel linearity are the important calibration activities for a photosensor. They are discussed below.

2.3.1 Flat Fielding

In an SiPM array, each pixel exhibits inherent variations in photon detection efficiency, gain, and electronic response. Without correction, these pixel-to-pixel differ-

ences degrade the uniformity of the recorded images and bias the reconstruction of shower parameters. To mitigate this, the camera response must be equalized relative to the average response of all pixels — a procedure referred to as *flat fielding*.

Flat fielding is typically performed by uniformly illuminating the camera with a calibrated light source (e.g. LEDs or lasers). The measured pixel responses are then compared to the mean camera response, and correction factors, known as flat field coefficients, are derived. These coefficients are subsequently applied to normalize the signal amplitudes across all channels, ensuring a uniform response of the detector over time. The procedure of flat fielding SSTCAM is discussed in detail in Chapter 6 (Section 6.3). In addition to artificial calibration sources, naturally occurring *muon rings* recorded during normal observations provide an independent method of flat fielding [73, 74]. However this method requires high enough statistics, at least one observation night's worth of observation is likely required to calculate the flat field coefficients for the SST [73].

2.3.2 Single Photoelectron Calibration

After a photoelectron is detected by the SiPM and its signal propagates through the readout and analysis chain, the charge in each pixel is typically reported in units of voltage or ADC counts. To translate these raw values into a physically meaningful measure of detected photons, a reliable calibration method is required. This conversion from ADC counts to the equivalent number of photoelectrons is achieved through single-photoelectron (SPE) calibration [75].

Several approaches have been proposed in the literature for extracting SPE calibration, but the most widely used technique employs a uniform illumination system (LED or laser) adjusted to single-photon intensity levels [74–76]. The resulting pixel responses (charge or amplitude) are accumulated into a histogram to form the single-photoelectron spectrum, where distinct peaks correspond to no photoelectrons (pedestal), one photoelectron, two photoelectrons, and so on. Owing to their excellent photon-counting capabilities, SiPMs provide much better resolved SPE peaks than traditional PMTs [30]. This contrast between SiPM and PMT response is illustrated in Figure 2.8.

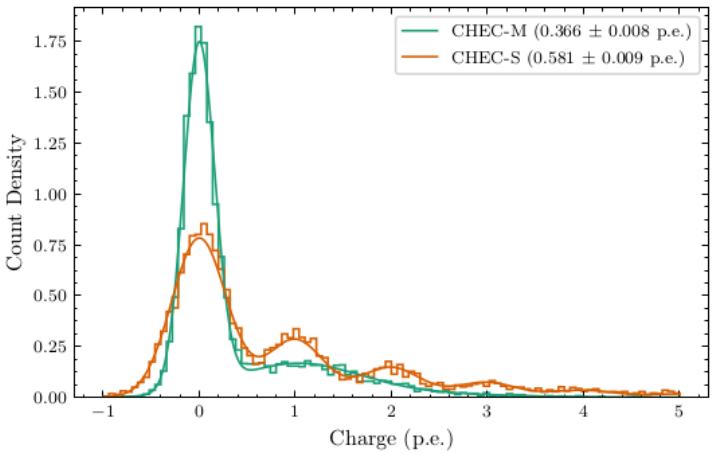

Figure 2.8: Comparision of SPE peaks between SiPM (*orange*) and MAPM (*green*) extracted from the CHEC-S and CHEC-M camera respectively. Values in the legend indicate the average illumination in photoelectrons obtained by fitting the Single Photoelectron (SPE) spectrum. The peaks are well resolved in the case of SiPM compared to the MAPM [30].

In addition to intrinsic photon-counting properties, the clarity of the SPEpeaks also depends on the performance of the charge extraction algorithm. A high signal-to-noise ratio is essential for resolving the discrete peaks in the spectrum. Further details on the implementation of SPE calibration in the SSTCAM are presented in Chapter 6 (Section 6.4).

2.3.3 Linearity

The SiPM is a photon counting device and it is biased to operate in its linear region, but due to high photon flux or faulty microcells in the SiPM pixel, it may deviate from its linear behaviour. Similarly, high optical crosstalk can also lead gain overestimation and non-linearity. This non-linearity can distort the reconstruction of signals, leading to an underestimation of the true photon count. Thus, monitoring the linearity by using a uniform light source with varying intensity is an important aspect of calibration. The linearity monitoring in SSTCAM is discussed in Chapter 6 (Section 6.2).

2.4 On Telescope Calibration Devices

As discussed in Section 2.3, reliable calibration of photosensors requires a dedicated illumination system. Such systems are typically based on either a monochromatic pulsed laser or a monochromatic pulsed LED which is capable of generating nanosecond pulses (resembling Cherenkov light in the atmosphere). While the concept is not new, every experiment necessarily incorporates its own device tailored to its calibration strategy, pixel arrangement, cost and camera design. In the following subsections, I briefly review the calibration instruments currently employed on the telescopes of other gamma-ray experiments.

2.4.1 VERITAS

The VERITAS telescopes are equipped with PMT-based cameras, calibrated using a system built around blue LEDs (Optek OVLGB0C6B9, 465 nm peak wavelength). These LEDs are mounted inside a weather-protected, modified Maglite housing, with a 50 mm opal diffuser at the front to ensure uniform illumination across the camera (see Figure 2.9). The illumination level is controlled by varying the number of LEDs pulsed. This system is employed for both flat-fielding and single-photoelectron calibration, and it achieves a performance comparable to the earlier laser-based setup, while operating at a much higher rate (400 Hz versus 10 Hz) [77].

2.4.2 MAGIC

The MAGIC telescopes employ an optical calibration system based on LEDs operating at three wavelengths (370 nm, 460 nm, and 520 nm). The system produces light pulses with a full width at half maximum (FWHM) of 3–4 ns and a flux of approximately 1.5×10^9 photons/sr, uniform within a 4° opening angle. The calibration unit consists of 16 pulser modules, each equipped with five LEDs covering different brightness ranges, enabling both flat fielding and SPE calibration. The pulser box is positioned 17 m in front of the camera to provide uniform illumination [78].

Figure 2.9: VERITAS LED based calibration system housed in a modified Maglite with diffuser and trigger input (*left*). Arrangement of the seven LEDs inside the housing (*right*) [77].

2.4.3 H.E.S.S

The H.E.S.S. telescopes use a pulsed LED source (HUVL400-520, 400 nm peak wavelength) mounted on the structure, approximately 15 m from the camera, to provide uniform illumination. The LED pulser generates short light pulses with a FWHM of about 5 ns, while a set of five neutral density filters control the brightness over a range from 10 to 200 photoelectrons [79]. The system can operate at frequencies up to 1 kHz. Dedicated calibration runs are conducted every two days to determine flat field coefficients, and separate LED runs are performed at the same interval for SPE calibration [80].

2.4.4 LST

The optical calibration system for the Large Size Telescope (LST), known as the Calibox, is based on a $1, \mu$J UV Q-switched laser that emits at 355 nm with a pulse width of 400 ps FWHM [81]. It can operate at frequencies between 1 and 2000 Hz. Figure 2.10 shows the Calibox setup.

The system includes two filter wheels, each equipped with five neutral density filters, allowing the photon flux to be adjusted from the single-photon level up to 10^5

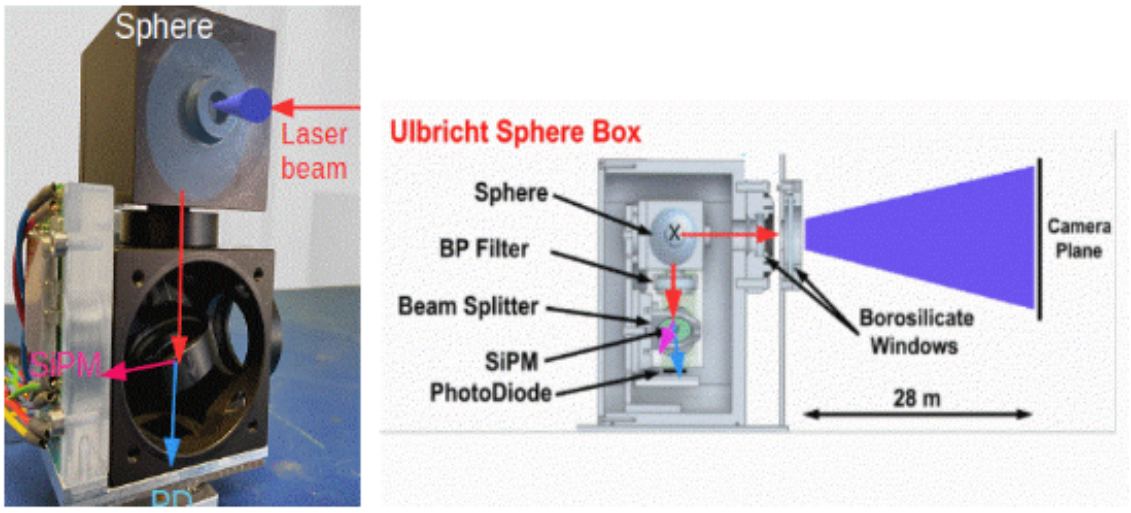

Figure 2.10: Calibration system Calibox for LST. The upper cube contains the diffuse sphere (Ulbricht sphere), while the lower cube hosts the beam splitter which passes the light to an SiPM and a photodiode. The SiPM monitors the low photon intensity while the photodiode monitors the high photon intensity. Right: Schematic layout showing the placement of the main optical calibration components. [81].

photons. After passing through the filters, the laser beam enters a 1-inch Ulbricht sphere, which diffuses the light uniformly. The diffused light is then collimated by an aluminium diaphragm before illuminating the camera, located 28 m from the Calibox. The laser pulses broaden to about 2.8 ns after exiting the Ulbricht sphere, consistent with the Cherenkov signals detected by the LST [81]. At the camera plane, the illumination uniformity is better than 2%, meeting the requirements set by CTAO.

2.4.5 MST

The NectarCAM camera of Medium Size Telescope (MST) employs a dedicated SPE calibration system designed to precisely measure the gain variation of its photo detection chain and minimize systematic uncertainties in gamma ray energy reconstruction. This system features a white-painted Poly Methyl Methacrylat (PMMA) screen placed approximately 15 mm above the focal plane (covering equivalent area of 51 PMTs), into which light from 12 LED (peak wavelength of 390 nm) is injected via a PMMA "fishtail" light guide [82, 83].

Mounted on XY motorized rails, the screen can be moved across the entire cam-

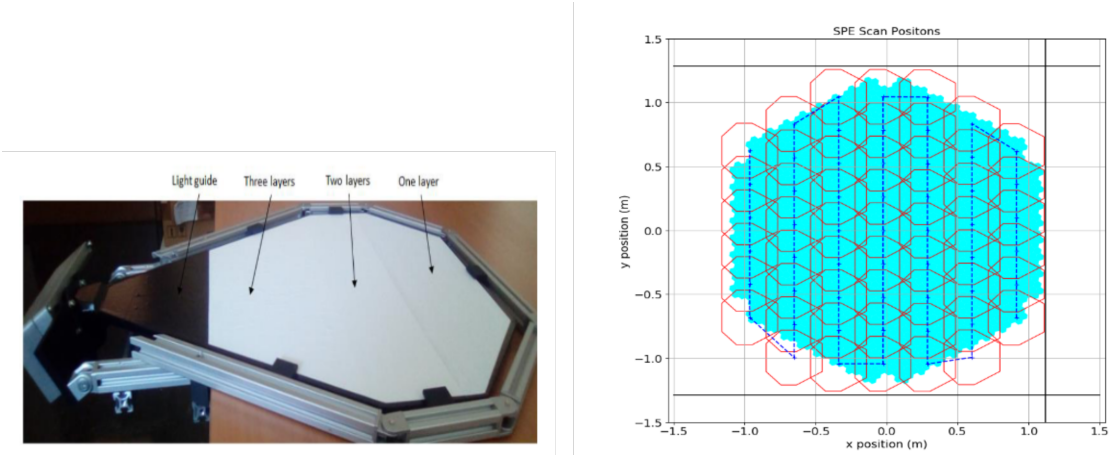

Figure 2.11: (*Left*) Calibration system MST's NectarCAM camera. The PMMA screen is fitted with a light guide, and a combination of 12 LEDs inject light pulses that calibrate the NectarCAM. [81]. (*Right*) The scanning position the calibration system infront of NectarCAM. The calibration system is moved across the camera focal plane by mounting it on the x-y rails. The estimated time to cover the entire focal plane is 17-28 minutes [83].

era plane, allowing illumination of all 1,855 PMT pixels for gain calibration scans and flat fielding. Additionally, the system's design ensures homogeneous light distribution through careful selection of screen geometry, reflectivity coatings, and paint application techniques. The calibration unit and its usage in scanning the focal plane of NectarCAM is depicted in Figure 2.11.

2.4.6 LHAASO WFCTA

The LHAASO Wide Field-of-View Cherenkov Telescope Array (WFCTA) is equipped with an SiPM-based camera. Its calibration system employs a cylindrical illuminator incorporating five LEDs at different wavelengths (360 nm, 405 nm, 450 nm, 505 nm, and 550 nm) [84]. The driving pulse is generated by a CMOS gate driver circuit, with its amplitude controlled via the supply voltage, while an FPGA-based logic circuit regulates the pulse shape and duty cycle. Together, these provide adjustable illumination pulses ranging from 15 to 1000 ns across a wide dynamic range. The cylindrical illuminator is used not only for single-photoelectron calibration but also for studying the Photon Detection Efficiency (PDE) and determining the absolute photon density at the camera plane. Calibration runs are conducted every 30 sec-

onds during observations, ensuring that variations in the operating environment are accurately tracked and corrected in the camera response [84].

2.5 CTAO Requirement

A similar system is also indispensable for SSTCAM. Thus, CTAO lays out a strict requirement on the performance of such a device. This has been outlined in Table 2.2.

Sl No	Material Name	Description
1	Flat-fielding system	The camera must include a flat-field system to illuminate the camera and flat field the camera pixel to a level of 2%
2	Illumination Level	The calibration system must provide an illumination intensity between 100 and 400 photons per camera pixel per pulse simultenously to the entire camera.
3	Pulse width	The calibration system must provide pulses with duration between 1 and 10 ns, known and stable to ±0.2 ns RMS.
4	Trigger rate	The calibration device should be able to operate at a settable trigger frequency between 1 and 100 Hz.
5	Event time	The time of illumination from the calibration system must not jitter relative to the trigger time of the camera unit by more than 0.5 ns RMS.
6	Pulse-to-pulse stability	The calibration systems pulse-to-pulse illumination intensity must not exceed that expected from Poisson fluctuations by more than 10% at constant temperature.
7	30 minutes stability	The calibration systems illumination intensity averaged over 10 seconds at 10 Hz must be stable to at least 2% over 30 minutes at constant temperature.

8	Night-to-night stability	The calibration systems illumination intensity averaged over 1 hour must be stable night-to-night to 5% at constant temperature.
9	Rate dependence	The calibration systems illumination intensity averaged over 1000 pulses must not vary by more than 1% between 1 Hz and 100 Hz at constant temperature.
10	Temperature stability	The calibration systems illumination intensity must not change by more than 0.1%/°C post offline temperature correction using pre-determined values.

Table 2.2: Requirements of the calibration device set by CTAO

2.6 Conclusion

This chapter has outlined the design and development of SSTCAM, focusing on its photosensor, data acquisition system, and the central role of calibration in IACT operations, culminating in the requirements set by CTAO. The final design of SSTCAM was achieved through an iterative process involving two prototype cameras, each contributing valuable insights toward the current configuration. The chosen photosensor, the Hamamatsu S14521-1720 (LVR3), provides a photon detection efficiency of 58% with exceptionally low optical crosstalk of only 3% [67]. The readout system, first validated with the prototype, has since undergone extensive characterization to ensure compliance with performance standards. Together, the well-characterized photosensor and the robust DAQ guarantee that low-level raw data (Data Level (DL)0) are reliably transformed into high-level science products (acDL5 and beyond). These considerations highlight the necessity of a dedicated and highly reliable calibration device, aligned with the strict requirements set by CTAO.

The following chapter will present the detailed design and characterization of the calibration device for SSTCAM. The requirement table introduced in this chapter will serve as a reference point throughout the subsequent discussions.

CHAPTER 3

Flasher Calibration System

In Chapter 2, the properties of the SiPM photosensors were discussed in detail (see Section 2.2.1), with particular emphasis on how their calibration directly affects the reliability of the resulting scientific data. To meet the performance requirements established by the CTAO (summarized in Table 2.2), a dedicated calibration system based on UV LEDs was developed for the SSTCAM with the primary design developed by Paul Clarke at Durham University. This chapter presents the description of the design and development history of this calibration device, hereafter referred to as the Flasher. Section 3.1 introduces the fundamental design principles and describes the components responsible for generating nanosecond pulses to mimic the Cherenkov time profile. Section 3.2 outlines the iterative development process undertaken by Paul Clarke, highlighting the evolution from the first to the third prototype board and the key lessons learned at each stage. I contributed by undertaking a detailed characterisation test of this system. This included drawing test plans, setting up of test environment, establishing automatic data acquisition system and data analysis of test results. Section 3.5 discusses the detailed characterization results of the version 3 Flasher board and demonstrates how its performance satisfies the requirements defined by the CTAO.

3.1 Design Description

The primary function of any calibration unit like Flasher is to generate short-duration (nanosecond-scale) optical pulses with a tunable intensity, ranging from a single photon to several thousand photons. To achieve this, the system architecture is organized into distinct operational blocks.

At its core, two main blocks define the functionality: the **timing block**, responsible for pulse generation, and the **intensity block**, which regulates the number of emitted photons. Supporting these are additional subsystems: a **control block** for managing overall operation, a **power block** to meet the electrical requirements of various components, and a **communication block** to enable user interaction with the system. The generated electrical pulses are then converted into photons by the **output block**, which forms the final stage of the design.

Beyond these essential subsystems, auxiliary components can be integrated to enhance functionality, such as temperature sensors for monitoring operational stability, photodiodes for reference photon flux measurement or identifiers for component tracking. These form the **additional block** of the system. The overall arrangement of these functional blocks, which together constitute a basic calibration device like Flasher, is illustrated in Figure 3.1. The following sections discuss the selection of electronic components used within each block and their role in fulfilling the design objectives.

3.1.1 Timing Block

The nanosecond pulse generation logic is not new. For example, VERITAS telescope calibration system uses a fast-switching device like a Bipolar Junction Transistor (BJT) to deliver a high-current, nanosecond-duration pulse to a cluster of LEDs [77].

In our case, the Flasher employs a combination of a MOSFET driver and a delay line chip to generate nanosecond-scale pulses. The MOSFET driver used in the Flasher is the LMG1025 from Texas Instruments [85]. This device is a single-channel, low-side, enhancement-mode gate driver originally designed for automotive applications. It offers typical rise and fall times of 650 ps and 850 ps, respectively,

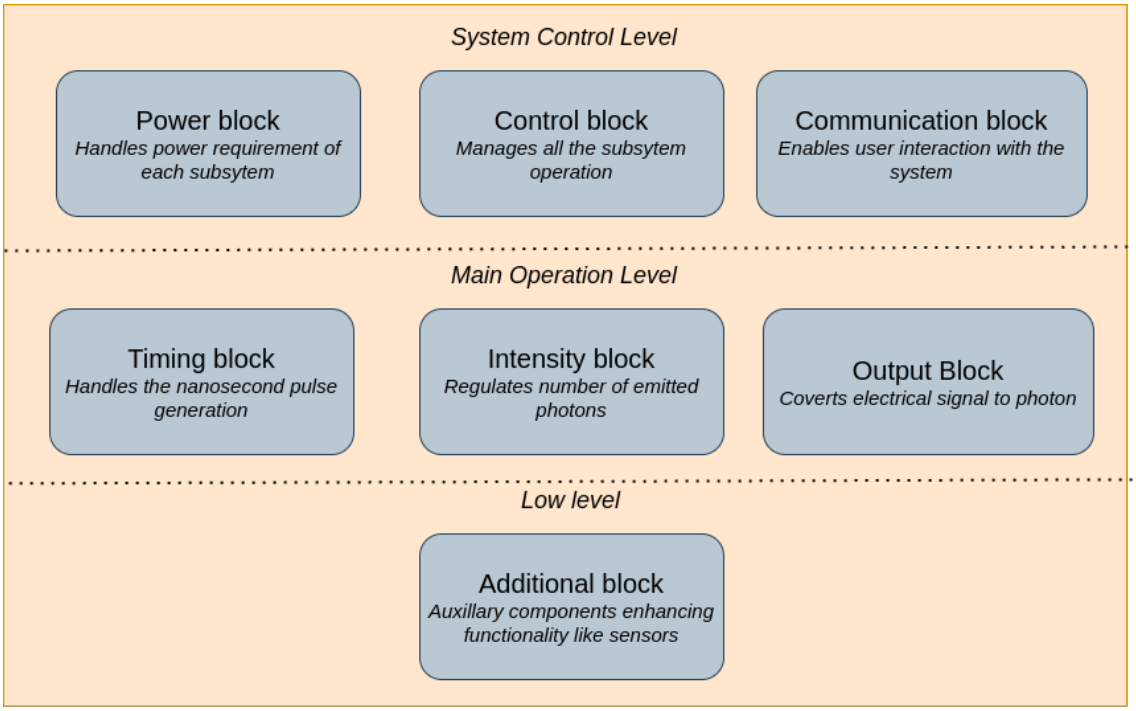

Figure 3.1: Fundamental operational blocks of a typical calibration device. Each block is annotated with its specific function, and the blocks are grouped according to their operational roles.

IN +	IN -	OUTH	OUTL
L	L	Open	L
L	H	H	Open
H	L	Open	L
H	H	Open	L

Table 3.1: Truth table for LMG1025

and is capable of producing 5 V pulses with widths as short as 1.25 ns [85].

The driver features two inputs (IN^+ and IN^-) and two outputs (OUTH and OUTL). When the outputs are combined into a single effective output (OUT), the logic summarized in Table 3.1 shows that OUT is active only when IN^+ is low and IN^- is high; in all other cases, OUT remains off. This switching behaviour provides exactly the timing logic required to control the LED at the nanosecond scale. In the Flasher design, both OUTH and OUTL are connected to the LED anode—one directly and the other through a resistor network—to enable brightness regulation (explored in Section 3.1.2).

The LMG1025 requires two synchronized input signals in order to generate

nanosecond-scale output pulses. This functionality is provided by the DS1023-25+, an 8-bit programmable delay line from Maxim Integrated [86]. The DS1023-25+ is capable of producing up to 255 digitally adjustable delay steps, covering a range from 0 ns to 64 ns in increments of 0.25 ns. The device supports both parallel and serial programming modes. In serial mode, delay values are loaded from the most significant bit (MSB) to the least significant bit (LSB) using eight clock pulses, with the latch enable (LE) pin held high during data loading. Once the data is latched (LE pulled low), the programmed delay is applied. The delay value is provided by the user as 'PW' in the firmware (discussed in Section 3.3) which is loaded onto DS1023.

Upon receiving a trigger signal, the DS1023-25+ generates two outputs: a delayed version of the input trigger signal at the OUT pin, and a reference copy at the REF pin (with an inherent propagation delay of approximately 18 ns). These two outputs are then fed into the inputs of the LMG1025, enabling precise nanosecond pulse generation. The schematics of the timing block component connection is shown in Figure 3.2, while Figure 3.3 illustrates the process of programming the delay and producing a nanosecond-scale pulse.

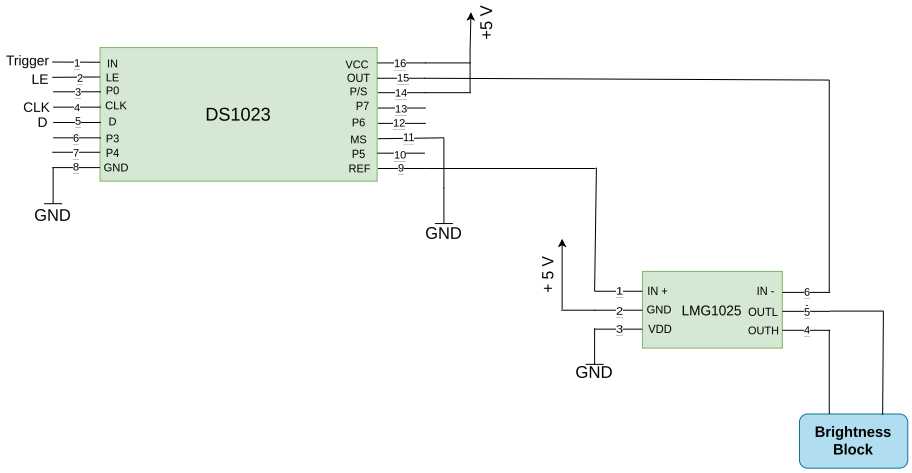

Figure 3.2: Connection between LMG1025 and DS1023 that forms the timing block of Flasher operation. Dual output from the LED driver LMG1025 is connected to the intensity block that further connects to the UV LED. The delay value in DS1023 is programmed in serial mode with data input through D (pin 5) on every CLK (pin 4) pulses with LE (pin 2) held high.

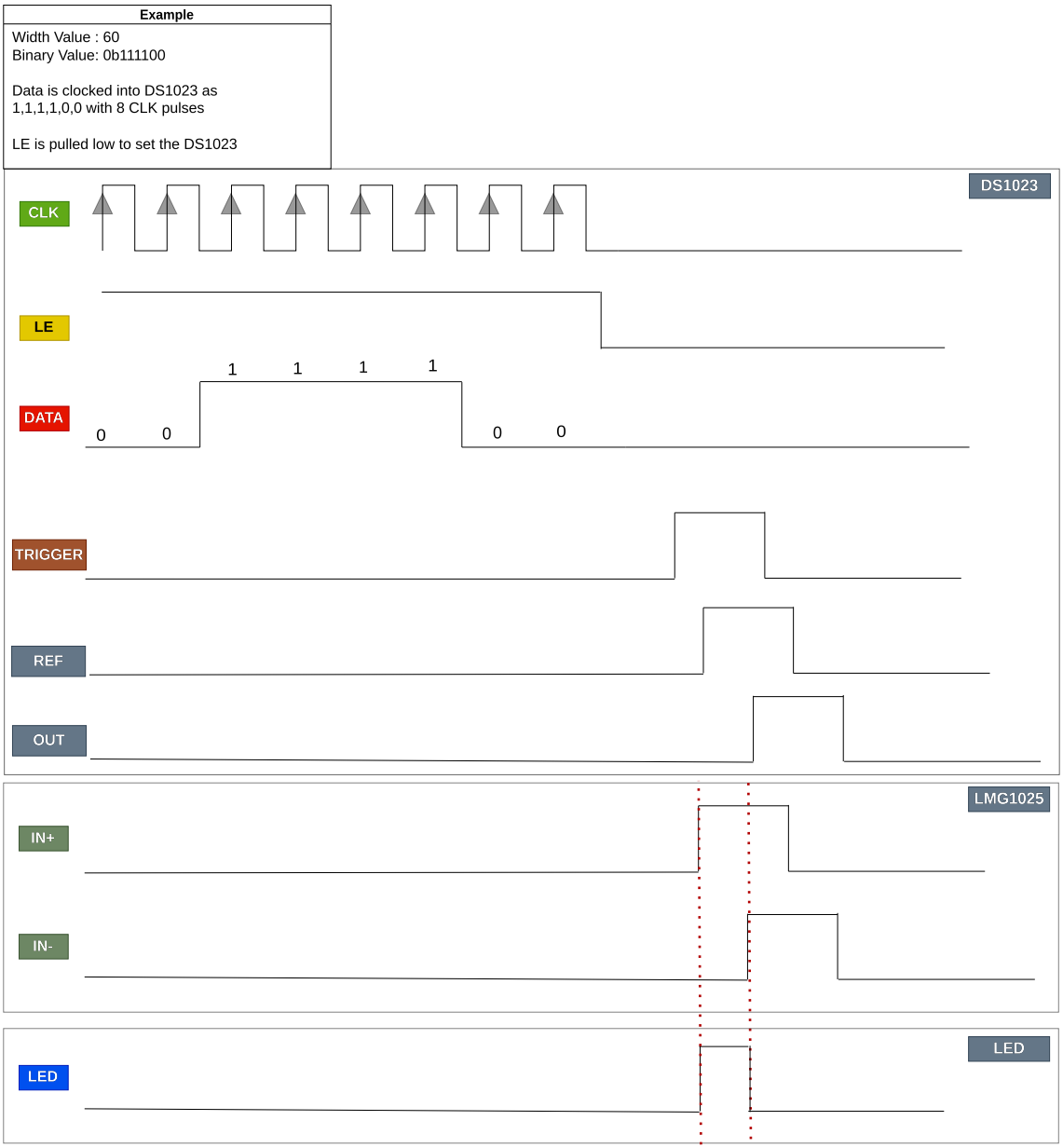

Figure 3.3: Time diagram showing the setup up of DS1023 chip with the requisite delay value through DATA, LE and CLK pulses. The delay value is stored after LE is pulled low. Two copies of the input trigger signal, delayed from each other by the specified delay value (0-64 ns), is passed from the REF and OUT pin of DS1023 into IN^+ and IN^- respectively. LMG1025 further creates a LED signal when IN^+ is high and IN^- is low, thus creating a nanosecond electrical pulse that drives the LED.

3.1.2 Intensity block

According to the requirements defined by CTAO (Table 2.2), the calibration device must provide a light output spanning more than three orders of magnitude in intensity. One way of controlling the brightness of an LED is by varying the series resistance in its current path. This principle forms the basis of the intensity block in the Flasher design.

The signal from the timing block is passed through a resistor network placed in series with the LED. This network consists of four resistors, each of which can be individually shorted using Toshiba TLP3475 photo relays [87]. In total, this configuration allows for 16 digitally selectable current settings. The resistor values used are 18 Ω, 22 Ω, 27 Ω, and 33 Ω. To guarantee that a minimum resistance is always present—even when all photo relays are shorted—an extra 10 Ω bias resistor is permanently included in the LED current line. As a result, the effective resistance in the circuit can be varied between 10 Ω and 110 Ω.

The current value (ranging from 0-16), denoted as 'I' in the firmware is provided by the user through the firmware. The control block converts the integer value into its binary equivalent (A0-A3) and passes that onto its four I/O pins that further controls the switching operation of the photo relays. Table 3.2 shows the logic value of A0-A3 and the corresponding effective resistance in the circuit. Figure 3.4 depicts the resistor network and the role of the microcontroller in setting the brightness.

3.1.3 Output Block

At the output stage, the LED is driven directly by the nanosecond electrical pulse. Operating LEDs at such short timescales is not a typical use case, and therefore their datasheets usually do not specify performance in this regime. For application in the SSTCAM, however, a UV LED capable of reliable operation on nanosecond timescales is required.

To identify a suitable candidate, a variety of LEDs were tested against this specification. After extensive evaluation, the Bivar UV3TZ-400-15 UV LED [88] was selected as the most suitable option. This device has a peak emission wavelength of

I Set	A0	A1	A2	A3	Effective R
0	0	0	0	0	110
1	0	0	0	1	92
2	0	0	1	0	88
3	0	0	1	1	70
4	0	1	0	0	83
5	0	1	0	1	65
6	0	1	1	0	61
7	0	1	1	1	43
8	1	0	0	0	77
9	1	0	0	1	59
10	1	0	1	0	55
11	1	0	1	1	37
12	1	1	0	0	50
13	1	1	0	1	32
14	1	1	1	0	28
15	1	1	1	1	10

Table 3.2: Effective resistance for different current settings. The current value is converted to its binary equivalent in the firmware. These binary values control the switching operation of photo relays that further control the effective resistance of the resistor network.

400 nm and produces a light beam with an opening angle of 15°. Although its output intensity exhibits temperature dependence (as outlined by the manufacturer and verified through laboratory tests), its specified operating range of −25°C to 80°C is well matched to the environmental conditions at the CTA-South site, where ambient temperatures typically vary between −15°C and 25°C (based on local weather station data at CTA-South site). The UV LED used in the Flasher employs a through-hole technology (THT) package with a width of 3 mm.

3.1.4 Power Block

Shifting the discussion to system-level operations, the first functional block is the power block. The Flasher is powered via a 5 V supply delivered through a USB-A port. For stable operation, it is recommended that the device be connected to a constant power source, since the LED light output is sensitive to variations in the input voltage (as noted by the manufacturer and confirmed through labora-

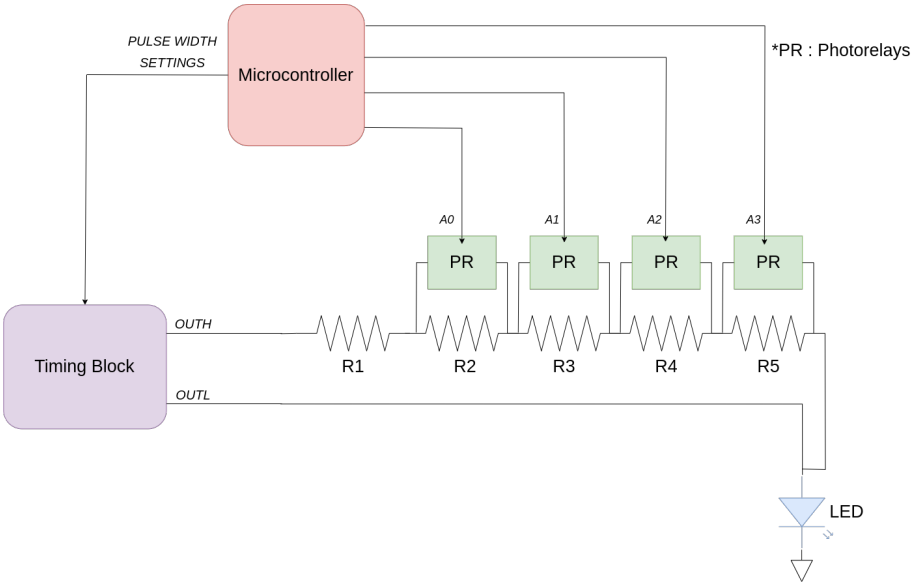

Figure 3.4: Intensity block diagram depicting the resistor network that manipulates the total brightness of the Flasher LED. A0-A3 are control pins that operate the switching of the photo relays (PR). Activating a photo relay shorts its corresponding resistor, thereby altering the effective resistance and the LED current. OUTH and OUTL are the outputs from the timing block. R1 to R5 are 10 Ω, 18 Ω, 22 Ω, 27 Ω, and 33 Ω respectively.

tory tests). Inconsistent power can therefore compromise the intensity-control logic described earlier. Most of the components in the system operate at 3.3 V. To accommodate this, the 5 V input is regulated down to 3.3 V using an SPX3819-3.3 voltage regulator [89]. The selection of this regulator was guided both by the operational requirements of the Flasher and its ready availability in the commercial market.

3.1.5 Control Block

The reliable operation of the Flasher system is coordinated by a microcontroller, which forms the core of the control block. For this purpose, the ATSAMD21G18 processor [90] was selected (the same microcontroller used in the Arduino Zero). It is a 32-bit ARM Cortex CPU operating at 48 MHz, offering 48 programmable I/O pins and a output voltage range of 1.6 V to 3.4 V. The device supports both Inter-Integrated Circuit (I^2C) and Serial Peripheral Interface (SPI) communication protocols, which are particularly useful for integrating peripherals such as the serial ID chip and the temperature monitoring sensor (discussed in Section 3.1.7).

The primary reason for choosing this microcontroller is its Arduino-compatible programming, which benefits from extensive community support and a vast library of resources, significantly simplifying development. Its ample I/O pins also meet all the operational requirements of the system. Its competitive pricing points delivers a cutting-edge product at low cost.

The main operation of the microcontroller is configuring the DS1023 width value by providing the clock signals and data line as well as driving the four photo relays that controls the LED intensity. This microcontroller does not have an onboard Ethernet driver. Thus it relies on an external Ethernet driver for user communication. Also, the serial ID data and the temperature data are packaged into the appropriate format to be sent to the Ethernet driver which further relays it to the user.

The firmware running on the microcontroller is implemented in C++ and is discussed in detail in Section 3.3. Figure 3.5 illustrates the pinout of the ATSAMD21G18 and its connections to the various operational blocks of the Flasher system.

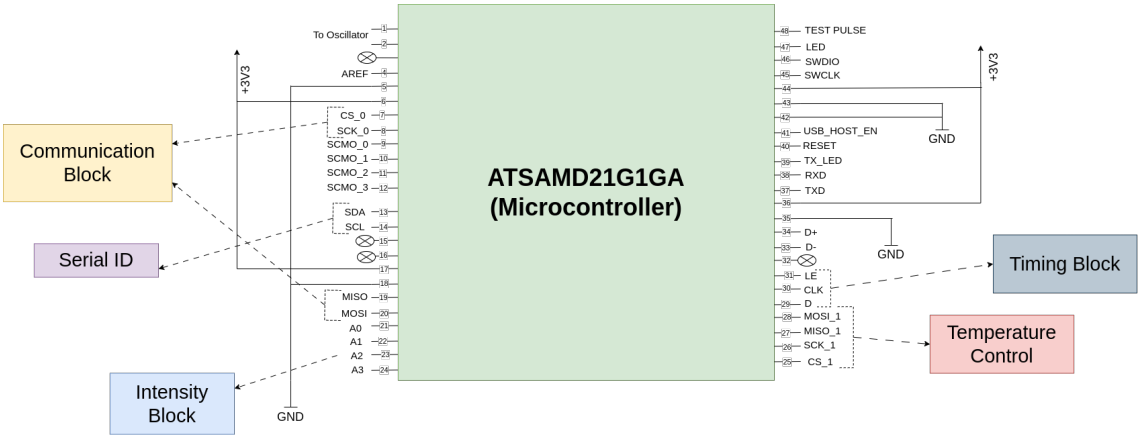

Figure 3.5: The pinout diagram of the microcontroller (adapted from the manufacturer datasheet) to show the connection of different pins to requisite operation blocks of the Flasher.

3.1.6 Communication Block

As described in Section 3.1.5, the chosen microcontroller does not feature a dedicated onboard Ethernet interface. To provide reliable network connectivity, the Flasher system incorporates an off-the-shelf Ethernet controller, the WIZnet W5500 [91]. This device includes an embedded 32 kB memory buffer for packet processing and communicates with the microcontroller via a high-speed SPI interface. To optimize power efficiency, the W5500 supports both Wake-on-LAN (WOL) and power-down modes. With a data rate of 100 Mbps, it enables fast configuration and control of the Flasher system.

The communication logic operates as follows: data packets generated by the device control software are transmitted through an RJ45 Ethernet connector and received by the W5500 driver. These packets are then relayed to the microcontroller via the SPI bus. Conversely, when information from the Flasher system (e.g. the serial ID or temperature readings) is requested, the microcontroller sends the relevant data to the W5500, which formats and transmits the response back through the RJ45 connector to the control software. The modular operation of the W5500 Ethernet driver is illustrated in Figure 3.6.

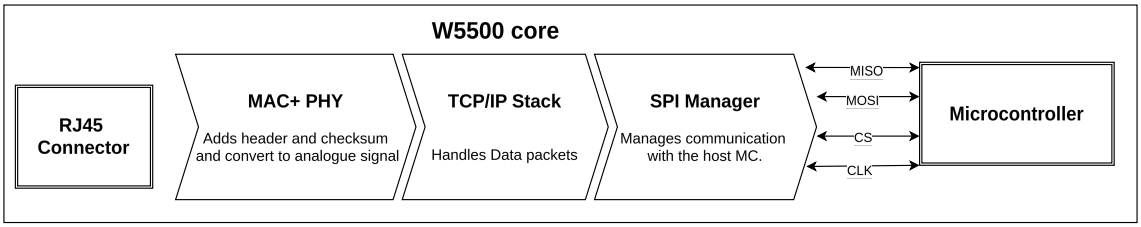

Figure 3.6: Adapted operation logic diagram of the Ethernet driver (WIZnet W5500). The configuration requests are sent by the user through RJ45 Ethernet connector. The Ethernet driver handles these information and communicates it to the microcontroller. Similarly, the data from the microcontroller are packaged by the Ethernet driver that is relayed back to the user.

3.1.7 Additional Block

In addition to the core functional blocks, several supporting components are integrated into the Flasher system. One such component is the Maxim DS28CM00 [92],

a low-cost device that provides a fast-read 64-bit unique identification number via the industry-standard I^2C interface. Operating in serial mode, the chip responds to microcontroller requests by transmitting its unique registration number.

The inclusion of a serial ID chip is particularly valuable during series production. Since each Flasher unit can exhibit slight variations in performance—most notably in LED intensity—the ID enables these differences to be systematically referenced when multiple devices are deployed. Moreover, the chip enhances traceability during maintenance and component tracking throughout the device's lifecycle.

As noted in the manufacturer's datasheet and confirmed through laboratory testing, the LED brightness exhibits a dependence on temperature. To monitor this effect, the LED is thermally coupled to an ADT7310 temperature sensor [93]. This device provides a measurement accuracy of $\pm 0.5°C$ over a temperature range of $-40°C$ to $105°C$. Communication of the temperature sensor with the microcontroller is established via an SPI interface. The measured LED temperature is subsequently incorporated into the temperature-dependent intensity calibration of the Flasher.

It can be configured to operate either with an internal trigger, generated by the microcontroller, or with an external trigger, supplied via an SMA cable. The selection between internal and external triggering is managed by a jumper that couples the two trigger sources (see Figure 3.7). When the jumper is connected, the internal trigger can also be monitored through the SMA output using an oscilloscope. The recommended trigger input voltage is 3.3 V. A trigger buffer, illustrated in Figure 3.7, is included to isolate the original trigger source while providing sufficient drive strength for the trigger signal.

3.2 Previous prototypes

Several prototype Flasher boards were developed at Durham University, and the system architecture described in Section 3.1 is the culmination of this multi-year effort. The first prototype was a two-board design built primarily to validate the concept of nanosecond pulse generation. This version lacked Ethernet communication capabilities and, instead of photo relays, employed rheostats to adjust the

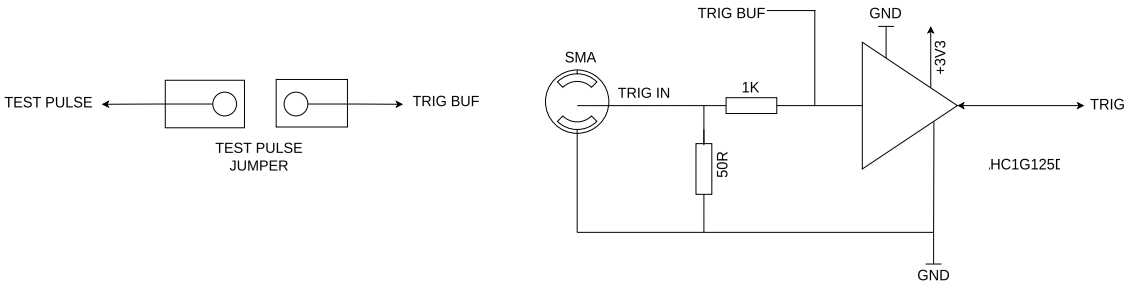

Figure 3.7: (*left*) Jumper pin to choose between internal and external trigger. (*right*) Trigger buffer circuit to isolate and provide driving power to the trigger signal. When the jumper pin is connected, the trigger signal can be read from the SMA connector.

effective resistance and thereby controlling LED intensity. To enhance intensity, ten LEDs were included on the board. Despite these limitations, the prototype successfully demonstrated the feasibility of using the LMG1025 driver and DS1023 delay line for generating nanosecond-scale pulses. The design is shown in Figure 3.8 (*left*).

The version 2 prototype represented a significant advancement. It incorporated Ethernet communication, implemented the photo-relay based resistance control, and was the first version tested not only in the laboratory but also in on-telescope conditions. Its distinctive triangular form factor was designed to fit into the corners of both the CHEC-M and CHEC-S cameras (see Section 2.1). Performance evaluation during an observation campaign with the GCT telescope has been reported in [74].

Although the use of multiple LEDs in the first two designs offered a wide dynamic range, it also introduced challenges. The light patterns resulting from different LED combinations were difficult to characterize, and scaling such a multi-LED system to a centralized board with multiple channels posed additional complications. For instance, directing light from multiple LEDs into a single optical fibre often results in poor coupling efficiency and substantial optical losses. Furthermore, inherent variations among individual LEDs contribute additional uncertainty to the overall system performance. Consequently, in the third design iteration, the number of LEDs was reduced to a single LED. This simplification made the design more compact, while reducing the overall system from three boards to two. Notably, the version 2 Flasher remains in use for a variety of calibration studies, including the inter-calibration of

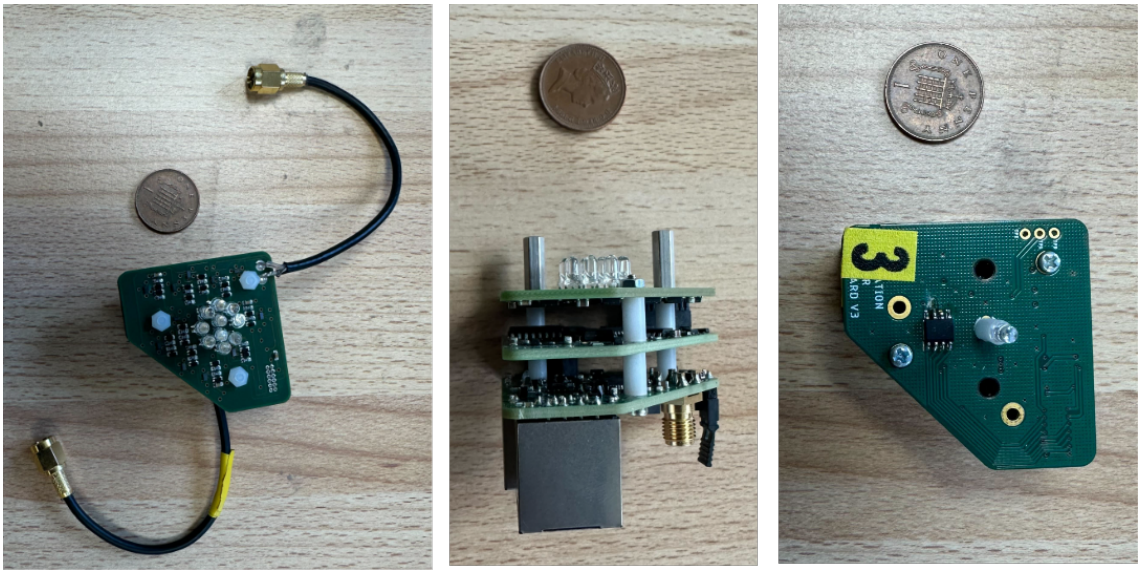

Figure 3.8: The version 1 (*left*), version 2 (*middle*) and version 3 (*right*) of the Flasher prototype board. One penny coin placed next to it provides the size reference.

Cherenkov telescopes using an unmanned aerial vehicle (UAV) [94], the photo sensor calibration of pSCT telescopes [95], and calibration activities within the Trinity experiment [96].

The current version (version 3), described in Section 3.1 and shown in Figure 3.8 (*right*), consists of two boards: a control board housing the interfaces and microcontroller, and an LED board containing the optical components. The Computer Aided Design (CAD) model of this version is shown in Figure 3.9. The following sections focus on the firmware development, concept of operation and detailed characterization of the version 3 prototype board.

3.3 Firmware Description

The firmware for the Flasher system is extensively developed in C++, with a Python wrapper provided for higher-level operation and user interaction. The core communication between the embedded device and the external control software is implemented through I/O stacks that rely on the User Datagram Protocol (UDP). This choice ensures lightweight and low-latency communication suitable for real-time calibration tasks. The firmware is responsible for parsing incoming requests, executing

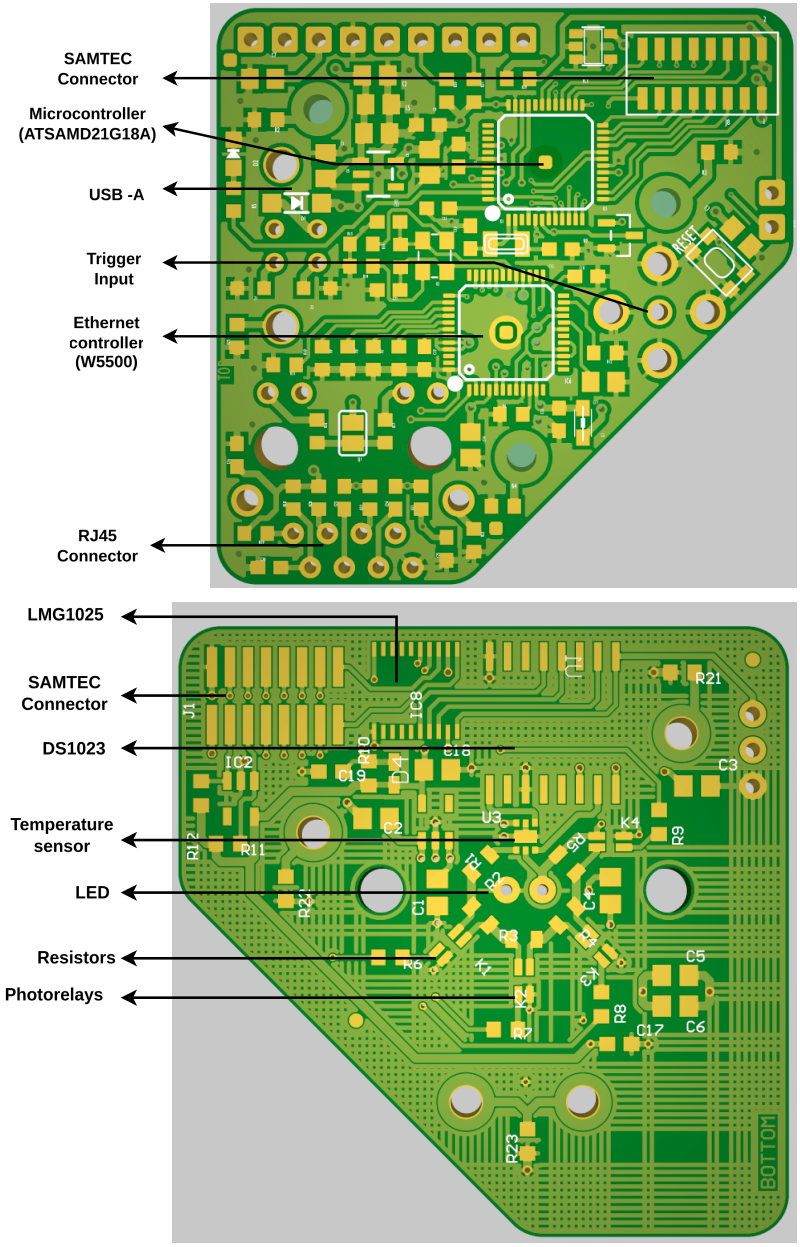

Figure 3.9: CAD model of version 3 of the Flasher prototype. The control board (*top*) houses the microcontroller and the interfaces for power, trigger and Ethernet. The LED board (*bottom*) contains the LMG1025 and DS1023 chip that generates the nanosecond pulse and operate the UV LED.

Sl No	Method Name	Method Description
1	read-serial-number	Reads the unique serial number of the board
2	read-temperature	Reads the output of the temperature sensor
3	set-led-current	Configures the LED current by controlling the photorelays
4	set-pulse-width	Configures the pulse width by manipulating the DS1023 chip
5	test-pulse	Generates a test pulse if internal trigger is ON

Table 3.3: Basic methods for Flasher operation

the corresponding hardware operations, and sending back structured responses or error codes to confirm successful execution or highlight issues.

The firmware can be programmed onto the ATSAMD21G18 microcontroller via a USB connection using the Arduino Studio development environment. Once installed, it initializes the hardware drivers for key system components such as the DS1023 delay line, photo-relay network, serial ID chip, temperature sensor, and Ethernet controller. Each of these devices is mapped to a set of firmware commands, making the system modular and extensible for future upgrades. Figure 3.10 illustrates the flow of requests and responses between the control software, Ethernet driver, microcontroller, and hardware blocks.

To simplify user interaction, a dedicated Flasher control software package has been developed around the Python wrapper. This software leverages the Click module [97] to provide a command-line interface for executing the most common operations described in Table 3.3. The control software is lightweight, can be independently installed on any system, and is designed to integrate seamlessly into the broader camera control software in later stages of development. Once installed, the software can be launched directly from the terminal, enabling straightforward and scriptable control of the Flasher system.

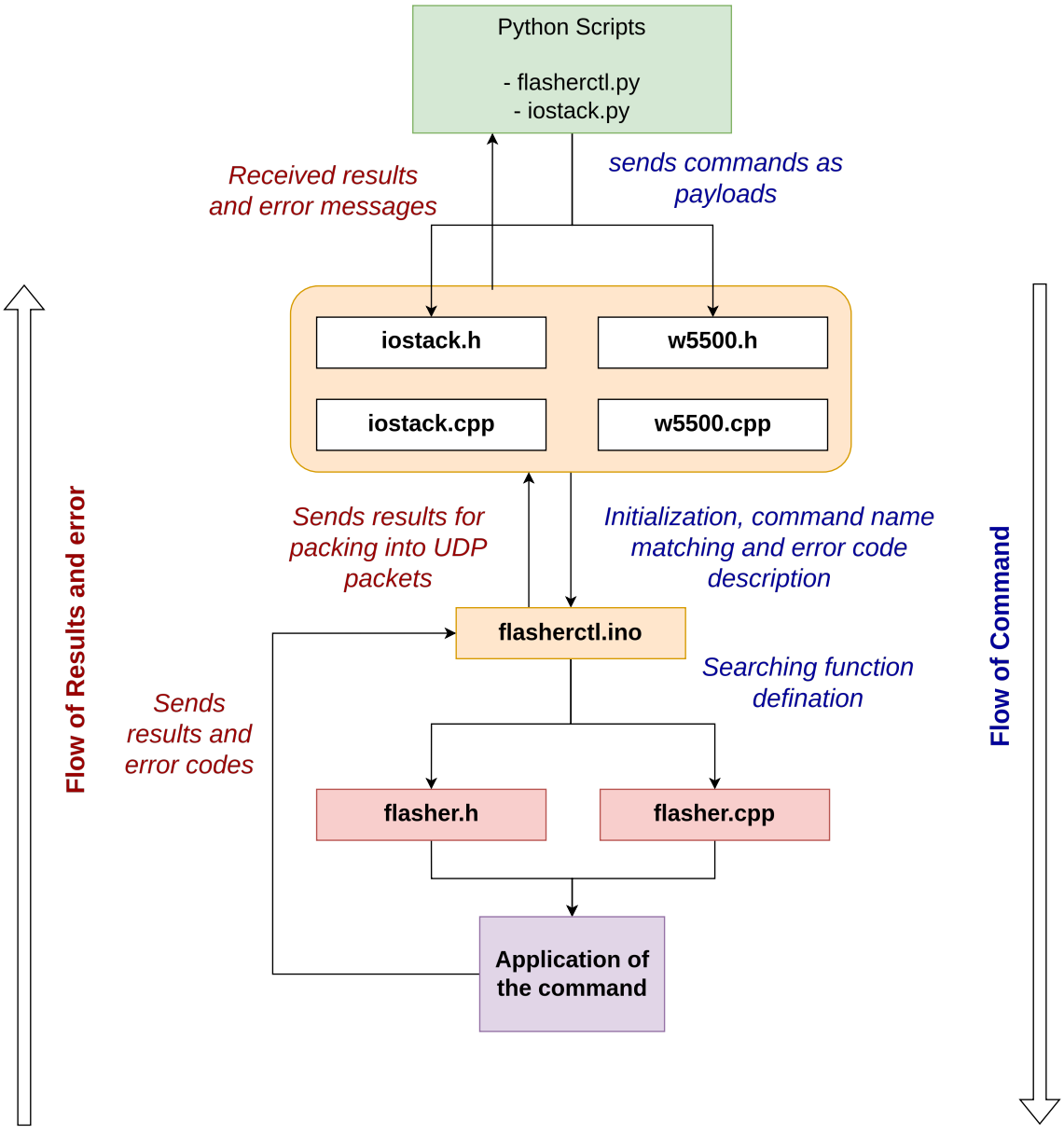

Figure 3.10: Description of the version 3 firmware showcasing the application of commands and the flow of results.

3.4 Concept of Operation

The operation of the Flasher system follows a straightforward sequence. The user specifies two parameters: the pulse width 'PW' (0–255) and the current value 'I' (0–16). The combination of these two parameters leads to 4096 Flasher settings. These inputs are first converted by the firmware into their binary equivalents and transmitted to the microcontroller.

The microcontroller then programs the DS1023 delay line: it pulls the latch enable (LE) pin high, loads the pulse width data sequentially over 8 clock pulses, and finally pulls the LE pin low, completing the configuration. Following this, the microcontroller sets the LED brightness by controlling the photo-relay network. It does so by applying the binary logic corresponding to the chosen current value across the relay control pins, thereby adjusting the effective resistance in the LED current path. At this stage, the system is fully configured. Once a trigger signal is provided—either internally from the microcontroller or externally via an SubMiniature version A (SMA) input—the LED produces optical flashes synchronized to the trigger frequency, with each pulse being an order of a nanosecond.

3.5 Characterisation Test setup

The characterisation tests on the Flasher system are essential to ensure its reliability, precision and suitability for use in high-performance optical calibration tasks. In order to ensure reproducible test results, a robust test setup is needed. The individual components of the test bench setup are discussed in the subsequent sections.

3.5.1 Silicon Photomultiplier (SiPM)

Since the Flasher system is being prepared for SSTCAM which is a SiPM based camera, a SiPM evaluation board, 'Onsemi Microfc-SMA-60035' was chosen for all the benchmarking tests. The SiPM on the evaluation board is from Sensl with a 6 mm active area, 41% photon detection efficiency, typical crosstalk value of 7% and has a peak wavelength sensitivity of 420 nm. Figure 3.11 depicts the SiPM

evaluation board, annotated with important components.

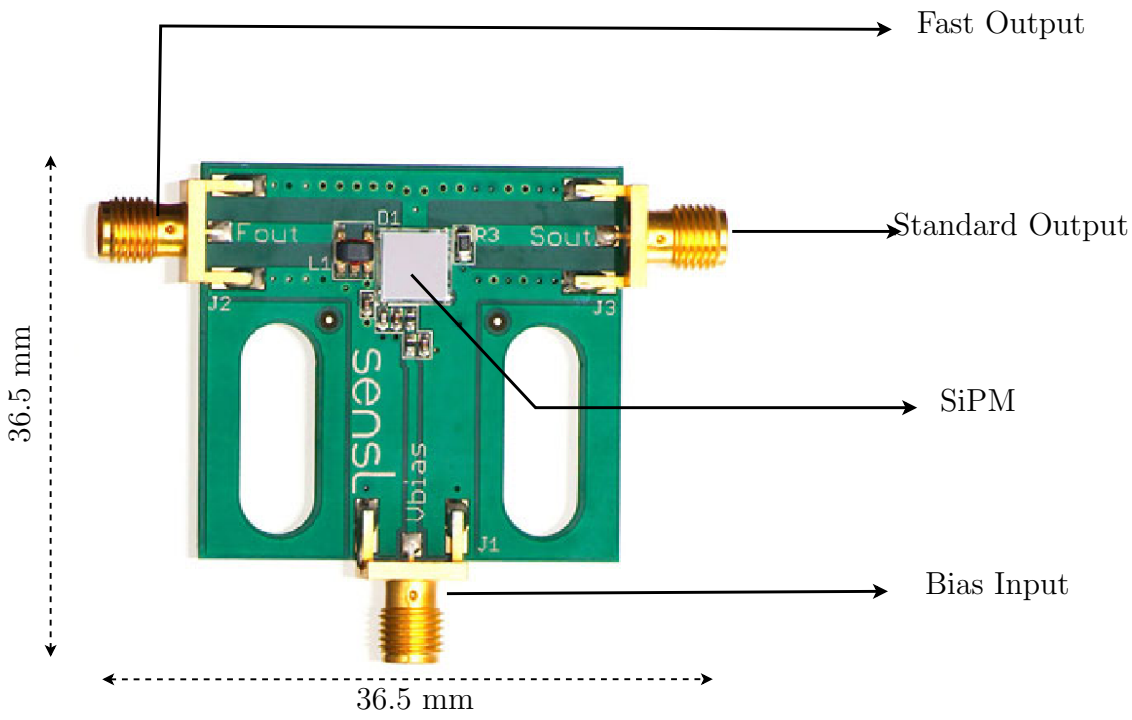

Figure 3.11: Onsemi MICROFC-SMA-60035 evaluation board with the Sensl SiPM used for benchmarking tests of the Flasher.

The primary reason behind choosing this SiPM for Flasher tests is its easy availability as well as its plug and play aspect. The evaluation board has three SMA terminals - one for power and two for signal output. The fast output has a capacitor readout node that offers faster fall time and the normal anode signal from the SiPM can be seen with the standard output. For all the tests, the SiPM was biased at (29±0.01) V.

3.5.2 Power Supply

The test setup utilizes two separate power supplies: one dedicated to the Flasher and the other for biasing the SiPM at 29V. The Flasher's power supply includes a remote control feature, enabling connection to the lab computer for automated switching operations.

3.5.3 Arbitrary Waveform Generator (AWG)

For all testing procedures, the external trigger signal is supplied by an Agilent function generator operating in continuous mode with a square wave output. The signal is split into two channels: one is routed to the Flasher's trigger input via an SMA connector, while the other is connected to the oscilloscope for both monitoring the trigger signal and synchronizing the oscilloscope.

3.5.4 Oscilloscope

As the SiPM was used to detect nanosecond-scale pulses, a high-bandwidth oscilloscope was essential for accurate data acquisition. A 20 GHz oscilloscope from Rohde & Schwarz (RS RTP Oscilloscope) [98] with a sampling rate of 4 GSa/s was employed for signal analysis. It operated in averaging mode with 1000 samples per trace, effectively reducing pulse-to-pulse fluctuations. However, for some specific test to measure intensity stability (see Section 3.7.2) per pulse, the averaging function was turned off. The captured waveform data was stored on the oscilloscope's internal disk for further offline analysis.

The oscilloscope's built-in measurement functionality was extensively utilized to extract key signal characteristics. Parameters such as peak-to-peak amplitude, pulse area, rise time, fall time, positive pulse width, and the time delay between the trigger and SiPM signals were continuously monitored and analysed. These measurements were saved locally or transferred to a connected computer via Ethernet upon request. Figure 3.12 illustrates a representative SiPM pulse as displayed on the oscilloscope, with relevant measurement annotations.

3.5.5 Climate Chamber

Semiconductor detectors like SiPMs are susceptible to ambient temperature. In order to have reliable results, the characterization tests were performed under constant temperature. This was facilitated by the ESPEC LU-114 temperature chamber. It has a temperature range of $-20°C$ to $85°C$. The remote connection feature enabled precise temperature control and automated temperature sweeps for specific test sce-

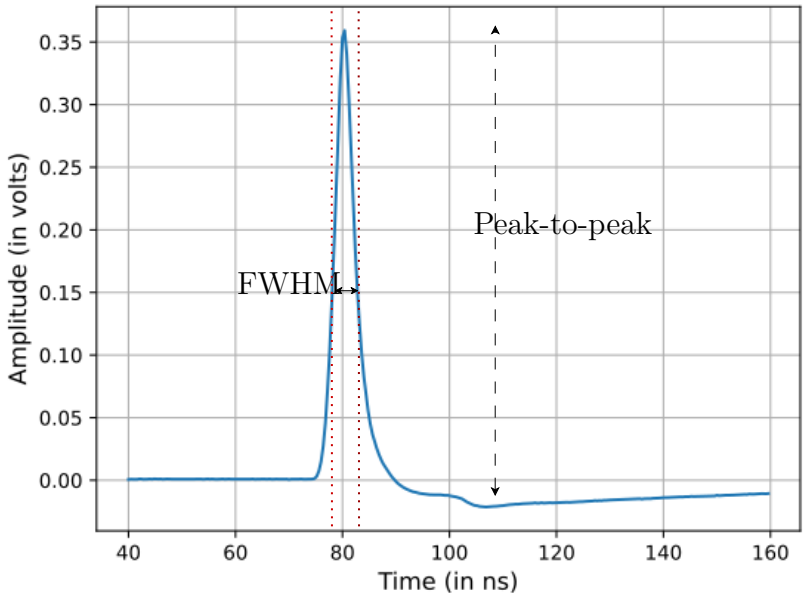

Figure 3.12: Characteristic Flasher signal observed by an SiPM detector (with signal averaging ON). The peak-to-peak amplitude and full width at half maxima (black arrow) is annotated. The dotted red lines represent the rise time and fall time respectively.

narios. The Flasher and the SiPM were placed inside the chamber throughout the test procedure. Extra precautions were taken to monitor humidity and put safety limits on the temperature variation of the temperature chamber in order to avoid condensation on the Flasher and sensors. Thus, the temperature in the chamber was not allowed to drop below 10°C or rise above 50°C.

3.5.6 Lab Computer

A Linux machine operates as the command centre for all the testing procedures. Linux terminal based Flasher software is installed on this system. Additional Python scripts (described in Section 3.6) are also available on this system. All the other subsystems like climate chamber, AWG, power supply and oscilloscope are connected via Ethernet to this system. The measurement data from the oscilloscope were acquired and stored on this PC and later accessed for further analysis. Figure 3.13 shows the test bench setup and the flow of commands/results.

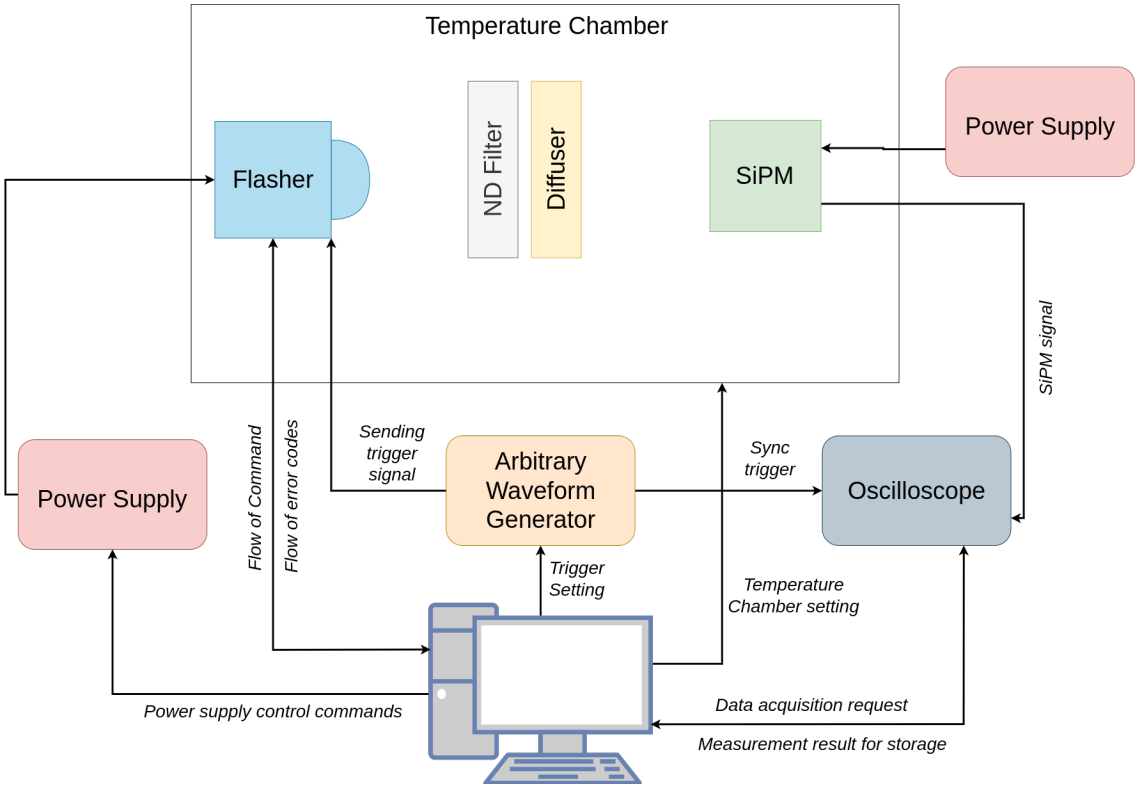

Figure 3.13: The test setup to perform different characterisation tests. It shows the flow of data and commands in the test setup. The diffuser is used in beam pattern scan and the Neutral Density filter is used during dynamic range scans (discussed in their respective sections). The power supply for SiPM and Flasher bias them at 29V and 5V respectively. All the subsystems were grounded appropriately. The scope averaging was turned off for specific tests related to pulse-to-pulse variation.

Subsystem: Power Supply	
Method Name	Method Description
check_connection	Pings the subsystem and returns basic instrument info
get_reading	Displays the set voltage and current values
output_on/off	Toggles output on/off
set_voltage	Sets the voltage for the output channel
set_current	Sets the maximum current for the output channel

Table 3.4: Basic methods to operate the power supply

Subsystem: AWG	
Method Name	Method Description
check_connection	Pings the subsystem and returns basic instrument info
get/set_voltage	Displays the set voltage or sets the given voltage
set_frequency	Sets the frequency of output channel
set_function	Sets the type of waveform to generate
open/close	Toggles output on/off

Table 3.5: Basic methods to operate the Arbitrary Waveform Generator (AWG)

3.6 Data Acquisition Software

The data acquisition process is completely automated. Since all the components of the test bench have Ethernet capabilities, they are connected to a control computer. Python based software using the module PyVisa [99] has been developed to communicate with individual subsystems so that each subsystem has a separate Python class and methods described in it. After establishing a formal connection handshake with each subsystem, different operations can be performed. Some of the important methods are described in individual subsystem Tables 3.4, 3.5, 3.6 & 3.7.

3.7 Characterisation Test Results

After establishing a stable and automated test bench, a comprehensive series of characterization tests were performed to benchmark the performance of the Flasher system. The results of these tests are presented in the following sections, where the

Subsystem: Climate Chamber	
Method Name	Method Description
check_connection	Pings the subsystem and returns basic instrument info
get_monitor	Displays set temperature, current temperature and operation state
set_temp	Sets the temperature of the chamber
set_temp_limit	Sets the upper and lower temperature limit
operate	Starts the climate chamber
stable_operation_mode	Starts chamber and return OK when Flasher temperature is ± 1.5° C of set temperature. This ensures the experiment starts only after Flasher has reached a stable temperature

Table 3.6: Basic methods to operate the temperature chamber

Subsystem: Oscilloscope	
Method Name	Method Description
check_connection	Pings the subsystem and returns basic instrument info
get/set_volt_div	Displays the set voltage or sets the given voltage
set_offset	Sets the y-scale offset for each channel
set_scale	Automatically adjusts the y-scale to accommodate the signal
clear_sweep	Resets the acquisition for a given channel
process_data	Sends a measurement query and returns the measurement data in table format

Table 3.7: Basic methods to operate the oscilloscope

measured performance of the Flasher is compared directly with the requirements specified by CTAO.

3.7.1 Visual check

As multiple units of Flasher were tested, it was necessary to set dedicated visual checks to rule out any obvious problems or missing components on the board. After the completion of visual checks, power cables, Ethernet cable and trigger SMA cable are connected for initial startup tests. All these tests and the associated reason to perform them are summarized in Table 3.8.

Visual Checks – Flasher Control Board		
Sl No	**Test Criteria**	**Risk / Remarks**
1	Check the presence of SMA connector, RJ45 connector and power connector and that there is no damage.	Ensures interface reliability.
2	Check the board has 9-pin GPIO connectors and the pins are intact.	These pins offer interrupt interface to the microcontroller.
3	Check the link between Test Pulse and Output Pulse pin.	Essential to know if the internal trigger or external trigger is going to be used.
4	Check the Samtec connector pins are intact.	Ensures delivery of the signal to LED board.
5	Check the presence of Wiznet 5500 and microcontroller chip and there is no obvious damage.	The pins can be damaged during soldering procedure.
6	Check if the reset button is present.	Ensures physical reset option is available.
7	Check the SJ1 pad is NOT soldered.	This pad connects the Ethernet LED. Connecting it might introduce additional an light source during tests.

Visual Checks – Flasher LED Board		
Sl No	**Test Criteria**	**Risk / Remarks**
1	Check the LED is present and there is no obvious damage to it.	LED might be burnt out or the connection might be broken.
2	Check if the temperature sensor, DS1023 and LMG1025 chips are present and there are no obvious sign of damage.	Connection may be broken during soldering process.
3	Check if the 16 pin connector to control board is not bent or damaged.	Ensures reliable transfer of the signal between two boards.
Startup Tests		
Sl No	**Test Criteria**	**Remarks**
1	Ping the Flasher with the set IP address.	Ensures connection to the board has been established.
2	Send a request to inquire serial ID.	Ensures serial ID chip is operating correctly.
3	Send a request to inquire the board temperature.	Ensures the temperature sensor is up and running.
4	Set an initial LED current setting of I = 12.	Ensures the photo relays are working correctly.
5	Set an initial pulse width setting of PW = 45.	Ensures the LMG1025 and DS1023 chips are up and running.
6	Set an external trigger and check the optical pulse with SiPM.	Ensures the LED is functional.

Table 3.8: Visual checks and startup tests for the Flasher

3.7.2 Intensity Stability

As we are dealing with integrated circuits which require a certain period to reach stable operation after power-up, it is essential to quantify this stabilization time.

For the start-up test, both the SiPM and Flasher were kept in a temperature chamber set at 25 °C. The flasher was switched on and it started to flash at a constant frequency of 1 kHz. The peak-to-peak amplitude data of the SiPM signal was taken every 2 seconds and plotted against time (shown in Figure 3.14). There is an initial degradation in the amplitude for about 20 minutes, after which it becomes stable. Thus, for all further operations, a warm up time of 20 minutes is allowed for the Flasher.

CTAO also outlines that pulse to pulse illumination intensity stability of the calibration unit must not exceed 10% Root Mean Square (RMS) fluctuation. This was tested by collecting amplitude data from 1000 pulses and plotting its distribution (Figure 3.15, top). The average RMS variation of pulse-to-pulse intensity calculated over 6 different illumination levels was (1.32±0.06)%. The pulse-to-pulse RMS variation in measured intensity for different illumination levels is shown in Figure 3.15 (*bottom*).

Additionally, CTAO outlines the illumination intensity averaged over 10 seconds must be stable to at least 2% over 30 minutes period at constant temperature. Thus, the test similar to pulse-to-pulse amplitude was carried out for 30 minutes with average illumination data collected every 10 seconds. The relative amplitude level is depicted in Figure 3.16. The variation in measured intensity over 30 minutes was (0.11±0.01)%.

3.7.3 Dynamic Range

As mentioned in Section 3.4, there are 4096 Flasher configurations. A scan of all these configurations was performed, and the LED intensity was measured for each of them. Only fast pulses (pulses with FWHM less than 8 ns) were included in the scan as wide pulses are not important for SSTCAM. To avoid saturating the SiPM due to the large dynamic range, different Neutral Density (ND) filters were

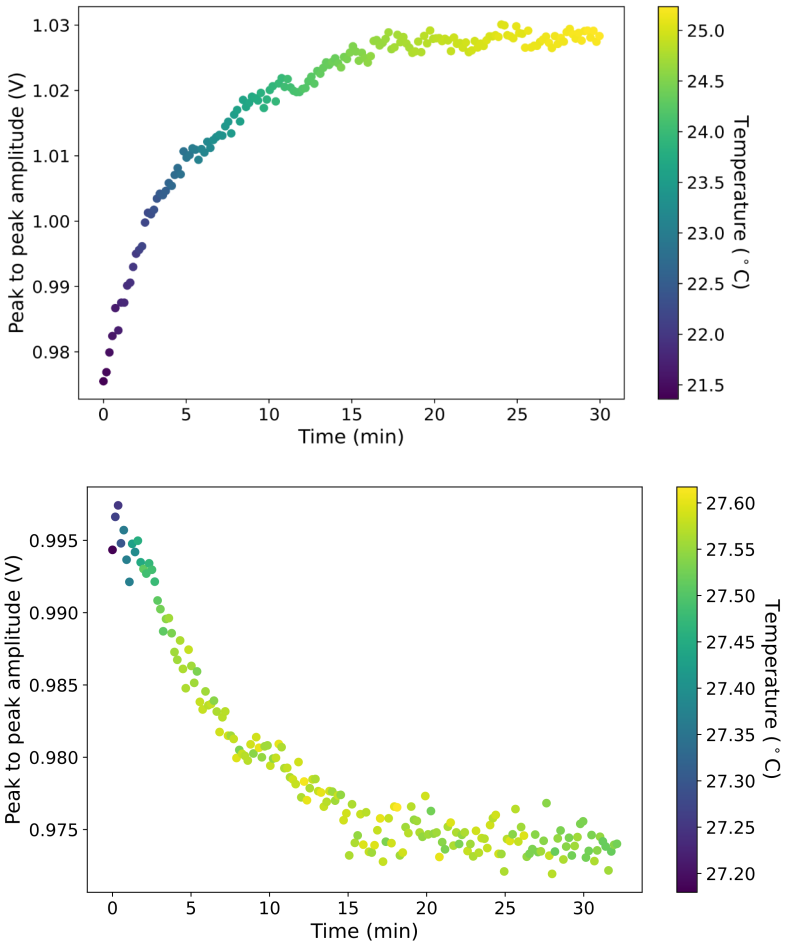

Figure 3.14: Time taken by the Flasher to reach a stable operation in the lab without the temperature chamber (*top*) and with the temperature chamber (*bottom*) set at 25°C. The amplitude of the Flasher pulses reach a stable level after 20 minutes in both cases. The temperature measurement was done with the onboard temperature sensor. The difference in the behaviour at ambient temperature and fixed temperature can be attributed to the initial junction temperature of the LED. In ambient conditions, the light output increases during warm-up before reaching thermal equilibrium, whereas in a temperature-controlled environment (25 °C) the output decreases as the junction temperature rises and then stabilizes, with both cases exhibiting a similar thermal settling time

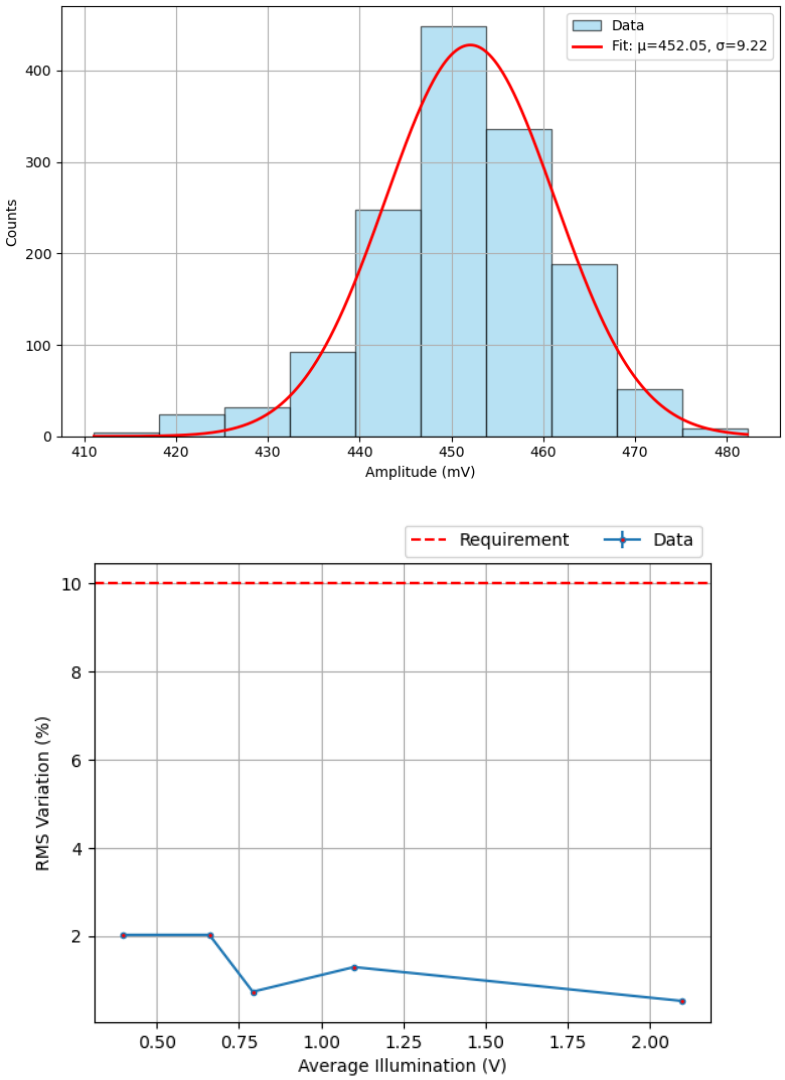

Figure 3.15: (*top*) An example of the measured intensity distribution for a Flasher setting of I=11 and PW=65. The RMS variation of measured intensity is 2.03%. (*bottom*) RMS variation measured for 6 different illumination levels of the Flasher. For all the illumination level, the RMS variation of intensity remains well below the set requirement of 10%.

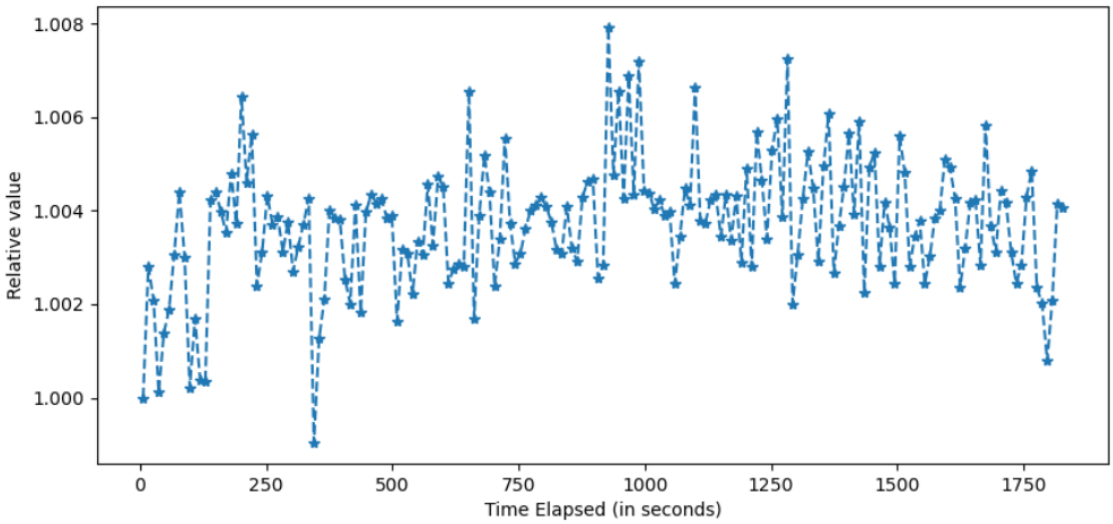

Figure 3.16: Measured pulse-to-pulse intensity of the Flasher over a 30 minutes period. The intensity is stable to 0.1% (calculated from the intensity distribution of the time series) which fulfils the requirement of 2% RMS variation set by CTAO.

placed between the LED and the SiPM. The ND filters were pre-calibrated with a fixed LED intensity and reference photodiode. A full configuration range scan was performed, recording SiPM peak-to-peak amplitude and FWHM. Although peak-to-baseline and peak area were initially recorded, the peak-to-peak amplitude was identified as the most representative measure of LED intensity. Consequently, the other two metrics were excluded in later measurements to reduce the volume of collected data. The test setup described in Figure 3.13 was used and the thermal chamber was operated at 25±0.01°C. Results are shown in Figure 3.17. The results indicated that the Flasher is capable of generating 4 orders of intensity with pulse width less than 5 ns.

With this dataset, a look-up table program is developed which links the desired intensity to the pulse width and current amplitude settings. This allows the user to set the Flasher to a specific intensity level (within tolerance) without dealing with the entire 2D Flasher settings phase space.

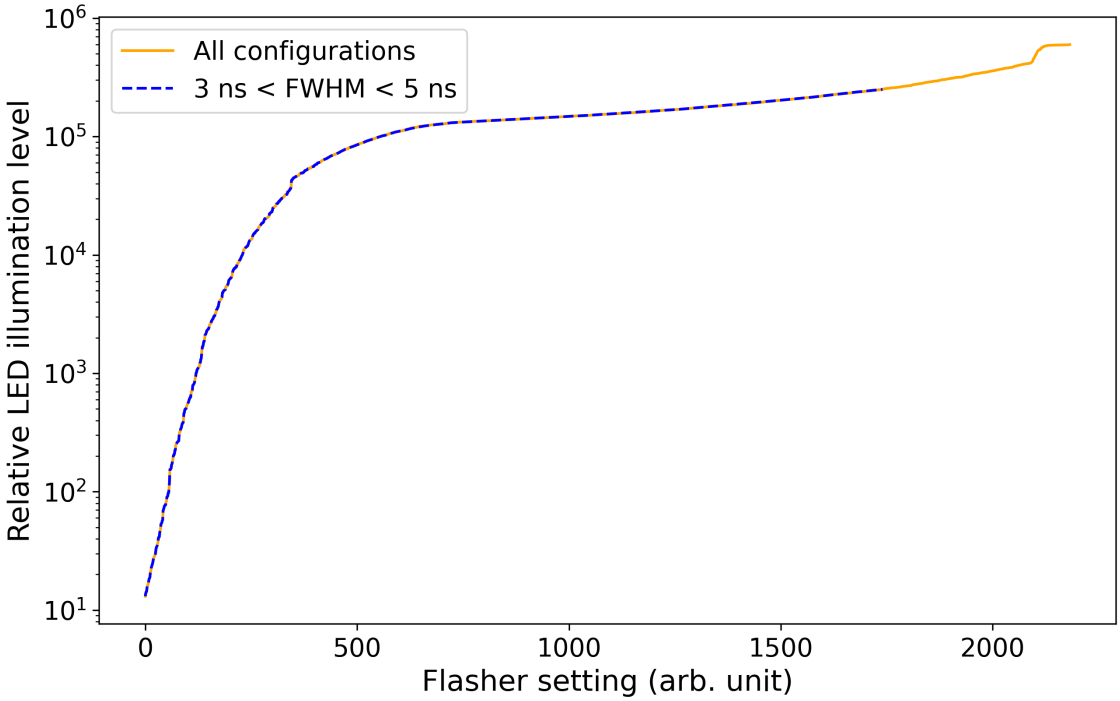

Figure 3.17: Dynamic range study of the Flasher system. The relative amplitude for pulses with FWHM less than 5 ns (*orange*) overlaid on the relative amplitude curve for all FWHM values (*blue*). 4 orders of intensity could be achieved with the Flasher.

3.7.4 Temperature dependence

Integrated circuits and the primarily the LEDs are sensitive to temperature variations, making it essential to evaluate the Flasher system's response to temperature changes. To perform this assessment, both the Flasher and the SiPM are placed inside a thermal chamber, where a Python based control program automates the temperature sweep. The SiPM temperature dependence was evaluated independently and the correction factor applied as a multiplier to the relative intensity using the peak-to-peak measurement. The SiPM correction factor is denoted by

$$\text{Correction Factor} = (1 + \alpha(T - T_{ref})) \tag{3.1}$$

where α is -0.0045 and the reference temperature is 20°C.

From Figure 3.14, we noticed that the Flasher board temperature sits at a higher value than the set temperature of thermal chamber. Thus, additional checks were carried out to quantify this. While the thermal chamber gradually approaches the

target temperature, observations revealed that the Flasher board requires additional time—typically a few minutes longer to reach thermal equilibrium. On average, the board's temperature stabilizes at approximately (1.5±0.5)°C above the chamber's temperature set point. The error on the measurement is dominated by the accuracy of the temperature sensor. Figure 3.18 and Figure 3.19 illustrates the time evolution of the Flasher's temperature during this stabilization phase and the inference about the temperature at which the Flasher board got settled. An exponential fit given by equation 3.2 to the time evolution curve provided the steady-state temperature of the Flasher.

$$T = T_0 + be^{-ct} \tag{3.2}$$

where t is time and T_0 represents the steady-state temperature reached by the Flasher board. Based on these observations, a criterion was established: the Flasher is considered thermally stable when its board temperature is within 1.5°C of the chamber's set temperature. This criterion was always ensured when deciding when to start a test.

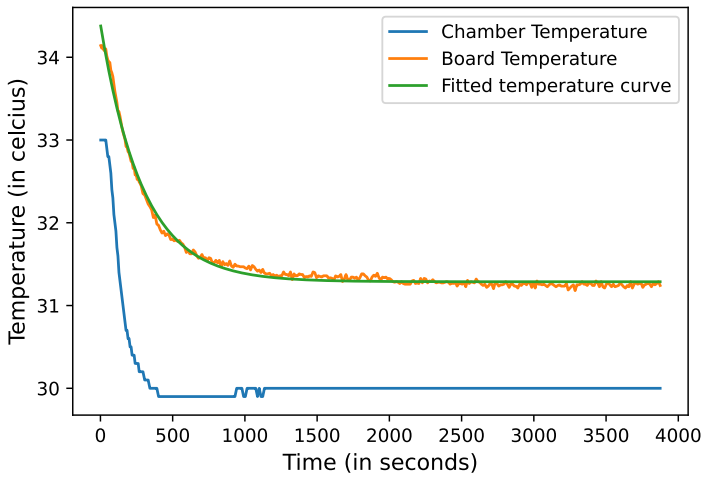

Figure 3.18: (*top*) Time evolution of the Flasher board temperature inside the thermal chamber. The chamber was set at a temperature of 30°C and the board temperature was monitored. The temperature of the temperature chamber (*blue*) reached stability before the Flasher board temperature (*orange*). An exponential fit (*green*) to the Flasher board temperature data provided the steady-state temperature of Flasher board.

Following the thermal stabilization procedure, a temperature sweep was con-

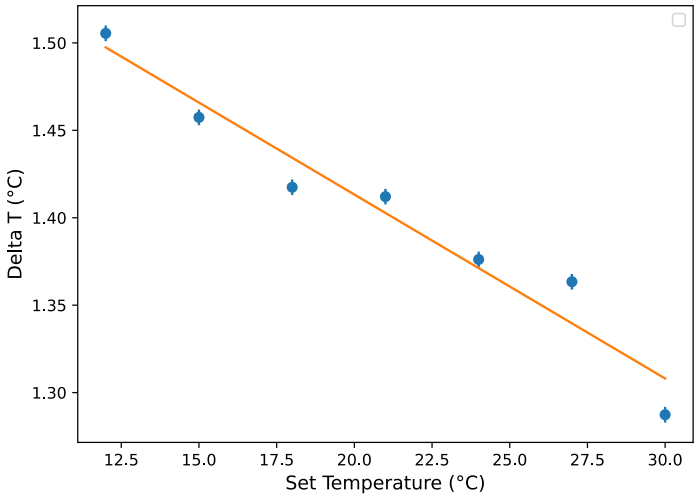

Figure 3.19: Temperature difference between the set temperature of the thermal chamber and the steady-state temperature of the Flasher (derived from the exponential fit in Figure 3.18) when it was placed inside the thermal chamber. The average temperature difference between them was (1.5 ± 0.5)°C.

ducted to study the effect of ambient temperature on Flasher performance. The chamber temperature was incrementally varied from 12°C to 40°C in 3°C steps. This emulated the operational temperature range on telescope. This also ensured that no condensation happens on the electronic components. At each temperature point, the Flasher was operated at three distinct brightness settings, and the average peak-to-peak amplitude was recorded over a 10 s interval. After applying the SiPM-temperature dependence correction, the plot between temperature and relative peak-to-peak amplitude values is denoted in Figure 3.20. We concluded there is a linear dependence of Flasher brightness on temperature. The linear fit to the data suggests there is a 7% drop in the brightness values over 10°C rise in temperature. The Flasher temperature dependence is taken into account in further measurements.

After confirming the linear temperature dependence of the Flasher, the efficiency of extracted thermal coefficients were tested in a simulated temperature environment. The chamber temperature was modulated sinusoidally, while the Flasher was operated continuously and the peak-to-peak amplitude values were recorded. After the application of previously determined correction factors, the amplitude variation was constant to within 0.2%. This consistency validates the correction factors

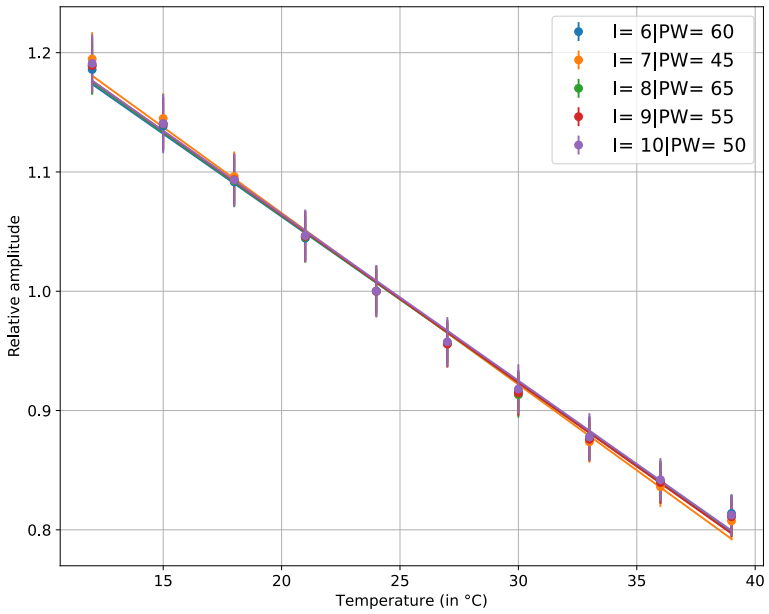

Figure 3.20: Linear dependence of the Flasher brightness on temperature. Different curves shows the dependence for different Flasher settings. On an average, there is 7% drop in amplitude per 10° rise in temperature.

found from the linear fit in Figure 3.20. The temperature variation correction for the simulated temperature environment is depicted in Figure 3.21.

3.7.5 Frequency dependence

The Flasher system is designed to operate across 5 orders of trigger frequencies, offering flexibility based on application requirements. For example - SSTCAM requires the calibration flashes at 10 Hz interleaved between observations and at 1 kHz for single photoelectron calibration. To ensure reliable performance across this range (10 Hz - 1 kHz), it is essential to characterize its response as a function of trigger frequency. According to the DS1023 datasheet [86], the minimum width of the input signal is 20 ns, which corresponds to a maximum input signal of 25 MHz. LMG1025 can also operate in the megahertz frequency range. The chosen LED does not have a rating for its frequency of operation but constant operation at high frequencies can lead to an increase in the forward current beyond its maximum rating of 20 mA [88].

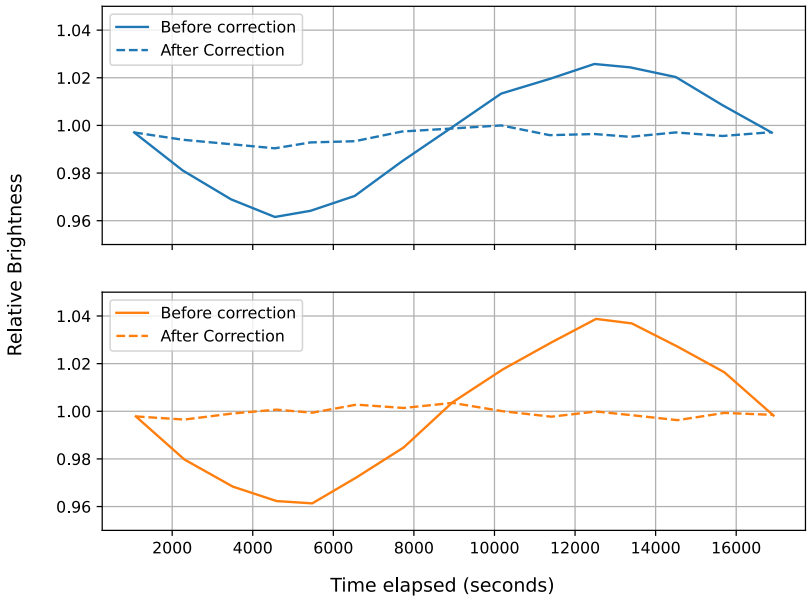

Figure 3.21: On the fly temperature dependence correction of the Flasher system. Two intensity settings are chosen and the correction factors evaluated from the linear fit in Figure 3.20 are incorporated. The variation remains constant to a level of 0.2% after the applying the correction factors.

Considering these timing characteristics for the individual components, a frequency sweep was performed from 10 Hz to 10^5 Hz. For each frequency, the Flasher's peak-to-peak amplitude, rise time, fall time, and pulse width were measured. The variation in amplitude across four decades of frequency was found to be minimal (less than 4%), indicating stable performance. The data was taken at a constant operation temperature of 25°C. The results of this characterization are shown in Figure 3.22.

Also, as per the requirement mentioned in Table 2.2, the calibration system's illumination intensity should not vary more than 1% in the trigger frequency range of 1 Hz and 100 Hz. Thus, a subset of the data (1-100) Hz represented in Figure 3.22 was chosen to determine the intensity variation and it is found to be $(0.246 \pm 0.04)\%$.

3.7.6 Beam Uniformity

Understanding the beam profile of the Flasher is crucial for evaluating its optical performance and ensuring uniform illumination of the SSTCAM camera. Thus,

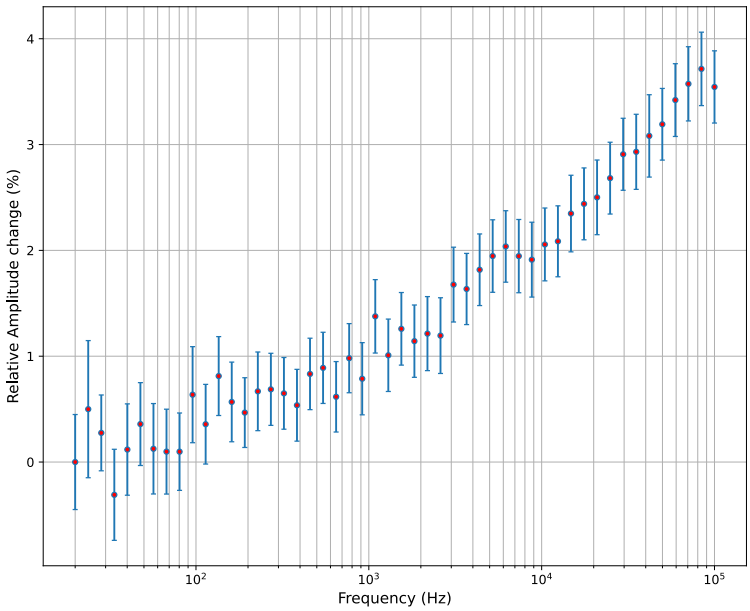

Figure 3.22: Relative change in the intensity of Flasher with frequency at which it is triggered. The overall variation in intensity is $\leq$4%.

a two dimensional beam scan was performed at Max Planck Institute of Nuclear Physics (MPIK). The SiPM (Onsemi MicroJ 60035) was mounted on a robotic arm, which was programmed via a Python script to move across a 2D plane at a fixed distance of 50 cm from the Flasher. This distance is representative of the distance between the secondary mirror (where the Flasher will be mounted) and the focal plane of the camera. The scan covered an area of 40 cm $\times$ 40 cm which is close to the dimension of the camera (30 cm $\times$ 30 cm). The experimental test setup is shown in Figure 3.23.

The inherent spot size of the Flasher LED is shown in Figure 3.24 (*top*). The LED beam pattern has a central bright spot with ring like structure around it which comes from the light refraction of the lens around the LED dome.

The inherent beam pattern is not very useful in calibration activities like flat fielding due to its non-uniform structure. Thus, to achieve uniformity, the beam is diffused with commercially available diffusers. Light falling on the diffusers are emitted at uniform angles which spreads the beam and make it more uniform. One such diffuser from Thorlabs (50°) was tested with the LED Flasher. The angular

response function, defined as the relative intensity at different angles, of the diffuser provided by manufacturer [100]. The beam pattern after using the diffuser is shown in Figure 3.24 (*bottom*). The resulting beam profile has a Gaussian like shape with an offset from the geometric centre. Data obtained from this scan are used to construct a beam model, which plays a key role in the flat fielding process. This application is discussed in detail in Chapter 6.

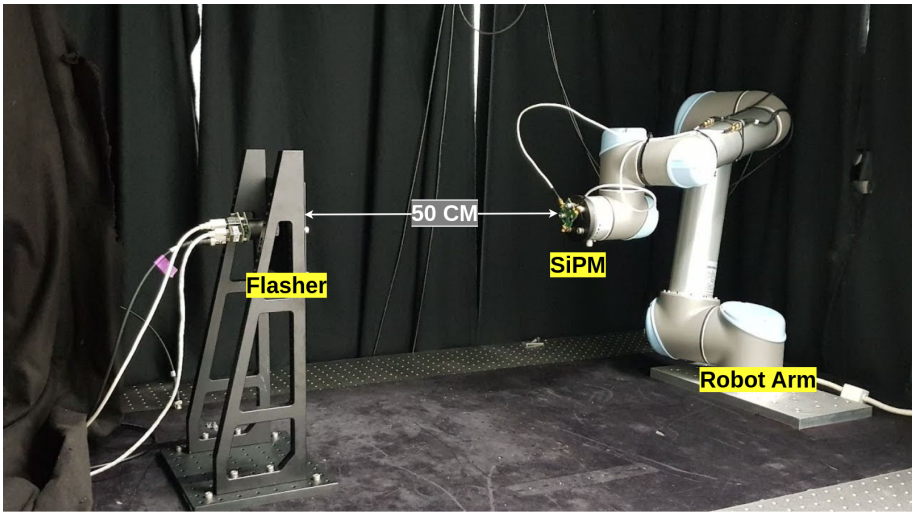

Figure 3.23: Robot arm setup used to scan the beam. The scanning plane is at a distance of 50 cm from the Flasher which is the characteristic distance between the secondary mirror and the focal plane of SST.

3.7.7 Timing Characteristics

We are dealing with nanosecond pulses that are observed by fast photodetectors. Thus it is necessary to understand the timing characteristics of the pulses generated by the Flasher. Also, CTAO outlines specific requirements of the timing characteristics of its calibration unit (shown in Table 2.2). Thus, the same test setup shown in Figure 3.13 (the diffuser and the Neutral Density (ND) filters are removed) is used to carry out the tests. Four timing parameters were monitored - pulse width, rise time, fall time and the event time[1]. This test was performed to understand the pulse-to-pulse fluctuation in above mentioned parameters and the results are

[1]Event time is described as the time difference between the trigger and the LED pulse. Two cursors at the centre of the trigger signal and LED signal on the oscilloscope measure this time difference

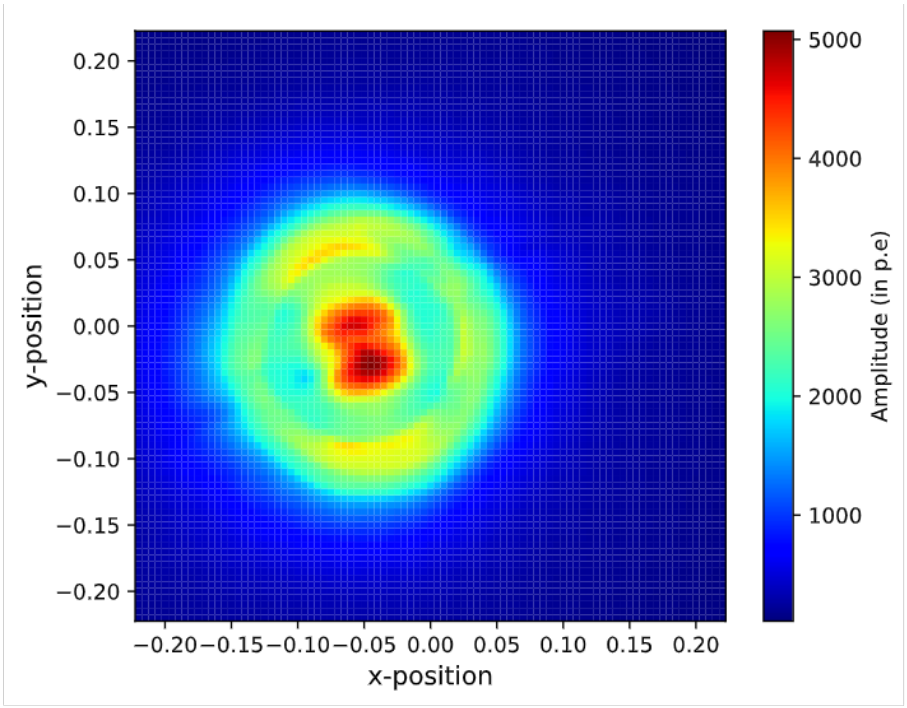

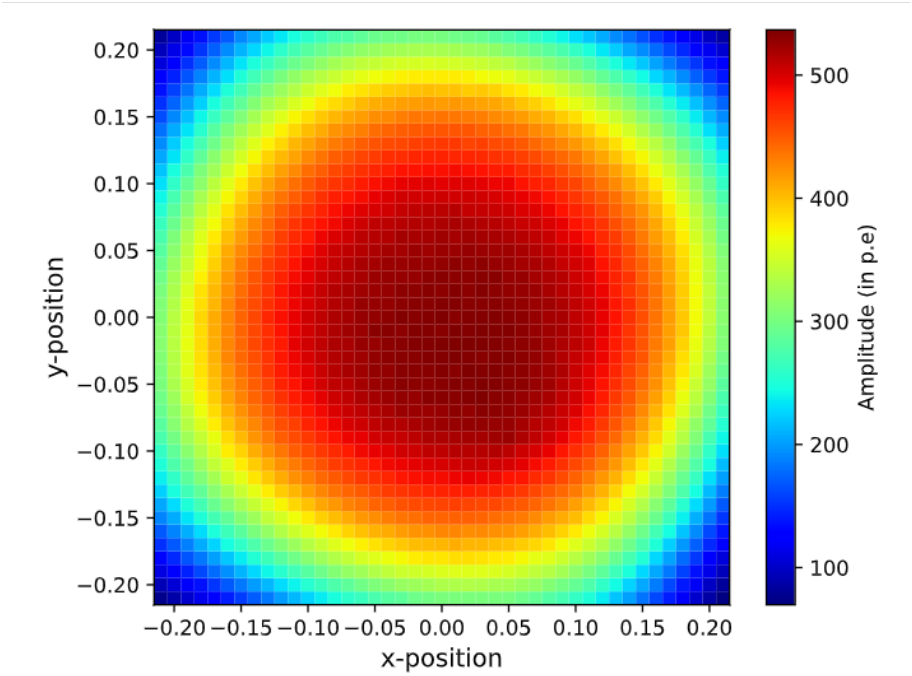

Figure 3.24: (top) Beam profile of the Flasher LED (without diffsuer) scanned with a SiPM mounted on a robot arm. It has a central bright spot with ring like structure around it which comes from the light refraction of the lens around the LED dome. (bottom) Beam profile of the Flasher LED diffuses with a 50° diffuser. The structure of the LED spot are averaged out with the help of the diffuser and a near Gaussian beam with shifted centre is observed. The reduction in the intensity between the two pattern is due to the use of the diffuser in second case.

discussed in the following sections. The visual representation of these parameters is shown in Figure 3.25.

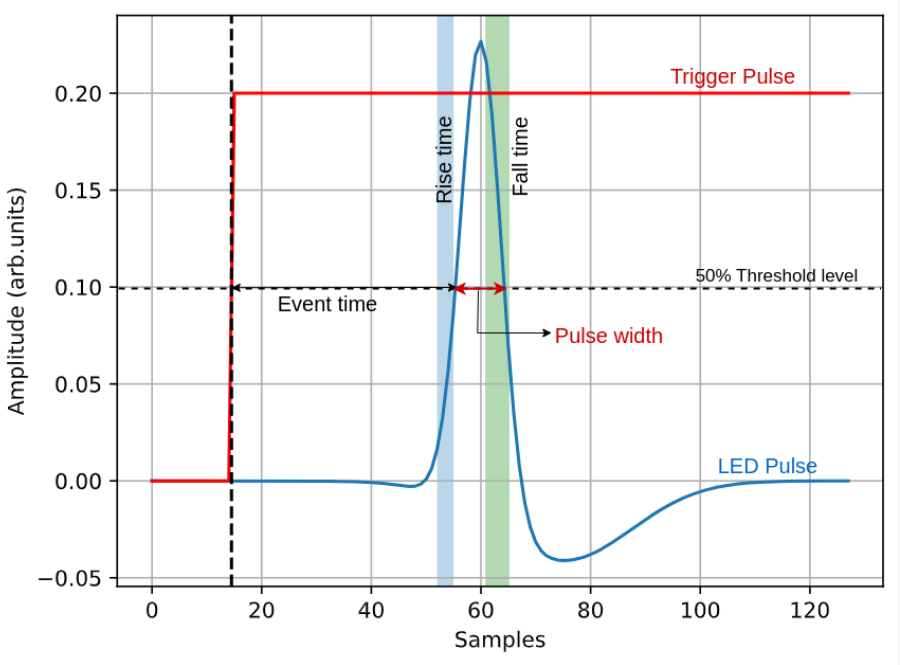

Figure 3.25: Representation of the timing parameter tested to bench mark the timing characteristics of the Flasher. Four parameters - event time, rise time, fall time and pulse width are shown. Event time and pulse width represented by the black arrow, rise time in the green shaded region and the fall time in the blue shaded region. Note the rise time and fall time are 10-90% threshold and the event time is measured at a fixed threshold of 50% of the signals.

Pulse Width

We have seen from Section 3.7.3 that the Flasher is able to generate pulses of width less than 5ns. CTAO also outlines that it should be known to a level of ±0.2 ns. The pulse width values were recorded over 1000 events and the distribution is shown in Figure 3.26. The Gaussian fit to the distribution indicates that the pulse width value is known a level of ±0.12 ns RMS, satisfying the requirement set by CTAO.

Event time

The event time is a critical parameter, as it determines when the camera should be triggered relative to the Flasher signal. Any mismatch between the two can result in missed calibration events. To prevent this, the CTAO specifies that the illumination

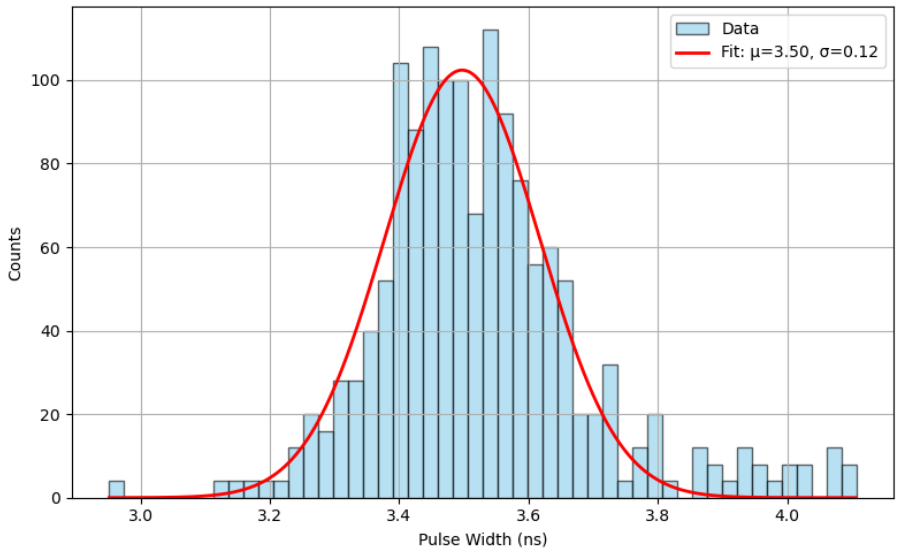

Figure 3.26: Pulse width distribution for a Flasher setting of I=11 and PW=65. Gaussian fit (*red*) indicates that the mean pulse width of 3.5 ns is stable to ±0.12 ns RMS. The outliers do not signify LED instability rather reflect measurement and readout effects from the oscilloscope.

timing from the calibration system must not deviate from the camera trigger time by more than 0.5 ns RMS. The measured event-time distribution is presented in Figure 3.27, where a Gaussian fit yields a jitter of 0.08 ns RMS relative to the trigger.

Rise and Fall time

The rise and fall time distribution for a Flasher setting (I=11 and PW=65) is shown in Figure 3.28. The pulse to pulse variation in these two parameters is (6.15±0.33)% and (6.62±0.35)% respectively.

3.7.8 Long term test

For SST telescopes, the calibration system will be in operation during regular data acquisition. Hence, it is essential to monitor the deviation of its optical properties and perform accelerated tests to investigate how and when it deviates from expected values.

After constantly running a single Flasher for about 120 days, we noticed that the brightness of the LED was reducing. Since we know the trigger frequency, we converted the time axis to number of fired pulses. This showed that after certain

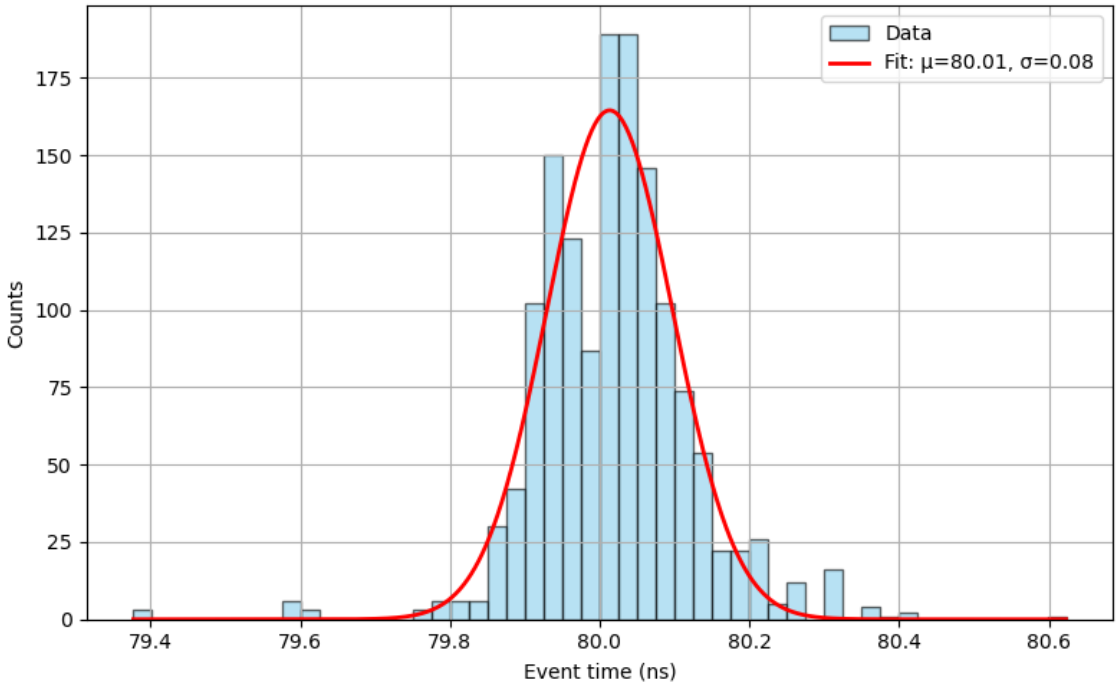

Figure 3.27: Event time distribution for a Flasher setting of I=11 and PW=65. Gaussian fit (*red*) indicates the mean event time of (80.01±0.08) ns RMS. Note that the event time is measured at 50% peak amplitude threshold of the LED signal.

number of pulses, the brightness becomes constant for a given setting. This indicated that the LED has a burn-in effect. Thus, in series production, each LED should be operated at a higher frequency to reach the burn-in region, after which it can be used in normal operation mode (i.e- at a low frequency of few tens of Hz). Figure 3.29 depicts the result of long term test. In future, this test would be repeated on multiple Flasher units to firmly establish the average burn-in time. The total number of pulses fired was equivalent to $\sim$ 10 years of CTA operation. Note that the longevity of the Flasher system is not a requirement but serves as an estimate of the number of years the LED can operate before failure.

3.8 Conclusion

This chapter began with an overview of the design specifications for the calibration system, referred to as the Flasher, developed for SSTCAM in line with the requirements set by CTAO. It then described the key components responsible for

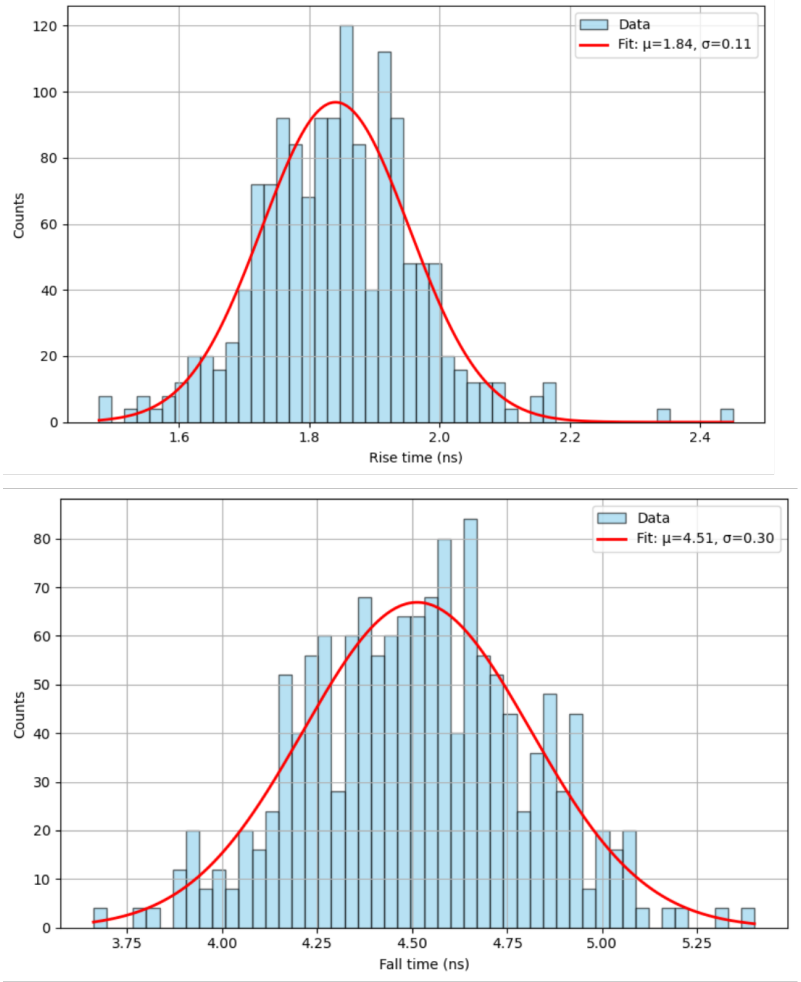

Figure 3.28: Rise time (*top*) and fall time (*bottom*) distribution for a Flasher setting of I=11 and PW=65. Gaussian fit (*red*) indicates the mean rise and fall time have (6.15±0.21)% and (6.62±0.25)% respectively. Note that rise and fall times are measured between 10% and 90% of the amplitude.

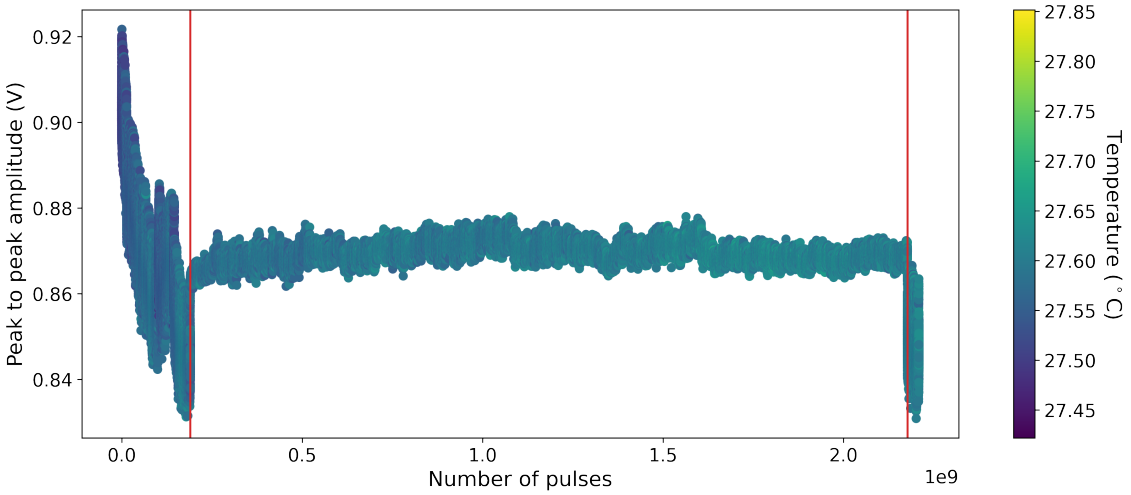

Figure 3.29: LED burn-in effect during a long term test. The Flasher was operated inside a thermal chamber set at 25°. The flasher brightness reduced over long term and then settled to a stable value (known as burn-in effect). Thus, every LED has to be burnt in at a higher frequency before using it in a normal operation mode during series production. The sudden drop in amplitude at the end is an indication of the burn-out of the LED.

generating nanosecond pulses and explained the overall concept of operation of the Flasher. In addition, the chapter outlined the structure of the latest firmware and its role in configuring the various subsystems within the Flasher unit. The firmware is primarily written in C++, with the microcontroller code developed within the Arduino environment.

After establishing the design specification of the Flasher system, this chapter presented the characterization tests carried out to benchmark the performance of the latest prototype (version 3). The test setup consisted of a single-pixel SiPM mounted on an Onsemi evaluation board (Microfc-SMA-60035), a thermal chamber to ensure stable operating conditions, an AWG for providing the trigger signal, and a 4 GSa/s oscilloscope for recording the SiPM response. Significant effort was invested in automating instrument control and data acquisition to streamline the testing process. After addressing the visual inspection requirements of the Flasher, detailed measurements were performed to evaluate the stability of the LED output. The pulse-to-pulse illumination intensity was found to vary by only 1.32%, well within the CTAO requirement of 10%. Likewise, the intensity drift over a 30-minute acquisition period was limited to just 0.1%, far surpassing the specified tolerance of

2%.

After establishing the stability of the Flasher intensity, extended tests were conducted to determine its dynamic range. Using calibrated neutral density (ND) filters to access higher intensity levels without saturating the SiPM, and a diffuser to ensure uniform illumination, it was demonstrated that the Flasher covers four orders of magnitude in intensity while maintaining pulse widths below 5 ns. This broad dynamic range makes the system versatile, enabling applications that span from flat-fielding with high-intensity pulses to single photoelectron calibration under low-level illumination.

Independent studies of the Flasher's dependence on temperature and trigger frequency provided further insights into its performance. The results showed an inverse correlation between temperature and light output, with intensity decreasing by approximately 0.7% per° C. Applying the derived temperature correction coefficients in a simulated environment demonstrated the effectiveness of on-the-fly corrections, reducing residual amplitude fluctuations to within 0.2% after offline correction. In addition,the illumination intensity has minimal dependency on the trigger frequency (less than 4%) and the RMS variation of the Flasher intensity in the range of 1-100 Hz was 0.25%, which is within the limit of 1% specified by CTAO.

The inherent beam profile of the LED was tested with a 2D scan using a SiPM mounted on robot arm. The non-uniform beam spot was further made uniform with the usage of a 50° diffuser. The beam pattern with the diffuser was Gaussian with a shifted centre. Beam modelling and the detailed usage of the system for flat fielding will be discussed in Chapter 6.

The dynamic range scan confirmed that the Flasher is capable of producing short pulses, with the shortest measured at 2 ns. Further timing profile test of the Flasher revealed that the pulse width value is known to a level of ±0.12 ns RMS, and rise and fall time had 6% pulse-to-pulse variation. The event time jitters around 0.12 ns RMS which is well within the requirement of 0.5 ns RMS variation. All the characterisation results have been summarised in Table 3.9. In the next chapter, the research behind development of a multi-channel Flasher system has been discussed.

Long-term stability tests carried out over 120 days revealed a burn-in effect

Sl no	Parameter	Requirement	Measured
1	Pulse width	1-10 ns pulse width with ±0.2ns stability	2-5 ns pulse width with ±0.12ns
2	30 minutes stability (Amplitude)	Variation ≤10%	Variation 1.3%
3	Event time	Jitter by ±0.5 ns	Jitter by ±0.08 ns
4	Rise and Fall time	-	6% variation
5	Trigger rate dependence	1% RMS variation	0.25% RMS variation
6	Temperature dependence	0.1%/C	0.01%/C

Table 3.9: Requirement vs Measured parameters for calibration system

in the LEDs, where the light intensity initially decreased before reaching a stable level. This will be tested further with multiple units of Flasher and in their series production, the LEDs will be operated at a higher frequency to burn them in so that their brightness does not fluctuate in further operations.

Taken together, these detailed characterisation tests confirm that the Flasher system has been thoroughly validated and meets all performance requirements set by CTAO. Nonetheless, several calibration activities in SSTCAM require multiple Flasher units positioned at different locations within the camera. This motivates the development of a centralized Flasher system with multiple channels to efficiently handle the calibration needs of SSTCAM. The developments towards such a multi-channel Flasher are the focus of the next chapter.

CHAPTER 4

Towards the Next Generation Flasher

In Chapter 3, the detailed characterization of the Flasher system was presented. Building upon those findings, this chapter focuses on the development of the next generation of the Flasher system. The motivations driving the need for a new design are outlined in Table 4.1. This study contributed to the decision making regarding the design of the next generation calibration system for the SSTCAM.

Sl No	Design Expectation	Description
1	Multi channel	Each channel caters for a particular aspect of calibration. A fast and uniform source to flat field all pixels; a second fast, low brightness source to perform SPE calibration; a third source to perform functional checks on pixels prior to observation runs; a fourth source for mirror condition checks.

2	Centralised	All the electronic components should be present on a single board controlled by a single microprocessor. This reduces the board to board operational fluctuations and offers uniform control. Also, a centralised board can be placed in a compact space inside the temperature stable camera enclosure.
3	Minimal interfaces	A single centralised board reduces the number of interfaces required from the camera's power (slow control board) and system control (back plane). A single trigger signal from the backplane can be fanned out to multiple channels and a single ethernet connection can be used for communication.
4	Lightning protection	A centralised board placed inside the charge-proof camera enclosure offers protection from power surges due to unforeseen circumstances like lightning strikes. In contrast, positioning a Flasher at the secondary mirror for flat-fielding—while still connected to critical and costly components within the camera (such as the backplane) via communication cables—would expose the system to greater risk.
5	Fast setup	A single microprocessor ensures multiple channels can be programmed quickly and uniformly. Also, each channel will reach stable operation range at same time after warm-up.

Table 4.1: Requirements for the next Flasher version.

To evaluate potential design pathways, two proof-of-concept studies were undertaken. The first explored a centralized Flasher board architecture, with LEDs coupled to optical fibres routed light to various locations within the camera—discussed

in Section 4.1. Based on the insights and limitations encountered in this configuration, a second approach was investigated using shielded coaxial cables to deliver signal to LEDs directly at target locations. This alternative setup is described in Section 4.2. My contributions to this work encompassed the selection of suitable optical fibres and coaxial cables, as well as the design, preparation, and commissioning of the fibre-testing bench at MPIK, Heidelberg. Dr. Richard White, Dr. Davide Depaoli and Isabella Sofia at MPIK helped in building the test rigs and assisted in SiPM handling. Apart from this, I developed and implemented the experimental setup for detailed noise-interference testing at University of Leicester. Will Oughton assisted in carrying out the tests in the lab. After conducting the systematic collection of experimental data, I carried out the complete analysis and interpretation of the collected datasets.

4.1 Flasher-Fibre system

As outlined in the first requirement in Table 4.1, multiple channels are needed, each catering for a particular calibration activity. To achieve this, different types of optical fibres are needed to route the light to different location within the camera. The list below describes the different types of fibres that are tested in this study and the ways in which they would be expected to carry out a particular calibration.

1. **Fibres for SPE calibration and functional checks.**

   This approach envisions placing a fibre in a specially engineered groove on the focal plane, directly coupled to a Flasher LED. With the camera door closed, the emitted light would reflect off the inside surface of the camera door, ensuring illumination of all camera pixels. With sufficient illumination levels the setup could be used for functional checks of individual pixels before observation runs. Additionally, by leveraging the Flasher's wide dynamic range (discussed in Section 3.7.3), lower-intensity pulses could be used to perform single photo-electron calibration. Thus, two fibre options were tested for this purpose: the BCF-10 scintillating fibre from Saint-Gobain Crystals [101], with a peak emission wavelength of 432 nm and a diameter of 1 mm; and a

light-diffusing glass optical fibre from Corning [**?**], covering a spectral range of 420 nm–700 nm with a diameter of 0.2 mm. These fibres comes under the category of under-lid fibres in subsequent sections. Characterization tests and illumination patterns of both the under-lid fibres are presented in Section 4.1.1 and Section 4.1.2 respectively.

2. **Fibres for flat fielding.**

   The traditional flat fielding method illuminates the camera's focal plane from the front using a bright and uniform source. To replicate this, I investigated the use of armoured optical fibres (which are both durable and protected from abrasion) coupled to the Flasher to deliver light directly onto the focal plane. Since flat-fielding requires both high intensity and uniformity, three fibre models from Thorlabs (M92L01 [102], M59L01 [103], and M93L01 [104]) were tested under this configuration. The detailed testing procedure and results are provided in Section 4.1.3.

4.1.1 Under-lid fibre: Profile Tests

The BCF-10 scintillating fibre consists of a polystyrene-based core surrounded by a Polymethyl Methacrylate (PMMA) cladding. When a minimum-ionizing particle interacts with the core, scintillation photons are produced and guided along the fibre by Total Internal Reflection (TIR) at the core–cladding boundary [101]. In practice, TIR is not perfectly efficient, and a fraction of the photons leak out through the fibre surface. Additionally, when exposed to Ultra Violet (UV) light, the core material absorbs photons and re-emits them isotropically [105], with some escaping through the sides of the fibre.

By coupling an LED to the fibre, these two effects—imperfect light guiding and absorption/re-emission—can be exploited to achieve controlled light emission along the entire length of the fibre. This enables illumination of the camera pixels, with the LED intensity setting the photoelectron levels recorded in different pixels.

On the other hand, the light diffusing fibre from Corning glass optical fibre are engineered with embedded scattering centres (nanostructures) in its silica core that

cause controlled leakage of light along its length [**?**]. Thus, by coupling the LED to this fibre and controlling the brightness setting of the Flasher, different illumination levels could be achieved within the camera.

The first test performed was to understand the light emission profile of both the fibres. In independent tests, 1 m lengths of the fibres (1 mm diameter for scintillating fibre and 0.2 mm diameter for light diffusing fibre) were coupled to the Flasher LED and the Flasher was triggered at 1 kHz. The SensL MicroJ 60035 SiPM [106] was mounted on a robot arm that was programmed to move parallel and perpendicular to the length of the fibre. A schematic of the test setup is shown in Figure 4.1.

Light attenuation along the scintillating fibre is expected due to intrinsic absorption in the fibre material and scattering losses at imperfections and boundaries. In the vertical scan, attenuation happens because of absorption and scattering within the fibre, combined with reduced light collection efficiency for a detector farther from the fibre axis. The emission profile of the light diffusing fibre is also explained by the same reason.

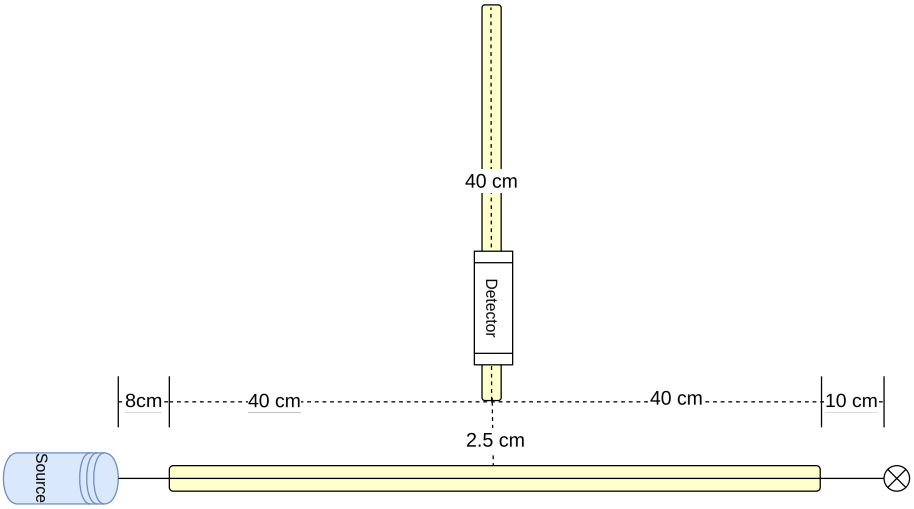

Figure 4.1: The experimental setup to perform the line scans on the scintillating fibre. The SiPM is connected to the oscilloscope for data acquisition. The robot arm can move parallel and perpendicular to the fibre. The fibre lies directly below the sensitive area of the SiPM.

The results from the line scan parallel and perpendicular to the scintillating fibre are shown in Figure 4.2. A decay profile was observed from the horizontal scan. It

was fitted with an exponential decay function defined by equation 4.1.

$$I = I_0 e^{-\frac{x}{\lambda}} \tag{4.1}$$

where λ is the attenuation length defined as the distance where the amplitude becomes $\frac{1}{e}$ times of the initial value. The fit gives an attenuation length of (0.305±0.019) m. An improved attenuation length measurement with advanced setup, better SiPM modules and a long length (2 m) of the fibre revealed an attenuation length of (0.70±0.03) m. The change in accuracy of measurement is a result of change in the measurement setup. Similarly, the emission profile is also measured from the vertical scan of the fibre at three different distances from the source (8, 18 and 28 cm away from the LED).

The parallel and transverse profile of the light diffusing fibre is shown in Figure 4.3. It can be inferred from the figure that the light diffusing fibre has a longer attenuation length. However, it could not be measured due to the short length of fibre available for testing. In the vertical scan, the pulse amplitude from the light diffusing fibre attenuates at a 10% shorter distance than the scintillating fibre. This behaviour can be attributed to the smaller core diameter of the light-diffusing fibre, which results in reduced light coupling and consequently a shorter effective attenuation length along the vertical direction.

After characterizing the emission profiles of the two fibres, it was essential to examine the timing profiles of the pulses generated by each fibre. The timing profile determines their compatibility with the camera electronics, as longer pulse widths can result in the integration of additional background photons, negatively impacting performance. The time spread introduced by the fibres was therefore calculated from the measurements using the following procedure.

Let the measured pulse width of the LED with the SiPM be σ_{total1} and the measured pulse width of the fibre illuminated with the LED and measured with the SiPM be σ_{total2}.

$$\sigma^2_{total1} = \sigma^2_{LED} + \sigma^2_{SiPM} \tag{4.2}$$

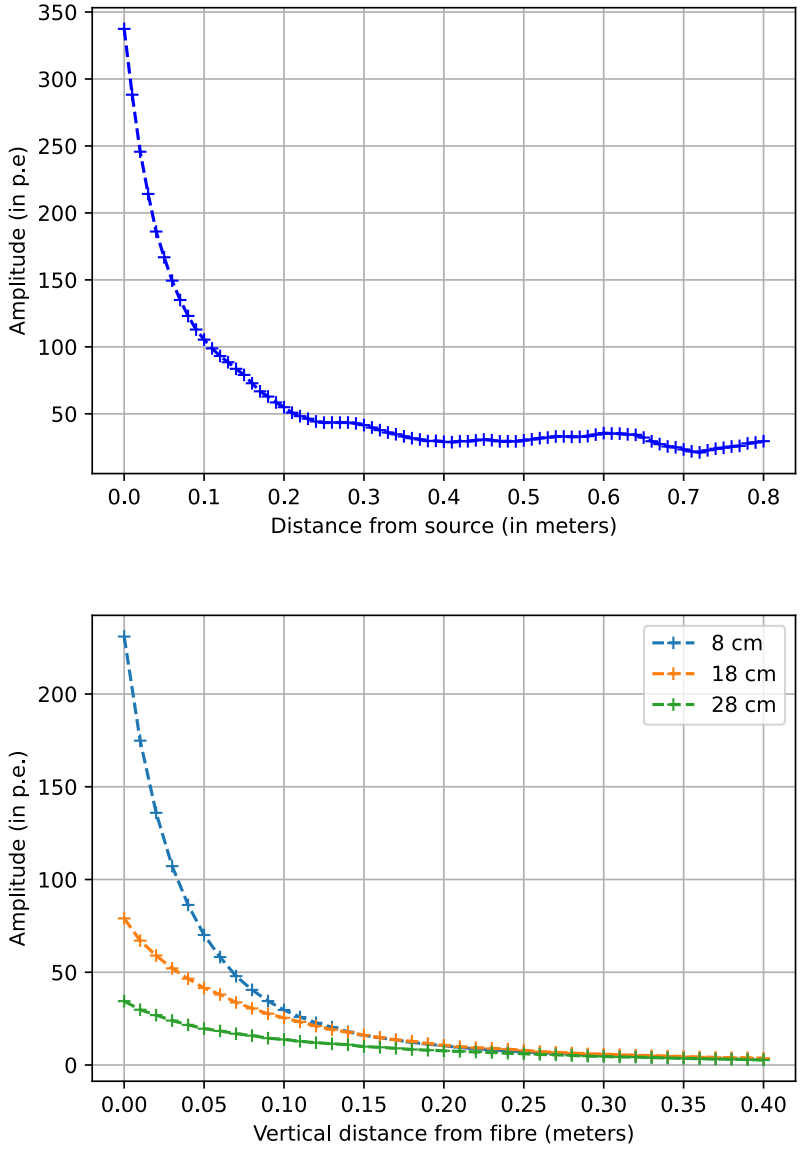

Figure 4.2: Line scan along the length of the scintillating fibre (*top*) and perpendicular to it (*bottom*). The three curves in the vertical scan correspond to three different distances from the LED as shown in the legend.

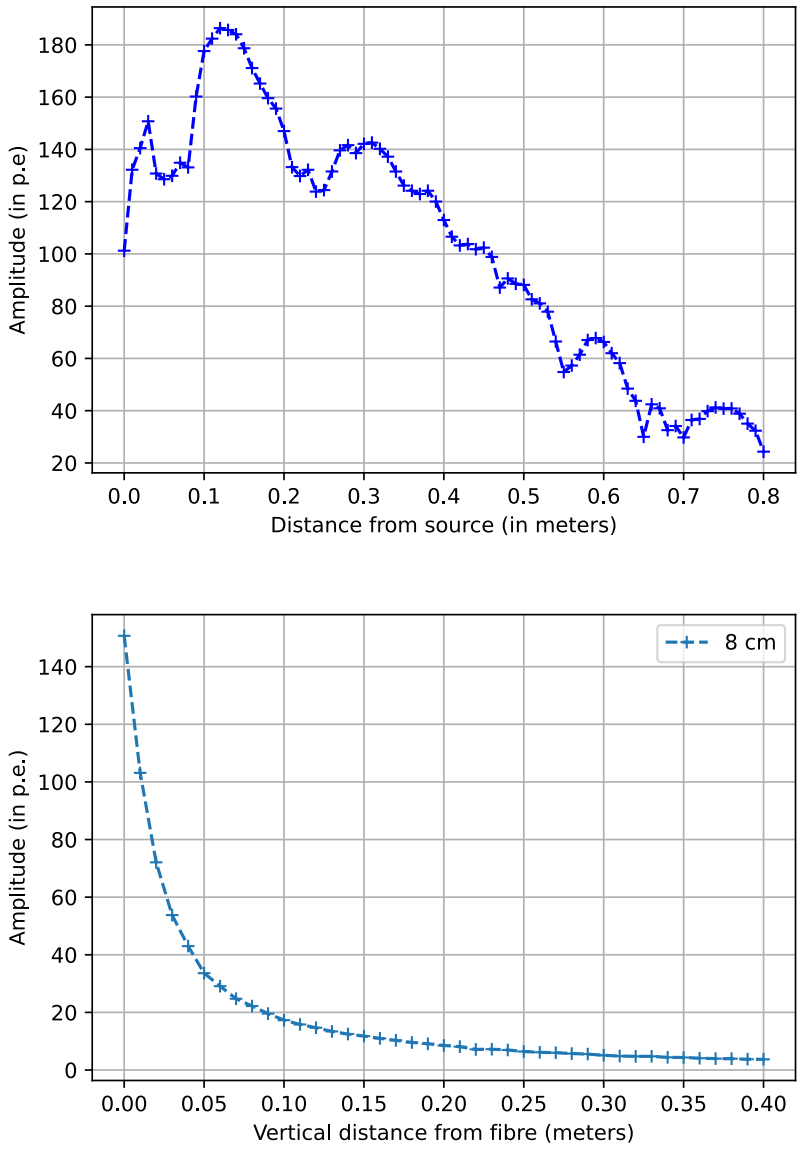

Figure 4.3: Line scan along the length of the light diffusing fibre (*top*) and perpendicular to it (*bottom*).

$$\sigma^2_{total2} = \sigma^2_{LED} + \sigma^2_{SiPM} + \sigma^2_{Fibre} \tag{4.3}$$

Plugging eq 4.2 into eq 4.3,

$$\sigma^2_{total2} = \sigma^2_{total1} + \sigma^2_{Fibre} \tag{4.4}$$

$$\sigma_{Fibre} = \sqrt{\sigma^2_{total2} - \sigma^2_{total1}} \tag{4.5}$$

The quadrature subtraction assumes a Gaussian error of pulse width distribution. The average pulse width measured with the scintillating fibre (σ_{total1}) was 13 ns, while the pulse width of the Flasher LED measured directly with the SiPM (σ_{total2}) was 5.5 ns. Substituting these values into Eq. 4.5, the additional time spread introduced by the scintillating fibre was determined to be (11.77 ± 0.60) ns. Using the same procedure, the time spread for the light-diffusing fibre along the whole length of the fibre (30 cm) was calculated as (2.49 ± 0.30) ns. The smaller time spread in the light-diffusing fibre arises because it only scatters the incoming LED light, whereas the scintillating fibre involves absorption and re-emission processes, which introduce greater temporal broadening.

4.1.2 Under-lid fibre: Response across camera

Initial Test

After characterising the emission profile of both the fibres, it was necessary to understand the illumination pattern and the timing profile created by the fibre across all pixels on the focal plane. To serve the purpose of functional checks and single p.e. calibration, all the pixels should be illuminated with at least a few p.e. level light. This is dictated by the location of the fibre on the focal plane plate of the camera, the reflectivity of the rear-side of the door and the illumination pattern created by the fibre. To address these factors, preliminary tests were conducted to determine the optimal fibre location, assess illumination levels, and evaluate the timing profile across the camera plane.

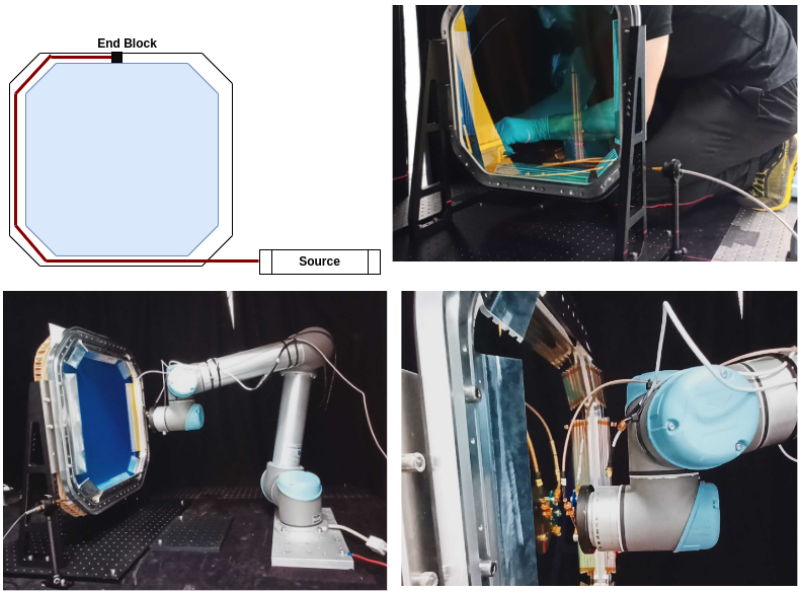

Figure 4.4: (*top left*) The diagram shows the mounting of the fibre and location of the light source. Note that the prototype fibre was quite short to cover the entire perimeter of the focal plane. (*top right*) Fibre mounting done on the temporary grooves attached to the window. The fibre was held in place with Kapton tapes. (*bottom left*) The final test setup with the window mounted and a white paper attached to the cardboard which emulates the camera door. The SiPM is mounted on the robot arm. (*bottom right*) A typical scan position. The distance of the SiPM from the window was 12 mm. This is the typical distance of the central SiPM pixel from the window in the final camera design.

The first step focused on identifying the most suitable position for the fibre. Before the construction of the focal plane plate, the location of the grooves had to be defined. For this purpose, grooves were machined into aluminium plates, which were then mounted onto the mechanical plate of the window. The mechanical plate, together with the window, was fixed to a sturdy frame (shown in Figure 4.4), and the fibres were routed through the grooves.

The initial 2D scans were carried out with the SensL MicroJ 60035 SiPM [106] mounted on a robot arm and emulating the pixel positions of the camera[3]. The fast signal output of the SiPM was connected to an oscilloscope outside the dark box which measured signal properties. The camera window was covered with a piece of white paper to simulate a closed door from which the light reflected and illuminated the focal plane. Other reflective materials were tested during a detailed test (discussed later in Section 4.1.2).

Illumination scans were then carried out with the fibre positioned in grooves ranging from the innermost to the outermost location. A modest increase of about 3% in illumination levels was observed from inner to outer positions. While the innermost groove did not significantly enhance brightness, it ensured that most of the central pixels were illuminated. Consequently, it was decided that the engineered groove on the focal plane plate should be placed as close as possible to the SiPM pixel array. In the final design, the groove is positioned 3 cm from the outer edge of the SiPM pixel module.

After deciding on the location of the fibre, the illumination pattern generated by both the fibres were tested. The illumination pattern by the BCF-10 scintillating fibre coupled with the Flasher is shown in Figure 4.5 (top); there is a drop of 90% in amplitude from the edge pixels to the central pixel. The overall variation, defined as the ratio of standard deviation to the mean of amplitude seen across all the pixel positions, in the illumination pattern is 67.14%. As expected, the illumination pattern is non-uniform. The illumination pattern of the light diffusing fibre was studied in a similar way (shown in Figure 4.5, bottom) resulting in a measured

[3]With this setup, only the approximate position of the SiPM pixels is known and the curvature of the focal plane plate in the actual camera was difficult to emulate with the robot arm scan.

overall variation across the focal plane of 65% but 80% lower average-illumination level across the focal plane compared to the scintillating fibre.

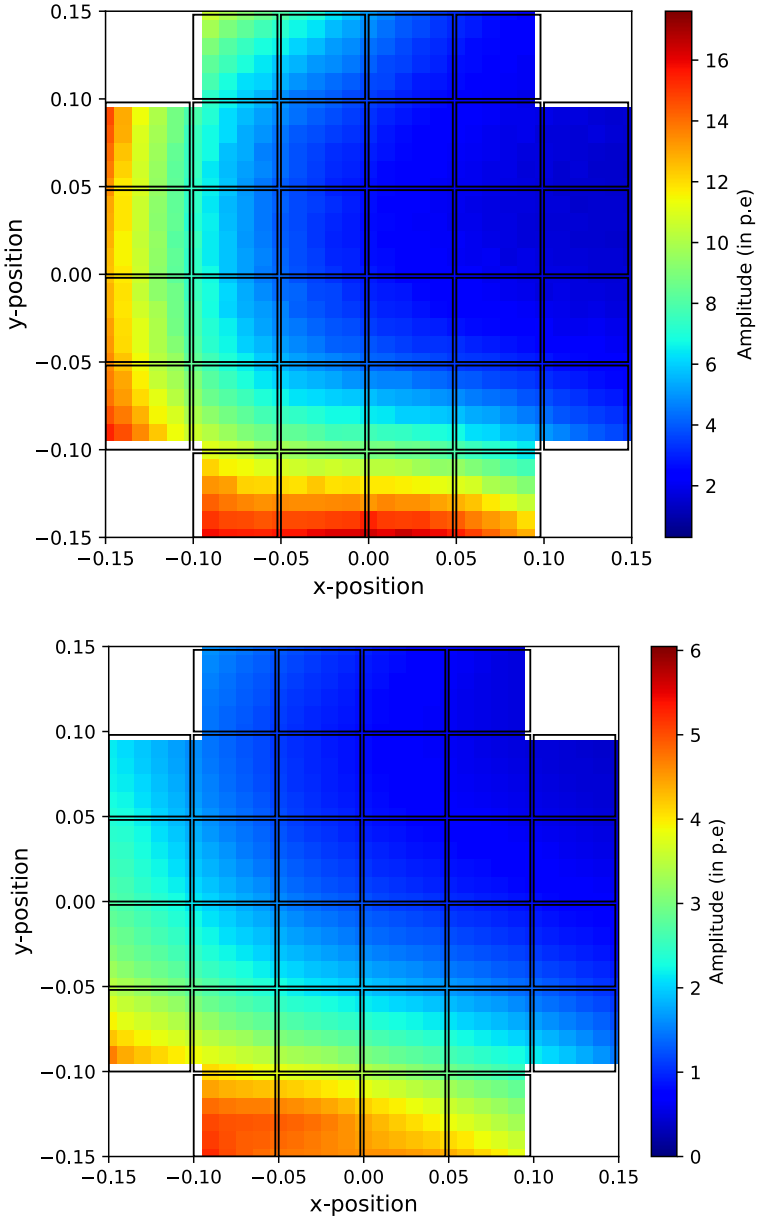

Figure 4.5: The illumination pattern generated by the scintillating fibre (*top*) and light diffusing fibre (*bottom*). The scan region replicates the SiPM pixel array of the actual camera which has an area of 30 cm × 30 cm. The overall variation across all pixels is 67% for the scintillating fibre whereas it is 65% for the light diffusing fibre.

The timing profile of the light detected across the pixels for both the scintillating fibre and the light-diffusing fibre is shown in Figure 4.6. For the scintillating fibre, most pixels are dominated by scintillation light, which is reflected in their longer

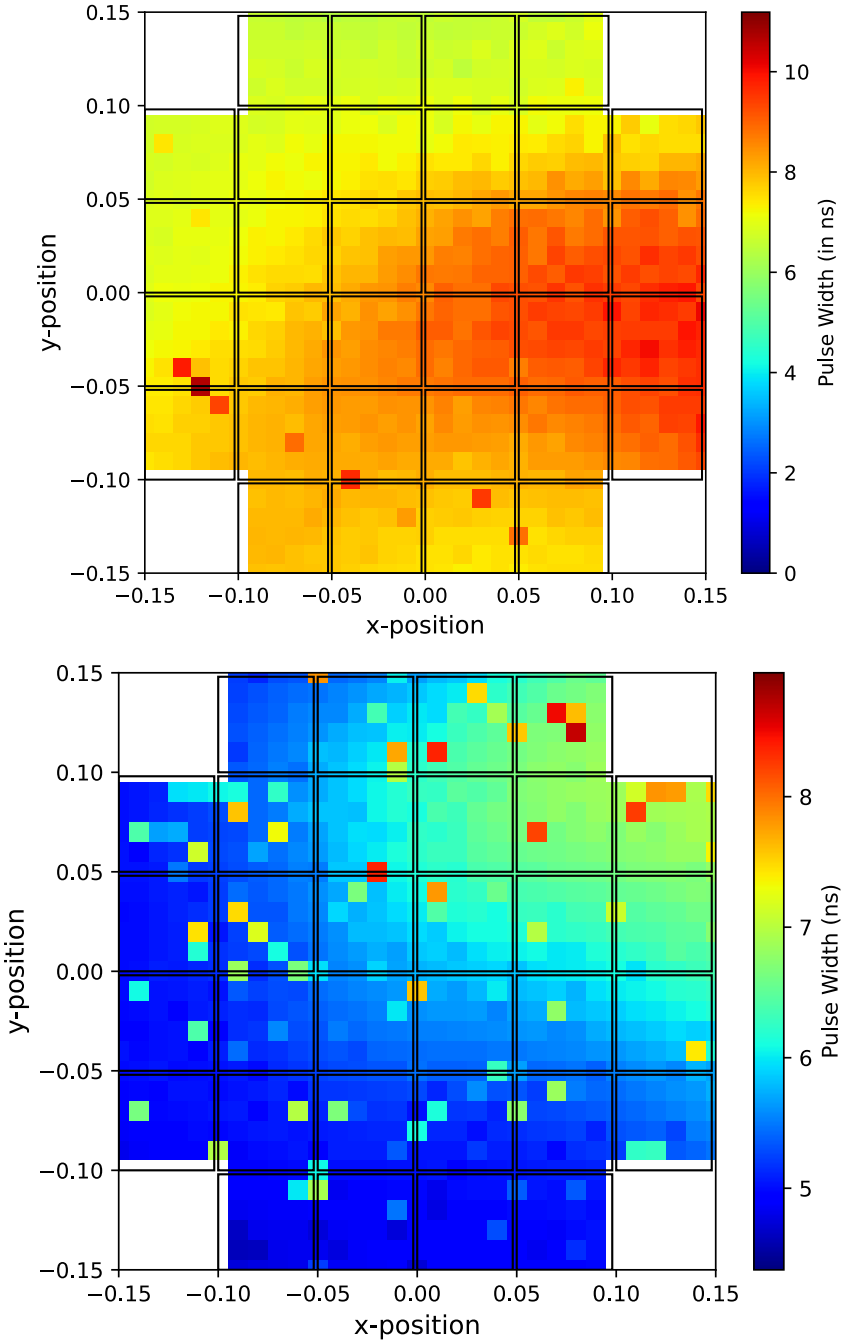

Figure 4.6: The pulse width seen by all the pixels when illuminated with the scintillating fibre (*top*) and light diffusing fibre (*bottom*). The scintillating fibre broadens the intrinsic pulse width of the Flasher. Most of the pixels are dominated by scintillated light except the top pixels which see some direct light. In the light diffusing fibre, pixels closer to the fibre have the pulse width similar to the Flasher LED. The pixels far away from the fibre have a broader pulse due to a longer optical path. Some of the random hot spots in both figures are due to erroneous measurement from the oscilloscope.

pulse widths. However, in the top-left corner, some pixels receive direct light from the fibre end; their time profile resembles that of the Flasher. This effect becomes even more evident with the light-diffusing fibre. Since most of the LED light is scattered along the fibre, pixels located closer to the fibre (on the left side) exhibit the characteristic Flasher-like pulse width of about 5 ns. In contrast, pixels farther from the fibre show broader pulses due to the longer optical path. The timing profile is revisited in the detailed test in Section 4.1.2.

By combining the amplitude and timing profile results from both fibres, it can be concluded that the light-diffusing fibre produces a time profile that closely resembles the Flasher LED. However, it suffers from a significant loss in illumination amplitude (about 80% lower than the scintillating fibre), largely due to the difficulty of coupling light into its small core. As a result, the central pixels may receive little or no light. In contrast, the scintillating fibre broadens the Flasher LED pulse (almost doubling its width), but its larger core enables more efficient light coupling, ensuring that even the central pixels are illuminated. Therefore, there is a trade-off between pulse amplitude and pulse width. Given the lack of larger-core light-diffusing fibres on market and the ready availability of scintillating fibres, the latter was chosen for under-lid illumination in SSTCAM.

Detailed Test

After the selection of the scintillating fibre for under-lid illumination and eventually the preparation of the focal plane plate with the machined groove, a detailed test was carried out at the Max Planck Institute of Nuclear Physics (MPIK) on a newer setup with the 64 pixel SiPM array from Hamamatsu which is the SiPM that will be used in the final camera (see in Chapter 2). The SiPM array was connected to a TARGET module, which was characterised at the University of Leicester who provided the requisite calibration files. A 2 m length of the fibre was terminated with an SMA connector and coupled to the Flasher behind the focal plane plate. The other end of the fibre was inserted through a dedicated hole in the focal plane plate and the fibre was placed in the machined groove. Kapton tapes were used to hold the fibre in place. The specialized camera window was screwed to the focal

plane plate and an aluminium sheet with a sheet of reflective material (discussed later) was attached on top of it. The purpose of the specialized camera window is to allow only a narrow UV wavelength band of Cherenkov spectrum and block all other night sky background (shown in Figure 2.4). The aluminium sheet with the reflective material emulated the door more accurately than the paper used in the earlier test. Since only a single well characterized TARGET module was available, the module had to to be moved to 32 different slots on the focal plane plate to generate the full illumination pattern. As there are dedicated slots on the focal plane plate to hold the SiPM, there is no approximation of pixel position and the curvature of the focal plane is also captured. Figure 4.7 shows the test bench preparation.

The Flasher and the TARGET module trigger (100 Hz) were synced and the collected waveform data from each pixel was stored for further analysis. The detailed procedure to go from the raw waveform data (known as R0) to pixel amplitude in mV (known as DL1) has been discussed in data level section of Jason Watson's thesis [66]. The DL1 data consists of peak-to-peak amplitude, rise time, fall time and pulse width measurement data of each pixel.

The first test with the improved setup was carried out to select a proper reflective material for the rear-side of the door. Therefore, several coating materials were tested, as summarized in Table 4.2.

Sl No	Material Name	Description
1	Aluminium	A single polished rectangular aluminium sheet. This is the material from which the camera doors are made of.
2	Glossy white paint	Another aluminium sheet of similar dimension was painted with a glossy white paint
3	Tyvek	A high density polythelene material with 92% reflectivity. It has high strength and excellent diffuse reflectivity in the near UV wavelength [107]. A rectangular sheet of this material was used in the experiment.

4	Spectralon	A fluropolymer with highest known diffuse reflectivity of $\geq 99\%$ [108] in the UV wavelength range. A rectangular sheet of this material was used in the experiment.

Table 4.2: Description of the materials tested for their reflectivity in order to choose a potential material for the inner surface of the door.

Sheets of each material were cut to the size of the camera window (Figure 4.8) and mounted on a pseudo-door (shown in Figure 4.7). The SiPM module attached to the TARGET module was then iteratively placed at three different positions (illustrated on the right of Figure 4.8), covering both central and edge pixels, and the pulse amplitudes after reflection from the materials were recorded. Since each module consists of 64 pixels in an 8×8 array, this configuration sampled 24 pixel positions along each column from the edge to the centre.

The relative reflected amplitudes from each material, normalized to aluminium, are shown in Figure 4.9. A summary of the reflectivity enhancement compared to aluminium is provided in Table 4.3. Among the tested materials, Tyvek produced the largest signal enhancement. Spectralon, while specified to provide $\sim 99\%$ diffuse reflectivity according to its datasheet, exhibited a practical performance comparable to Tyvek. Considering 2-3 orders of cost difference between the two, Tyvek was recommended as the most suitable and cost-effective material for the final camera door. So for all the further test, the emulated door was used with Tyvec as the rear surface material.

	White Paint	Tyvek	Spectralon
Position 1	48%	60%	30%
Position 2	44%	43%	42%
Position 3	41%	54%	45%
Average	**44%**	**52%**	**39%**

Table 4.3: Percentage increase in reflected amplitude compared to aluminium for three different materials at three different SiPM module positions (averaged over 24 pixels). Position 1, 2 and 3 refers to the module positions 31, 26 and 20 respectively (shown in Figure 4.8).

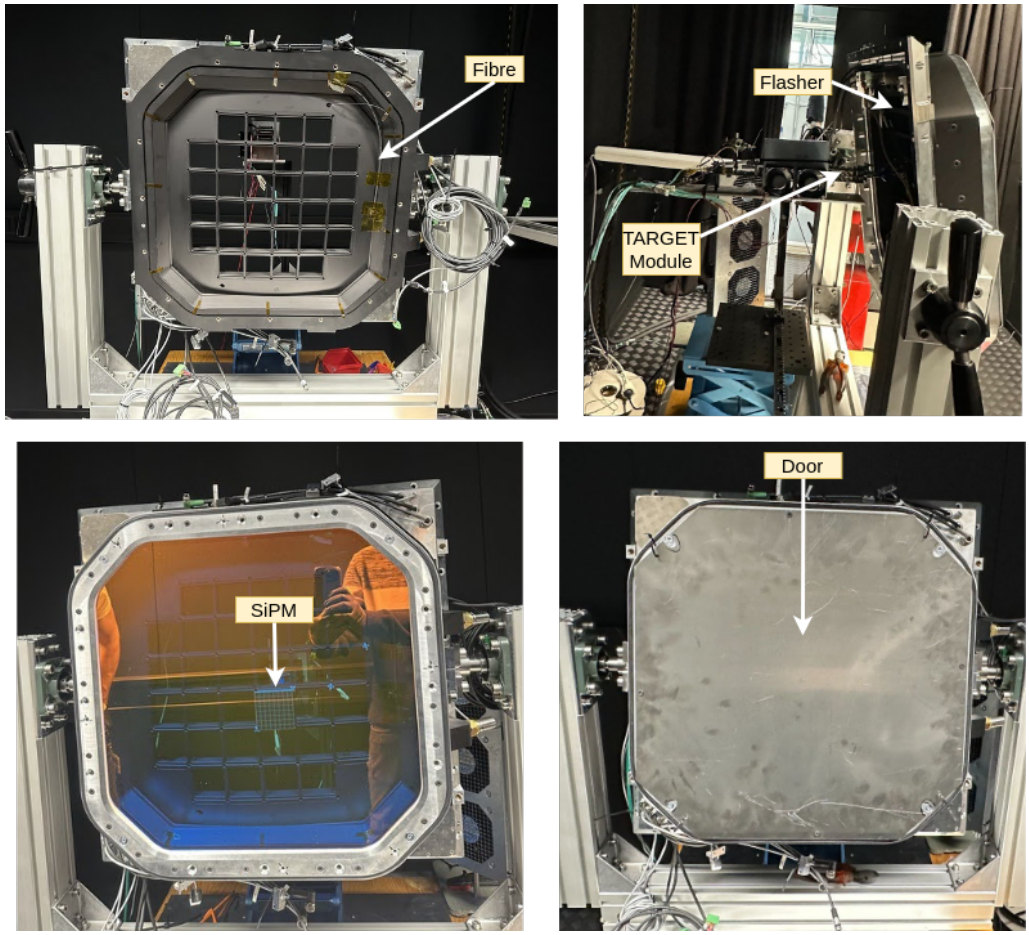

Figure 4.7: (*top left*) The diagram shows the layout of the fibre in the engineered groove with Kapton tapes holding the fibre in place. (*top right*) This shows the location of the Flasher and TARGET module behind the focal plane plate. The scintillating fibre was connected to the Flasher using an SMA connector. (*bottom left*) The SiPM was attached to the TARGET module and the coated window was attached to the focal plane plate. For every iteration of SiPM location, the window was unscrewed and the SiPM + TARGET module location was shifted. (*bottom right*) The aluminium plate which emulated a door was attached with a reflective material and screwed on top of the window. After attaching the pseudo door, data acquisition was started.

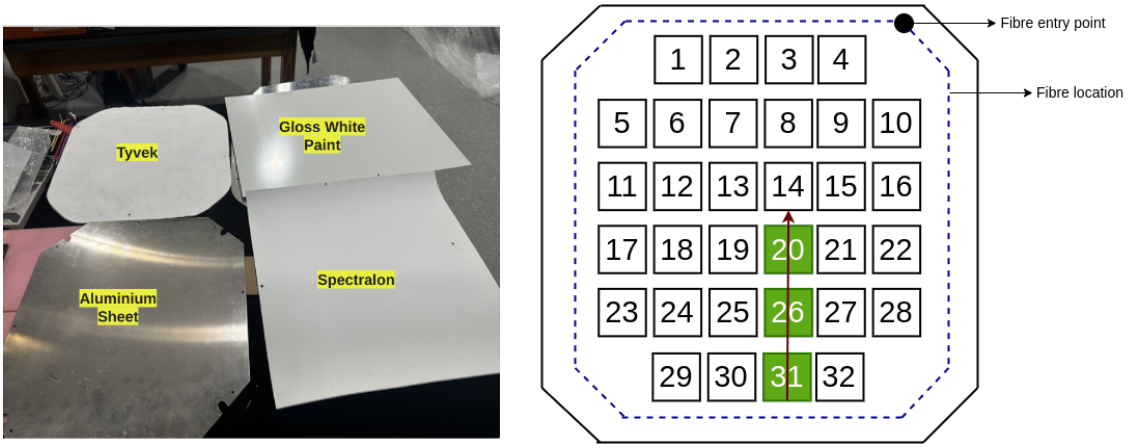

Figure 4.8: (left) An annotated pictures of materials tested for their reflectivity. Sheets from different materials were cut to mimic the backside of the door. (right) Different locations of the SiPM module while testing the reflectivity of the material. The under-lid scintillating fibre illuminated the SiPM modules after reflection from behind the door. The signal amplitude values for each pixels were recorded for further analysis. As each SiPM module has 64 pixels arranged in a 8×8 array, there are 24 pixel position along the arrow shown. Note that the amplitude values along each row are averaged to give 24 distinct values along the arrow direction.

After the choice of door coating material, the illumination pattern by the scintillating fibre across the full focal plane was produced. The illumination pattern by the scintillating fibre is depicted in Figure 4.10.

The overall variation across all of the camera pixel is 55% and the drop in amplitude from the brightest pixel to the faintest pixel is 98%; the variation across individual quarters is shown in Figure 4.11. The largest variation is in the top right quarter (quarter 1) as the fibre after attaching to the Flasher enters into the focal plane from top right (as shown in Figure 4.8). A significant variation in the third quarter suggests that even if the amplitude decays along the length of the fibre (see Figure 4.2), the variation is still dominated by the distance of the pixel from the fibre. The initial 30 cm of the scintillating fibre resides on the right edge of the SiPM array. Thus, the pixels in the upper diagonal are at least 12% brighter than lower diagonal pixels. This also justifies the non-uniformity in the illumination pattern.

The timing profile of the signal seen by each pixel is depicted in Figure 4.12. The mean value of pulse width is (14.37±1.23) ns with an overall variation of 6.5% across the camera.

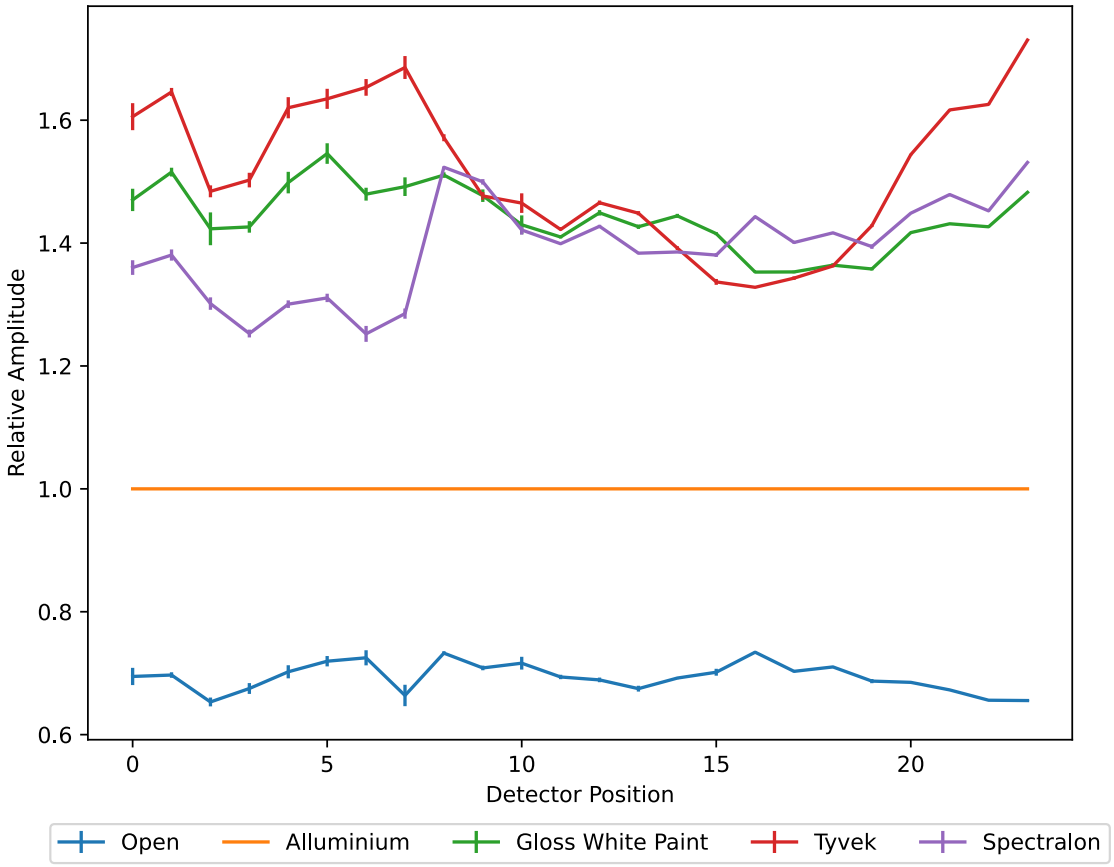

Figure 4.9: Relative amplitudes after reflection for different door materials, with aluminium taken as the reference since it is the construction material of the door. Tyvek and Spectralon exhibit comparable reflectivity. “Open” refers to the configuration without a door attached. The amplitude seen in the ”open” configuration is from the direct illumination and from reflection within the dark box. The detector position refers to the 24 position shown in Figure 4.8 (right, along the arrow).

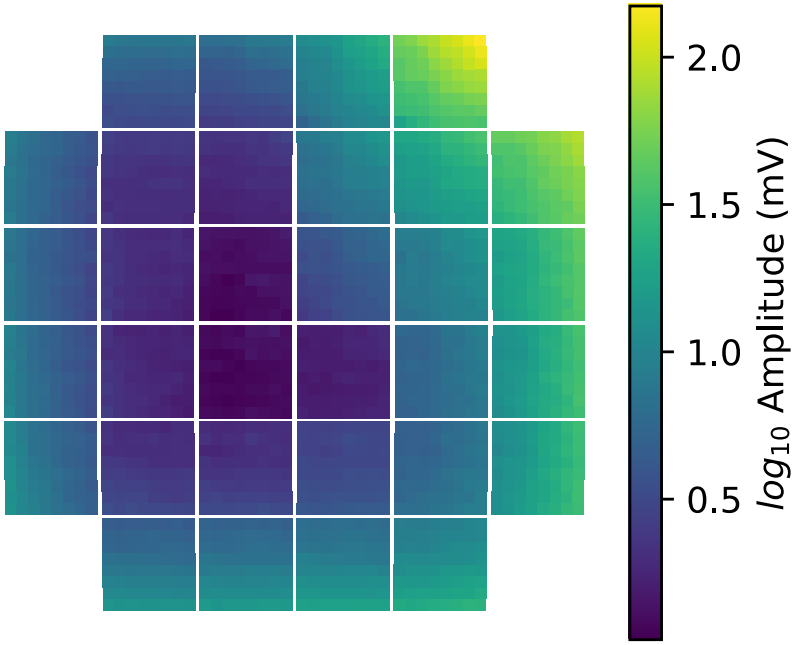

Figure 4.10: The illumination pattern with a 2 m length of scintillating fibre. The fibre enters into the focal plane from the top right corner, thus the amplitude is more in the top corner pixels. The range of variation across all the pixels is 78%.

4.1.3 Fibre for flat fielding: Profile Tests

Unlike the scintillating fibre that illuminates the focal plane of the camera non-uniformly via scintillation, an armoured optical fibre (due to its reinforced protective sheath) could carry the light pulses from the Flasher and illuminate the focal plane uniformly from the front of the camera (i.e - at the centre of the secondary mirror). As mentioned in the Table 2.2, the calibration unit should provide a uniform illumination intensity between 100 and 400 photons per pixel per pulse. Thus, there was a need of a fibre that could couple maximum light from the Flasher LED. Hence, different optical fibres from Thorlabs were tested for their light output. The fibres were terminated with SMA connector and either butt-coupled to the LED (LED and SMA touches face to face) or by introducing a ball-lens setup between the fibre and the LED to redirect more light into the fibre (shown in Figure 4.13). The first test was to check the amplitude of the light coming out from different fibres for the two coupling mechanisms. The test employed a straight forward setup: the Flasher was coupled to the fibre at one end, while the other end was positioned 4 cm away

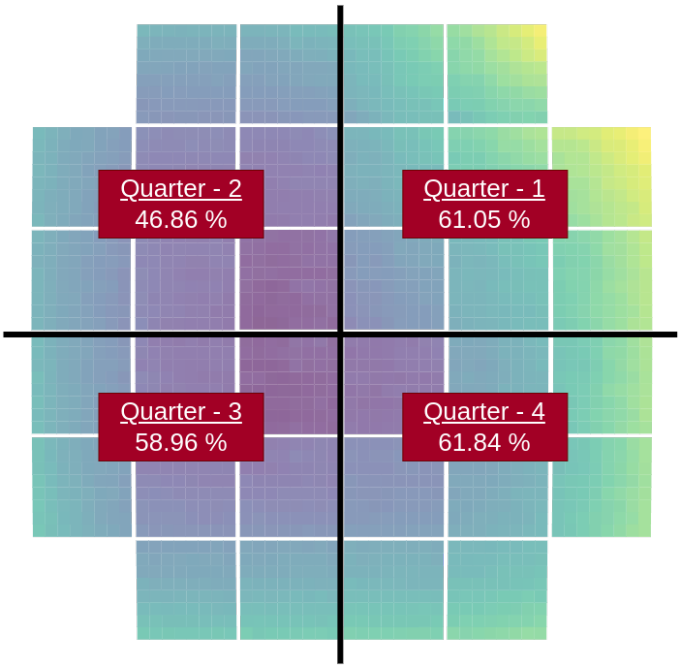

Figure 4.11: The SiPM pixel area is divided into 4 quarters and the amplitude variation across each quarter is calculated. The highest variation observed in the first quarter can be explained by the fibre's entry point, as it is coupled to the Flasher and enters the focal plane from the corner of this region. Meanwhile, the notable variations in the third and fourth quarters indicate that the dominant factor influencing amplitude is the pixel's distance from the fibre, rather than its position along the length of the scintillating fibre.

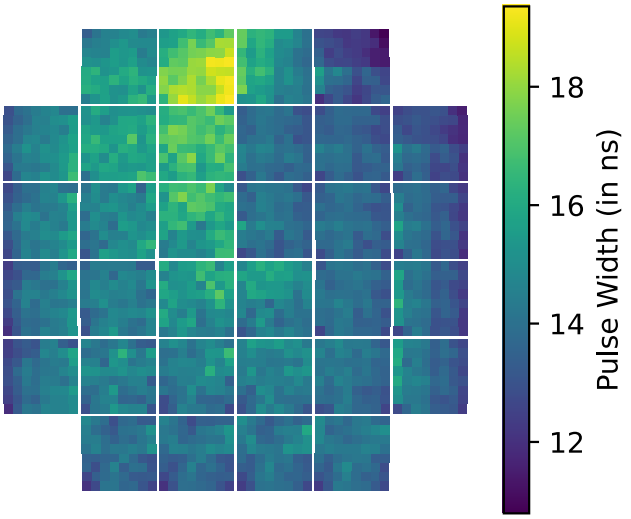

Figure 4.12: The pulse width distribution across all the pixels is shown here. The mean pulse width value is 14 ns with an overall variation of 6.5%.

from the SiPM with a diffuser in-between both. The comparative profiles obtained for the different fibres are summarized in Table 4.4.

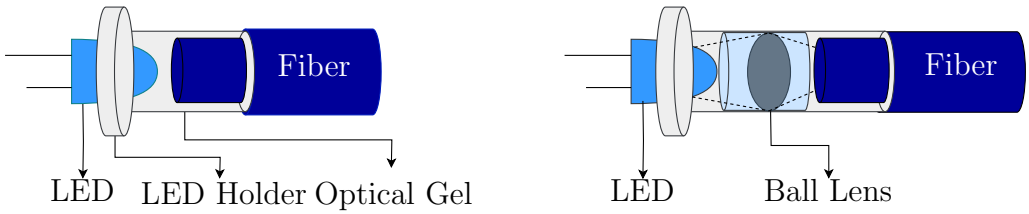

Figure 4.13: (Left) The butt-coupling mechanism is shown here. The SMA attaches head on with the LED. A small amount of optical gel in between the fibre and LED enhances the light output from the fibre. (Right) The ball-lens setup is shown here. The ball lens converges light from the LED into the fibre.

Sl No	Part No	Diameter	NA	Coupling	Amplitude	FWHM
1	Flasher	–	–	–	407 mV	1.7 ns
2	M93L01	1500	0.39	BC	139 mV	1.8 ns
3	M59L01	1000	0.5	BC	70 mV	1.8 ns
4	M92L01	200	0.22	BC	3.5 mV	1.9 ns
5	M93L01	1500	0.39	BL	124 mV	1.8 ns
6	M59L01	1000	0.5	BL	47 mV	1.9 ns
7	M92L01	200	0.22	BL	1.8 mV	2 ns

Table 4.4: Armoured fibre profile summary. BC is the acronym for butt-coupled and BL is the acronym for ball-lens setup. NA stands for Numerical Aperture of the fibre.

From the results in Table 4.4, the M93L01 fibre with a 1500 µm core diameter was selected for further testing, as it demonstrated superior light collection from the LED. Out of the two coupling methods, the ball-lens configuration did not yield a notable improvement in brightness. Thus, for further tests, the fibres were directly coupled to the LED with a small amount of index matching gel (G608N3 Index Matching Gel [109]) to fill the air gap between them.

4.1.4 Fibre for flat fielding: Illumination Pattern

After choosing M93L01 for its high optical output, the next test was to understand the beam pattern generated by the optical fibre at the focal plane of the camera. The test setup used to scan the beam pattern of the Flasher (shown Figure 3.24 in Chapter 3) was used in this case as well. The diffuser configuration mentioned in the beam scan of the Flasher (i.e. one 50° and another 5° with approximately 5 mm air gap between them) was also retained. The illumination pattern was scanned at a distance of 50 cm which is representative of the distance between the secondary mirror and the focal plane in the SST telescopes. Figure 4.14 depicts the observed illumination pattern. The variation across the camera pixel is 7.2%

The illumination pattern is uniform across the focal plane but about a 65% reduction in the brightness from the direct Flasher LED reduces its dynamic range of operation. Secondly, these fibres, due to their large core, have a larger minimum bend radius (158 mm for M93L01 [104]) which poses additional difficulty of routing them through the compact geometry of the camera.

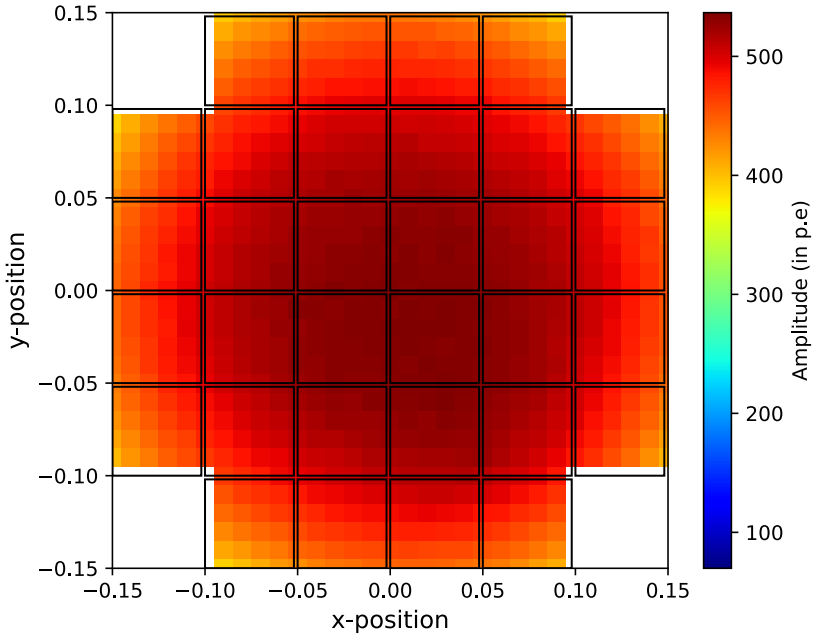

Figure 4.14: The illumination pattern by the M93L01 fibre coupled with the Flasher and attached with a 50° + 5° diffuser on top. The overall variation across the focal plane is 7.2%.

4.1.5 Lessons from Flasher-fibre work

The key findings from the Flasher–fibre proof-of-concept study are summarized below:

1. The light from the under-lid fibre is able to reach all the pixels on the focal plane thereby making it ideal to carry out functional checks on the SiPM pixels prior to observation runs. The details of these functional checks are discussed in Chapter 6.

2. A reduction of approximately five orders of magnitude was observed between the direct Flasher brightness and the scintillating fibre brightness. This significant attenuation is advantageous, as it enables the under-door scintillating fibre to provide light levels appropriate for SPE calibration. A detailed discussion of this application is presented in Chapter 5.

3. The armoured optical fibre demonstrated about 92% beam uniformity across the focal plane, making it well-suited for flat fielding. However, as shown in Table 4.4, fibre coupling resulted in a 65% reduction in brightness, which reduces its dynamic range compared to a direct LED.

4. Further, the armoured optical fibre has a specified long-term bend radius of 158 mm [104]. Such a constraint complicates routing the fibre to multiple locations within the compact geometry of the camera, thereby limiting its practical implementation. Another possible option is the use of a multi-core fibre bundle. For instance, a bundle consisting of seven 600 μm cores would provide coupling equivalent to a single $\sim$1600 μm core, with a minimum bend radius of 60 mm. However, such fibre bundles are costly, less readily available, and introduce additional complexity when coupling to the Flasher Board inside the camera.

Based on these findings, the under-door scintillating fibre was selected for functional checks and SPE calibration. For flat field correction, alternative solutions were required, leading to the exploration of a Flasher–coaxial cable system, which is discussed in the following section.

4.2 Flasher-Coaxial Cable System

As discussed in Section 4.1, coupling LED light efficiently into optical fibres proved to be a significant challenge. To address this, an alternative approach was considered in which the LEDs are connected directly to the central board via long coaxial cables. High-quality industrial coaxial cables provide strong electromagnetic shielding, while their flexibility allows for easier routing within the compact geometry of the camera. An external surge protector installed in line with the coaxial cable offers lightning protection. However, this approach also raises several concerns: potential pulse broadening as the signal travels through long cable lengths (3 m at maximum), possible interference of the fast coaxial signals with the operation of the TARGET modules, and overall signal degradation introduced by the additional cabling. The tests carried out to check the feasibility of coaxial cable usage are described in Section 4.2.1 and Section 4.2.2. Since the LED directly sits at the end of the coaxial cable, it was susceptible to signal reflection. But there was no noticeable change in the pulse width after using the coaxial cable (as reported in Table 4.5). But in future, additional design change like addition of an series resistor to damp the reflection will be incorporated.

For the prototype tests, an RG174/U PVC coaxial cable [110] was selected, primarily due to its low cost and ready availability, making it a practical choice for initial evaluations. A 3 m section of the cable was prepared for testing, with the LED connected directly to one end and the other end interfaced to the LED terminals on the Flasher board. The modified Flasher board incorporating this setup is shown in Figure 4.15[4].

4.2.1 Optical Signal Test

It was necessary to monitor the optical signal when the LED sits on the board and when the LED sits at the end of a long coaxial cable. Three different brightness settings were chosen (corresponding to a low, medium and high intensity level) and

[4]The coaxial cable shown in the figure is a short length (rather than 3 m long) cable prepared for other lab tests

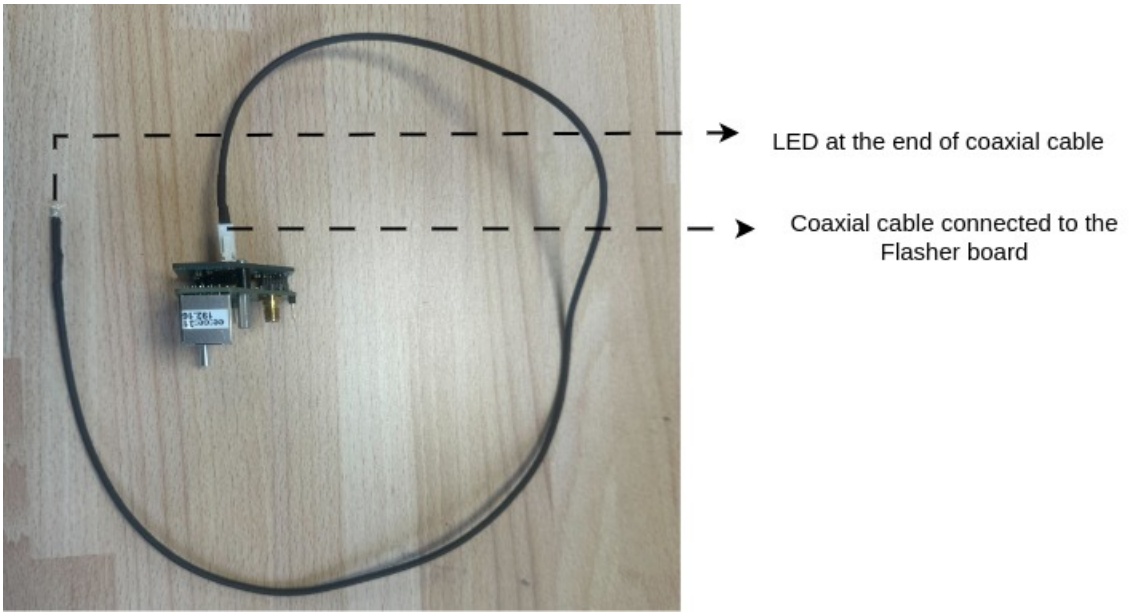

Figure 4.15: (*left*) One end of the coaxial cable is connected to the LED terminal on the Flasher board. (*right*) The UV LED is connected to the other end of the coaxial cable.

the Flasher was operated at 1 kHz. The signal was monitored using the Onsemi MICROFC-SMA-60035 SiPM [106] readout module with its output connected to the oscilloscope. The measurement values are shown in Table 4.5

	Setting 1			Setting 2			Setting 3		
	Direct	Coax	% Change	Direct	Coax	% Change	Direct	Coax	% Change
Pulse Width (ns)	4.57	4.69	2.60	4.68	5.00	6.80	5.10	4.80	6.20
Rise Time (ns)	3.40	3.36	1.11	3.45	3.60	4.30	2.95	2.80	5.35
Fall Time (ns)	4.48	4.74	5.80	4.39	4.60	4.78	3.94	4.10	4.00
Trigger Delay (ns)	7.75	9.42	21.55	7.67	9.27	20.86	7.21	8.94	24.00

Table 4.5: The table shows the timing characteristics of the optical signal with and without the coaxial cable attached for three different brightness settings of the Flasher. Direct refers to the values when the LED is on the Flasher board and coax refers to the values when the LED is the end of the coaxial cable. The largest difference is in the Trigger delay. This is expected because the signal takes longer to reach the LED at the end of the coaxial cable.

4.2.2 Coaxial Cable Noise Test

During the Flasher operation, fast signals would continuously travel down the coaxial cable. Since the coaxial cable would be routed inside the camera, the TARGET module might pick up some noise from the cable. Hence, a dedicated noise test was performed with the help of the coaxial cable and the TARGET module. Figure 4.16 depicts the test setup arrangement.

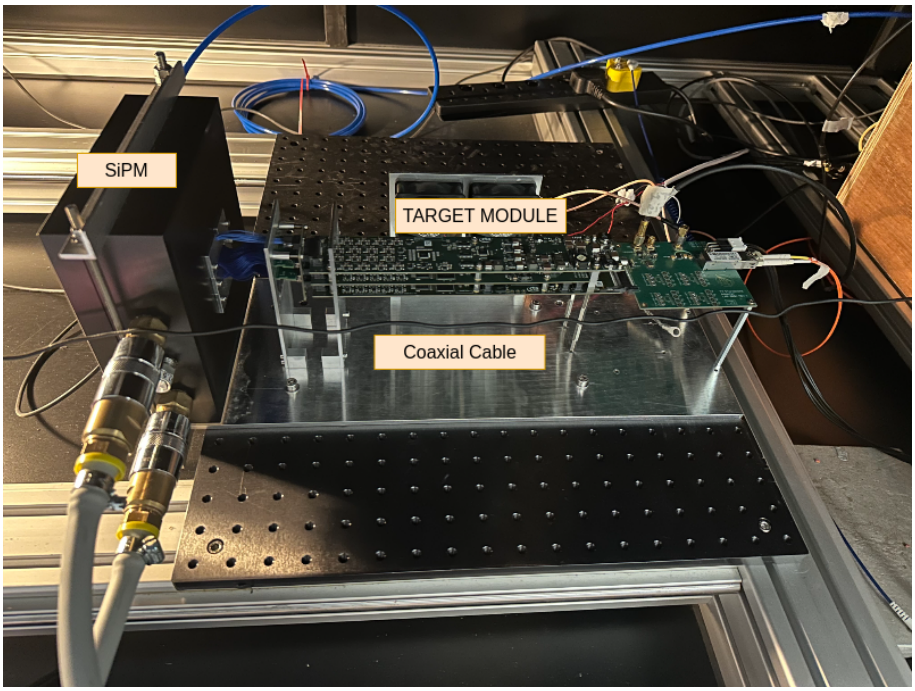

Figure 4.16: This depicts the arrangement of coaxial cable near the TARGET module for the noise induction test. The SiPM module is inside a safety box with a chiller pipe connected to it to keep it at a constant temperature. The coaxial cable is routed next to the TARGET module.

The TARGET module has a switched capacitor array that stores up to 4096 charge values and upon receiving a trigger signal, it looks back the preceding 128 samples and digitises them. The noise can be present in any of this 128 sample window. Thus, all the 4096 samples are digitized and a long baseline waveform is generated. From the average waveform of all the 64 pixels, the mean amplitude value is found for two cases - when the Flasher is ON and when the Flasher is OFF. This is plotted in the Figure 4.17. The average change in baseline over all pixels is 0.09 ADC. This confirms there is no significant induction of noise by the coaxial cable.

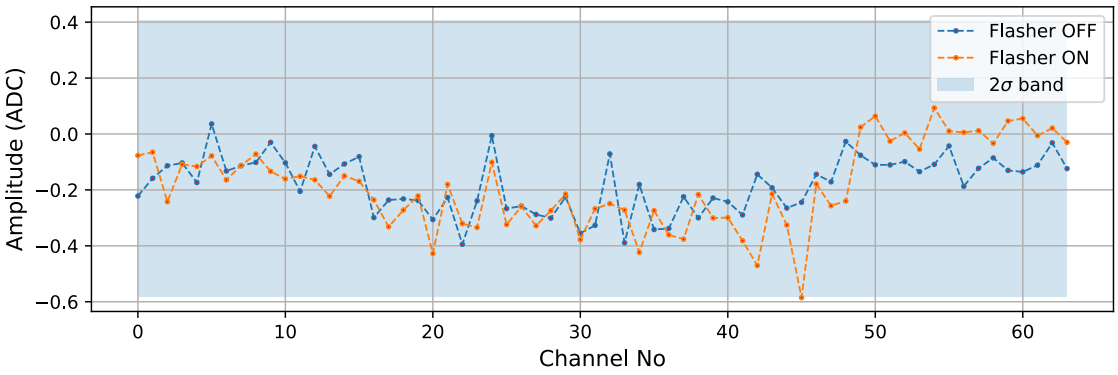

Figure 4.17: The baseline amplitude values for each pixel when the Flasher is ON (*orange*) and the Flasher is OFF (*blue*).

4.2.3 Lessons from Flasher-coaxial cable work

The key findings from the Flasher–fibre proof-of-concept study are summarized below:

1. The maximum pulse width broadening with the coaxial cable is ∼7%. It is inferred that the coaxial cable does not impact the pulse width of the Flasher.

2. The delay between the trigger signal and the LED signal increases on average by 20%. This can be incorporated into the camera software to set the appropriate trigger time.

3. The noise test of the coaxial cable with the TARGET module indicated that there is no interference from the electrical signal in the coaxial cable with the TARGET module.

4.3 Conclusion

This chapter examined two proof-of-concept approaches for delivering the Flasher signal with the SSTCAM: fibre-based systems and coaxial-cable systems. These studies were motivated by the need for a reliable and flexible calibration source capable of supporting flat fielding, SPE calibration, and functional checks.

The fibre study revealed both strengths and limitations. Scintillating fibres provided illumination visible to all pixels and, due to their strong attenuation, are well

suited for SPE calibration and functional checks on the camera pixels prior to observation runs. Armoured optical fibres, which can illuminate the camera from the front, offered high beam uniformity but suffered significant amplitude losses and were impractical to route within the compact camera geometry.

The coaxial-cable study showed more promising results. A 3 m RG174/U PVC coaxial cable introduced only minor pulse broadening ($\sim$7%) and a manageable trigger delay ($\sim$20%), which can be corrected in software. Tests also confirmed there was no interference with TARGET module operation. In addition to preserving signal integrity, coaxial cables provide strong shielding, lightning protection, and routing flexibility.

Overall, these results established coaxial cables as the most practical basis for the next-generation Flasher system. Their adoption ensures reliable, stable, and easily integrated light delivery. The design and development of this new system are detailed in the next chapter.

CHAPTER 5

Flasher Version 4 Calibration System

Chapter 4 described two proof-of-concept studies that were carried out to evaluate how the Flasher system could be extended into a centralised, multi-channel board that supports easy integration while meeting the calibration requirements of the SSTCAM. From these studies, LEDs connected via shielded coaxial cables were identified as the most practical approach for routing light to different locations within the camera.

This chapter presents the design of the next-generation Flasher calibration system (Version 4). Section 5.1 describes the technical design of the system, providing justification for the chosen components, along with the concept of operation and PCB layout in section 5.2. Section 5.3 outlines the planned firmware implementation. The envisioned test procedures for benchmarking system performance are described in Section 5.4. Finally, the integration of the new version into SSTCAM is outlined in Section 5.5.

My contributions to this work included a detailed study to determine the required number of I/O pins, followed by the selection of a new microcontroller in consultation with Dr. Sheridan Lloyd and CfAI engineer, Dr. Deli Geng. I led the pin-optimisation process through the implementation of serial-in–parallel-out

(SIPO) expanders and adopted a black-box design approach for the PCB, producing the initial schematic and layout. I coordinated closely with Dr. Deli Geng, throughout multiple design iterations, contributed to component selection, and supported Dr. Sheridan during the PCB ordering process. In parallel, I developed the core firmware logic for the system, attached CAD models of the revised PCB to the camera assembly to determine optimal placement and clearances, and drafted the initial characterisation tests to be performed on the new system.

5.1 Design Description

Chapter 3 demonstrated that the designed calibration unit successfully meets the requirements set by CTAO (2.2). Table 4.1 outlined the need for multi-channel calibration unit and the proof-of-concept studies in Chapter 4 provided a pathway to extend the functionality of Flasher to multiple channels. Building on these results, the next step was to evolve the prototype into a multi-channel system by consolidating all components onto a single centralised Printed Circuit Board (PCB). This board is equipped with multiple SMA connectors to interface with coaxial cables terminated with LEDs, enabling scalable and efficient light delivery.

The only viable location for such a PCB within the camera was identified at the top of the TARGET module rack, adjacent to the Slow Control Assembly board. This choice was driven entirely by space availability inside the camera enclosure. Given this placement, the board's maximum allowable dimensions were constrained to 200 mm$\times$130 mm$\times$40 mm, including the necessary stand off for secure mounting. The envisioned location of the centralised board within the CAD model of the camera is shown in Figure 5.1.

The layout of the board was designed using the maximum allowable dimensions as a guideline and the corresponding block diagram of its operational units is shown in Figure 5.2. The core logic for nanosecond pulse generation, based on the LMG1025 and DS1023, remains unchanged from Version 3 of the Flasher system (see Figure 3.3). To meet the new multi-channel requirement, additional components were incorporated to enable channel selection and triggering. A detailed description of each

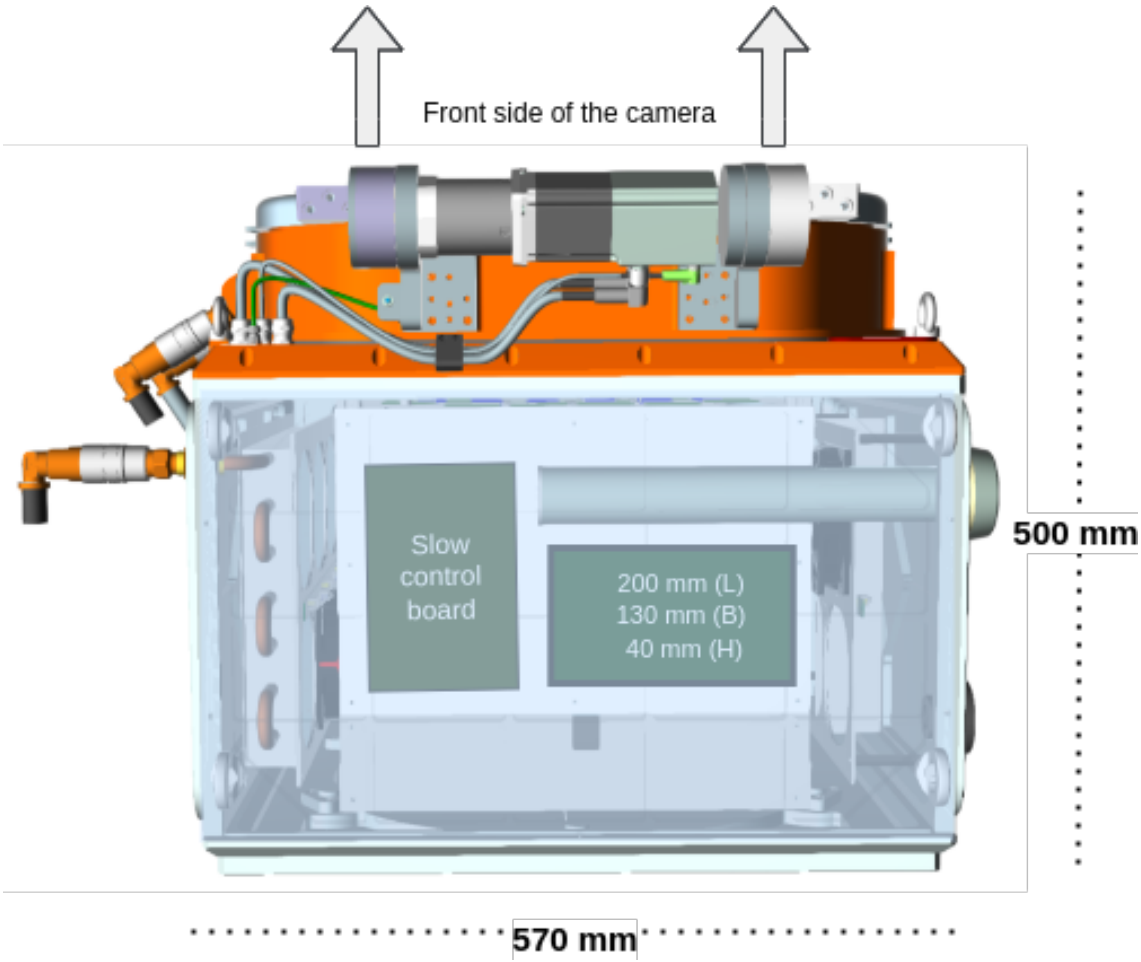

Figure 5.1: A top down view of the CAD model of camera showing the potential position next to the slow control assembly of the camera for placing the Flasher control assembly. The choice is purely driven by availability of space and easy accessibility to the focal plane. The maximum space available including the stand offs is 200 mm×130 mm×40 mm.

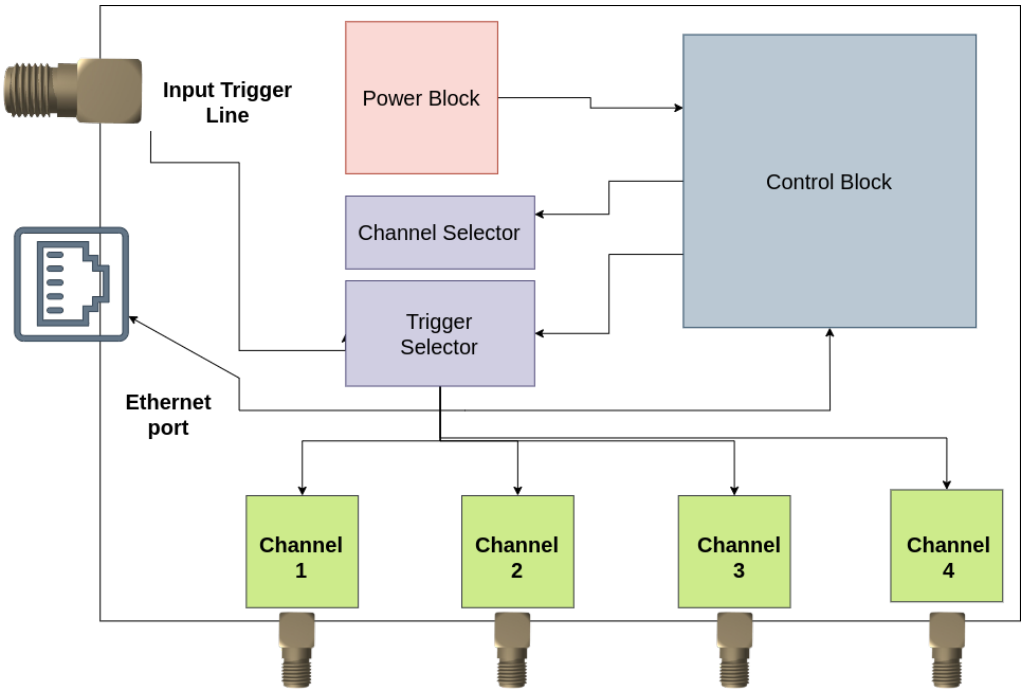

Figure 5.2: The block diagram shows important operational blocks of version 4 of the Flasher. A single microcontroller independently sets up individual output channels. Coaxial cables terminated with LEDs can be attached to the SMA connectors on the output. A smart trigger selection, as described in Section 5.1.3, chooses which channel to operate.

operational block is provided in the subsequent section.

5.1.1 Power Block

The USB-A connector from the previous design (Section 3.1.4) has been replaced with a USB-C connector, reflecting advancements in USB technology as well as the wide availability and cost-effectiveness of USB-C components. A PRTR5V0U2X device [111] provides electrostatic discharge (ESD) protection, while an SPX3819-3.3 voltage regulator [89] (used in version 3 Flasher) steps down the input 5 V supply to the required 3.3 V.

5.1.2 Control Block

As outlined in Section 3.1, Version 3 of the Flasher board employed the ATSAMD21G18A microcontroller, which provided 48 programmable I/O pins—sufficient for operating a single channel. However, the SSTCAM requires at least four channels for its calibration activities, creating the need for additional I/O capacity. The ATSAMD21 family supports a maximum of 52 pins [90], which is still inadequate for this requirement. Consequently, a new microcontroller with a larger number of I/O pins and improved architecture was selected for multi-channel operation.

The new design incorporates the WCH CH32V307 microcontroller, a 32-bit RISC-V device operating at 144 MHz, with 128 KB of RAM and 480 KB of program memory [112]. This marks a substantial upgrade from the ATSAMD21G18A used previously, which provided only a 48 MHz core and 32 KB of RAM. The CH32V307 supports up to 64 programmable I/O pins, expandable to 80 with other devices in the same family, and includes two I^2C and three Serial Peripheral Interface (SPI) communication interfaces. A key advantage of this microcontroller is its integrated Gigabit Ethernet controller, eliminating the need for the external WIZnet W5500 used in the earlier design. This reduces the additional firmware needed for data packet handling and it also reduces latency as data packets do not need to hop between external driver and the microcontroller. Finally, this microcontroller operates at a rated voltage of 3.3 V and within a temperature range of $-40°C$ to $85°C$. This

is ideal as the air temperature at the site location swings between $-15°$ to $35°$.

5.1.3 Channel Selector and Trigger Selector

As detailed in Section 3.1, the nanosecond pulse generation using the DS1023 and LMG1025 requires careful I/O management. Configuring the pulse width alone needs at least three I/O pins: DATA, CLK, and LE (described in Section 3.1.1). In addition, four photo relays, which adjust the effective resistance and thereby control the LED intensity, require four more I/O pins (3.1.2). This brings the total to seven pins per channel, or 28 pins for a four-channel setup. To reduce this demand, the DATA and CLK lines are shared across all four channels, with separate LE lines used to select which DS1023 chip is programmed, providing channel selection. This optimization reduced the requirement from 28 to 22 pins.

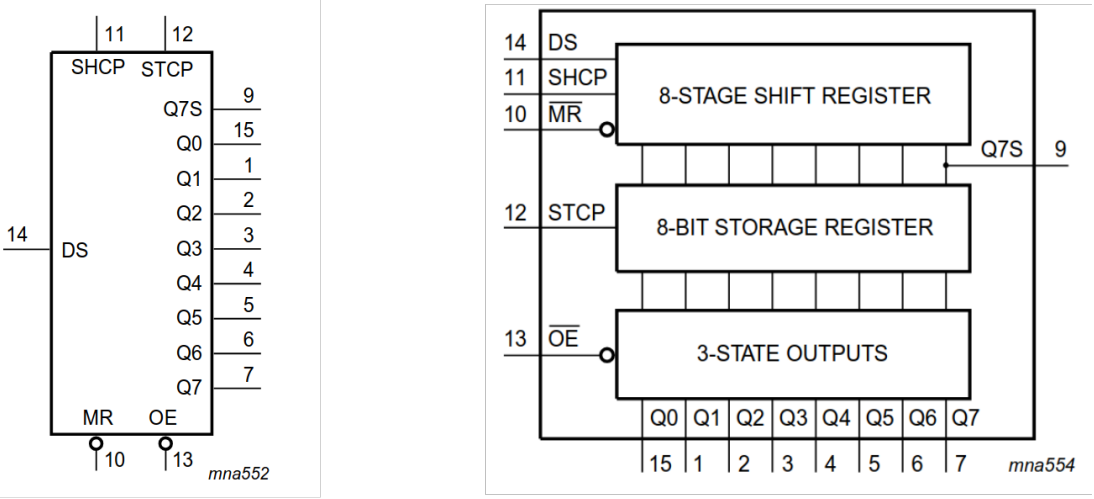

Figure 5.3: (top) The pinout diagram for the Serial In Parallel Out (SIPO) register. DS is the data input pin. MR, OE, SHCP and STCP are control pins. Q0 - Q7 are parallel output pins and Q7S is the serial output pin. (bottom) The three stage bits transfer in the SIPO is shown. The data at the DS pin is shifted into the shift register on the rising edge of the SHCP input. The data in the shift register are shifted into output register and subsequently into output on the rising edge of the STCP input. $\overline{\text{MR}}$ and $\overline{\text{OE}}$ are control pins which reset the register and enables/disables output respectively. The diagram has been taken from 74AHCT595D datasheet [113].

Further reduction in pin requirement was achieved by replacing the 16 relay-control pins with Serial In Parallel Out. The Nexperia 74AHCT595D [113], offering eight parallel outputs per device, was selected for this purpose, with one register assigned

to each channel. The selected SIPO has three stage output: data are loaded serially into the shift register and transferred into the storage stage and further moved into output stage (shown in Figure 5.3). With this design, the total I/O requirement for operating four Flasher channels was brought down to just six pins. The SIPO also facilitates selecting which LED should be triggered for operation. The triggering of each LED channel is also managed through a photorelay. After passing through a series of resistor networks (similar to the illumination control block of version 3 Flasher described in Section 3.1.2), the output line is connected to another photorelay, the control bit of which is driven by the final bit of the SIPO. This arrangement allows selective enabling of channels after setup. The detailed concept of operation is discussed in Section 5.2.

Using this technical design, a prototype version of the board has been designed. Multiple test points are provided on the board to monitor and debug the signals going through different components. The annotated CAD model of this PCB is shown in Figure 5.4.

5.2 Concept of Operation

According to the DS1023 datasheet [86], when operated in serial mode, data is shifted in from the most significant bit (MSB) to the least significant bit (LSB) through pin number 5 (pinout shown in Figure 3.2). Simultaneously, the previously stored pulse-width values are shifted out through pin 3. In the Version 3 Flasher board, this output pin was tied low and left unused. In the Version 4 design, however, this feature is utilized as a key part of the operation.

In this scheme, pin 3 of the DS1023 is connected directly to the data input of the SIPO register, unlike pulling it low in version 3 of the Flasher (see Section 3.1). LE and CLK lines are shared between the DS1023 and the SIPO to synchronize their operation. As a result, each time a bit is clocked into the DS1023, the corresponding bit previously stored is shifted out via pin 3 and loaded into the SIPO.

The operation proceeds in three stages. In the first stage, with LE held high, the first eight clock pulses are used to load the state information for the relay-control

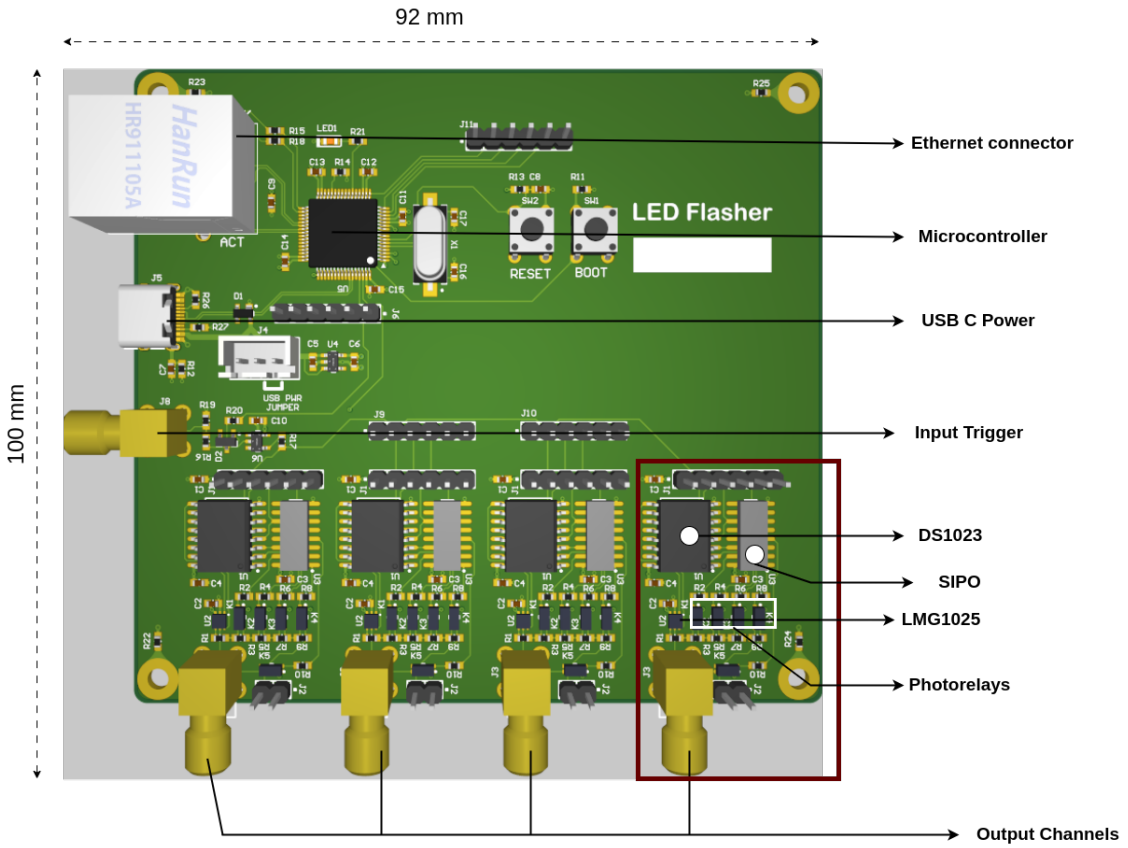

Figure 5.4: CAD model of the V4 Flasher with the important components of the PCB marked. The red rectangle shows the components of a single output channel on the board. Three other channels are repeated next to it. The board is powered via USB-C connector and had RJ45 connector for Ethernet communication. The output is provided via SMA connector and multiple test points are present to check for internal signals.

pins into the DS1023. These bits, shifted out simultaneously, are captured by the SIPO. After this, the LE line is toggled low and then high again to mark the end of this step. In the second stage, the next set of eight clock pulses is applied to load the desired pulse-width value into the DS1023. At the same time, the data flushed out carry the relay-control information into the SIPO registers. Once these 8 bits are received, the LE is pulled low to latch the new settings. Finally, in the third stage a low–high–low transition on the LE line transfers the data within the SIPO from its input registers into its storage registers and subsequently to the output pins, thus updating the photo-relay control signals. The block diagram of this operation is depicted in Figure 5.5 and an example of different stages of bit transfer during setup is shown in Figure 5.6.

Thus, in version 4 of Flasher, the brightness and pulse width are configured through a serial mode logic, unlike version 3 of the Flasher where the microcontroller independently controlled the DS1023 and the photorelays. The setup time in version 4 is on the order of milliseconds, which is negligible in practice. More importantly, the significant reduction in pin requirements (from 28 pins down to just 6 for a 4-channel Flasher) far outweighs the loss of flexibility in independently configuring the components.

5.3 Firmware Description

Like the ATSAMD21G18A, the CH32V307R microcontroller is programmed primarily in C++. However, unlike the previous design which used the Arduino Studio IDE, the recommended development environment for the CH32V307R is MounRiver Studio [114]. An important improvement in this version is the embedded Ethernet controller on the CH32V307R, which eliminates the need for the low-level SPI communication routines previously handled by a dedicated C++ program, iostacks.cpp (see Figure 3.10). This integration significantly reduces firmware complexity for managing data transfer of requests, results, and error codes between the microcontroller and the network.

A critical aspect of the firmware design is the handling of the DS1023 and SIPO

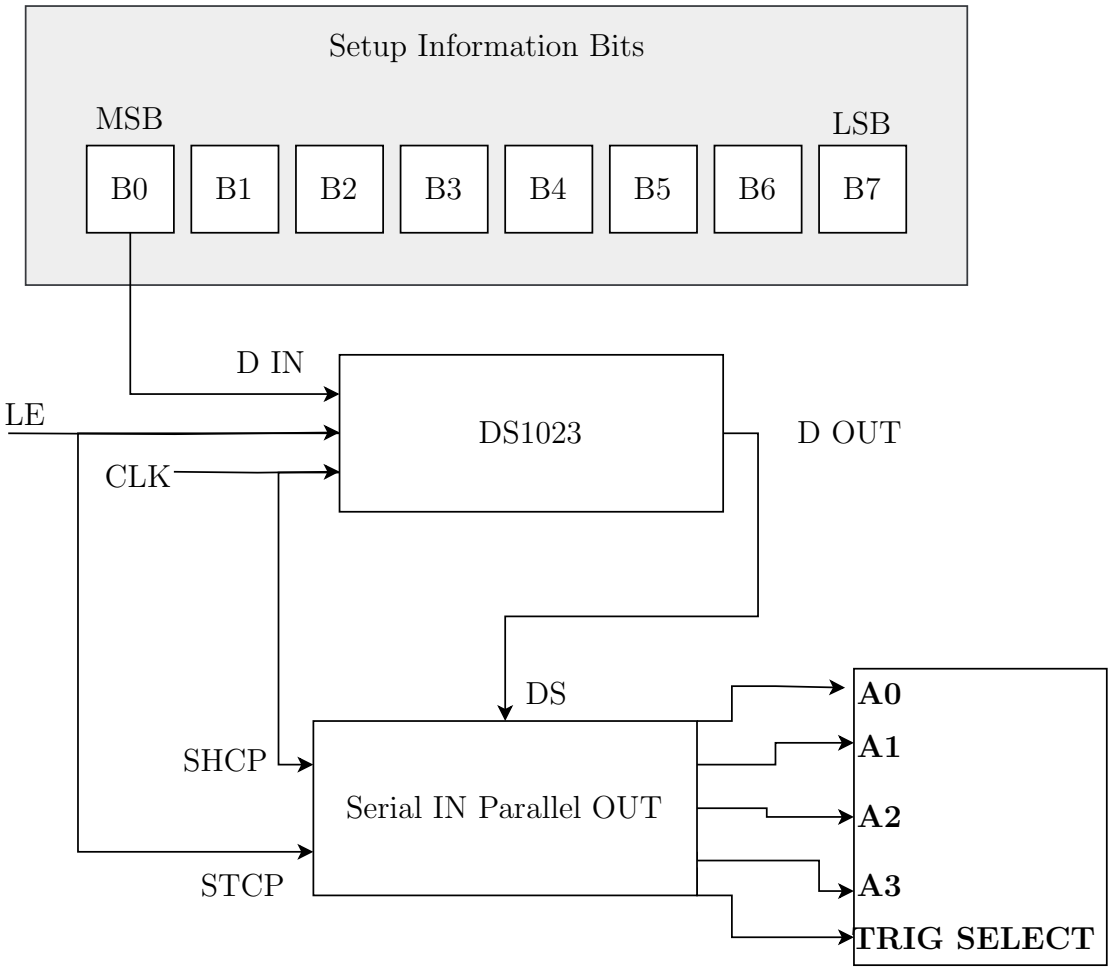

Figure 5.5: The setup sequence begins with loading 8-bit data (B0–B7). The latch enable (LE) signal is shared between the DS1023 and the STCP control pin of the SIPO, while the clock (CLK) signal is shared between the DS1023 and the SHCP control pin of the SIPO. During each setup step, the control states for the photorelays (managing brightness and trigger) are shifted through the DS1023's serial-in/serial-out path into the SIPO. Subsequently, the pulse-width information is programmed into the DS1023. In this way, the Flasher system is configured with the required intensity, trigger state, and pulse-width settings.

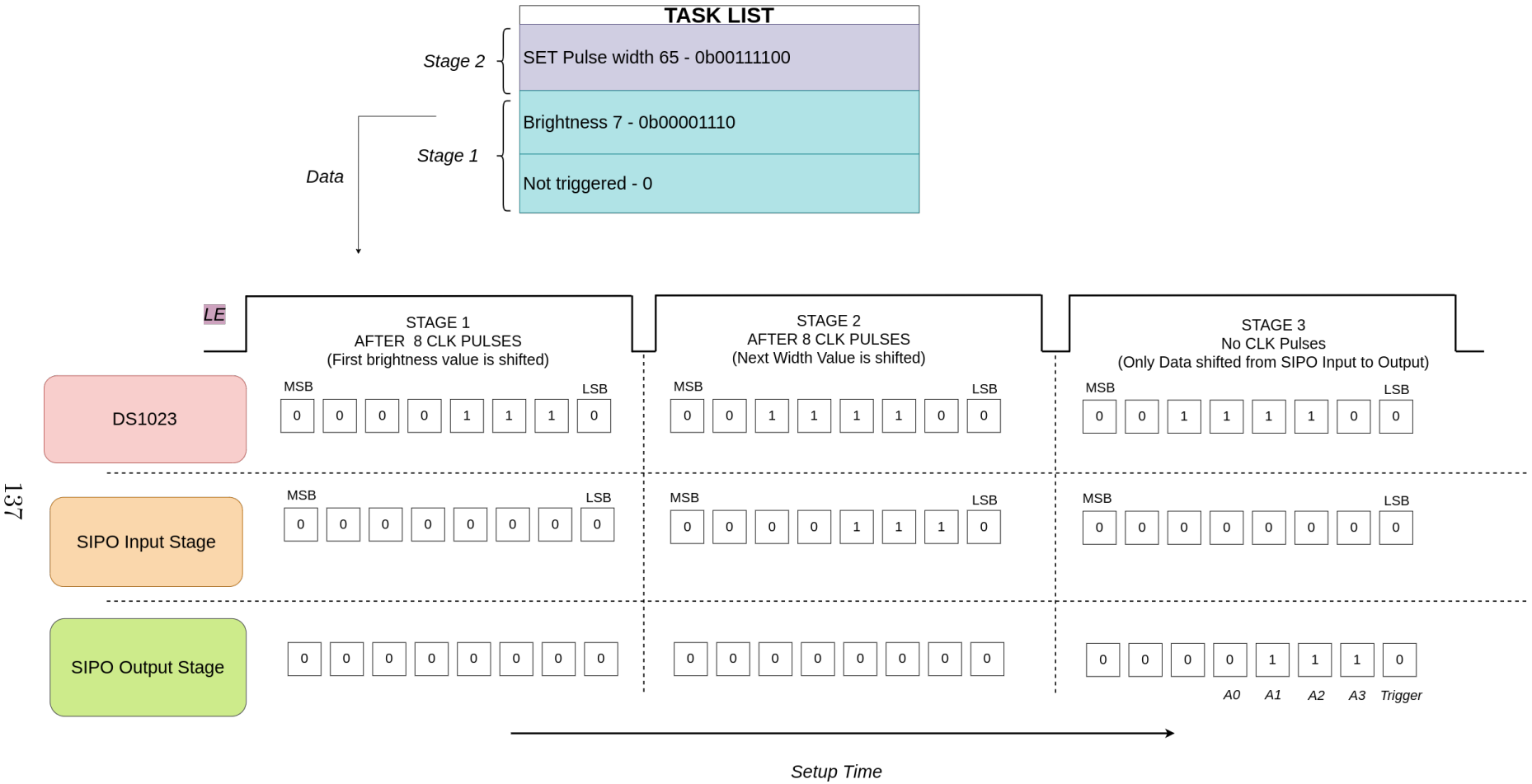

Figure 5.6: In this example, a pulse width of 65, an intensity setting of 7, and a "NOT triggered" state are selected. During the first stage, the control logic for the photorelays (managing intensity and trigger) is loaded into the DS1023 with the LE signal held high. The LE is then toggled low and high to complete the stage. In the second stage, the next eight clock pulses load the pulse-width value into the DS1023, while the previously stored control data is flushed out and passed into the SIPO. A final LE toggle transfers the SIPO input data into its parallel output pins, completing the setup for the channel.

registers. As the setup process is inherently serial, the firmware must always store the previous state of these registers in memory. This ensures that if an intermediate setting needs to be modified, for example, adjusting the LED brightness after the pulse-width values have already been programmed, the firmware can shift the new brightness data while simultaneously restoring the existing pulse-width configuration. At the end of the programming sequence, the firmware must also toggle the LE signal to transfer data from the input registers to the storage registers of the SIPO, thereby updating the outputs correctly.

The firmware for the new Flasher system is currently (September 2025) under active development. Once the core functionality is stable, Python wrappers and application-level software will be implemented on top of it, enabling both laboratory testing and seamless integration into the SSTCAM camera software.

5.4 Benchmarking Tests Description

The version 3 of the Flasher board underwent detailed characterisation tests and their tests results were reported in Chapter 3. Similar tests will be carried out for the version 4 of the Flasher after the firmware development is complete. This would ensure the reliability of results from this prototype board. The test name, short description and the justification for carrying out such a test is summarised in Table 5.1.

Sl No	Test Name	Description
1	Setup Test	The initial setup test will verify that each Flasher channel can be independently programmed as intended. Performing this check is essential to ensure the firmware correctly configures all channels and to identify any setup errors at an early stage.

2	Test point checks	The Version 4 board includes numerous test points for debugging. These will be systematically measured to confirm that the internal signals behave reliably, providing a foundation for diagnosing issues during integration.
3	Warm up test	Since Version 3 of the Flasher required approximately 20 minutes to reach stable operation, it is important to assess whether all channels of the new system stabilize within a similar timeframe after power-up. This ensures predictable performance during observations.
4	LED Signal Test	After configuration, the electrical output of each channel will be examined in detail using an oscilloscope. This will confirm that amplitude levels and timing jitter remain consistent across channels, ensuring uniform switching performance.
5	Optical signal test	Similar to the Version 3 characterization, the optical pulses delivered through coaxial-terminated LEDs in version 4 will be measured with a SiPM. These measurements will characterize the pulse intensity, timing, and pulse-to-pulse fluctuations, as well as inter-channel variations. Such testing is necessary to validate the stability and uniformity of the optical output.
6	Signal leakage test	To ensure clean operation, the output channels will be checked for leakage current when not triggered. Verifying negligible leakage is important for maintaining signal integrity across all channels.

7	Temperature dependence	Test procedure similar to the version 3 temperature dependence test (outlined in Section 3.7.4)
8	Frequency dependence	Test procedure similar to the version 3 frequency dependence test (outlined in Section 3.7.5)
9	Channel dependency	To ensure clean operation, the output channels will be checked for leakage current when not triggered. Verifying negligible leakage is important for maintaining signal integrity across all channels.
10	Long term test	Tests will be performed to benchmark the long-term stability of each channel and to estimate the mean time between failures. This will provide insight into the durability and operational reliability of the system.
11	Stability Test	Dedicated tests will be carried out to monitor the 30 minutes and 300 minutes illumination level stability for each channel as outlined by the CTAO requirements in Table 2.2

Table 5.1: Envisioned test procedures for the version 4 Flasher

5.5 Integration into SSTCAM

In the previous prototype (CHEC-M and CHEC-S), the calibration units were placed at the corner of the camera and illuminated the focal plane via reflection from the secondary mirror [74]. This added additional uncertainty due to the introduction of the mirror substructure in the optical path. Thus, in the new ASTRI telescopes, a 30 mm hole will be made in the secondary mirror structure to accommodate a Flasher LED that illuminates the focal plane directly. Apart from this, there are two more

locations within the camera to which LED-terminated coaxial cables must be routed to deliver the required calibration light. The centralised Flasher board is mounted on top of the TARGET module rack, with coaxial cables terminated with an LED extending from it to the designated sites to perform specific calibration tasks. The locations of these LED outputs are illustrated in Figure 5.7. The following section examines each location in greater detail.

5.5.1 M2 Flasher Integration

A Flasher positioned behind the secondary mirror (M2) will serve as the primary channel for flat fielding all camera pixels. To achieve uniform illumination, a 50° diffuser is mounted in front of the LED. As with the corner Flasher, the setup uses a forward-facing LED on a compact PCB equipped with an SMA connector. For environmental protection, the PCB is enclosed in a water-tight housing, as illustrated in Figure 5.8. A hole matching the diffuser's dimensions is made at the front of the box for light output. At the rear, a cable gland is incorporated to route the coaxial cable into the enclosure while preserving its water-tight integrity. Depending on the available mechanism to attach the box to the secondary mirror structure, the box can either be rectangular or cylindrical. One possible attachment of the Flasher assembly to telescope structure is shown in Figure 5.9

Unlike the other Flasher channels, this unit is located outside the main camera enclosure (Figure 5.7), making it more vulnerable to electrical surges for example from lightning strikes. In order to safeguard the central board and the backplane, a surge protector will be installed on this channel's LED signal line. A potential off-the-shelf component that has been discussed to be used is QK-AS15 Coaxial lightning surge protector [115]. This arrangement is shown in Figure 5.7.

5.5.2 Corner Flasher Integration

In both CHEC-M and CHEC-S, four calibration units were positioned at the corners of the camera, illuminating the focal plane through reflection from the secondary mirror [74]. During dedicated calibration runs of CHEC-S, the camera recorded an

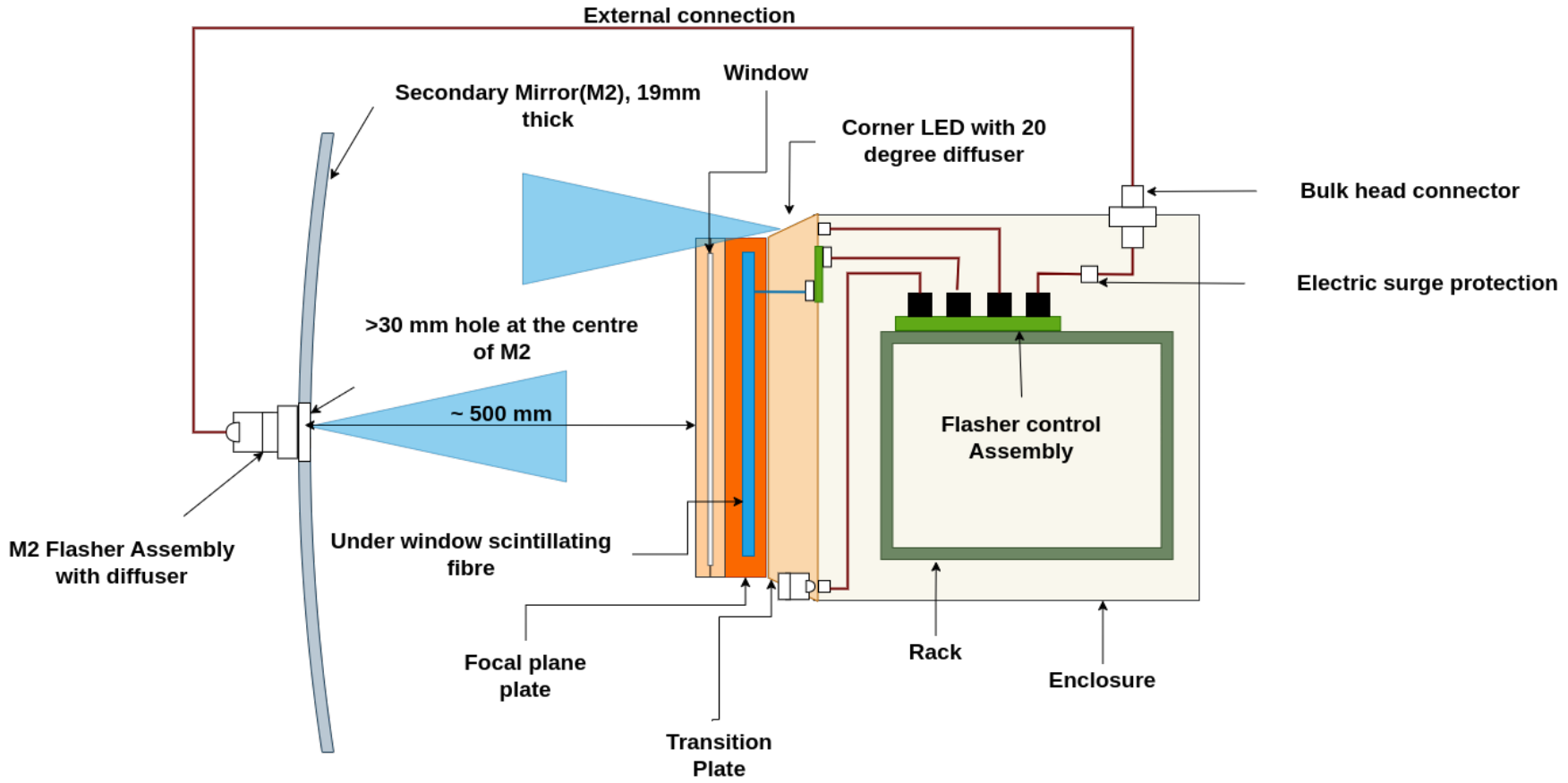

Figure 5.7: The location of different Flasher channels is shown. One Flasher channel is connected to the scintillating fibre placed underneath the window for functional checks and SPE measurements. Two Flasher channels are placed at the corners of the camera that illuminate the focal plane via reflection from the mirror in order to monitor mirror condition. The final flasher channel is placed behind the secondary mirror (with a diffuser) and illuminates the camera from the front for flat fielding.

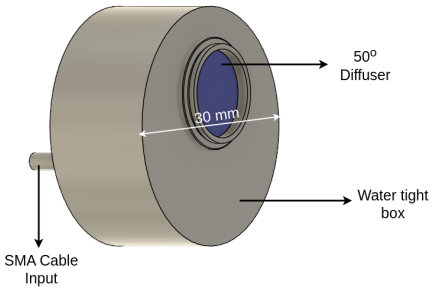

Figure 5.8: A simple CAD model of a possible water-tight enclosure housing the M2 Flasher channel. The PCB design inside this enclosure is similar to that shown in Figure 5.11. A hole matching the diffuser's dimensions is made at the front of the box for light output. At the rear, a cable gland is incorporated to route the coaxial cable into the enclosure while preserving its water-tight integrity.

arc-shaped illumination pattern, as shown in Figure 5.10. Since this feature persisted even when each calibration units were operated individually, it was concluded that the observed pattern originated from the condition of the mirror rather than from the calibration units themselves.

So, even though the flat fielding of SSTCAM will be carried out by the M2 Flasher (discussed in Section 5.5.1), the corner Flasher is still included to monitor mirror condition by analysing variations in the illumination pattern formed after reflection from the secondary mirror. Two Flashers positioned at opposite corners are sufficient to illuminate all pixels through this reflective path, as illustrated in Figure 5.11 (right). This calibration strategy has already been explored with the version 1 Flasher and CHEC-M [74]. Unlike the fibre-coupled Flasher LED, the corner Flasher uses a forward-facing LED mounted on a compact PCB equipped with an SMA connector for coaxial cable attachment. To ensure broad coverage, a 20° engineered diffuser is placed in front of the LED, spreading the emerging light to reach more pixels after reflection. The PCB, together with the diffuser assembly, is shown in Figure 5.11.

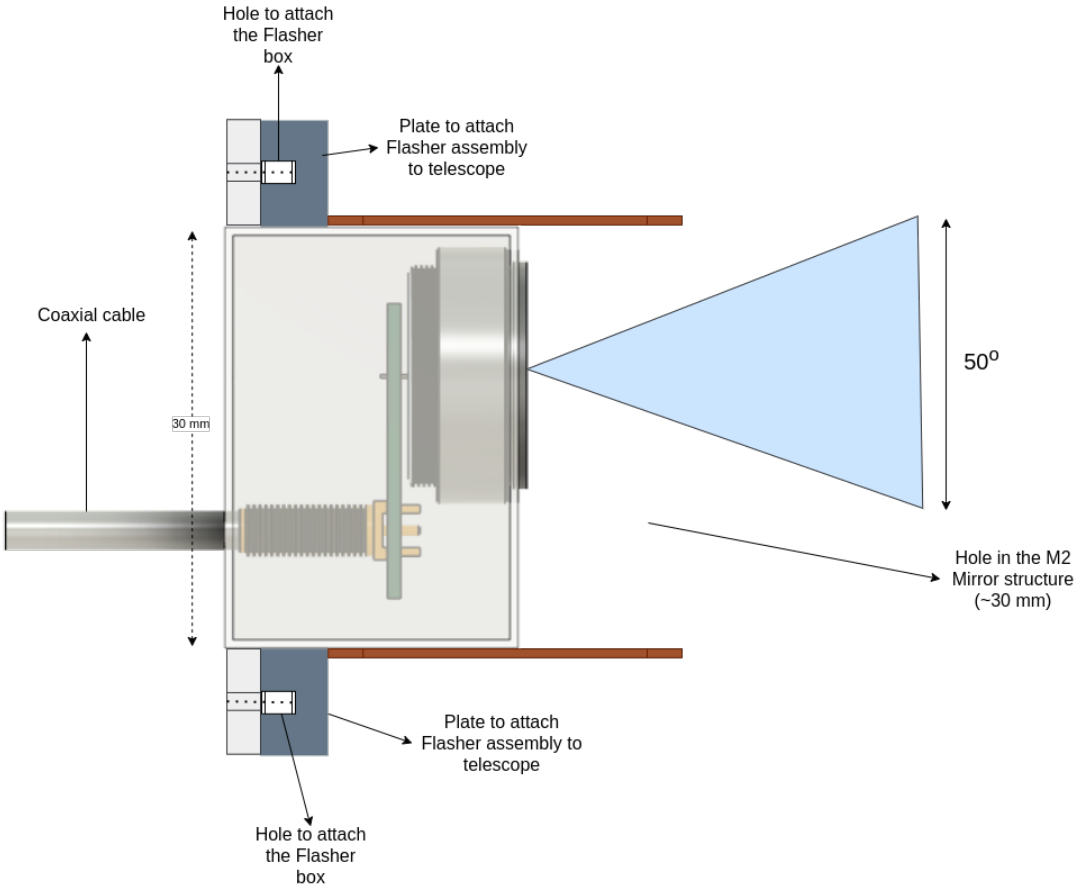

Figure 5.9: A possible attachment of Flasher assembly to the telescope structure is shown here. The box enclosing the Flasher assembly attaches to a plate behind the M2. The M2 mirror structure has $\sim$ 30 mm hole at the centre. The coaxial cable attaches to the box at the back.

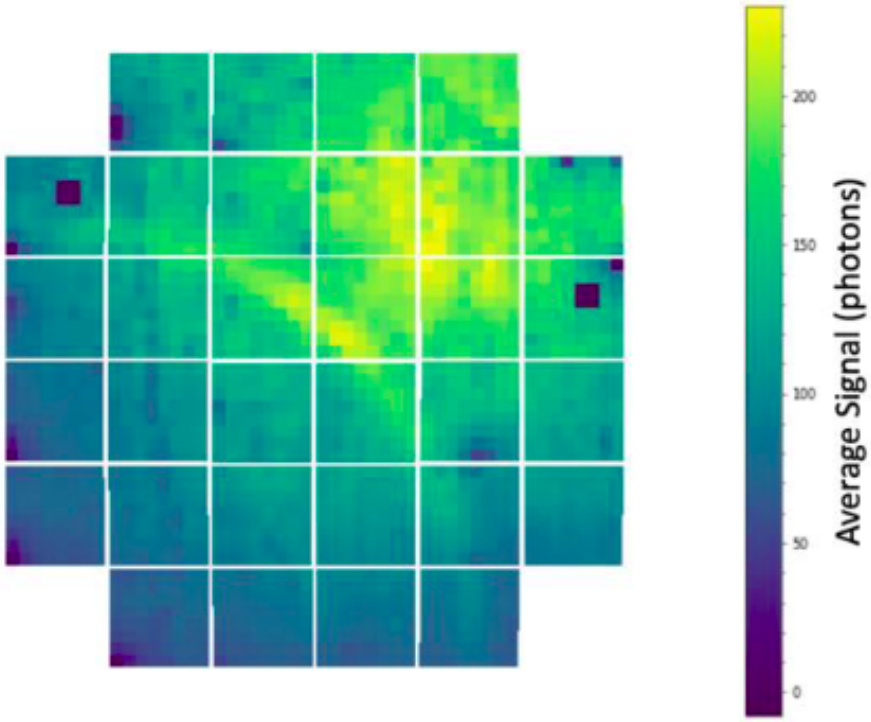

Figure 5.10: The illumination pattern observed on the CHEC-S camera during the observing campaign. The pattern persisted even when each of the four calibration unit was operated individually, it was determined that the observed pattern originated from the condition of the mirror rather than from the calibration units themselves.

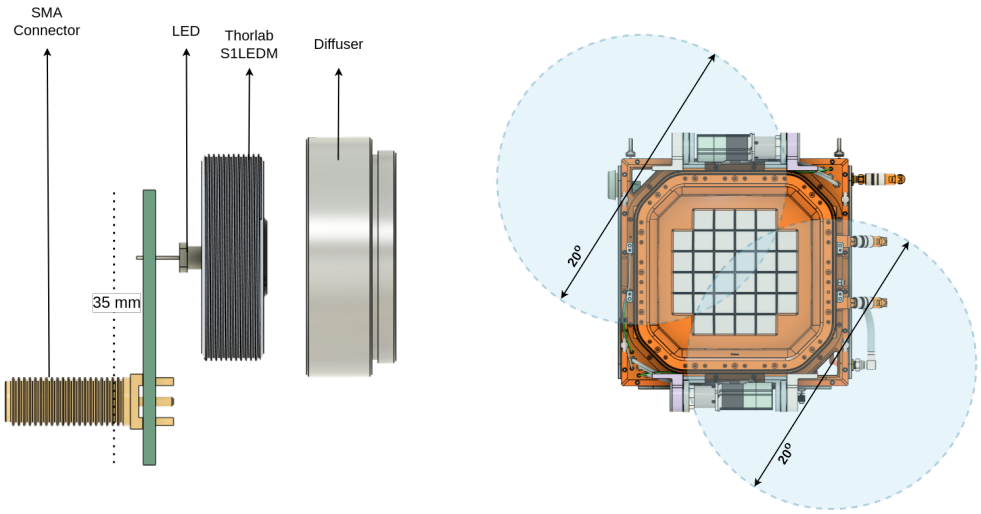

Figure 5.11: (*left*) The exploded view of the corner flasher assembly. A forward facing UV LED is connected to the SMA connector on a simple PCB. S1LEDM [116] grooved connector from Thorlabs helps in attaching the engineered diffuser to the PCB. (*right*) Two Flashers located at diagonally opposite corners of the camera will illuminate all the camera pixels via reflection from the secondary mirror. A 20° diffuser evenly spreads out the light. These illumination pattern helps in monitoring the mirror condition.

5.5.3 Flasher Fibre Integration

The main purpose of the underlid Flasher channel is to carry out functional checks on the SiPM pixels prior to the observation runs. The envisioned procedure to carry out functional checks will be discussed in Chapter 6. Apart from it, the low illumination level provided by the scintillating fibre (discussed in Section 4.1.5) makes it an excellent candidate to carry out single photoelectron calibration (theory has been discussed in 2.3.2).

Thus, a groove has been machined into the focal plane plate for placing the scintillating fibre. Figure 7.1 shows a generalized view of the focal plane plate indicating the grooves and the placement of the scintillating fibre. Further, a zoomed in version of the corner of the Flasher is also shown in Figure 5.13 that shows the position where the scintillating fibre emerges from behind the focal plane plate. A fibre sheath covers the initial length of the fibre to block the direct light reaching the corner pixels.

The scintillating fibre connects to an LED behind the focal-plane plate. To

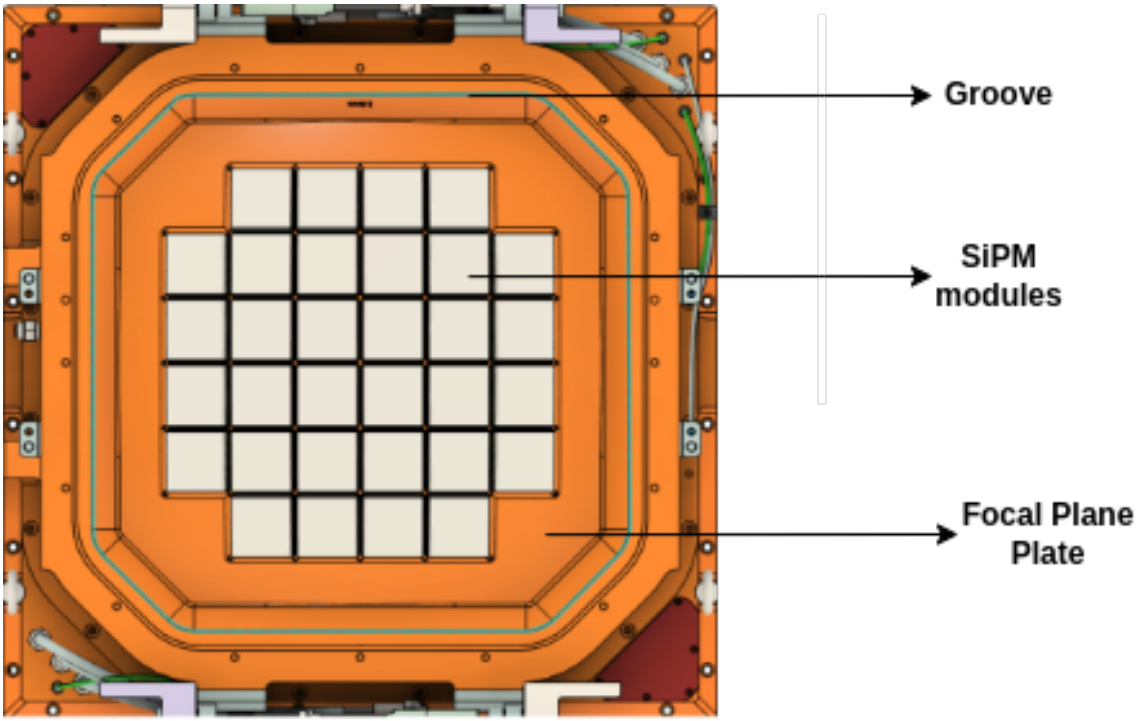

Figure 5.12: A generalised CAD view of the focal plane plate showing the scintillating fibre (green) placed in the groove.

enable this configuration, the fibre is terminated with an SMA connector, requiring the LED to be mounted on a compact PCB equipped with the necessary optical couplers and another SMA connector for attaching the coaxial cable carrying the LED signal. The design of this PCB, along with the optical coupler and stand offs is shown in Figure 5.14. The optical coupler itself is 3D-printed to hold a 90° angled LED, a choice motivated by mechanical constraints. This arrangement ensures the board can be securely attached to the camera structure while also allowing the coaxial cable to be routed easily to the board. The CAD model in Figure 5.15 depicts the final placement of the PCB and its coupling to the fibre behind the focal-plane plate.

5.6 Conclusion

The firmware for this version of the board is currently (September 2025) being developed by Dr. Sheridan Lloyd and will subsequently undergo extensive testing according to the procedures outlined in Table 5.1. The prototype board has al-

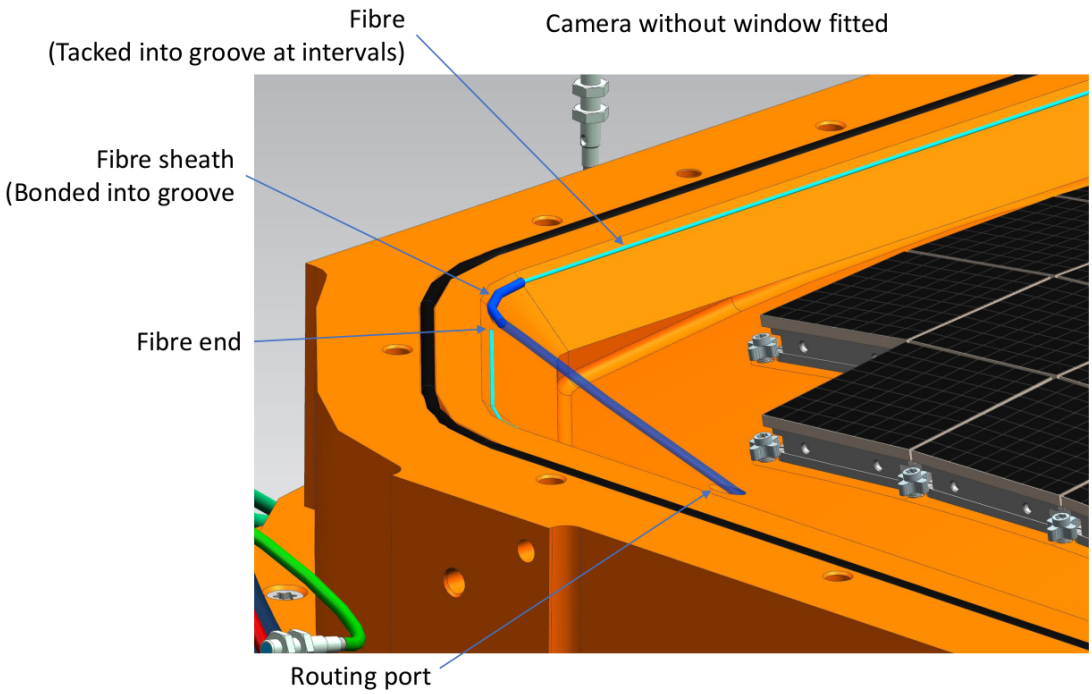

Figure 5.13: A zoomed in view of the corner of the camera showing where the scintillating fibre emerges from behind the focal plane plate. A fibre sheath covers the initial lengths of the fibre to block the direct light from reaching the camera pixels.

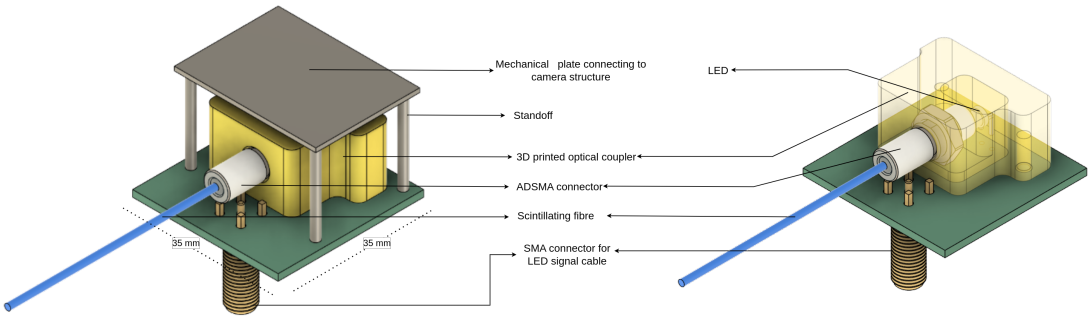

Figure 5.14: (*left*) A CAD model showing an UV LED and an SMA connector to connect the coaxial cable carrying LED driver signal. A 3D printed coupler with Thorlab ADSMA connector is attached to the LED. The fibre with an SMA termination can easily attach to the connector. Also shown is the mechanical plate that helps in connecting the PCB to the camera structure. (*right*) The 3D printed coupler has been faded to show the coupling of the LED into the ADSMA connector which further connects the scintillating fibre.

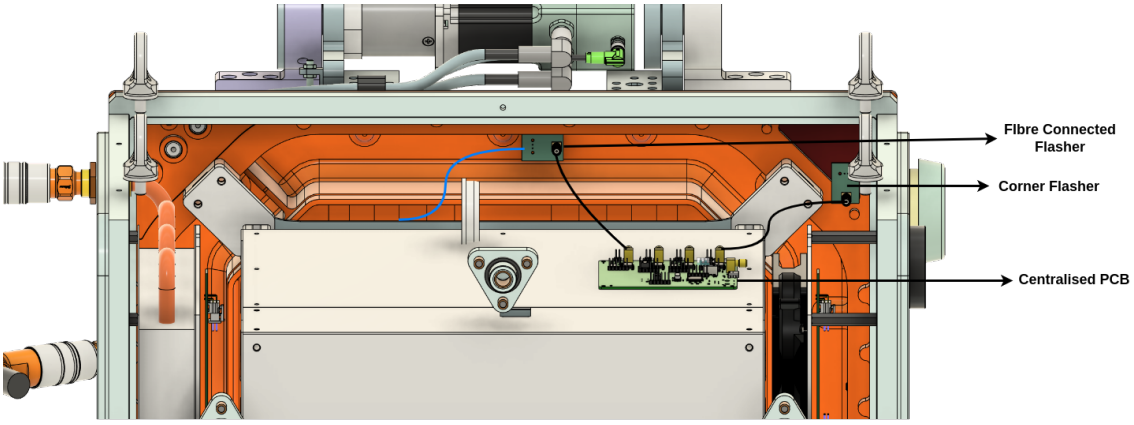

Figure 5.15: This CAD model depicts the centralised Flasher board placed on the top of the TARGET module rack. It is connected to the PCB containing the LED with a coaxial cable (*black*). The fibre (*blue*) emerges from the PCB and enters the focal plane. It also shows the connection to the corner Flasher (discussed in Section 5.5.2)

ready been fabricated and assembled with all required components, as shown in Figure 5.16. Its final dimensions are well within the recommended limits, ensuring compatibility with the intended installation location.

The adoption of the new microcontroller significantly enhances the system's scalability. Considering the drive strength of the GPIO pins and the capacitive load of the DS1023 inputs, a safe configuration allows up to eight channels to share the same DATA and CLK lines. With the available pins on the CH32V307R, three sets of DATA and CLK lines combined with 20 LE lines can control up to 20 Flasher channels. This marks a substantial improvement over the previous version, greatly extending the functionality of the Flasher system. The open-source architecture of the microcontroller further enables flexible development and future upgrades.

Nevertheless, improvements remain possible. At present, the LEDs are driven directly from the output of the LMG1025, which in certain settings does not provide sufficient current to switch them on. This limitation can be overcome by incorporating a field-effect transistor (FET) at the LMG1025 output [85], thereby boosting the drive current. Such a modification would allow the LEDs to flash across a wider range of settings, effectively increasing the system's dynamic range.

In summary, the Version 4 Flasher system combines compact design, enhanced scalability, and robust control features, positioning it as a versatile and reliable

calibration source for the SSTCAM. Future refinements, such as improved LED driving circuits, will further strengthen its performance and broaden its operational capabilities.

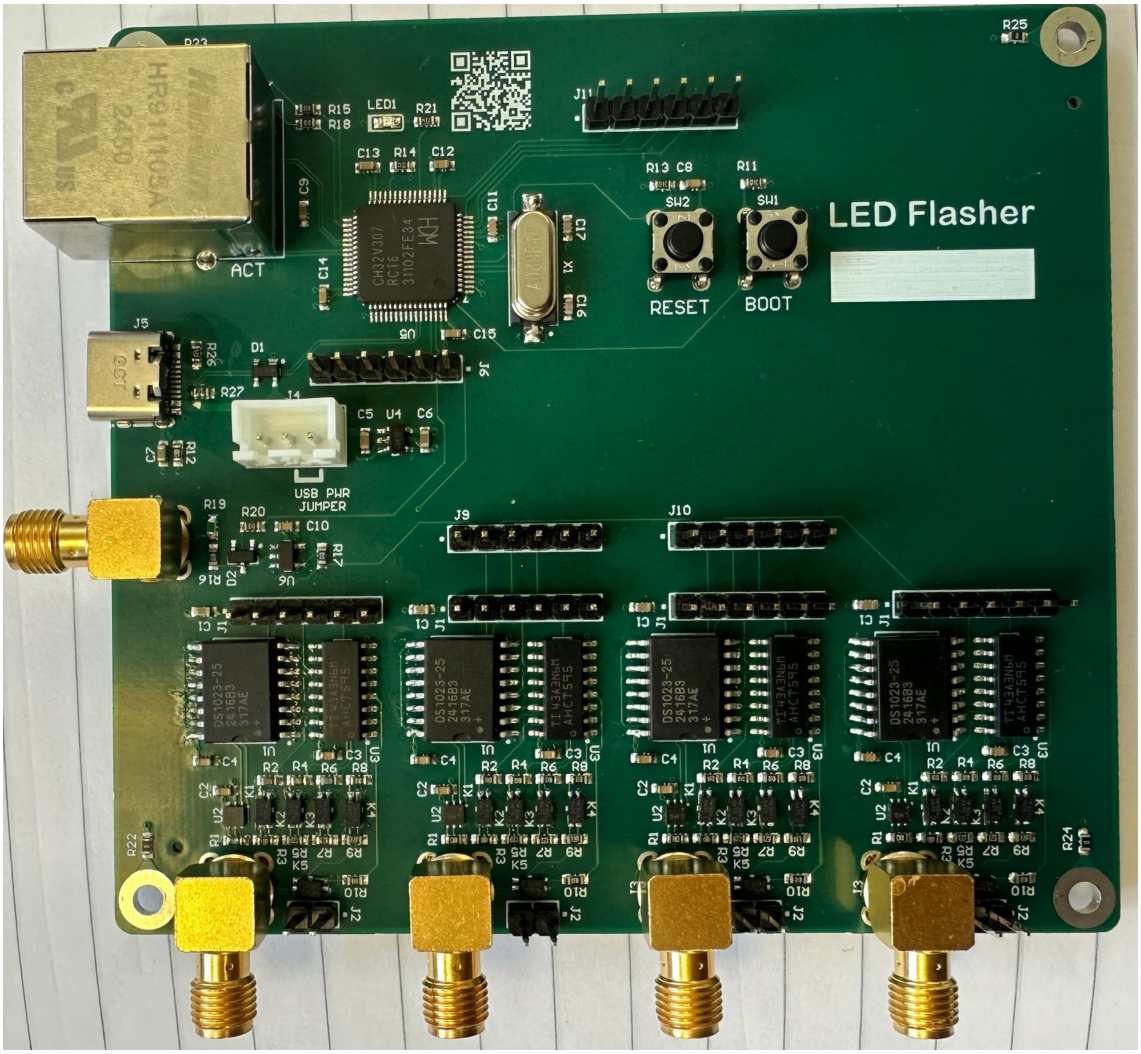

Figure 5.16: Prototype Flasher V4 board with all the components populated.

CHAPTER 6

Application of the Flasher Systems in SSTCAM

In Chapter 5, the design of the next-generation Flasher system was described, including the placement of its various channels within the camera structure to support different calibration tasks.

This chapter shifts focus from design to application, demonstrating how the Flasher subsystem is employed within SSTCAM to meet the stringent calibration requirements set by the CTAO collaboration 2.2. Calibration is essential to ensure reliable and uniform performance of all camera pixels, and encompasses several key activities: functional checks, pixel linearity monitoring, flat field correction and single-photoelectron (SPE) calibration for pixel gain monitoring.

This chapter is organized around these activities. Section 6.1 discusses how functional checks will be carried out using the under-lid Flasher channel coupled with a scintillating fibre. Section 6.2 introduces the methodology for monitoring pixel linearity, with results from a single SiPM module (64 pixels). Section 6.3 presents the approach to flat field correction, including simulations of realistic illumination patterns and their impact on pixel-to-pixel response before and after correction. Finally, Section 6.4 details the procedure for SPE calibration using dark count photons, and explores its extension to the low-level illumination provided by the under-lid

scintillating fibre. All these simulation activities and the associated data analysis and visualization are carried out independently by me.

6.1 Functional checks

Section 5.5.3 described the integration of the scintillating fibre into SSTCAM. The fibre illuminates the camera pixels indirectly, after reflecting from the inner surface of the camera door. This reflected illumination enables functional checks on all pixels during the initialization phase, i.e. the period when the camera is powered on and prepared for observation runs. With the preparation of the engineering camera (and later the full camera), fully populated with all SiPM modules, it will be possible to generate illumination patterns similar to those shown in Figure 4.10 of Chapter 4. Such patterns provide a straightforward way to identify bad pixels: any pixel that fails to respond to the illumination can be flagged immediately, allowing timely maintenance.

Also, for the identical illumination settings of the Flasher, the measured SiPM amplitudes can also be compared with previously stored reference values. This enables the detection of gradual performance degradation in individual pixels over time, complementing the routine functional checks performed on the SiPM modules before observation runs. It also offers a functionality to check the pulse shape and timing characteristics of each pixel. A bad pixel might deviate from its pulse shape indicating underlying electronic problems. Trigger behaviour can also be monitored to ensure that both pixel-level and camera-level trigger rates remain stable and consistent with their nominal settings. With the preparation of the engineering camera and full camera, additional functional checks will be incorporated into this under-lid flasher procedure, ensuring that any anomalies are detected prior to observation runs.

6.2 Pixel Linearity

All SiPMs in the camera are biased to operate within their linear response region. This is essential because a non-linear response directly impacts gain calibration, energy reconstruction, and ultimately the overall performance of the detector. Therefore, continuous monitoring of pixel linearity is essential (discussed previously in Section 2.3.3).

As discussed in Chapter 4, the Flasher channel located behind the secondary mirror provides illumination across the focal plane. Owing to its wide dynamic brightness range (see Figure 3.17), this channel can be used to probe pixel linearity by delivering light at different intensities and recording the corresponding pixel responses. Pixels that deviate from expected linear behaviour can then be flagged for detailed maintenance checks or recalibration.

One well characterised SiPM module with the attached data acquisition module (TARGET module) was tested to construct the test procedure for the whole camera. The module was illuminated from a distance of about 50 cm at three different Flasher illumination levels, corresponding to zero (Flasher was off), low and high intensity settings. The average waveforms recorded from one of the pixel for the three different level of Flasher brightness is shown in Figure 6.1.

The peak amplitude was extracted from the waveforms. The average amplitude across all the 64 pixels for each Flasher setting was chosen as the mean illumination level. Finally, the peak amplitude recorded across each pixel was normalised by the average amplitude corresponding to the low brightness level. A scatter plot of relative amplitude versus mean illumination level was constructed, and a linear regression fit was applied to each pixel's response. The slope of this regression provides a quantitative measure of linearity, serving as an indicator for identifying non-linear pixels. Figure 6.2 shows both the fits and the distribution of fitted slope values across the pixels. The plot indicates that the response of the SiPM pixel is linear and the linearity values are within 3 sigma bound. As responses of all the 64 pixels to different illumination levels are closely bunched together (black blobs), it suggests the response of all the pixels in the SiPM module are quite similar. This is also another way of visually isolating faulty pixels.

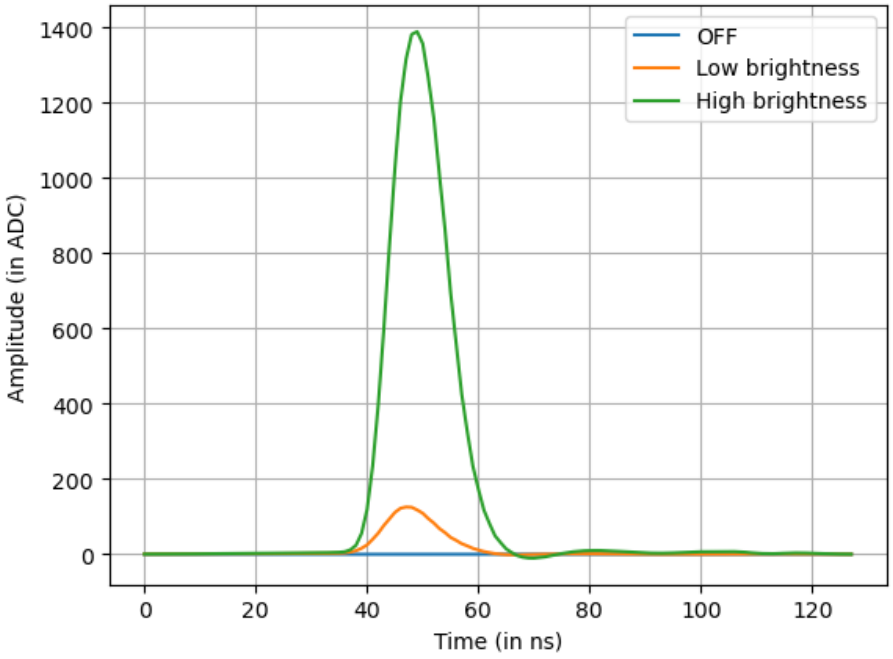

Figure 6.1: Average waveforms recorded by the SiPM for three different level of Flasher illumination level. The peak amplitude is calculated from these waveforms.

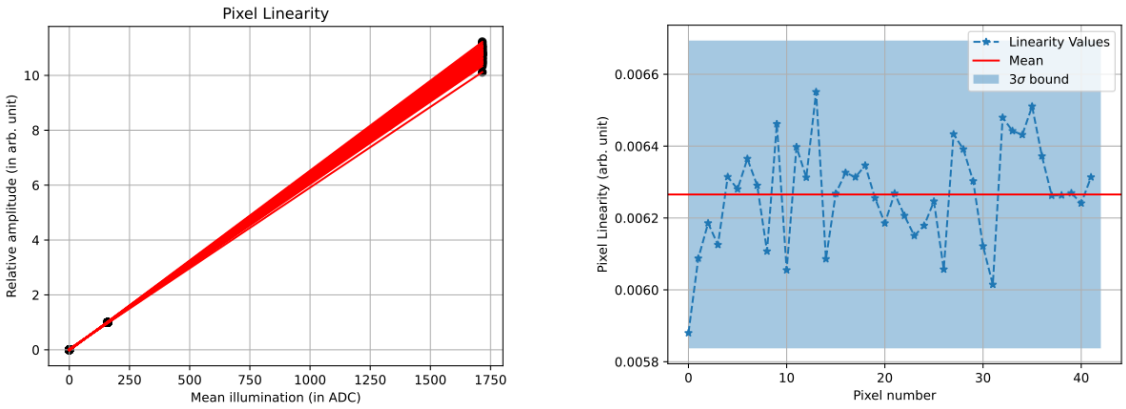

Figure 6.2: *(left)* Scatter plot between mean illumination level and the normalised amplitude (black blobs) seen by each pixel. A linear fit to the data points (red lines) from each pixel gives the slope which is a veto for the linearity. *(right)* The distribution of the slope value with the pixel number in the SiPM. The a 3σ error bound on the distribution is also shown. Para

With the full camera, the pixel linearity monitoring will be performed with increased number of Flasher illumination levels. Dedicated calibration runs will monitor the drift of pixel linearity and flag the faulty pixels.

6.3 Flat Fielding

The response of all the pixels will inherently be different due to difference in their gain and photon detection efficiency (discussed in Section 2.3.1 of Chapter 2). The gain can be manipulated by independently tuning the over-voltage of each individual pixel; residual variation is corrected by performing flat field operation. The objective of flat fielding is that for uniform illumination of all pixels their response should be uniform. This ensures that subsequent measurements truly reflect astrophysical signals rather than instrumental effects. The specific requirements on the calibration device set by CTAO are discussed in Table 2.2. Alongside, CTAO also outlines the acceptable flat field uniformity levels for the camera as shown in the box below.

CTAO requirement for flat fielding SSTCAM

The calibration device should provide a uniform illumination pattern across the camera focal plane and the RMS variation should be known to a level of 2% post offline corrections.

To evaluate whether the flat field requirement of 2% RMS variation can be met, simulation of three different illumination patterns were tested, and the corresponding flat field coefficients were extracted. The details of these test cases are summarized in Table 6.1. For each case, the baseline noise map was derived from the measurement of a single SiPM module. The SiPM module was placed inside a dark box and 1000 events were recorded. The distribution of the amplitude from 1000 events in each pixel was fitted with a 1D-Gaussian function. This distribution for one of the pixels is shown in Figure 6.3. The mean and standard deviation of this distribution was used to construct the baseline noise map in the simulation.

Test Case	Description
Case 1	10% gain matched SiPM pixels and an uniform illumination pattern
Case 2	10% gain matched SiPM pixels with 2D Gaussian illumination pattern
Case 3	10% gain matched SiPM pixels with 2D Gaussian illumination pattern convolved with the response function of a 50° engineered diffuser [100]

Table 6.1: Simulated illumination patterns tested for the purpose of flat fielding. As an initial assumption, the pixels are gain matched to a level of 10%.

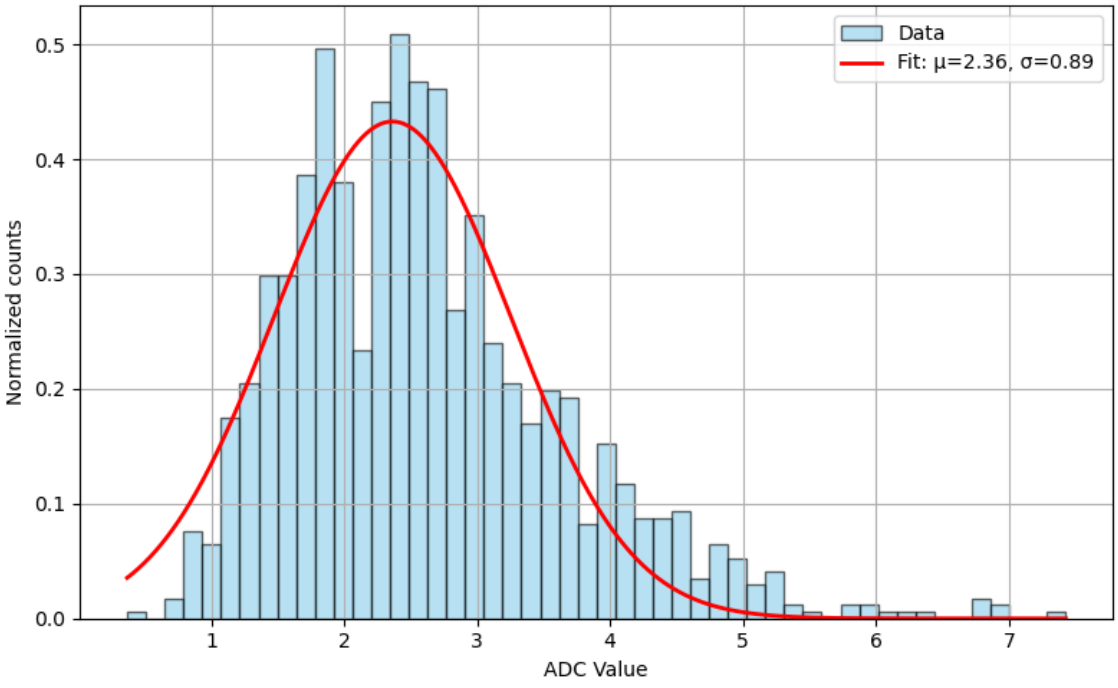

Figure 6.3: Amplitude distribution for pedestal events from a single SiPM pixel. The Gaussian fit provided the mean and standard deviation of the noise level for each pixel that was later used in flat field simulation.

After simulating the response of camera for different illumination patterns, the

amplitude variation across the camera consisting of 2048 pixels is found out. The flat field coefficients are calculated and camera response is corrected using the procedure shown below.

Step 1: Normalised Response

$$N_i = \frac{R_i}{I_i}, \quad i = 1 \text{ to } 2048 \tag{6.1}$$

where R_i and I_i refer to the pixel response and the illumination level at the i^{th} pixel.

Step 2: Flat Field Coefficients

$$FF_i = \frac{N_i}{\langle N_i \rangle}, \quad i = 1 \text{ to } 2048 \tag{6.2}$$

where $\langle N_i \rangle$ is the average of normalised response over 2048 pixels.

Step 3: Corrected Response

$$C_i = \frac{N_i}{FF_i}, \quad i = 1 \text{ to } 2048 \tag{6.3}$$

where C_i is the response of each pixel after flat field correction.

Step 4: Overall Variation (in %)

$$\frac{\sigma(C_i)}{\langle C_i \rangle} \times 100, \quad i = 1 \text{ to } 2048 \tag{6.4}$$

where $\sigma(\mathrm{C}_i)$ and $\langle \mathrm{C}_i \rangle$ are the mean and the standard deviation of the corrected response.

6.3.1 Case 1: Uniform Illumination

In the case of uniform illumination, the dominant sources of signal variation are the intrinsic gain differences between pixels, and the baseline noise level. The convolution of the gain map and addition of the baseline noise to get the on-camera response is shown in Figure 6.4. In the simulation, the average baseline noise across all 2048 pixels was found to be approximately 3 ADC. At low illumination levels, pixel-to-pixel variations appear larger because they are dominated by Poisson fluc-

tuations. As the illumination increases, these statistical fluctuations become less significant, and the true non-uniformity of the camera response is revealed. Figure 6.5 shows the relationship between illumination level and the average RMS variation of pixel response across the camera. The results demonstrate that for an uniform illumination above 100 ADC, Poisson fluctuations are effectively suppressed and the flat field coefficient variation remains below 2%.

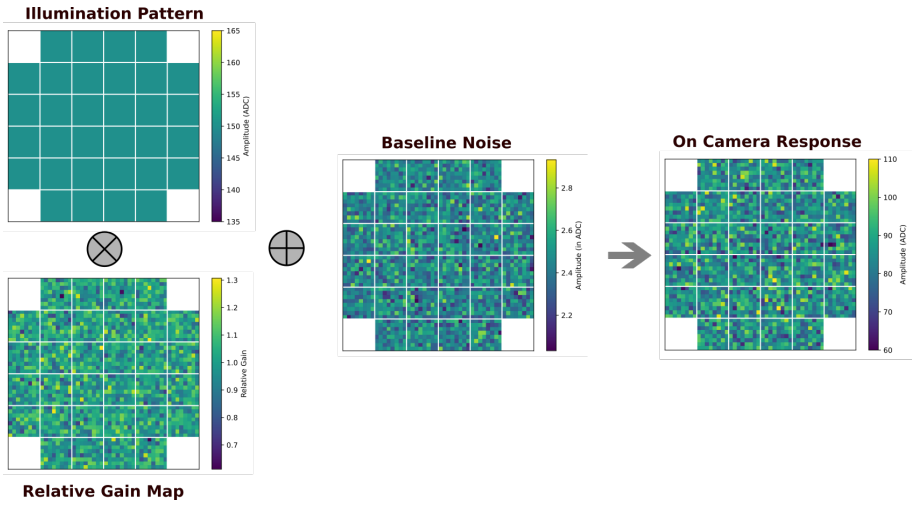

Figure 6.4: [Case 1] The procedure to generate the camera response to an uniform illumination. The uniform illumination map is convolved with a gain map (10% RMS spread) and the baseline noise was added to it. The resulting on-camera response is then used to derive the flat field coefficients.

The flat field coefficients were derived using 100 simulated events. To validate their effectiveness, a new set of responses was generated by the similar process shown in Figure 6.4 and the previously determined coefficients were applied to these responses to test the correction. The pixel response and the peak amplitude distribution before and after the flat field correction are shown in Figure 6.6. The overall variation post flat field correction was $\leq 2\%$

6.3.2 Case 2: Gaussian Illumination

The case of uniform illumination firmly established the method of flat fielding. However, achieving a perfectly uniform illumination is challenging. Therefore, it was important to investigate whether a non-uniform illumination source could still satisfy the flat fielding requirement set by CTAO. Based on the measured LED beam

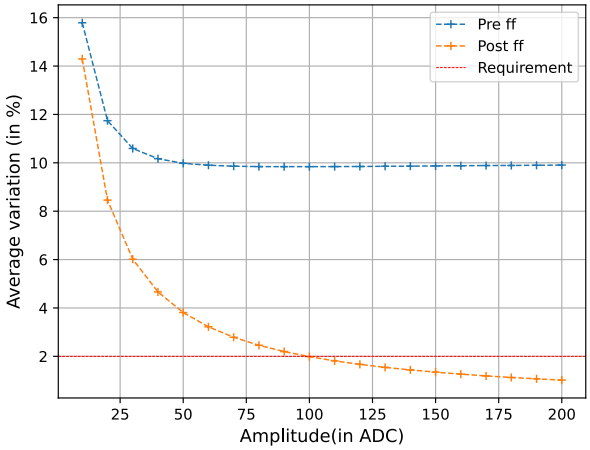

Figure 6.5: [Case 1] Dependence of RMS variation across camera pixels on the uniform illumination amplitude level. The red line is the CTAO requirement of 2%. Above an illumination amplitude of 100 ADC, the Poisson fluctuation is suppressed and the overall variations across all the pixels of camera was below 2% post flat field correction. The 10% asymptote in pre-flat field is the assumed 10% gain mismatch.

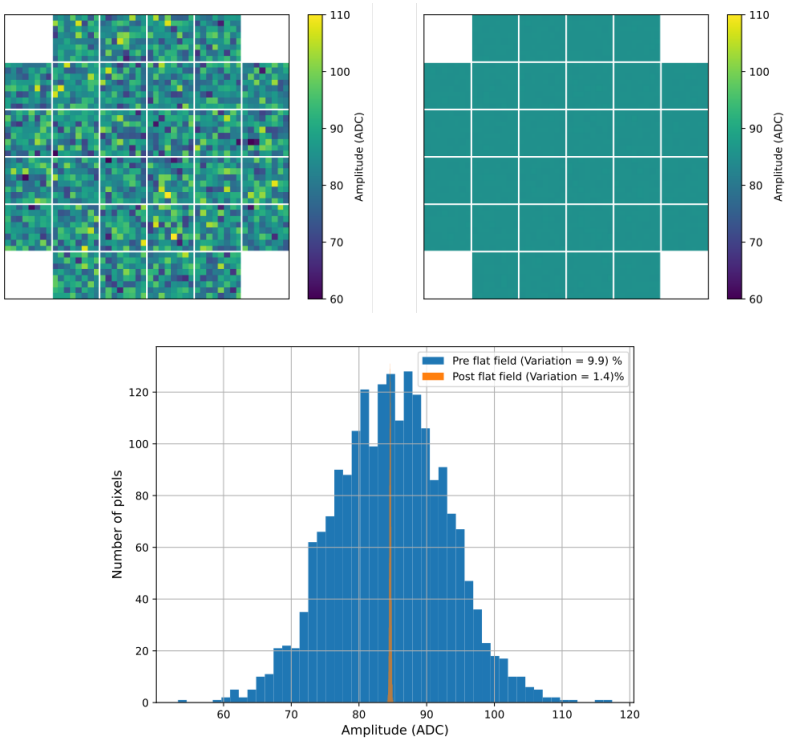

Figure 6.6: [Case 1] The pixel response before (*left*) and after (*right*) flat field correction. The RMS variation before correction was 9.9% and after correction was 1.4% (evident from the distribution in the *bottom*.

profile (Figure 3.24), a Gaussian beam was chosen as a realistic approximation for the illumination pattern. The overall process of simulating the camera response is illustrated in Figure 6.7.

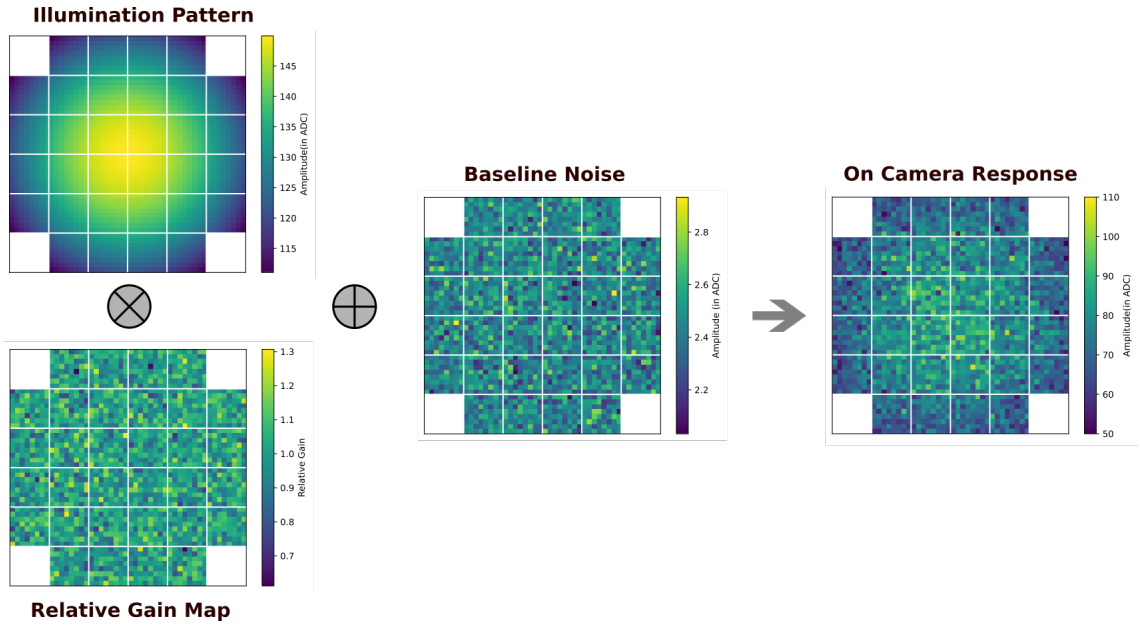

Figure 6.7: [Case 2] The procedure to generate the camera response to a Gaussian illumination. The illumination map is convolved with a gain map (10% RMS spread) and the baseline noise was added to it. The on-camera response is further used to determine the flat field coefficients.

There are three free parameters in the Gaussian beam approximation, namely, the peak position, amplitude, and beam width. The dependence of RMS variation across the focal plane on the illumination amplitude is shown in Figure 6.8. Similar to the case of uniform illumination, Poisson fluctuation dominates at low illumination levels and suppressed at higher illumination levels. If the Gaussian beam were perfectly aligned with the centre, the 2% flat field requirement would be satisfied for amplitudes above 150 ADC. However, additional non-uniformities arise due to uncertainties in the peak position and beam width. Therefore, for the subsequent analysis, the Gaussian amplitude is fixed at 150 ADC while the other two parameters are investigated.

The Gaussian beam width and its uncertainty in the peak position primarily determine the spatial uniformity of the illumination pattern seen by the camera. The beam width and the peak position uncertainty is defined as in equation 6.5 and

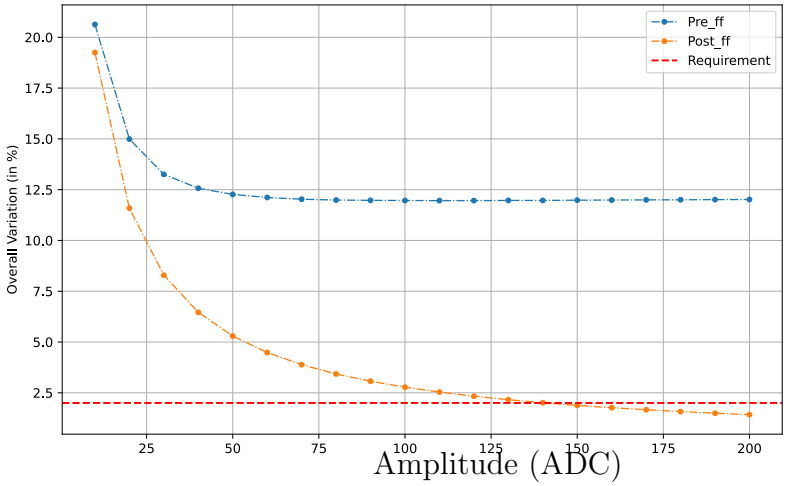

Figure 6.8: [Case 2] Dependence of RMS variation across camera pixels on the Gaussian illumination amplitude level before (blue curve) and after flat fielding (orange curve). The red line is the CTAO requirement of 2%. Above an illumination amplitude of 150 ADC, the Poisson fluctuation is suppressed and the overall variations across all the pixels of camera was below 2% post flat field correction.

equation 6.6 respectively. Finally, the spatial uniformity is expressed according to the equation 6.7.

$$\text{Beam Width (\%)} = \frac{\text{Gaussian distribuition } \sigma}{\text{Effective diameter of SSTCAM}} \times 100 \tag{6.5}$$

where the effective diameter of SSTCAM is 30 cm.

$$\text{Peak position uncertainty (\%)} = \frac{\text{Distance to peak from centre}}{\text{Effective radius of SSTCAM}} \times 100 \tag{6.6}$$

where effective radius of SSTCAM is 15 cm.

$$\text{Spatial Uniformity (\%)} = 1 - \frac{\sigma(R_i)}{\langle R_i \rangle} \times 100 \tag{6.7}$$

where R_i is the response of the i^{th} pixel.

Their combined influence is shown in the 2D distribution of Figure 6.9. Spatial uniformity sets the limit on whether the 2% RMS variation requirement can be achieved. From the plot in Figure 6.9, it can be concluded that to flat field SSTCAM within the required tolerance, the Gaussian beam must have a uniformity above 90%.

This corresponds to a minimum beam width of 70% and a maximum peak position uncertainty of 30%.

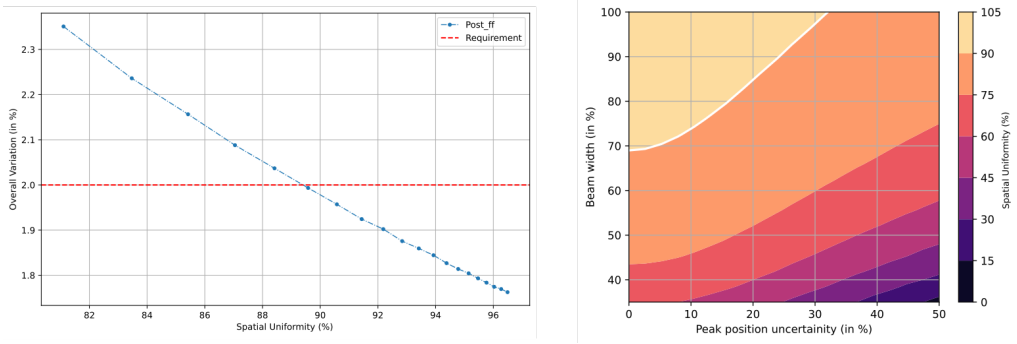

Figure 6.9: (*left*) The dependence of overall RMS variation on the spatial uniformity after flat field correction. The red line indicates the CTAO requirement of 2% RMS variation. It can be concluded that at least 90% uniform beam is required to meet the CTAO requirement. (*right*) The dependence of spatial uniformity on Gaussian peak position uncertainty and its beam width. The white line indicates the contour for 90% spatial uniformity. The minimum beam width should be 70% and the maximum tolerable peak position uncertainty is 30% to achieve $\geq$ 90% uniform beam.

Finally, the estimated flat field coefficients were validated by applying them to a simulated response. The comparison of pixel amplitudes before and after flat field correction is shown in Figure 6.10. These results confirmed that a Gaussian illumination pattern can be used to flat field SSTCAM reliably.

6.3.3 Case 3: Gaussian Illumination + Diffuser

In practical operation, a diffuser will be used to uniformly illuminate the camera's focal plane. To evaluate this scenario, the Gaussian illumination pattern described in the previous section was convolved with the response function of a 50° engineered diffuser [100]. The diffuser response describes how the relative light intensity varies with the scatter angle, defined as the angle between the detection point and the optical axis. A comparison of spatial uniformity between Gaussian-only and Gaussian-plus-diffuser illumination is shown in Figure 6.11. The addition of the diffuser improves the uniformity by at least 3 ± 0.3% across a range of beam widths. The workflow from illumination pattern to on-camera response is illustrated in Figure 6.12.

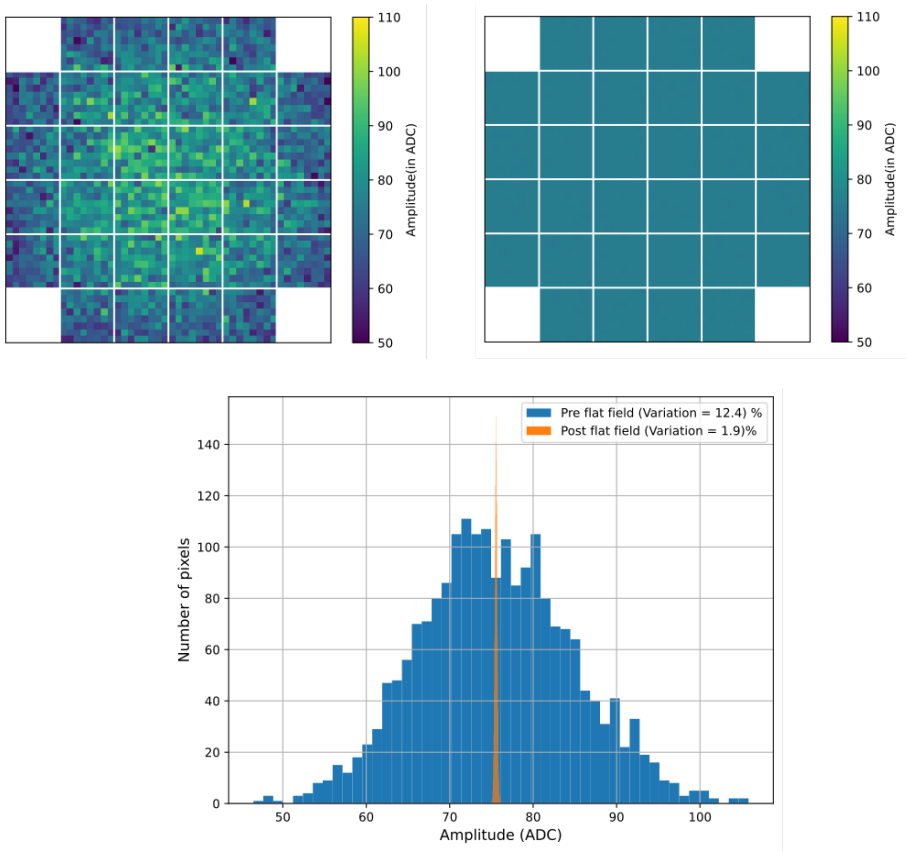

Figure 6.10: [Case 2] The pixel response before (*left*) and after (*right*) flat field correction. The RMS variation before correction was 12% and after correction was 1.9% (evident from the distribution in the *bottom*.

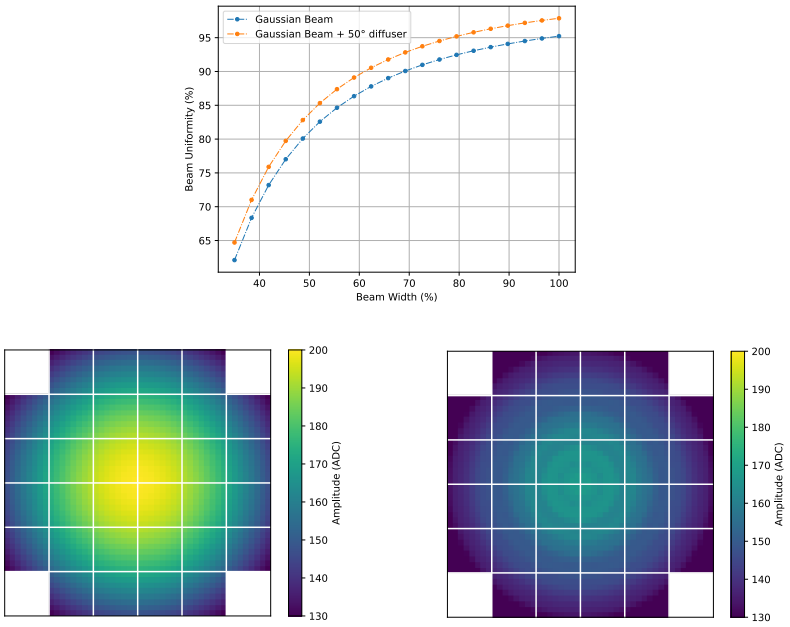

Figure 6.11: (*top*) The dependence of spatial uniformity on beam width for Gaussian (blue) and Gaussian-plus-diffuser illumination (orange). The Gaussian illumination pattern before (*bottom left*) and after (*bottom right*) convolution with the diffuser response function becomes at least 3% more uniform.

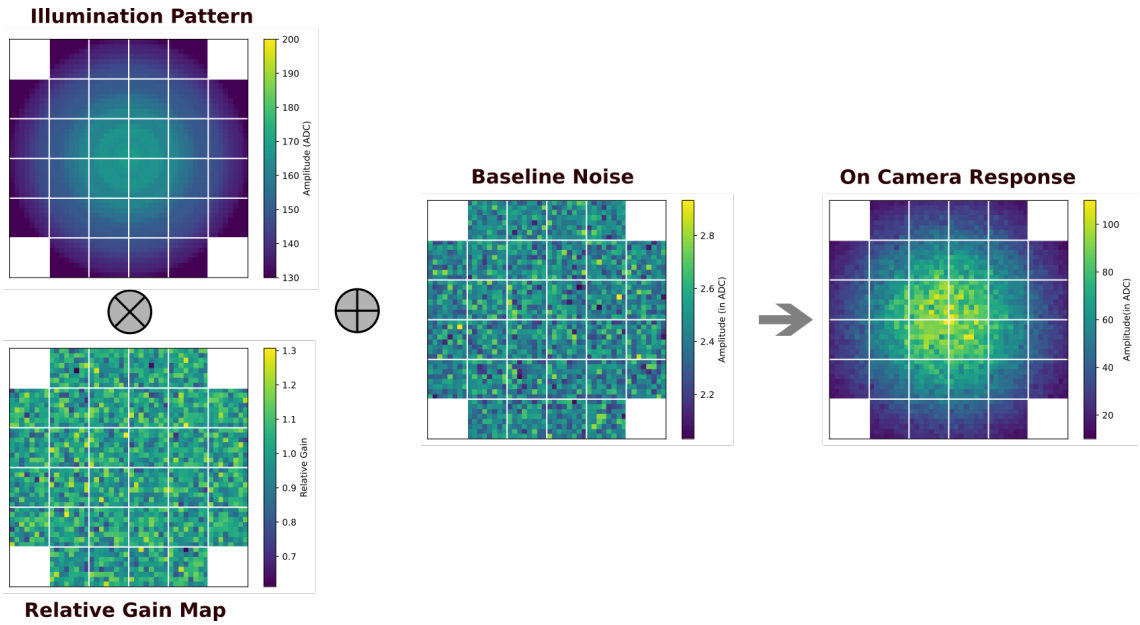

Figure 6.12: [Case 3] The procedure to generate the camera response after convolution of Gaussian illumination with the diffuser response function. This is then convolved with the gain map, which has 10% RMS variation and added baseline noise to it. The on-camera response is further used to determine the flat field coefficients.

As before, the minimum usable illumination amplitude was determined by plotting RMS variation against amplitude level. In this case, the CTAO flat field requirement of $< 2\%$ RMS variation was met for amplitudes above 175 ADC (shown in Figure 6.13), but to allow additional margin, 200 ADC was selected for further analysis. The higher amplitude requirement can be explained by the trade-off between spatial uniformity and photon statistics: while the diffuser improves uniformity compared to the Gaussian case, it also spreads the light more evenly across pixels, reducing per-pixel photon counts. As a result, a stronger illumination is required to meet the 2% flat field criterion.

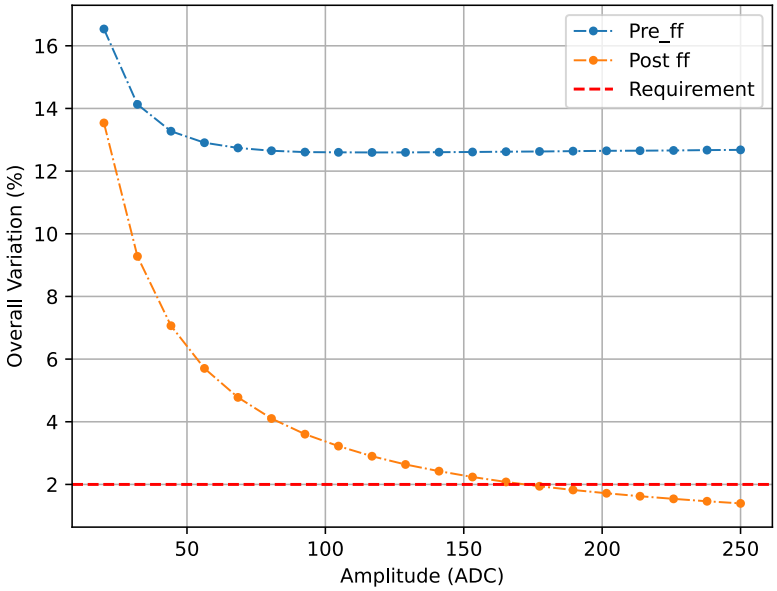

Figure 6.13: [Case 3] Dependence of RMS variation across camera pixels on the illumination amplitude level. The red line is the CTAO requirement of 2%. Above an illumination amplitude of 175 ADC, the Poisson fluctuation is suppressed and the overall variations across all the pixels of camera was below 2% post flat field correction.

The relationship between spatial uniformity and RMS variation after flat field correction (Figure 6.14) showed that the CTAO requirement is satisfied for beam uniformities above 85%. A 2D distribution of beam width and peak position uncertainty (Figure 6.14) further demonstrated that the diffuser significantly relaxes the tolerance compared to the Gaussian-only case. Specifically, the minimum acceptable beam width decreased from 70% to 50%, while the maximum permissible peak position uncertainty increased from 30% to 45%.

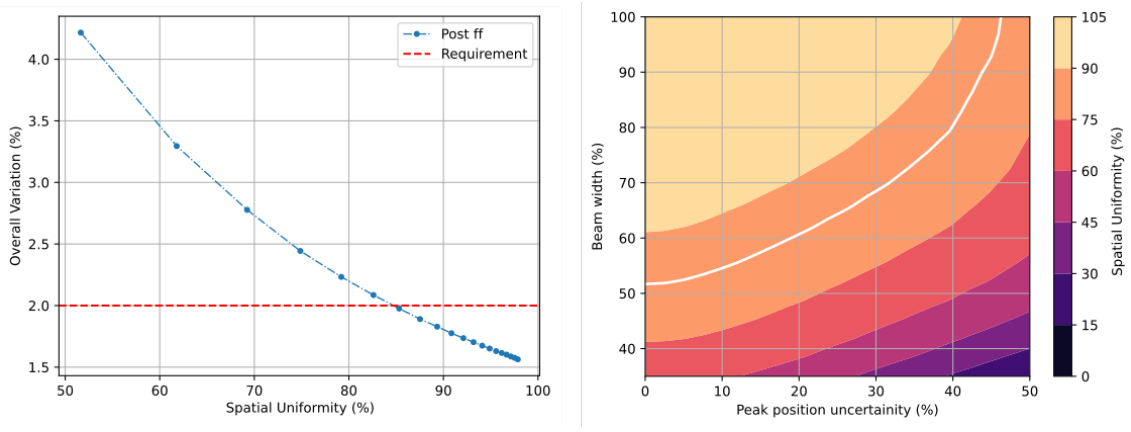

Figure 6.14: (*left*) Overall RMS variation as a function of spatial uniformity after flat field correction. The red dashed line marks the CTAO requirement of 2% RMS, indicating that an spatial uniformity of at least 85% is necessary to meet this standard. (*right*) Dependence of spatial uniformity on the Gaussian peak position uncertainty and beam width. The white contour highlights the 85% uniformity threshold, showing that a minimum beam width of 50% and a peak position uncertainty below 45% are required to achieve ≥85% uniformity.

Finally, the derived flat field coefficients were validated by applying them to a simulated camera response. The comparison of pixel amplitudes before and after flat field correction is shown in Figure 6.15, confirming that diffuser-assisted illumination can reliably meet CTAO flat fielding requirements.

6.4 Single Photoelectron Calibration

Single Photoelectron (SPE) calibration is essential to characterize the response of each SiPM pixel at the fundamental level of detecting a single photon (discussed in detail in Section 2.3.2). The SiPMs along with the TARGET module converts single photons into discrete charge pulses, SPE spectrum provides a direct measurement of the SiPM gain. As discussed in Chapter 1, the gain calibration is directly related to energy reconstruction and long-term stability monitoring of the camera performance.

In this work, two potential sources of single-photoelectron signals are investigated to assess the feasibility of SPE calibration. The first arises from the intrinsic thermal noise in silicon, where carrier generation through thermal agitation produces single-photon–like events. A dedicated simulation was carried out to study how optical crosstalk and night-sky background affect the gain extraction under these conditions.

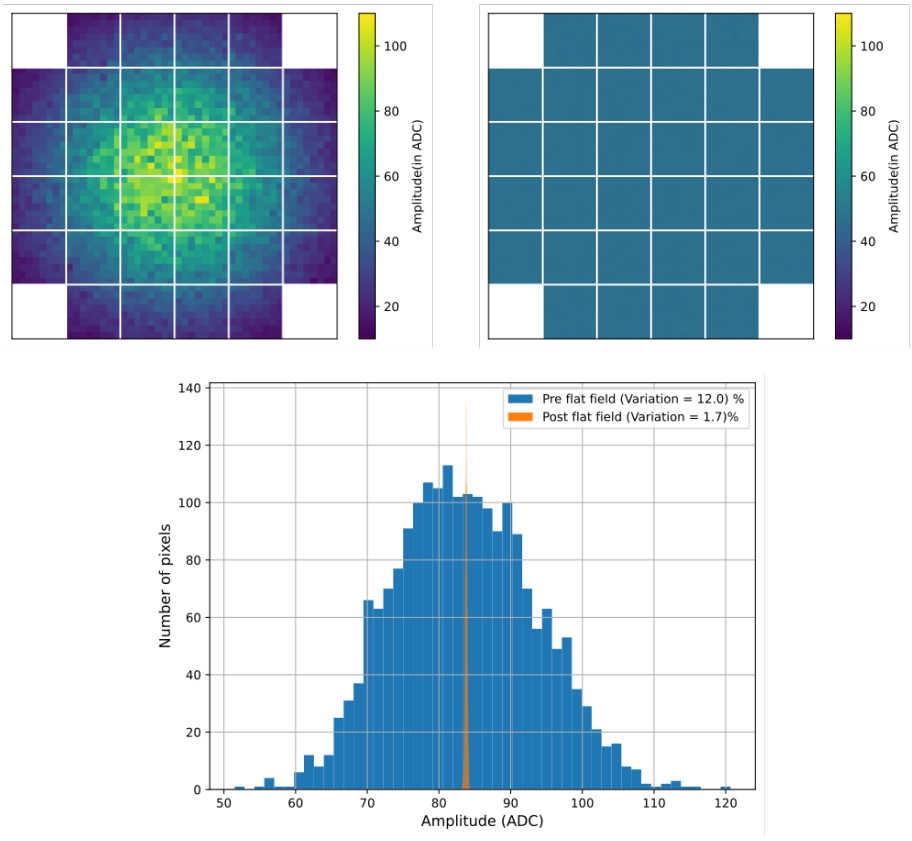

Figure 6.15: [Case 3] The pixel response before (*left*) and after (*right*) flat field correction. The RMS variation before correction was 12% and after correction was 1.7% (evident from the distribution in the *bottom*).

The second source is the under-lid Flasher channel, which can provide low-level, controlled illumination to emulate SPE signals. The detailed calibration procedures using these two approaches are presented in the following sections.

6.4.1 Dark Count Photons

As discussed in Section 2.3.2, the thermally generated charge carriers can cause avalanche in the SiPM microcells which appears as single photoelectron event. The night sky background can also increase the probability of these single photoelectron events. In addition, the optical crosstalk level of the SiPMs dictates the resolution of SPE peaks in the SPE spectrum, resulting in better gain extraction. Thus, a detailed simulation using the SSTCAM camera simulation software (sstcam_simulation[5]) was carried out to investigate the dependence of SiPM parameters(dark count rate and optical crosstalk) and observing conditions(night sky background) on the gain calibration of SiPM pixels.

Methodology

The sstcam_simulation framework [117] provides a flexible way to simulate different illumination sources and night-sky background (NSB) levels, while incorporating SiPM characteristics such as photon detection efficiency, gain, crosstalk, and timing jitter. From these inputs, the simulation generates a photoelectron list, which records the arrival time and charge of each detected photon. This list is then passed to the **event acquisition class**, which models the readout electronics by applying AC coupling, electronic noise, and pulse shaping (using a reference pulse), thereby producing a continuous readout signal. The **digitisation class** subsequently samples this signal to generate event waveforms, each 128 samples long, matching the format of SSTCAM data. At this stage, digitisation noise is also included to closely mimic realistic conditions. Figure 6.16 illustrates the overall structure of the simulation software, showing the different Python classes and methods involved in this

[5]A dedicated internal simulation software based on Python to carry out performance benchmarking of SSTCAM (https://github.com/sstcam/sstcam-simulation). The software is developed and maintained by Dr Jason Watson.

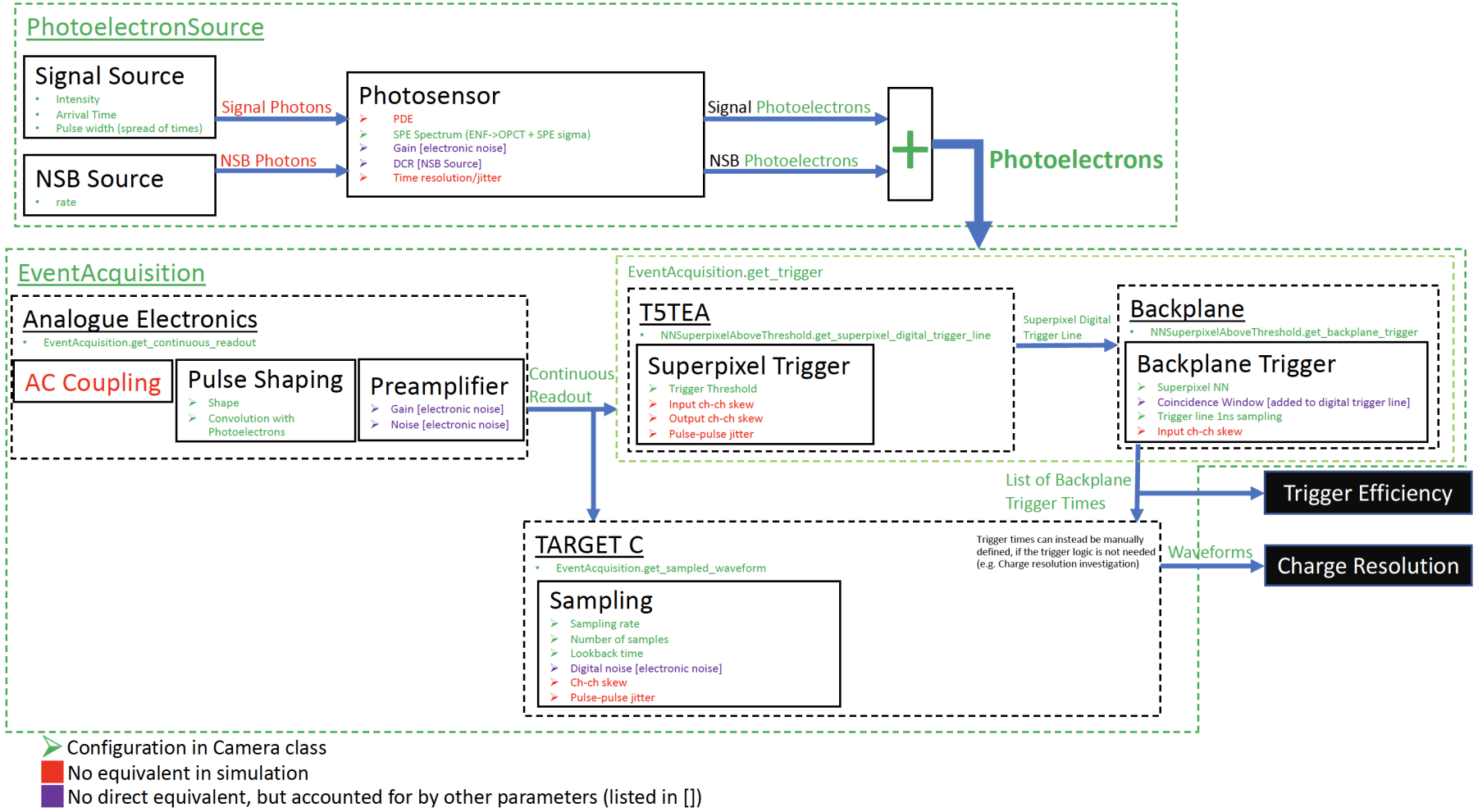

Figure 6.16: Structure of the SSTCAM simulation software, organized into Python classes and methods. The framework consists of two main classes: Photoelectron Source and Event Acquisition. The Photoelectron Source simulates NSB and signal photons to generate a photoelectron list, which is then passed to the Event Acquisition class. This class applies camera-level effects such as SiPM gain, noise, AC coupling, and digitisation, producing 128-sample event waveforms for each camera pixel [117].

process.

In this study, only night-sky background (NSB) events—that is, events without source photons—were simulated at different NSB rates. The simulated NSB photons were combined with various levels of optical crosstalk, electronic noise, and a Gaussian reference pulse shape to generate realistic waveforms for each pixel. These waveforms were stored for detailed offline analysis. This broad dataset enabled a systematic investigation of how different parameters affect the efficiency of SiPM gain extraction.

The core idea of the analysis was to recover the injected charge from each waveform using a reference pulse through an iterative subtraction method. In each iteration, the reference was subtracted after the extraction of charge until only baseline noise remained in the waveform. The process was terminated once the extracted charge fell below 0.25 photoelectrons (p.e). This threshold was deliberately chosen to suppress the pedestal peak (first peak in Figure 2.8), thereby enhancing the separation of the 1 p.e peak. The complete charge-extraction procedure is illustrated in Figure 6.17. The Gaussian reference pulse used for simulated data and the SSTCAM reference pulse used for experimental data is shown in Figure 6.18.

Simulation Setup

In the simulation of SPE spectrum from NSB photon events, three parameters were considered.

- Night sky backgorund level (10 MHz and 40 MHz)
- Baseline noise level (0 to 5 p.e.)
- Optical crosstalk (0 to 20%)

Using the SSTCAM simulation framework, datasets consisting of large number of event waveforms are created using the combination of these three parameters and the methodology described in Section 6.4.1 was used to create the SPE spectrum and extract the gain of the simulated photosensors. The result from this analysis are discussed next.

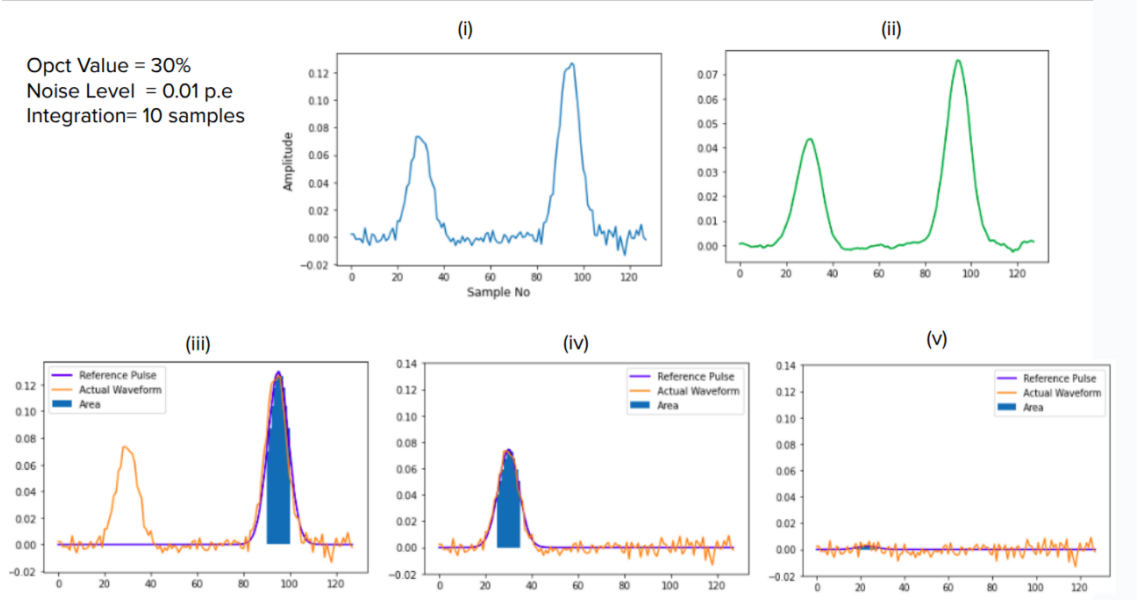

Figure 6.17: (i) A sample waveform for one of the event having two injected NSB photons. (ii) Waveform after convolution of the reference waveform (shown in Figure 6.18) to smooth out some of the noise. (iii) The method identifies the first peak, extracts the charge by summing over 10 samples and subtracts the reference waveform from it. (iv) A similar process is carried out for the next peak. (v) The residual baseline noise remains after the extraction of all the peaks.

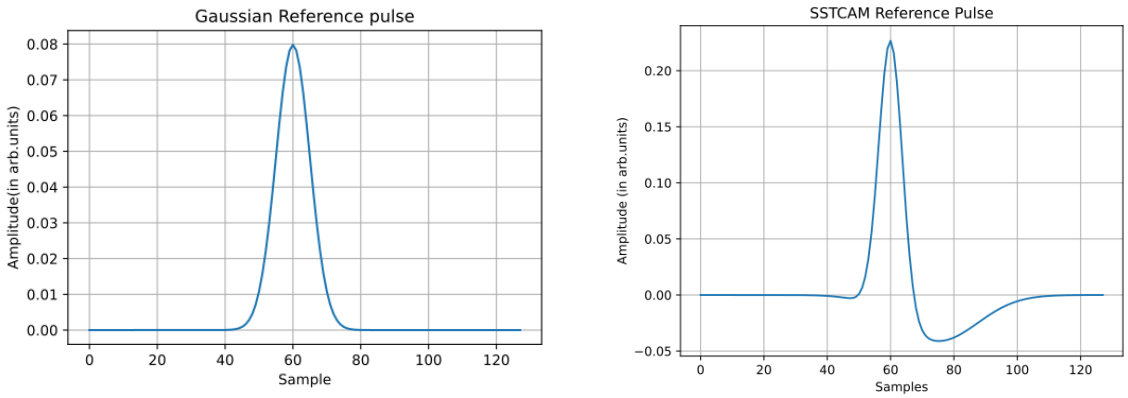

Figure 6.18: (*left*) Gaussian reference pulse for charge extraction from simulation data. (*right*) SSTCAM reference pulse shape for charge extraction from experimental data.

Simulation Result

The simulation framework provides the exact photon arrival times, which serve as ground truth for validating the charge extraction algorithm. The extracted arrival times from each waveform were compared against these true values to determine the extraction efficiency, defined in Eq. 6.8.

$$\text{Efficiency}(\%) = \frac{\text{Number of true peaks}}{\text{Number of inserted peaks}} \times 100 \tag{6.8}$$

An extracted peak was considered a true match if it fell within ±3 samples of the inserted peak. As shown in Figure 6.19 (*top*), the efficiency remained stable below a noise level of 1 p.e, but decreased approximately linearly once the noise level exceeded this threshold. Similarly, the dependence of efficiency on optical crosstalk was investigated and found to be minimal, with only about a 1% change in efficiency for a 20% variation in crosstalk. The primary influence of optical crosstalk on efficiency arises from the presence of multiple closely spaced peaks in the signal waveform as the modelling included only prompt optical crosstalk.

To further assess performance, a charge histogram was constructed from the extracted charges to study how the SiPM gain varied with both noise level and optical crosstalk. Since the extracted charges were expressed in units of p.e, the gain corresponded to the position of the first peak in the single photoelectron (SPE) spectrum. The peak position was determined by fitting the spectrum with the spefit module [118], and the resulting best-fit gain parameter was compared to the true value. The deviation from unity was reported as the gain error (%). A representative SPE spectrum with its best-fit curve is shown in Figure 6.20.

The dependence of gain error on noise level (Figure 6.21, *top*) showed that the error worsened once noise exceeds 1.5 p.e, consistent with the observed drop in extraction efficiency beyond that point. Conversely, the plot of gain error versus optical crosstalk (Figure 6.21, *bottom*) indicated that higher crosstalk reduces the error. This improvement arises because increasing crosstalk enhances the relative prominence of the 2 p.e and 3 p.e peaks, making the overall SPE spectrum more structured and easier to fit accurately.

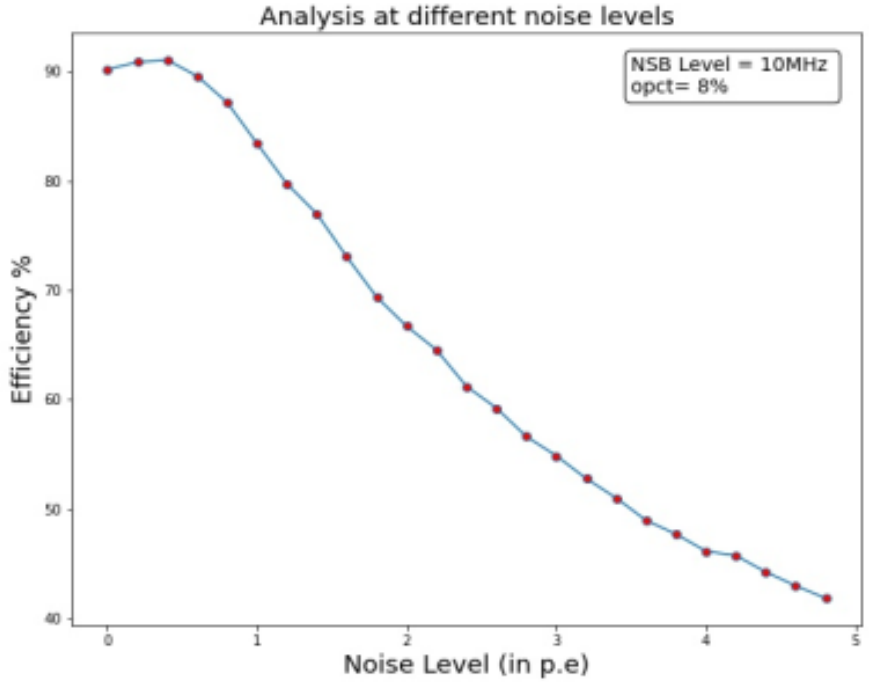

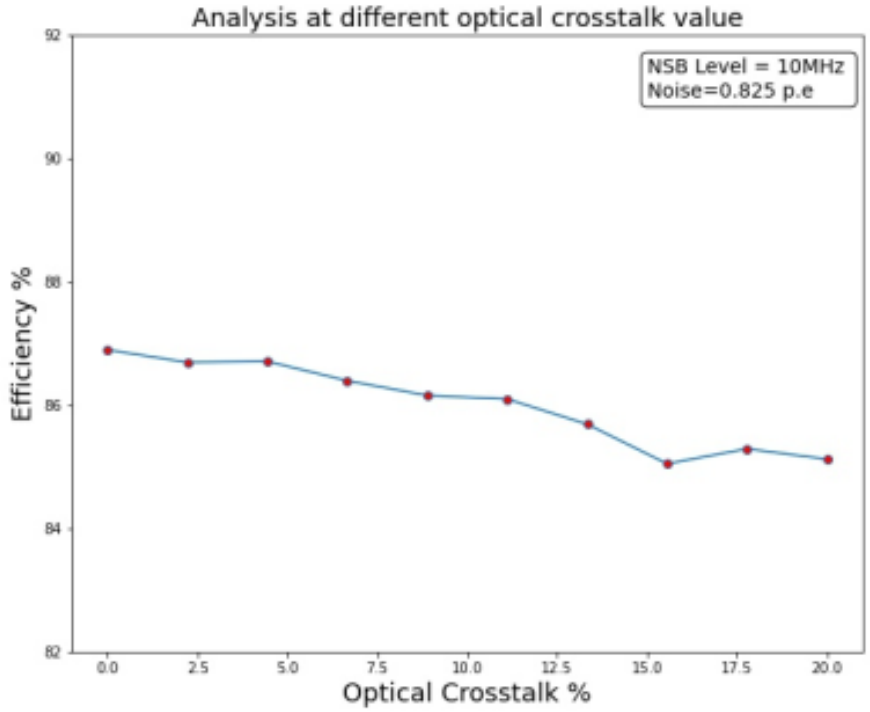

Figure 6.19: (*top*) Plot between the efficiency of charge extraction and noise level. The efficiency decreases beyond 1 p.e noise level as the method faces difficulty in extracting the true peaks. True peaks are the peaks that are within 3 samples of the injected peak. (bottom) Plot between the efficiency of charge extraction and optical crosstalk. This remains flat versus 20% change in the optical crosstalk values.

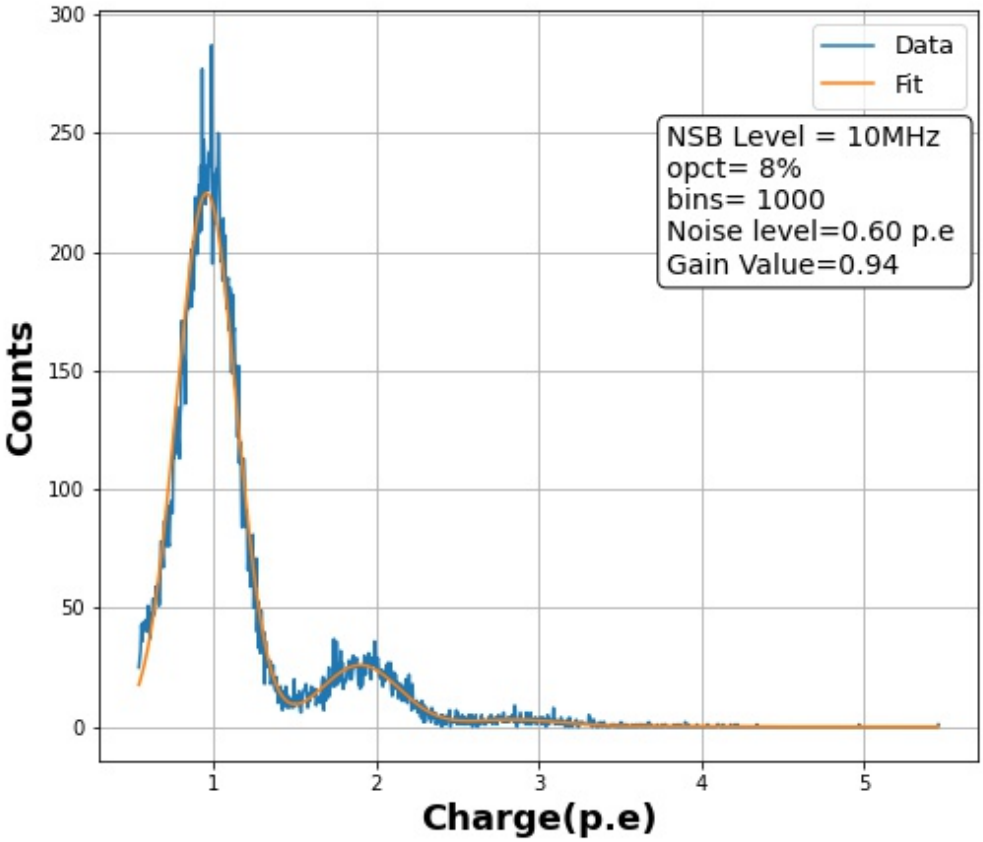

Figure 6.20: A representative SPE spectrum from simulated data with 8% optical cross talk, 0.6 p.e level noise and 10 MHz NSB level. The orange line indicates the best fit SPE curve. The waveform amplitudes were measured in p.e, so the peaks corresponds to different photoelectron levels. The gain value is close to 1 p.e. indicating the effectiveness of charge extraction method.

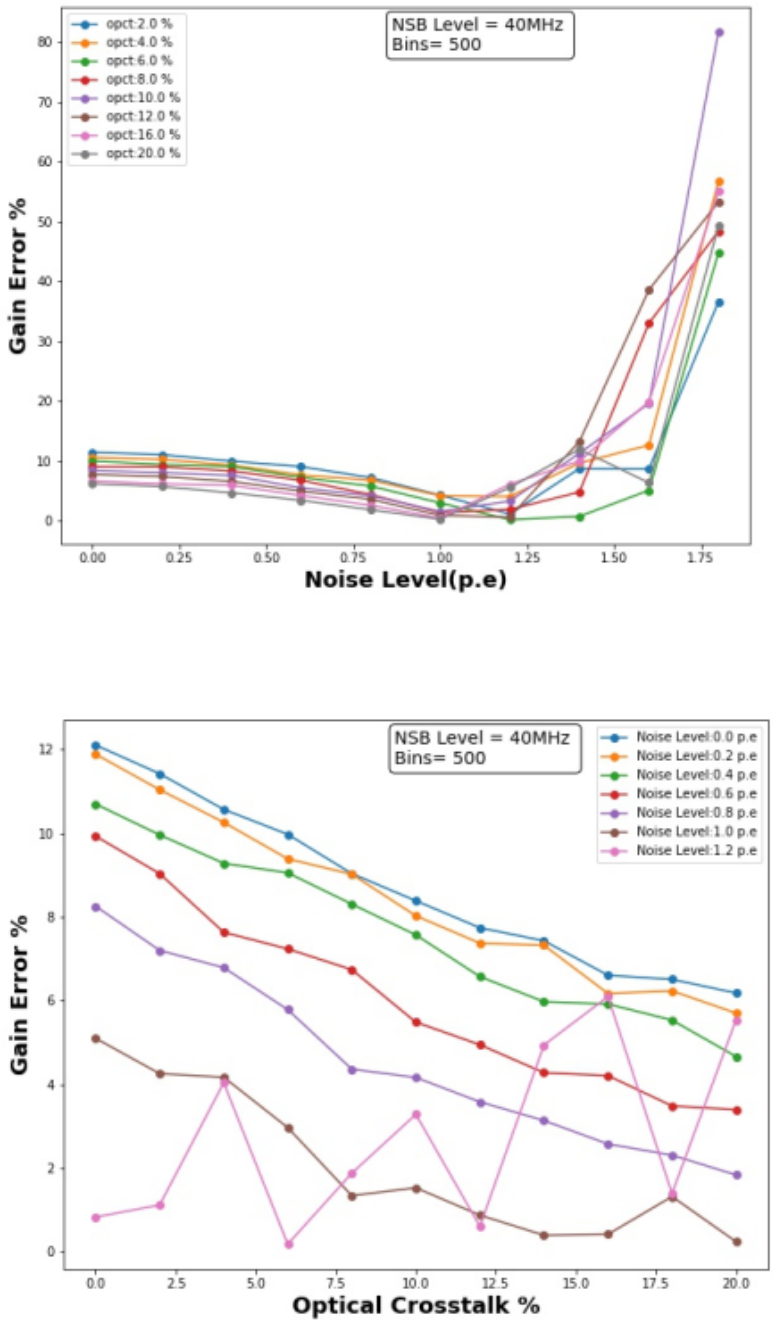

Figure 6.21: (*top*) Plot of gain error against noise level. Different curves indicate different optical crosstalk levels. Noise starts to dominate over 1 p.e noise level so that the peak extraction algorithm fails and the gain error increases. The decrease in gain error below 1 p.e noise level is a caveat of the specific fitting algorithm. (*bottom*) Plot of gain error as a function of optical crosstalk, with different curves representing varying noise levels. As optical crosstalk increases, higher-order photoelectron peaks become more distinct, improving the accuracy of the fit and leading to better gain estimation. However, higher noise levels degrade the precision of the gain extraction.

Experimental Setup

The simulation studies confirmed the effectiveness of the iterative reference pulse subtraction method for SiPM gain extraction, motivating its application to experimental data. For this purpose, a SiPM module was placed inside a dark box and illuminated with an NSB LED operated at rates ranging from 10 MHz to 60 MHz. The recorded waveforms, measured in mV, were analysed using a template pulse that closely matched the SSTCAM pulse shape (shown in Figure 6.18).

Experimental Result

The iterative reference pulse subtraction method was used to extract the charges from the waveforms. Charge lists were generated and stored, which were then used to construct the SPE spectrum. Each spectrum was fitted with the spefit module to extract the gain. Representative spectra at different NSB levels, together with their best-fit curves, are presented in Figure 6.22. As the NSB level increases, the prominence of the discrete SPE peaks diminishes, leading to reduced accuracy in gain extraction. This degradation is illustrated by the relationship between NSB rate and extracted gain, shown in Figure 6.23.

6.4.2 Underlid Flasher

Beyond its role in functional checks prior to observation runs, the under-lid Flasher also enables SPE calibration. As discussed in Chapter 4, coupling a Flasher channel to a scintillating fibre provides light levels comparable to single photoelectrons at the camera pixels, making it a promising approach for gain calibration. To test this, a well-calibrated SiPM module was positioned near the centre of the camera (Figure 6.24), carefully chosen to avoid direct illumination from the fibre. The charge was extracted by integrating 10 samples around the waveform peak, and the resulting charge histogram (SPE spectrum) was constructed. The SPE spectrum is depicted in Figure 6.24.

This procedure requires further validation based on data from the recent observation campaign (QCAM in September 2025). With improved SiPM and an

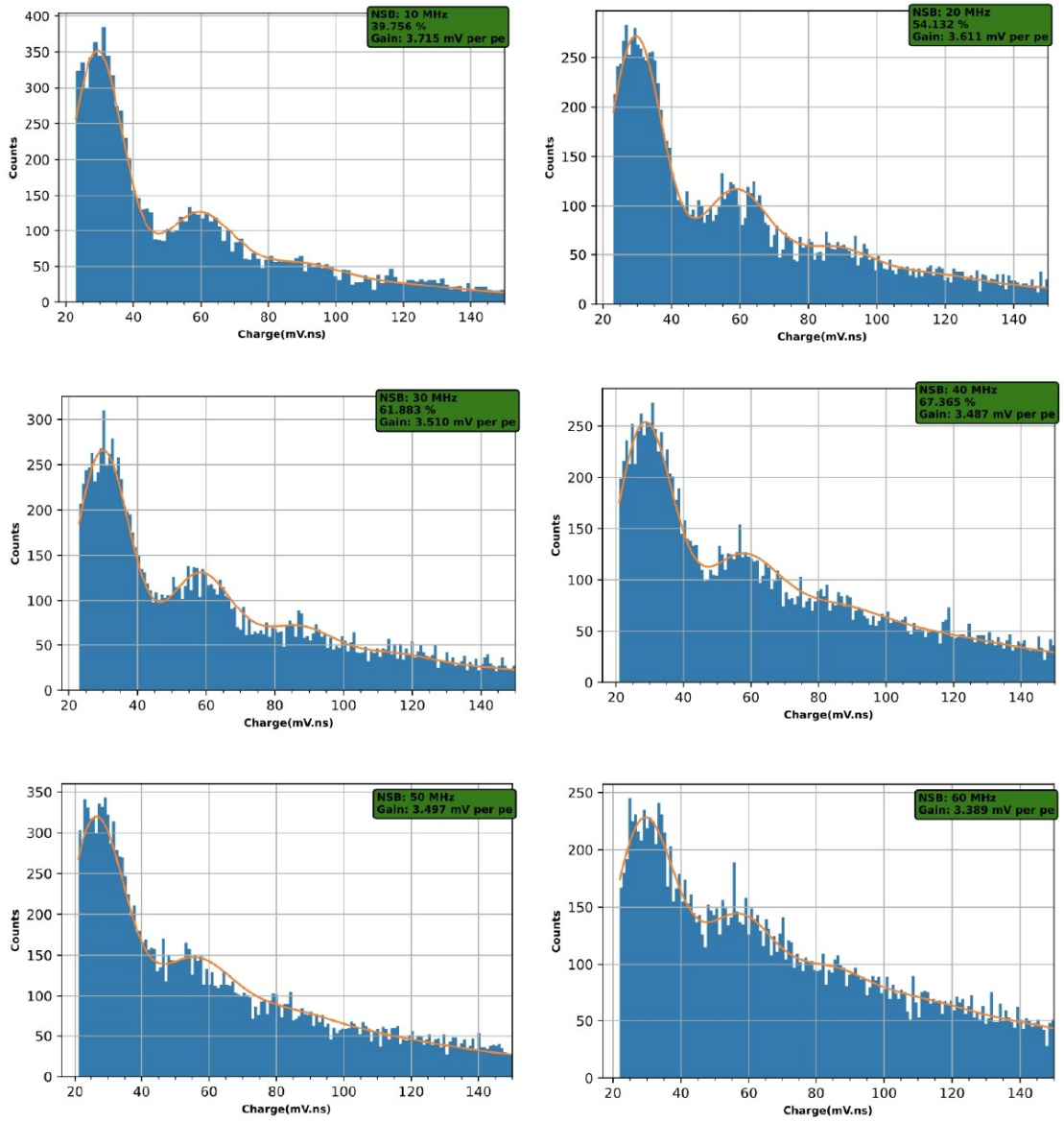

Figure 6.22: SPE spectrum for the experimental data ranging from an NSB level of 10 MHz to 60 MHz along with the best fit SPE parameters (orange curve). With increase in NSB level, the prominence of 2 p.e peak decreases due to the false peaks extracted from the waveform.

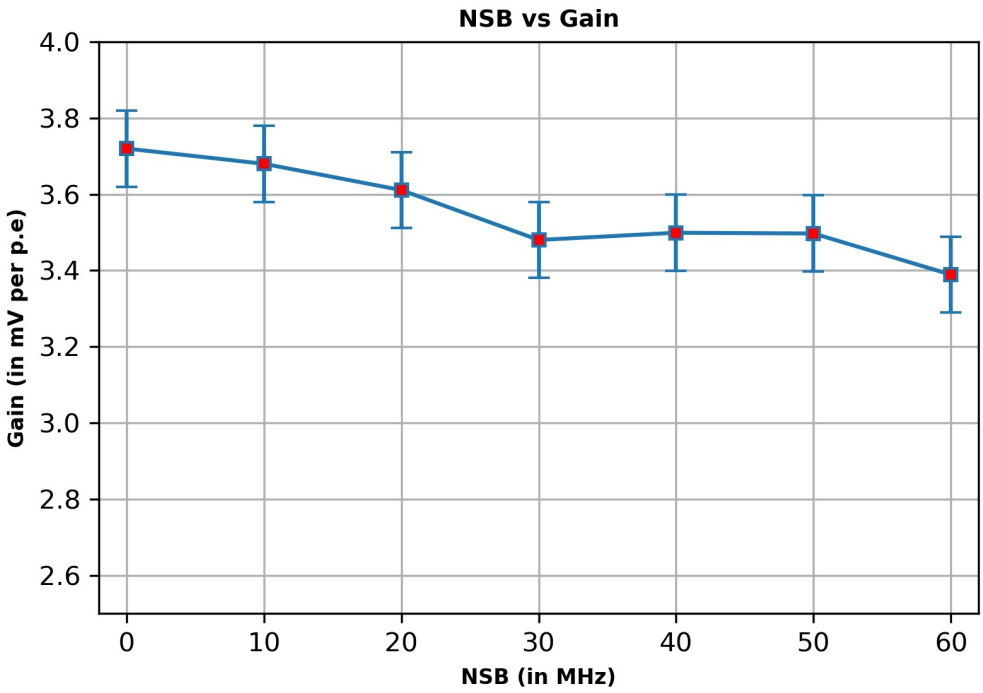

Figure 6.23: The variation of best fit gain parameter with NSB level.

improved high gain pre-amplifier, this method of SPE spectrum through underlid Flasher would be established.

6.5 Conclusion

This chapter presented the usage of Flasher system in the SSTCAM camera. The underlid Flasher coupled to scintillating fibre illuminates the focal plane of the camera after reflection from behind the camera door. This offers an excellent source to carry out initial functional checks on the camera prior to observation runs. Beyond identifying faulty pixels, tracking performance degradation, and monitoring trigger thresholds, additional tests will be implemented as the engineering camera (and subsequently the full camera) are constructed.

Next, the Flasher channel behind the secondary mirror can potentially monitor the linearity of the camera pixels. As discussed in Chapter 3, the Flasher system offers 5 orders of illumination levels. By using a diffuser, the camera focal plane can be uniformly illuminated over multiple brightness levels and the pixels that deviate

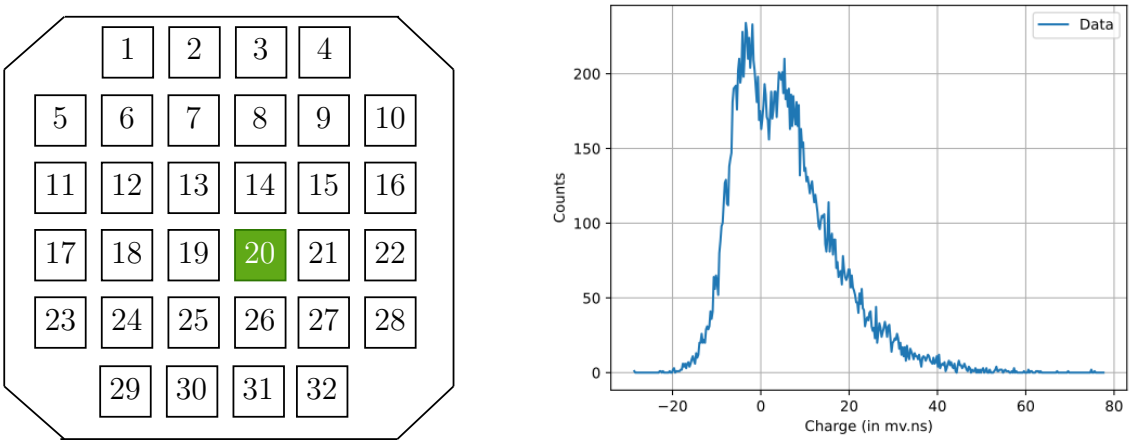

Figure 6.24: (*left*) Location of the SiPM module on the camera plane to investigate SPE calibration using underlid Flasher channel. The central location was chosen to avoid direct light from the scintillating fibre. (*right*) SPE spectrum for one pixel from the charges extracted over all events.

from the linear response could be flagged for further investigations.

Further, the flat fielding studies demonstrated that the CTAO requirement of $\leq 2\%$ RMS variation across camera pixels can be achieved with realistic illumination patterns. While uniform illumination provides the simplest path, both Gaussian and diffuser-convolved Gaussian beams also satisfy the requirement, provided the illumination amplitude is sufficiently high (200 ADC counts) and the spatial uniformity exceeds defined thresholds (90% for Gaussian illumination and 85% for Gaussian illumination convolved with diffuser response). In particular, the addition of a diffuser significantly relaxes constraints on beam width and peak alignment, offering a more robust and practical solution. These results confirm that the proposed Flasher system can reliably deliver the flat field calibration essential for accurate gain matching and consistent pixel response in SSTCAM. It will be thoroughly tested after the development of the engineering version of the camera in the next observation campaign.

This study confirmed that reliable SPE calibration of SSTCAM pixels is achievable using both thermally generated dark counts and low-level illumination from the under-lid Flasher coupled to a scintillating fibre. While dark count events provide a natural calibration source, they require long acquisition times to accumulate sufficient statistics for a well-defined SPE spectrum. In contrast, the Flasher operating at

1 kHz with low illumination significantly reduces calibration time. A representative calculation using the NSB level at the site (40 MHz) has been done in Appendix A. To ensure robustness, both approaches will be implemented to provide redundancy. The SPE calibration method is currently (as of September 2025) under evaluation with QCAMi data and will be further validated on the engineering and full cameras.

Together with the flat fielding , pixel linearity studies and SPE calibration, the calibration work presented in this chapter establishes a complete framework for characterising and monitoring SSTCAM performance, forming the basis for its reliable operation in future observation campaigns.

CHAPTER 7

Summary and Future Work

This thesis has presented the development, characterization, and testing of a dedicated calibration system for the Cherenkov Telescope Array (CTA) Small Sized Telescope (SST) camera, known as SSTCAM. The discussion began with an introduction to gamma-ray astronomy, outlining the physical processes responsible for high-energy photon production and the techniques used for their detection. The motivation for large ground-based detectors was established, leading into the central role of the Cherenkov Telescope Array Observatory (CTAO) and its anticipated performance compared to existing Imaging Atmospheric Cherenkov Telescopes (IACT).

Chapter 2 provided the foundation for this work through a focused literature review of IACT calibration. It introduced the prototype cameras developed for CTA's SST (CHEC-M and CHEC-S) and discussed the lessons learned from their observation campaigns. Compact High Energy Camera (CHEC)-M demonstrated the feasibility of the readout module design, while CHEC-S highlighted the performance gains achieved by transitioning from PMTs to SiPMs. Since this thesis centers on the photosensor calibration system, particular attention was given to the SiPMs chosen for SSTCAM. The discussion outlined how the performance of a Silicon Photomultiplier (SiPM) is governed by its intrinsic parameters (dark count

rate,Photon Detection Efficiency (PDE), optical crosstalk, and afterpulsing) and external factors (temperature and night sky background). A well-calibrated photosensor, coupled with a robust DAQ, ensures that raw data (DL0) are reliably transformed into higher-level science products (DL5 and beyond). These considerations underlined the necessity for a precise and reliable calibration device, designed to meet the stringent requirements of CTAO (Table 2.2).

Chapter 3 presented the detailed design architecture of the calibration device for SSTCAM, known as the Flasher. At the core of its operation, LMG1025 from Texas Instruments working together with delay line chip DS1023 generate a nanosecond scale pulse that drives an UV LED. The timing characteristics matches the intrinsic timing properties of Cherenkov light. Multiple prototype boards were prepared and tested at Durham University. The first two versions demonstrated that the principle of nanosecond pulse generation operated as intended. In version 3, the design transitioned from a multiple-LED configuration to a single-LED configuration to eradicate the problem of variation in the 2D distribution of the illumination pattern, while maintaining a comparable dynamic range. This prototype was more compact, reducing the design from three boards to two, and provided the basis for a potential multi-channel Flasher system. The detailed characterization of version 3 and the corresponding results form the main focus of Chapter 3.

The benchmarking tests of the Flasher Version 3 demonstrated that the system meets, and in many cases exceeds, the stringent requirements defined by CTAO for the calibration of SSTCAM. Comprehensive tests confirmed its stability, with pulse-to-pulse intensity variations limited to 1.3% (well within the 10% requirement) and long-term stability better than 0.1% over 30 minutes (compared to the 2% threshold). The device was shown to deliver a wide dynamic range, generating nanosecond-scale pulses with intensities spanning four orders of magnitude, enabling applications from flat-fielding to single photoelectron calibration. Timing characterisation further confirmed its suitability, with pulse widths as short as 2 ns, event-time jitter of only 0.12 ns RMS, and rise/fall time variations of about 6%, all compliant with CTAO specifications.

Also, long-term operation revealed an initial LED burn-in effect, after which

Sl no	Parameter	Requirement	Measured
1	Pulse width	1-10 ns pulse width with ±0.2ns stability	2-5 ns pulse width with ±0.12ns
2	30 minutes stability (Amplitude)	Variation ≤10%	Variation 1.3%
3	Event time	Jitter by ±0.5 ns	Jitter by ±0.08 ns
4	Rise and Fall time	-	6% variation
5	Trigger rate dependence	1% RMS variation	0.25% RMS variation
6	Temperature dependence	0.1%/C	0.01%/C

Table 7.1: Requirement vs measured parameters for calibration system

the brightness stabilised, suggesting that LEDs should be pre-conditioned at higher frequencies before deployment. Additional studies demonstrated reliable operation across different trigger frequencies and temperatures. The results showed an inverse correlation between temperature and light output, with intensity decreasing by approximately 0.7%/°C, for which effective correction coefficients were developed to account for temperature-dependent drifts. In addition, the illumination intensity exhibited minimal dependency on the trigger frequency (less than 4%), with an RMS variation of 0.25% in the operational range of 1–100 Hz, well within the 1% stability limit specified by CTAO. Beam-profile scans further validated the optical performance, showing that diffuser integration successfully produces a near-uniform beam (92% spatial uniformity) suitable for calibration activities. Collectively, these results (summarized in Table 7.1) established Flasher version 3 as a robust and high-performance calibration system for SSTCAM and provided a solid foundation for extending the concept towards a multi-channel flasher systems required for full camera calibration.

In parallel to benchmarking the standalone Flasher, two proof-of-concept studies were conducted in Chapter 4 to evaluate methods for delivering the calibration signal to different location within SSTCAM. This was needed to understand the best possible way of extending the Flasher operation to multiple channels, each

catering to a particular calibration activity. Fibre-based approaches demonstrated partial suitability. BCF-10 scintillating fibres coupled to LED and illuminating the camera pixels through under door reflection, reduced the per pixel illumination by 5 orders of magnitude. This low-level illumination showed the potential for Single Photoelectron (SPE) calibration. On the other hand, armoured optical fibres carrying the LED light to illuminate the camera from the centre of the secondary mirror offered a good spatial uniformity (92%, similar to direct LED illumination) for flat fielding but suffered from significant transmission losses ($\sim$80%) and had impractical routing constraints due to their tight bend radius. In contrast, light delivery at the secondary mirror through a LED terminated coaxial-cable proved to be a robust and versatile solution, maintaining signal integrity with only minor effect on timing (6% pulse width broadening). With their shielding to avoid signal interference, protection, and routing flexibility, coaxial cables were identified as the most practical foundation for the next-generation Flasher system.

The development of Flasher version 4 introduced a more compact and scalable system architecture, significantly extending the functionality of the calibration device. By adopting a new open-source microcontroller, the system now supports up to 4 independent channels (which can be extended to 20), offering far greater flexibility compared to earlier versions. The fabricated centralised board prototype is quite compact (100 mm by 92 mm) well within the available space inside the camera. The use of coaxial cables terminated with LEDs allows for easy connection and facilitates straightforward LED replacement during maintenance. The chapter also presented the integration plan for the 4 different Flasher channel within the camera with the centralised Flasher V4 board. One Flasher channel connected to a single scintillating fibre will illuminate the focal plane through reflection from the rear-side of the closed door, thus offering functional checks on pixels as well as SPE calibration. Two Flasher channels located at the diagonally opposite corners will illuminate the focal plane through reflection from the secondary mirror offering a clear pathway to monitor the mirror conditions. Finally, one Flasher channel placed inside a water-tight protective box behind the secondary mirror will illuminate the focal plane directly and perform the flat fielding operation interleaved between observa-

tions. Overall, Flasher version 4 provides a strong foundation for a multi-channel, high-performance calibration source tailored to the needs of SSTCAM, with clear upgrade paths for future refinements.

The application of the Flasher system within SSTCAM demonstrated its versatility across a wide range of calibration tasks. The under-lid Flasher, coupled to a scintillating fibre, provides a practical means for performing pre-observation functional checks, while the channel behind the secondary mirror enables detailed studies of pixel linearity across multiple brightness levels. Simulation of flat fielding operation confirmed that the CTAO requirement of $\leq$2% RMS pixel-to-pixel variation can be achieved under realistic illumination conditions post correction. In addition, the system supports efficient SPE calibration, reducing acquisition time compared to dark count–based approach and ensuring redundancy through complementary approaches. Collectively, these results establish the Flasher as a comprehensive calibration tool for SSTCAM, capable of supporting functional checks, flat-fielding, pixel linearity studies, and gain calibration, thereby ensuring the long-term stability and reliability of the camera.

While the Flasher system has demonstrated excellent performance, several avenues for improvement remain. The dynamic range, currently limited by driving the LED directly from the LMG1025 output, can be extended by introducing a Field Effect Transistor (FET) at the output stage to boost the drive current. Following the completion of firmware development for Flasher Version 4, comprehensive characterisation tests mentioned in this thesis will be required to benchmark its capabilities. The LED burn-in effect observed in Version 3 also warrants further investigation, to outline pre-production procedure needed to stabilise LEDs prior to large-scale deployment. On the application side, the under-lid Flasher channel requires additional testing to fully validate its role in SPE calibration. This will be done with the new SiPM modules and carefully chosen low intensity levels. A new preamplifer is currently under study at University of Leicester. The development of this pre-amplifier will improve the SPE calibration using dark count photons. As development progresses from Quarter Camera (QCAM) to Mechanical Camera (MCAM) and ultimately the full SSTCAM, the flat-fielding and pixel linearity

methods described in this thesis will be further tested and refined to ensure robust calibration during future observation campaigns.

The Flasher system developed in this thesis, while tailored for the specific needs of SSTCAM, offers a versatile and robust platform with plethora of applications. The fiber-coupled LED component has a direct application in the calibration of Photomultiplier Tubes (PMT)s of the upcoming Southern Wide-field Gamma-ray Observatory (SWGO) [28]. Similarly, the multi-channel Flasher unit would be beneficial for calibrating the wide-field camera of the Trinity experiment [96]. Beyond astrophysics, the system's nanosecond pulsed LEDs can serve as excitation sources in Fluorescence Lifetime Imaging Microscopy (FLIM) to measure fluorescence lifetimes in biological samples [119]. These LEDs are also suitable for use in Time-of-Flight (ToF) LiDAR systems for precise distance measurements [120]. This demonstrates that the work presented here has manifold applications across diverse scientific and technological fields, validating its broader significance.

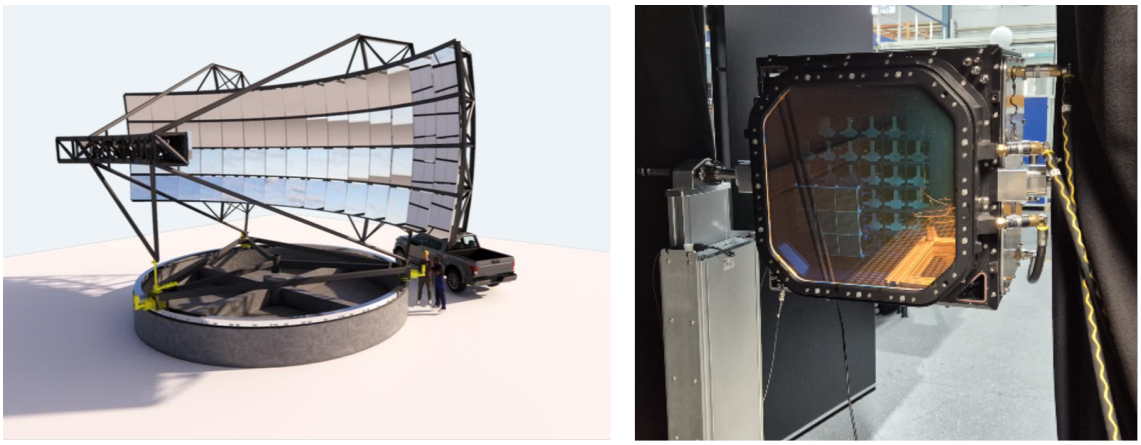

Figure 7.1: (*left*) CAD model for Trinity telescope showcasing the wide field camera [96]. (*right*) QCAM placed in the dark box for testing.

APPENDIX A

Dark count vs Flasher - Which is Faster?

In Chapter 6, two complimentary method of performing the single photoelectron calibration was performed. One with the dark count photons and NSB photons and the other with the intrinsic Flasher events. Here is a simplistic calculation to find out which method is faster to collect events in order to prepare the SPE spectrum and thus estimate the gain.

Lets say 10000 SPE events are required to prepare the spectrum. Case 1: The Flasher and the camera are triggered at 1 kHz. Case 2: The camera is triggered at 1 kHz, and the Dark Count Rate (NSB) and the Dark Count Rate (DCR) are 40 MHz and 3 MHz respectively.

Flasher Events

The flasher events are synced with the camera trigger. Considering only 90% of the SPE events are captured during the 128 ns waveform window, the total time required to build the 10000 events spectrum is:

$$T_{acq} = \frac{N_{spe}}{f_{trig} \times \epsilon} \tag{A.0.1}$$

where N_{spe} is the number of events required for the spectrum, f_{trig} is the trigger frequency and ϵ is the efficiency to capture the a SPE event during the 128 ns

window. 90% efficiency is a conservative assumption that some of the events missed due to trigger mismatch. By plugging in the requisite values, the acquisition time comes out to be **11 seconds**.

Dark Count and NSB photon events

The measured NSB rate at the site location is measured to be 40 MHz and the dark count rate for the chosen SiPM is 3 MHz. Thus, resulting in a cummulative event rate of 43 MHz. The process of SPE event is Poisson distribution dominated, thus the probability of 1 p.e event in 128 ns waveform window is given by:

$$\lambda = RT \tag{A.0.2}$$

$$P_1 = \lambda e^{-\lambda} \tag{A.0.3}$$

where R is the combined rate of NSB and dark count and T is the length of time window. Plugging in the values, the probability of SPE event is 0.0225. The effective event rate combined with the camera trigger rate of 1 kHz is calculated as:

$$R_{eq} = f_{trig} \times P_1 \tag{A.0.4}$$

This amounts to 22.5 events/second. Considering this effective event rate, the acquisition time comes out to be **444 seconds**.

Thus, the usage of Flasher for SPE calibration is 40 times faster than calculating it with the dark count and NSB events. It also has the added benefit of the known pulse time aiding in synching the camera trigger system.

Bibliography

[1] CERN timeline, "Discovery of cosmic rays," 4 1912. [Online]. Available: https://timeline.web.cern.ch/victor-hess-discovers-cosmic-rays-0 1.1

[2] T. K. Gaisser, R. Engel, and E. Resconi, *Cosmic Rays and Particle Physics*, 2016. 1.1, 1.7

[3] W. F. Hanlon, "The energy spectrum of ultra high energy cosmic rays measured by the High Resolution Fly's Eye observatory in stereoscopic mode," Ph.D. dissertation, Utah University, 2008. 1.1

[4] J. Blümer, R. Engel, and J. R. Hörandel, "Cosmic rays from the knee to the highest energies," *Progress in Particle and Nuclear Physics*, vol. 63, no. 2, p. 293–338, Oct. 2009. [Online]. Available: http://dx.doi.org/10.1016/j.ppnp.2009.05.002 1.1, 1.1

[5] R. Nemmen, D. F. Carlos, R. de Menezes, and L. Siconato, "Fermi sky map with 13 years of observations, in color," 8 2024. [Online]. Available: https://figshare.com/articles/figure/Fermi_sky_map_with_13_years_of_observations_in_color/26862556 1.2

[6] R. P. Lin, S. Krucker, G. J. Hurford, D. M. Smith, H. S. Hudson, G. D. Holman, R. A. Schwartz, B. R. Dennis, G. H. Share, R. J. Murphy, A. G. Emslie, C. Johns-Krull, and N. Vilmer, "RHESSI Observations of Particle Acceleration and Energy Release in an Intense Solar Gamma-Ray Line Flare," *The Astrophysical Journal*, vol. 595, no. 2, p. L69, sep 2003. [Online]. Available: https://dx.doi.org/10.1086/378932 1.3.1

[7] T. Linden, J.-T. Li, B. Zhou, I. John, M. Crnogorčević, A. H. G. Peter, and J. F. Beacom, "First Observations of Solar Halo Gamma Rays Over a Full Solar Cycle," 2025. [Online]. Available: https://arxiv.org/abs/2505.04625 1.3.1, 1.3.2

[8] B. M. Gaensler and P. O. Slane, "The Evolution and Structure of Pulsar Wind Nebulae," *Annual Review of Astronomy and Astrophysics*,

vol. 44, no. 1, p. 17–47, Sep. 2006. [Online]. Available: http://dx.doi.org/10.1146/annurev.astro.44.051905.092528 1.3.1

[9] A. Mucke, "Modeling the April 1997 flare of Mkn 501," in *AIP Conference Proceedings*, vol. 515. AIP, 2000, p. 149–153. [Online]. Available: http://dx.doi.org/10.1063/1.1291360 1.3.1

[10] T. Armstrong, "Monte Carlo studies of the GCT for the Cherenkov Telescope Array and the search for VHE AGN using cluster analysis," Ph.D. dissertation, University of Durham, Durham, UK, 2016, phD thesis. [Online]. Available: https://etheses.dur.ac.uk/11815/ 1.3.2, 1.4, 1.7, 1.12, 1.8

[11] C. A. Argüelles, F. Halzen, and N. Kurahashi, "From the Dawn of Neutrino Astronomy to A New View of the Extreme Universe," 2025. [Online]. Available: https://arxiv.org/abs/2405.17623 1.3.2

[12] R. Diehl, H. Halloin, K. Kretschmer, G. G. Lichti, V. Schönfelder, A. W. Strong, A. von Kienlin, W. Wang, P. Jean, J. Knödlseder, J.-P. Roques, G. Weidenspointner, S. Schanne, D. H. Hartmann, C. Winkler, and C. Wunderer, "Radioactive ^{26}Al from massive stars in the Galaxy," , vol. 439, no. 7072, pp. 45–47, Jan. 2006. 1.3.2

[13] C. Rulten, "Performance studies for the Cherenkov Telescope Array (CTA) with prospects for detecting pulsed gamma-ray emission." Ph.D. dissertation, University of Durham, Durham, UK, 2012, phD thesis. [Online]. Available: https://etheses.dur.ac.uk/3632/ 1.4, 1.8, 1.8

[14] W. Kraushaar, G. W. Clark, G. Garmire, H. Helmken, P. Higbie, and M. Agogino, "Explorer XI Experiment on Cosmic Gamma Rays." , vol. 141, p. 845, Apr. 1965. 1.5.1

[15] C. J. Cesarsky and J. A. Paul, "Gamma ray astronomy and the COS-B satellite." *Endeavour*, vol. 8, no. 1, pp. 9–16, Jan. 1984. 1.5.1

[16] G. Kanbach, D. L. Bertsch, C. E. Fichtel, R. C. Hartman, S. D. Hunter, D. A. Kniffen, B. W. Hughlock, A. Favale, R. Hofstadter, and E. B. Hughes, "The project EGRET (energetic gamma-ray experiment telescope) on NASA's Gamma-Ray Observatory GRO," , vol. 49, no. 1-2, pp. 69–84, Jan. 1989. 1.5.1, 1.6

[17] W. B. Atwood, A. A. Abdo, M. Ackermann, W. Althouse, B. Anderson, M. Axelsson, L. Baldini, J. Ballet, D. L. Band, G. Barbiellini, J. Bartelt, D. Bastieri, B. M. Baughman, K. Bechtol, D. Bédérède, F. Bellardi, R. Bellazzini, B. Berenji, G. F. Bignami, D. Bisello, E. Bissaldi, R. D. Blandford, E. D. Bloom, J. R. Bogart, E. Bonamente, J. Bonnell, A. W. Borgland, A. Bouvier, J. Bregeon, A. Brez, M. Brigida, P. Bruel, T. H. Burnett, G. Busetto, G. A. Caliandro, R. A. Cameron, P. A. Caraveo, S. Carius, P. Carlson, J. M. Casandjian, E. Cavazzuti, M. Ceccanti, C. Cecchi, E. Charles, A. Chekhtman, C. C. Cheung, J. Chiang, R. Chipaux, A. N. Cillis, S. Ciprini, R. Claus,

J. Cohen-Tanugi, S. Condamoor, J. Conrad, R. Corbet, L. Corucci, L. Costamante, S. Cutini, D. S. Davis, D. Decotigny, M. DeKlotz, C. D. Dermer, A. de Angelis, S. W. Digel, E. do Couto e Silva, P. S. Drell, R. Dubois, D. Dumora, Y. Edmonds, D. Fabiani, C. Farnier, C. Favuzzi, D. L. Flath, P. Fleury, W. B. Focke, S. Funk, P. Fusco, F. Gargano, D. Gasparrini, N. Gehrels, F. X. Gentit, S. Germani, B. Giebels, N. Giglietto, P. Giommi, F. Giordano, T. Glanzman, G. Godfrey, I. A. Grenier, M. H. Grondin, J. E. Grove, L. Guillemot, S. Guiriec, G. Haller, A. K. Harding, P. A. Hart, E. Hays, S. E. Healey, M. Hirayama, L. Hjalmarsdotter, R. Horn, R. E. Hughes, G. Jóhannesson, G. Johansson, A. S. Johnson, R. P. Johnson, T. J. Johnson, W. N. Johnson, T. Kamae, H. Katagiri, J. Kataoka, A. Kavelaars, N. Kawai, H. Kelly, M. Kerr, W. Klamra, J. Knödlseder, M. L. Kocian, N. Komin, F. Kuehn, M. Kuss, D. Landriu, L. Latronico, B. Lee, S. H. Lee, M. Lemoine-Goumard, A. M. Lionetto, F. Longo, F. Loparco, B. Lott, M. N. Lovellette, P. Lubrano, G. M. Madejski, A. Makeev, B. Marangelli, M. M. Massai, M. N. Mazziotta, J. E. McEnery, N. Menon, C. Meurer, P. F. Michelson, M. Minuti, N. Mirizzi, W. Mitthumsiri, T. Mizuno, A. A. Moiseev, C. Monte, M. E. Monzani, E. Moretti, A. Morselli, I. V. Moskalenko, S. Murgia, T. Nakamori, S. Nishino, P. L. Nolan, J. P. Norris, E. Nuss, M. Ohno, T. Ohsugi, N. Omodei, E. Orlando, J. F. Ormes, A. Paccagnella, D. Paneque, J. H. Panetta, D. Parent, M. Pearce, M. Pepe, A. Perazzo, M. Pesce-Rollins, P. Picozza, L. Pieri, M. Pinchera, F. Piron, T. A. Porter, L. Poupard, S. Rainò, R. Rando, E. Rapposelli, M. Razzano, A. Reimer, O. Reimer, T. Reposeur, L. C. Reyes, S. Ritz, L. S. Rochester, A. Y. Rodriguez, R. W. Romani, M. Roth, J. J. Russell, F. Ryde, S. Sabatini, H. F. W. Sadrozinski, D. Sanchez, A. Sander, L. Sapozhnikov, P. M. S. Parkinson, J. D. Scargle, T. L. Schalk, and G. Scolieri, "The Large Area Telescope on the Fermi Gamma-Ray Space Telescope Mission," , vol. 697, no. 2, pp. 1071–1102, Jun. 2009. 1.6

[18] N. Gehrels, "The Swift Gamma-Ray Burst Mission," in *AIP Conference Proceedings*, vol. 727. AIP, 2004, p. 637–641. [Online]. Available: http://dx.doi.org/10.1063/1.1810924 1.5.1

[19] Tavani, M., Barbiellini, G., Argan, A., Boffelli, F., Bulgarelli, A., Caraveo, P., Cattaneo, P. W., Chen, A. W., Cocco, V., Costa, E., D'Ammando, F., Del Monte, E., De Paris, G., Di Cocco, G., Di Persio, G., Donnarumma, I., Evangelista, Y., Feroci, M., Ferrari, A., Fiorini, M., Fornari, F., Fuschino, F., Froysland, T., Frutti, M., Galli, M., Gianotti, F., Giuliani, A., Labanti, C., Lapshov, I., Lazzarotto, F., Liello, F., Lipari, P., Longo, F., Mattaini, E., Marisaldi, M., Mastropietro, M., Mauri, A., Mauri, F., Mereghetti, S., Morelli, E., Morselli, A., Pacciani, L., Pellizzoni, A., Perotti, F., Piano, G., Picozza, P., Pontoni, C., Porrovecchio, G., Prest, M., Pucella, G., Rapisarda, M., Rappoldi, A., Rossi, E., Rubini, A., Soffitta, P., Traci, A., Trifoglio, M., Trois, A., Vallazza, E., Vercellone, S., Vittorini, V., Zambra, A., Zanello, D., Pittori, C., Preger, B., Santolamazza, P., Verrecchia, F., Giommi, P., Colafrancesco, S., Antonelli, A., Cutini, S., Gasparrini, D., Stellato, S., Fanari, G., Primavera, R., Tamburelli, F., Viola, F., Guarrera, G., Salotti,

L., D'Amico, F., Marchetti, E., Crisconio, M., Sabatini, P., Annoni, G., Alia, S., Longoni, A., Sanquerin, R., Battilana, M., Concari, P., Dessimone, E., Grossi, R., Parise, A., Monzani, F., Artina, E., Pavesi, R., Marseguerra, G., Nicolini, L., Scandelli, L., Soli, L., Vettorello, V., Zardetto, E., Bonati, A., Maltecca, L., D'Alba, E., Patané, M., Babini, G., Onorati, F., Acquaroli, L., Angelucci, M., Morelli, B., Agostara, C., Cerone, M., Michetti, A., Tempesta, P., D'Eramo, S., Rocca, F., Giannini, F., Borghi, G., Garavelli, B., Conte, M., Balasini, M., Ferrario, I., Vanotti, M., Collavo, E., and Giacomazzo, M., "The AGILE Mission," *AA*, vol. 502, no. 3, pp. 995–1013, 2009. [Online]. Available: https://doi.org/10.1051/0004-6361/200810527 1.5.1

[20] C. Winkler, T. J. L. Courvoisier, G. Di Cocco, N. Gehrels, A. Giménez, S. Grebenev, W. Hermsen, J. M. Mas-Hesse, F. Lebrun, N. Lund, G. G. C. Palumbo, J. Paul, J. P. Roques, H. Schnopper, V. Schönfelder, R. Sunyaev, B. Teegarden, P. Ubertini, G. Vedrenne, and A. J. Dean, "The INTEGRAL mission," , vol. 411, pp. L1–L6, Nov. 2003. 1.5.1

[21] M. Errando and T. Saito, *How to Detect Gamma Rays from Ground: An Introduction to the Detection Concepts*. Springer Nature Singapore, 2023, p. 1–37. [Online]. Available: http://dx.doi.org/10.1007/978-981-16-4544-0_61-1 1.5.2

[22] P. Mohanty, "Recent results from the GRAPES-3 experiment," in *Proceedings of 38th International Cosmic Ray Conference — PoS(ICRC2023)*, vol. 444, 2023, p. 535. 1.5.2

[23] A. L. Ivanova, I. Astapov, P. Bezyazeekov, E. Bonvech, A. Borodin, N. Budnev, A. Bulan, D. Chernov, A. Chiavassa, A. Dyachok, A. Gafarov, A. Garmash, V. Grebenyuk, E. Gress, O. Gress, T. Gress, A. Grinyuk, O. Grishin, A. D. Ivanova, N. Kalmykov, V. Kindin, S. Kiryuhin, R. Kokoulin, K. Kompaniets, E. Korosteleva, V. Kozhin, E. Kravchenko, A. Kryukov, L. Kuzmichev, A. Lagutin, M. Lavrova, Y. Lemeshev, B. Lubsandorzhiev, N. Lubsandorzhiev, A. Lukanov, D. Lukyantsev, S. Malakhov, R. Mirgazov, R. Monkhoev, E. Osipova, A. Pakhorukov, L. Pankov, A. Pan, A. Panov, A. Petrukhin, I. Poddubnyi, D. Podgrudkov, V. Poleschuk, V. Ponomareva, E. Popova, E. Postnikov, V. Prosin, V. Ptuskin, A. Pushnin, R. Raikin, A. Razumov, G. Rubtsov, E. Ryabov, Y. Sagan, V. Samoliga, A. Satyshev, A. Silaev, A. Silaev, A. Sidorenkov, A. Skurikhin, A. Sokolov, L. Sveshnikova, V. Tabolenko, L. Tkachev, A. Tanaev, M. Ternovoy, R. Togoo, N. Ushakov, A. Vaidyanathan, P. Volchugov, N. Volkov, D. Voronin, A. Zagorodnikov, D. Zhurov, and I. Yashin, "The Tunka-Grande scintillation array: current results," 2022. [Online]. Available: https://arxiv.org/abs/2207.09680 1.5.2

[24] M. Wommer and KASCADE-Grande-Collaboration, "Status and results of the KASKADE-Grande experiment," *Verhandlungen der Deutschen Physikalischen Gesellschaft*, no. Karlsruhe 2011 issue, p. [1 p.], 2011. 1.5.2

[25] Q. Zhang, Y. Wang, J. Zhang, J. Cao, T. Kwok, Y.-K. Hor, J. Chen, L. Ma, J. Han, and S. Qian, "An underground cosmic-ray

detector made of RPC," *Nuclear Instruments and Methods in Physics Research Section A: Accelerators, Spectrometers, Detectors and Associated Equipment*, vol. 583, no. 2, pp. 278–284, 2007. [Online]. Available: https://www.sciencedirect.com/science/article/pii/S0168900207020876 1.5.2

[26] G. Di Sciascio, "ARGO-YBJ: Status and Highlights," in *Vulcano Workshop 2012: Frontier Objects in Astrophysics and Particle Physics*, 10 2012. 1.5.2

[27] A. Abeysekara, A. Albert, R. Alfaro, C. Alvarez, J. Álvarez, M. Araya, J. Arteaga-Velázquez, K. Arunbabu, D. A. Rojas, H. A. Solares, R. Babu, A. Barber, A. Becerril, E. Belmont-Moreno, S. BenZvi, O. Blanco, J. Braun, C. Brisbois, K. Caballero-Mora, J. C. Martínez, T. Capistrán, A. Carramiñana, S. Casanova, M. Castillo, O. Chaparro-Amaro, U. Cotti, J. Cotzomi, S. C. de León, E. de la Fuente, C. de León, T. De Young, R. D. Hernandez, B. Dingus, M. DuVernois, M. Durocher, J. Díaz-Vélez, R. Ellsworth, K. Engel, C. Espinoza, K. Fan, K. Fang, B. Fick, H. Fleischhack, J. Flores, N. Fraija, J. García-González, G. Garcia-Torales, F. Garfias, G. Giacinti, H. Goksu, M. González, A. González-Muñoz, J. Goodman, J. Harding, E. Hernandez, S. Hernandez, J. Hinton, B. Hona, D. Huang, F. Hueyotl-Zahuantitla, C. Hui, T. Humensky, P. Hüntemeyer, A. Iriarte, A. Imran, A. Jardin-Blicq, V. Joshi, S. Kaufmann, D. Kieda, G. Kunde, A. Lara, R. Lauer, W. Lee, D. Lennarz, H. L. Vargas, J. Linnemann, A. Longinotti, G. Luis-Raya, J. Lundeen, K. Malone, V. Marandon, A. Marinelli, O. Martinez, I. Martínez-Castellanos, J. Martínez-Castro, H. Martínez-Huerta, J. Matthews, P. Miranda-Romagnoli, T. Montaruli, J. Morales-Soto, E. Moreno, M. Mostafá, A. Nayerhoda, L. Nellen, M. Newbold, M. Nisa, R. Noriega-Papaqui, T. Oceguera-Becerra, L. Olivera-Nieto, N. Omodei, A. Peisker, Y. P. Araujo, E. Pérez-Pérez, E. Ponce, J. Pretz, C. Rho, D. Rosa-González, E. Ruiz-Velasco, H. Salazar, D. Salazar-Gallegos, F. S. Greus, A. Sandoval, M. Schneider, H. Schoorlemmer, J. Serna-Franco, G. Sinnis, A. Smith, Y. Son, K. S. Woodle, R. Springer, I. Taboada, A. Tepe, O. Tibolla, K. Tollefson, I. Torres, R. Torres-Escobedo, R. Turner, F. Ureña-Mena, T. Ukwatta, E. Varela, M. Vargas-Magaña, L. Villaseñor, X. Wang, I. Watson, F. Werner, S. Westerhoff, E. Willox, I. Wisher, J. Wood, G. Yodh, D. Zaborov, A. Zepeda, and H. Zhou, "The High-Altitude Water Cherenkov (HAWC) observatory in México: The primary detector," *Nuclear Instruments and Methods in Physics Research Section A: Accelerators, Spectrometers, Detectors and Associated Equipment*, vol. 1052, p. 168253, Jul. 2023. [Online]. Available: http://dx.doi.org/10.1016/j.nima.2023.168253 1.5.2

[28] R. Conceição, "The Southern Wide-field Gamma-ray Observatory," 2023. [Online]. Available: https://arxiv.org/abs/2309.04577 1.5.2, 7

[29] M. S. Longair, *High Energy Astrophysics*, 2011. 1.7

[30] J. Watson, "Calibration and analysis of the GCT camera for the Cherenkov Telescope Array," Ph.D. dissertation, University of Oxford, 2018, phD thesis. 1.9, 2.1, 2.2.1, 2.2.1, 2.2.2, 2.3.2, 2.8

[31] P. A. Čerenkov, "Visible radiation produced by electrons moving in a medium with Velocities exceeding that of light," *Phys. Rev.*, vol. 52, pp. 378–379, Aug 1937. [Online]. Available: https://link.aps.org/doi/10.1103/PhysRev.52.378 1.7

[32] D. Depaoli, "Development of a SiPM-based camera for the Large Size Telescope of CTA and study of its performance," Ph.D. dissertation, Università degli Studi di Torino, Torino, Italy, Feb. 2022, phD thesis. [Online]. Available: https://hdl.handle.net/20.500.14242/198546 1.8, 2.2.1, 2.3, 2.2.1, 2.7

[33] H. J. Völk and K. Bernlöhr, "Imaging very high energy gamma-ray telescopes," *Experimental Astronomy*, vol. 25, no. 1–3, p. 173–191, Mar. 2009. [Online]. Available: http://dx.doi.org/10.1007/s10686-009-9151-z 1.13, 1.14

[34] M. de Naurois, "Analysis methods for Atmospheric Cherenkov Telescopes," 2006. [Online]. Available: https://arxiv.org/abs/astro-ph/0607247 1.8

[35] A. Demichev and A. Kryukov, "Using deep learning methods for IACT data analysis in gamma-ray astronomy: A review," *Astronomy and Computing*, vol. 46, p. 100793, 2024. [Online]. Available: https://www.sciencedirect.com/science/article/pii/S2213133724000088 1.8

[36] D. Malyshev and L. Mohrmann, "Analysis Methods for Gamma-ray Astronomy," 09 2023. 1.8

[37] W. Hofmann, "Data analysis techniques for stereo IACT systems," in *GeV-TeV Gamma Ray Astrophysics Workshop : towards a major atmospheric*, ser. American Institute of Physics Conference Series, B. L. Dingus, M. H. Salamon, and D. B. Kieda, Eds., vol. 515, Jun. 2000, pp. 318–322. 1.8

[38] T. Miener, R. López-Coto, J. L. Contreras, J. G. Green, D. Green, E. Mariotti, D. Nieto, L. Romanato, and S. Yadav, "IACT event analysis with the MAGIC telescopes using deep convolutional neural networks with CTLearn," 2021. [Online]. Available: https://arxiv.org/abs/2112.01828 1.8

[39] T. C. Weekes, M. F. Cawley, D. J. Fegan, K. G. Gibbs, A. M. Hillas, P. W. Kowk, R. C. Lamb, D. A. Lewis, D. Macomb, N. A. Porter, P. T. Reynolds, and G. Vacanti, "Observation of TeV Gamma Rays from the Crab Nebula Using the Atmospheric Cerenkov Imaging Technique," , vol. 342, p. 379, Jul. 1989. 1.8

[40] R. Mirzoyan, R. Kankanian, F. Krennrich, N. Müller, H. Sander, P. Sawallisch, F. Aharonian, A. Akhperjanian, A. Beglarian, J. Fernandez, V. Fonseca, W. Grewe, A. Heusler, A. K. Konopelko, E. Lorenz, M. Merck, A. V. Plyasheshnikov, D. Renker, M. Samorski, K. Sauerland, E. Smarsch, W. Stamm, M. Ulrich, C. A. Wiedner, and H. Wirth, "The first telescope of the HEGRA air Cherenkov imaging telescope array," *Nuclear Instruments and Methods in Physics Research A*, vol. 351, no. 2-3, pp. 513–526, Dec. 1994. 1.8

[41] S. Ohm and S. Wagner, "Current status and operation of the H.E.S.S. array of imaging atmospheric Cherenkov telescopes," *Nuclear Instruments and Methods in Physics Research Section A: Accelerators, Spectrometers, Detectors and Associated Equipment*, vol. 1055, p. 168442, 2023. [Online]. Available: https://www.sciencedirect.com/science/article/pii/S0168900223004321 1.8

[42] A. Moralejo and MAGIC Collaboration, "The MAGIC telescope for gamma-ray astronomy above 30 GeV," , vol. 75, p. 232, Jan. 2004. 1.8

[43] J. Holder, R. W. Atkins, H. M. Badran, G. Blaylock, S. M. Bradbury, J. H. Buckley, K. L. Byrum, D. A. Carter-Lewis, O. Celik, Y. C. K. Chow, P. Cogan, W. Cui, M. K. Daniel, I. de la Calle Perez, C. Dowdall, P. Dowkontt, C. Duke, A. D. Falcone, S. J. Fegan, J. P. Finley, P. Fortin, L. F. Fortson, K. Gibbs, G. Gillanders, O. J. Glidewell, J. Grube, K. J. Gutierrez, G. Gyuk, J. Hall, D. Hanna, E. Hays, D. Horan, S. B. Hughes, T. B. Humensky, A. Imran, I. Jung, P. Kaaret, G. E. Kenny, D. Kieda, J. Kildea, J. Knapp, H. Krawczynski, F. Krennrich, M. J. Lang, S. LeBohec, E. Linton, E. K. Little, G. Maier, H. Manseri, A. Milovanovic, P. Moriarty, R. Mukherjee, P. A. Ogden, R. A. Ong, D. Petry, J. S. Perkins, F. Pizlo, M. Pohl, J. Quinn, K. Ragan, P. T. Reynolds, E. T. Roache, H. J. Rose, M. Schroedter, G. H. Sembroski, G. Sleege, D. Steele, S. P. Swordy, A. Syson, J. A. Toner, L. Valcarcel, V. V. Vassiliev, S. P. Wakely, T. C. Weekes, R. J. White, D. A. Williams, and R. Wagner, "The first VERITAS telescope," *Astroparticle Physics*, vol. 25, no. 6, pp. 391–401, Jul. 2006. 1.8

[44] S. P. Wakely and D. Horan, "TeVCat: An online catalog for Very High Energy Gamma-Ray Astronomy," *International Cosmic Ray Conference*, vol. 3, pp. 1341–1344, 2008. 1.8

[45] *Science with the Cherenkov Telescope Array*. WORLD SCIENTIFIC, Feb. 2018. [Online]. Available: http://dx.doi.org/10.1142/10986 1.9, 1.9.1, 1.9.4

[46] CTA Observatory and CTA Consortium, "CTAO Instrument Response Functions - prod5 version v0.1 ," Sep. 2021. [Online]. Available: https://doi.org/10.5281/zenodo.5499840 1.15, 1.16

[47] J. Cortina, "Status of the Large Size Telescopes of the Cherenkov Telescope Array," 2019. [Online]. Available: https://arxiv.org/abs/1907.10146 1.9.2

[48] CTAO, "CTAO homepage," 4 2024. [Online]. Available: https://www.ctao.org/ 1.9.2, 1.1, 1.9.2, 1.9.2, 1.2, 1.3, 1.9.3, 1.19

[49] J. M. Davies and E. S. Cotton, "Design of the quartermaster solar furnace," *Solar Energy*, vol. 1, no. 2, pp. 16–22, 1957. [Online]. Available: https://www.sciencedirect.com/science/article/pii/0038092X57901160 1.9.2

[50] F. Bradascio, "Status of the Medium-Sized Telescopes for the Cherenkov Telescope Array Observatory," 2023. [Online]. Available: https://arxiv.org/abs/2310.02127 1.9.2

[51] "NectarCAM, a camera for the medium sized telescopes of the Cherenkov telescope array," in *AIP Conference Proceedings*, vol. 1792. Author(s), 2017, p. 080009. [Online]. Available: http://dx.doi.org/10.1063/1.4969030 1.9.2

[52] G. Puhlhofer, C. Bauer, A. Biland, D. Florin, C. Fohr, A. Gadola, G. Hermann, C. Kalkuhl, J. Kasperek, T. Kihm, J. Koziol, A. Manalaysay, A. Marszalek, P. J. Rajda, T. Schanz, S. Steiner, U. Straumann, C. Tenzer, P. Vogler, A. Vollhardt, Q. Weitzel, K. Winiarski, K. Zietara, and C. Consortium, "FlashCam: A fully digital camera for CTA telescopes," in *AIP Conference Proceedings*. AIP, 2012, p. 777–780. [Online]. Available: http://dx.doi.org/10.1063/1.4772375 1.9.2

[53] K. Schwarzschild, "Untersuchungen zur geometrischen Optik II,," *Astronomische Mitteilungen der Universitaets-Sternwarte zu Goettingen*, vol. 10, p. 1, Jan. 1905. 1.9.2

[54] G. Tagliaferri, A. Antonelli, T. Arnesen, J. Aschersleben, P. Attinà, M. Balbo, S. Bang, M. Barcelo, A. Baryshev, G. Bellassai, D. Berge, C. Bicknell, C. Bigongiari, G. Bonnoli, F. Bouley, A. Brown, A. Bulgarelli, M. Cappi, P. Caraveo, S. Caschera, P. Chadwick, F. Conte, G. Cotter, P. Cristofari, F. D. Frondat, E. D. G. D. Pino, N. D. Simone, D. Depaoli, J.-L. Dournaux, C. Duffy, S. Einecke, C. Fermino, S. Funk, C. Gargano, G. Giavitto, A. Giuliani, T. Greenshaw, J. Hinton, J.-M. Huet, S. Iovenitti, N. L. Palombara, J. Lapington, P. Laporte, S. Leach, L. Lessio, G. Leto, S. Lloyd, F. Lucarelli, S. Lombardi, A. Macchi, E. Martinetti, A. Miccichè, R. Millul, T. Mineo, T. Mitsunari, A. Nayak, G. Nicotra, A. Okumura, G. Pareschi, M. Penno, H. Prokoph, E. Rebert, C. Righi, C. Rulten, F. Russo, R. Z. Sanchez, F. G. Saturni, J. Schaefer, B. Schwab, S. Scuderi, G. Sironi, V. Sliusar, H. Sol, S. Spencer, A. Stamerra, H. Tajima, F. Tavecchio, G. Tosti, A. Trois, M. Vecchi, S. Vercellone, J. Vink, R. Walter, J. Watson, R. White, R. Zanin, L. Zampieri, A. Zech, and A. Zink, "The small-sized telescope of CTAO," in *Ground-based and Airborne Telescopes IX*, H. K. Marshall, J. Spyromilio, and T. Usuda, Eds., vol. 12182, International Society for Optics and Photonics. SPIE, 2022, p. 121820K. [Online]. Available: https://doi.org/10.1117/12.2627956 1.9.2

[55] D. Depaoli, "Status of the SST Camera for the Cherenkov Telescope Array," 2023. [Online]. Available: https://arxiv.org/abs/2310.01183 1.9.2

[56] J. Lapington, "The silicon photomultiplier-based camera for the Cherenkov Telescope Array small-sized telescopes," *Nuclear Instruments and Methods in Physics Research Section A: Accelerators, Spectrometers, Detectors and Associated Equipment*, vol. 1055, p. 168433, 2023. [Online]. Available: https://www.sciencedirect.com/science/article/pii/S0168900223004230 1.9.2

[57] B.S. Acharya et al., "Introducing the CTA concept," *Astroparticle Physics*, vol. 43, pp. 3–18, 2013, seeing the High-Energy Universe with the Cherenkov Telescope Array - The Science Explored with the CTA. [Online]. Available: https://www.sciencedirect.com/science/article/pii/S0927650513000169 1.9.3

[58] Abdalla et al., "Sensitivity of the Cherenkov Telescope Array for probing cosmology and fundamental physics with gamma-ray propagation," *Journal of Cosmology and Astroparticle Physics*, vol. 2021, no. 02, p. 048–048, Feb. 2021. [Online]. Available: http://dx.doi.org/10.1088/1475-7516/2021/02/048 1.9.4

[59] S. Abe. et al., "Dark matter line searches with the Cherenkov Telescope Array," *Journal of Cosmology and Astroparticle Physics*, vol. 2024, no. 07, p. 047, Jul. 2024. [Online]. Available: http://dx.doi.org/10.1088/1475-7516/2024/07/047 1.9.4

[60] R. A. Ong, "The Cherenkov Telescope Array Science Goals and Current Status," *EPJ Web of Conferences*, vol. 209, p. 01038, 2019. [Online]. Available: http://dx.doi.org/10.1051/epjconf/201920901038 1.9.4

[61] K. Abe et al., "Galactic transient sources with the Cherenkov Telescope Array Observatory," *Monthly Notices of the Royal Astronomical Society*, vol. 540, no. 1, p. 205–238, Apr. 2025. [Online]. Available: http://dx.doi.org/10.1093/mnras/staf655 1.9.4

[62] S. Abe et al., "Prospects for a survey of the galactic plane with the Cherenkov Telescope Array," *Journal of Cosmology and Astroparticle Physics*, vol. 2024, no. 10, p. 081, Oct. 2024. [Online]. Available: http://dx.doi.org/10.1088/1475-7516/2024/10/081 1.9.4

[63] A. Brown, "Active Galactic Nuclei population studies with the Cherenkov Telescope Array," *PoS*, vol. ICRC2021, p. 887, 2021. 1.9.4

[64] J. J. Watson, A. De Franco, A. Abchiche, D. Allan, J.-P. Amans, T. P. Armstrong, A. Balzer, D. Berge, C. Boisson, J.-J. Bousquet, A. M. Brown, M. Bryan, G. Buchholtz, P. M. Chadwick, H. Costantini, G. Cotter, M. K. Daniel, F. De Frondat, J.-L. Dournaux, D. Dumas, J.-P. Ernenwein, G. Fasola, S. Funk, J. Gironnet, J. A. Graham, T. Greenshaw, O. Hervet, N. Hidaka, J. A. Hinton, J.-M. Huet, I. Jegouzo, T. Jogler, M. Kraus, J. S. Lapington, P. Laporte, J. Lefaucheur, S. Markoff, T. Melse, L. Mohrmann, P. Molyneux, S. J. Nolan, A. Okumura, J. P. Osborne, R. D. Parsons, S. Rosen, D. Ross, G. Rowell, C. B. Rulten, Y. Sato, F. Sayède, J. Schmoll, H. Schoorlemmer, M. Servillat, H. Sol, V. Stamatescu, M. Stephan, R. Stuik, J. Sykes, H. Tajima, J. Thornhill, L. Tibaldo, C. Trichard, J. Vink, R. White, N. Yamane, A. Zech, A. Zink, J. Zorn, and for the CTA Consortium, "Inauguration and first light of the GCT-M prototype for the Cherenkov telescope array," *AIP Conference Proceedings*, vol. 1792, no. 1, p. 080006, 01 2017. [Online]. Available: https://doi.org/10.1063/1.4969027 2.1

[65] J. Zorn, R. White, J. Watson, T. Armstrong, A. Balzer, M. Barcelo, D. Berge, R. Bose, A. Brown, M. Bryan, P. Chadwick, P. Clark, H. Costantini, G. Cotter, L. Dangeon, M. Daniel, A. De Franco, P. Deiml, G. Fasola, S. Funk, M. Gebyehu, J. Gironnet, J. Graham, T. Greenshaw, J. Hinton, M. Kraus, J. Lapington, P. Laporte, S. Leach, O. Le Blanc, A. Malouf, P. Molyneux,

P. Moore, H. Prokoph, A. Okumura, D. Ross, G. Rowell, L. Sapozhnikov, H. Schoorlemmer, H. Sol, M. Stephan, H. Tajima, L. Tibaldo, G. Varner, and A. Zink, "Characterisation and testing of CHEC-M—A camera prototype for the small-sized telescopes of the Cherenkov telescope array," *Nuclear Instruments and Methods in Physics Research Section A: Accelerators, Spectrometers, Detectors and Associated Equipment*, vol. 904, p. 44–63, Oct. 2018. [Online]. Available: http://dx.doi.org/10.1016/j.nima.2018.06.078 2.1, 2.1

[66] J. J. Watson and J. Zorn, "Commissioning and Performance of CHEC-S – a compact high-energy camera for the Cherenkov Telescope Array," 2019. [Online]. Available: https://arxiv.org/abs/1907.09252 2.1, 4.1.2

[67] D. Depaoli, J. Lapington, S. Leach, A. Okumura, I. Sofia, and H. Tajima, "Silicon photomultipliers for the SST camera of the Cherenkov Telescope Array," *Nuclear Instruments and Methods in Physics Research Section A: Accelerators, Spectrometers, Detectors and Associated Equipment*, vol. 1060, p. 169047, 2024. [Online]. Available: https://www.sciencedirect.com/science/article/pii/S0168900223010471 2.2, 2.1, 2.6, 2.6

[68] W. Wild, "Small-Sized Telescope Harmonization Process and Status," 10 2019. [Online]. Available: https://www.ctao.org/news/small-sized-telescope-harmonization-process-and-status/ 2.2

[69] B. Schwab, A. Zink, G. Varner, D. Depaoli, J. Hinton, G. Liu, A. Okumura, D. Ross, J. Schäfer, H. Schoorlemmer, H. Tajima, J. Vandenbroucke, R. White, J. Watson, J. Zorn, and S. Funk, "CTC and CT5TEA: An advanced multi-channel digitizer and trigger ASIC for imaging atmospheric Cherenkov telescopes," *Nuclear Instruments and Methods in Physics Research Section A: Accelerators, Spectrometers, Detectors and Associated Equipment*, vol. 1069, p. 169841, 2024. [Online]. Available: https://www.sciencedirect.com/science/article/pii/S0168900224007678 2.2, 2.2.2

[70] A. Otte, J. Hose, R. Mirzoyan, A. Romaszkiewicz, M. Teshima, and A. Thea, "A measurement of the photon detection efficiency of silicon photomultipliers," *Nuclear Instruments and Methods in Physics Research Section A: Accelerators, Spectrometers, Detectors and Associated Equipment*, vol. 567, no. 1, pp. 360–363, 2006, proceedings of the 4th International Conference on New Developments in Photodetection. [Online]. Available: https://www.sciencedirect.com/science/article/pii/S0168900206009788 2.2.1

[71] Y. Nakamura, A. Okumura, H. Tajima, N. Yamane, and A. Zenin, "Characterization of SiPM Optical Crosstalk and Its Dependence on the Protection-Window Thickness," in *Proceedings of the 5th International Workshop on New Photon-Detectors (PD18)*. Journal of the Physical Society of Japan, Nov. 2019. [Online]. Available: http://dx.doi.org/10.7566/JPSCP.27.011003 2.2.1, 2.5

[72] S. Funk, D. Jankowsky, H. Katagiri, M. Kraus, A. Okumura, H. Schoorlemmer, A. Shigenaka, H. Tajima, L. Tibaldo, G. Varner, A. Zink, J. Zorn, and for the CTA consortium, "TARGET: A digitizing and trigger ASIC for the Cherenkov telescope array," *AIP Conference Proceedings*, vol. 1792, no. 1, p. 080012, 01 2017. [Online]. Available: https://doi.org/10.1063/1.4969033 2.2.2

[73] M. Gaug, S. Fegan, A. M. W. Mitchell, M. C. Maccarone, T. Mineo, and A. Okumura, "Using Muon Rings for the Calibration of the Cherenkov Telescope Array: A Systematic Review of the Method and Its Potential Accuracy," *The Astrophysical Journal Supplement Series*, vol. 243, no. 1, p. 11, jul 2019. [Online]. Available: https://dx.doi.org/10.3847/1538-4365/ab2123 2.3.1

[74] A. M. Brown, T. Armstrong, P. M. Chadwick, M. Daniel, and R. White, "Flasher and muon-based calibration of the GCT telescopes proposed for the Cherenkov Telescope Array," 2015. [Online]. Available: https://arxiv.org/abs/1509.00185 2.3.1, 2.3.2, 3.2, 5.5, 5.5.2, 5.5.2

[75] A. Vacheret, G. Barker, M. Dziewiecki, P. Guzowski, M. Haigh, B. Hartfiel, A. Izmaylov, W. Johnston, M. Khabibullin, A. Khotjantsev, Y. Kudenko, R. Kurjata, T. Kutter, T. Lindner, P. Masliah, J. Marzec, O. Mineev, Y. Musienko, S. Oser, F. Retière, R. Salih, A. Shaikhiev, L. Thompson, M. Ward, R. Wilson, N. Yershov, K. Zaremba, and M. Ziembicki, "Characterization and simulation of the response of Multi-Pixel Photon Counters to low light levels," *Nuclear Instruments and Methods in Physics Research Section A: Accelerators, Spectrometers, Detectors and Associated Equipment*, vol. 656, no. 1, p. 69–83, Nov. 2011. [Online]. Available: http://dx.doi.org/10.1016/j.nima.2011.07.022 2.3.2, 2.3.2

[76] S. R. Patel, G. Grolleron, H. Ashkar, J. Biteau, F. Bradascio, F. Brun, C. Dubos, J. F. Glicenstein, G. Hull, P. Jean, M. Josselin, D. Kerszberg, J. P. Lenain, V. Marandon, K. Pressard, P. Sharma, P. Sizun, and T. Suomijärvi, "A single photo-electron calibration of NectarCAM," *PoS*, vol. ICRC2023, p. 648, 2023. 2.3.2

[77] D. Hanna, A. McCann, M. McCutcheon, and L. Nikkinen, "An LED-based flasher system for VERITAS," *Nuclear Instruments and Methods in Physics Research Section A: Accelerators, Spectrometers, Detectors and Associated Equipment*, vol. 612, no. 2, p. 278–287, Jan. 2010. [Online]. Available: http://dx.doi.org/10.1016/j.nima.2009.10.107 2.4.1, 2.9, 3.1.1

[78] T. Schweizer, E. Lorenz, M. Martinez, A. Ostankov, and D. Paneque, "The optical calibration of the MAGIC telescope camera," in *2001 IEEE Nuclear Science Symposium Conference Record (Cat. No.01CH37310)*, vol. 1, 2001, pp. 437–441 vol.1. 2.4.2

[79] k. Aye, P. Chadwick, and A. Noutas, "A novel alternative to UV-Lasers used in flat fielding VHE Gamma ray telescopes," in *ICRC 2003 proceedings*, 2003. 2.4.3

[80] F. Aharonian, A. Akhperjanian, K.-M. Aye, A. Bazer-Bachi, M. Beilicke, W. Benbow, D. Berge, P. Berghaus, K. Bernlöhr, O. Bolz, C. Boisson, C. Borgmeier, F. Breitling, A. Brown, P. Chadwick, V. Chitnis, L.-M. Chounet, R. Cornils, L. Costamante, B. Degrange, O. de Jager, A. Djannati-Ataï, L. Drury, T. Ergin, P. Espigat, F. Feinstein, P. Fleury, G. Fontaine, S. Funk, Y. Gallant, B. Giebels, S. Gillessen, P. Goret, J. Guy, C. Hadjichristidis, M. Hauser, G. Heinzelmann, G. Henri, G. Hermann, J. Hinton, W. Hofmann, M. Holleran, D. Horns, I. Jung, B. Khélifi, N. Komin, A. Konopelko, I. Latham, R. L. Gallou, M. Lemoine, A. Lemière, N. Leroy, T. Lohse, A. Marcowith, C. Masterson, T. McComb, M. de Naurois, S. Nolan, A. Noutsos, K. Orford, J. Osborne, M. Ouchrif, M. Panter, G. Pelletier, S. Pita, M. Pohl, G. Pühlhofer, M. Punch, B. Raubenheimer, M. Raue, J. Raux, S. Rayner, I. Redondo, A. Reimer, O. Reimer, J. Ripken, M. Rivoal, L. Rob, L. Rolland, G. Rowell, V. Sahakian, L. Sauge, S. Schlenker, R. Schlickeiser, C. Schuster, U. Schwanke, M. Siewert, H. Sol, R. Steenkamp, C. Stegmann, J.-P. Tavernet, C. Théoret, M. Tluczykont, D. van der Walt, G. Vasileiadis, P. Vincent, B. Visser, H. Volk, and S. Wagner, "Calibration of cameras of the H.E.S.S. detector," *Astroparticle Physics*, vol. 22, no. 2, p. 109–125, Nov. 2004. [Online]. Available: http://dx.doi.org/10.1016/j.astropartphys.2004.06.006 2.4.3

[81] M. Iori, F. Ferrarotto, L. Recchia, A. Girardi, and R. Lunadei, "Test results of the optical calibration system for the Large Sized Telescope camera," 2024. [Online]. Available: https://arxiv.org/abs/2410.08341 2.4.4, 2.10, 2.4.4, 2.11

[82] B. Biasuzzi, K. Pressard, J. Biteau, B. Geoffroy, C. D. Goncalves, G. Hull, M. Imre, M. Josselin, A. Maroni, B. Mathon, L. Seminor, T. Suomijarvi, T. N. Trung, L. Vatrinet, P. Brun, S. Caroff, S. Fegan, O. Ferreira, P. Jean, S. Karkar, J.-F. Olive, S. Rivoire, P. Sizun, F. Thiant, A. Tsiahina, F. Toussenel, and G. Vasileiadis, "Design and characterization of a single photoelectron calibration system for the NectarCAM camera of the medium-sized telescopes of the Cherenkov Telescope Array," *Nuclear Instruments and Methods in Physics Research Section A: Accelerators, Spectrometers, Detectors and Associated Equipment*, vol. 950, p. 162949, Jan. 2020. [Online]. Available: http://dx.doi.org/10.1016/j.nima.2019.162949 2.4.5

[83] P. Sharma, B. Biasuzzi, J. Biteau, M. Bourgaux, S. Caroff, G. Hull, M. Josselin, K. Pressard, P. Sizun, T. Suomijarvi, and T. N. Trung, "A single photoelectron calibration system for the NectarCAM camera of the Cherenkov Telescope Array Medium-Sized Telescopes," in *Proceedings of 37th International Cosmic Ray Conference — PoS(ICRC2021)*, ser. ICRC2021. Sissa Medialab, Jul. 2021, p. 698. [Online]. Available: http://dx.doi.org/10.22323/1.395.0698 2.4.5, 2.11

[84] F. Aharonian, Q. An, Axikegu, L. Bai, Y. Bai, Y. Bao, D. Bastieri, X. Bi, Y. Bi, H. Cai, J. Cai, Z. Cao, Z. Cao, J. Chang, J. Chang, B. Chen, E. Chen, J. Chen, L. Chen, L. Chen, L. Chen, M. Chen, M. Chen, Q. Chen, S. Chen, S. Chen, T. Chen, X. Chen, Y. Chen, N. Cheng, Y. Cheng, S. Cui,

X. Cui, Y. Cui, B. Dai, H. Dai, Z. Dai, Danzengluobu, D. della Volpe, B. D. Piazzoli, X. Dong, K. Duan, J. Fan, Y. Fan, Z. Fan, J. Fang, K. Fang, C. Feng, L. Feng, S. Feng, Y. Feng, Y. Fu, H. Gan, B. Gao, C. Gao, L. Gao, Q. Gao, W. Gao, M. Ge, L. Geng, G. Gong, Q. Gou, M. Gu, F. Guo, J. Guo, X. Guo, Y. Guo, Y. Guo, Y. Han, H. He, H. He, J. He, S. He, X. He, Y. He, M. Heller, Y. Hor, C. Hou, H. Hu, S. Hu, S. Hu, X. Hu, D. Huang, Q. Huang, W. Huang, X. Huang, X. Huang, Z. Huang, F. Ji, X. Ji, H. Jia, K. Jiang, Z. Jiang, C. Jin, T. Ke, D. Kuleshov, K. Levochkin, B. Li, C. Li, C. Li, F. Li, H. Li, H. Li, H. Li, J. Li, K. Li, W. Li, X. Li, X. Li, X. Li, Y. Li, Y. Li, Z. Li, Z. Li, E. Liang, Y. Liang, S. Lin, B. Liu, C. Liu, D. Liu, H. Liu, H. Liu, J. Liu, J. Liu, J. Liu, J. Liu, M. Liu, R. Liu, S. Liu, W. Liu, Y. Liu, Y. Liu, Z. Liu, W. Long, R. Lu, H. Lv, B. Ma, L. Ma, X. Ma, J. Mao, A. Masood, Z. Min, W. Mitthumsiri, T. Montaruli, Y. Nan, B. Pang, P. Pattarakijwanich, Z. Pei, M. Qi, Y. Qi, B. Qiao, J. Qin, D. Ruffolo, V. Rulev, A. Sáiz, L. Shao, O. Shchegolev, X. Sheng, J. Shi, H. Song, Y. Stenkin, V. Stepanov, Y. Su, Q. Sun, X. Sun, Z. Sun, P. Tam, Z. Tang, W. Tian, B. Wang, C. Wang, H. Wang, H. Wang, J. Wang, J. Wang, L. Wang, L. Wang, R. Wang, W. Wang, W. Wang, X. Wang, X. Wang, X. Wang, Y. Wang, Y. Wang, Y. Wang, Y. Wang, Z. Wang, Z. Wang, Z. Wang, Z. Wang, D. Wei, J. Wei, Y. Wei, T. Wen, C. Wu, H. Wu, S. Wu, W. Wu, X. Wu, S. Xi, J. Xia, J. Xia, G. Xiang, D. Xiao, G. Xiao, H. Xiao, G. Xin, Y. Xin, Y. Xing, D. Xu, R. Xu, L. Xue, D. Yan, J. Yan, C. Yang, F. Yang, J. Yang, L. Yang, M. Yang, R. Yang, S. Yang, Y. Yao, Z. Yao, Y. Ye, L. Yin, N. Yin, X. You, Z. You, Y. Yu, Q. Yuan, H. Zeng, T. Zeng, W. Zeng, Z. Zeng, M. Zha, X. Zhai, B. Zhang, H. Zhang, H. Zhang, J. Zhang, J. Zhang, L. Zhang, L. Zhang, L. Zhang, P. Zhang, P. Zhang, R. Zhang, S. Zhang, S. Zhang, X. Zhang, X. Zhang, Y. Zhang, Y. Zhang, Y. Zhang, Y. Zhang, B. Zhao, J. Zhao, L. Zhao, L. Zhao, S. Zhao, F. Zheng, Y. Zheng, B. Zhou, H. Zhou, J. Zhou, P. Zhou, R. Zhou, X. Zhou, C. Zhu, F. Zhu, H. Zhu, K. Zhu, and X. Zuo, "Absolute calibration of LHAASO WFCTA camera based on LED," *Nuclear Instruments and Methods in Physics Research Section A: Accelerators, Spectrometers, Detectors and Associated Equipment*, vol. 1021, p. 165824, 2022. [Online]. Available: https://www.sciencedirect.com/science/article/pii/S0168900221008093 2.4.6

[85] *LMG1025-Q1 Automotive Low Side GaN and MOSFET Driver For High Frequency and Narrow Pulse Applications*, Texas Instruments, 01 2020, Datasheet, Accessed: Apr. 2022. [Online]. Available: https://www.ti.com/lit/ds/symlink/lmg1025-q1.pdf 3.1.1, 5.6

[86] *DS1023 8-Bit Programmable Timing Element*, Dallas Semiconductor, 01 2015, Datasheet, Accessed: Apr. 2022. [Online]. Available: https://www.analog.com/media/en/technical-documentation/data-sheets/ds1023.pdf 3.1.1, 3.7.5, 5.2

[87] *TLP3475 Photorelay*, Toshiba, 01 2025, Datasheet, Accessed: May 2022. [Online]. Available: https://toshiba.semicon-storage.com/info/TLP3475_datasheet_en_20250519.pdf?did=15256&prodName=TLP3475 3.1.2

[88] *Bivar UV LED 400 nm*, Bivar, 01 2020, Datasheet, Accessed: Feb. 2022. [Online]. Available: https://www.mouser.co.uk/datasheet/3/112/1/UV3TZ-XXX-XX.pdf 3.1.3, 3.7.5

[89] *SPX3819 500mA Low-Noise LDO Voltage Regulator* , MaxLinear, 01 2019, Datasheet, Accessed: Mar. 2022. [Online]. Available: https://www.maxlinear.com/ds/spx3819.pdf 3.1.4, 5.1.1

[90] *ATSAMD21G18A Low-Power, 32-bit Cortex-M0+ MCU with Advanced Analog and PWM*, Microchip, 01 2018, Datasheet, Accessed: Apr. 2022. 3.1.5, 5.1.2

[91] *W5500*, WIZnet, 01 2013, Datasheet, Accessed: Apr. 2022. [Online]. Available: https://docs.wiznet.io/Product/Chip/Ethernet/W5500 3.1.6

[92] *DS28CM00 I2C/SMBus Silicon Serial Number*, Dallas Semiconductor, 01 2020, Datasheet, Accessed: May 2022. [Online]. Available: https://www.analog.com/media/en/technical-documentation/data-sheets/DS28CM00.pdf 3.1.7

[93] *ADT7310 16-Bit Digital SPI Temperature Sensor*, Analog Devices, 01 2015, Datasheet, Accessed: May. 2022. [Online]. Available: https://www.analog.com/media/en/technical-documentation/data-sheets/ADT7310.pdf 3.1.7

[94] A. M. Brown, J. Muller, M. de Naurois, and P. Clark, "Inter-calibration of atmospheric Cherenkov telescopes with UAV-based airborne calibration system," *Astroparticle Physics*, vol. 140, p. 102695, 2022. [Online]. Available: https://www.sciencedirect.com/science/article/pii/S092765052200010X 3.2

[95] L. Taylor, "Design and upgrade of the prototype Schwarzschild-Couder Telescope," 2022. [Online]. Available: https://arxiv.org/abs/2209.02680 3.2

[96] A. M. Brown, M. Bagheri, M. Doro, E. Gazda, D. Kieda, C. Lin, Y. Onel, N. Otte, I. Taboada, and A. Wang, "Trinity: An Imaging Air Cherenkov Telescope to Search for Ultra-High-Energy Neutrinos," 2021. [Online]. Available: https://arxiv.org/abs/2109.03125 3.2, 7, 7.1

[97] Click, *Click Module*, 4, Software. [Online]. Available: https://click.palletsprojects.com/en/stable/ 3.3

[98] *RS RTP 16 MHz Oscilliscope*, Rhode and Schwarz, 01 2023, Datasheet, Accessed: Sep. 2023. [Online]. Available: https://scdn.rohde-schwarz.com/ur/pws/dl_downloads/pdm/cl_brochures_and_datasheets/product_brochure/3683_5616_12/RTP_bro_en_3683-5616-12_v1100.pdf 3.5.4

[99] PyVISA, *PyViSA Module homepage*, 4, Software. [Online]. Available: https://pyvisa.readthedocs.io/en/latest/ 3.6

[100] *Polymer engineered diffuser*, Thorlabs, 01 2020, Datasheet, Accessed: Apr. 2022. [Online]. Available: https://www.thorlabs.com/item/ED1-S50-MD 3.7.6, 6.1, 6.3.3

[101] *BCF 10 Plastic scintillating fibre*, Sain Gobain Crystals, 01 2017, Datasheet, Accessed: Aug. 2022. [Online]. Available: https://luxiumsolutions.com/sites/default/files/2021-11/Fiber-Product-Sheet.pdf 1, 4.1.1

[102] *M92L01 Ø200 µm, 0.22 NA, SMA-SMA Fiber Patch Cable*, ThorLabs, 01 2020, Datasheet, Accessed: Aug. 2022. [Online]. Available: https://www.thorlabs.com/item/M92L01 2

[103] *M59L01 Ø1000 µm, 0.50 NA, SMA-SMA Fiber Patch Cable*, ThorLabs, 01 2020, Datasheet, Accessed: Aug. 2022. [Online]. Available: https://www.thorlabs.com/item/M59L01 2

[104] *M93L01 Ø1500 µm, 0.39 NA, Stainless Steel SMA-SMA Fiber Patch Cable*, ThorLabs, 01 2020, Datasheet, Accessed: Aug. 2022. [Online]. Available: https://www.thorlabs.com/item/M93L01 2, 4.1.4, 4

[105] C. A. Whittaker, "Radiation sensitive optical fibres for radiation detection and dosimetry," Ph.D. dissertation, University of Adelaide, Adelaide, Australia, Feb. 2018, phD thesis. [Online]. Available: http://hdl.handle.net/2440/127168 4.1.1

[106] *Sensl microfc Low-Noise, Blue-Sensitive 6mm SiPM*, Onsemi, 01 2020, Datasheet, Accessed: Mar. 2022. [Online]. Available: https://www.onsemi.com/pdf/datasheet/microc-series-d.pdf 4.1.1, 4.1.2, 4.2.1

[107] *Tyvek Sheets*, Dupont, 01 2020, Datasheet, Accessed: Mar. 2024. [Online]. Available: https://spenic.com/product-category/tyvek-paper-style-category/dupont-tyvek-white-graphics-grade/dupont-tyvek-105gsm-1082d/ 4.2

[108] *High reflective spectralon sheet*, Edmund, 01 2020, Datasheet, Accessed: Mar. 2024. [Online]. Available: https://www.edmundoptics.co.uk/p/12quot-white-balance-target/15456/ 4.2

[109] *G608N3 - Index Matching Gel*, ThorLabs, 01 2013, Datasheet, Accessed: Feb. 2024. [Online]. Available: blob:https://www.thorlabs.com/97cf805e-a49e-4904-9b9b-1d8d3a4a5b7d#G608N-Spec-Sheet.pdf 4.1.3

[110] *RG-174/U Coaxial Cables*, Mouser, 01 2006, Datasheet, Accessed: Jan. 2025. [Online]. Available: https://www.mouser.co.uk/datasheet/3/6/1/8216_techdata.pdf 4.2

[111] *PRTR5V0U2X Ultra low capacitance double rail-to-rail ESD protection diode*, Nexperia, 01 2017, Datasheet, Accessed: June 2024. [Online]. Available: https://www.nexperia.com/product/PRTR5V0U2X 5.1.1

[112] *CH32V307R mcrocontroller manual*, WCH, 01 2019, Datasheet, Accessed: June 2024. [Online]. Available: https://www.wch-ic.com/products/CH32V307.html 5.1.2

[113] *74AHCT595D 8-bit serial-in/serial-out or parallel-out shift register*, Nexperia, 01 2025, Datasheet, Accessed: June 2024. [Online]. Available: https://www.nexperia.com/product/74AHCT595D 5.3, 5.1.3

[114] Moun river, *Moun river homepage*, 4 2024, Software, Accessed: Dec. 2024. [Online]. Available: https://www.mounriver.com/ 5.3

[115] *QK-AS15 Coaxial Lightning Surge Protector*, Quark Elec, 01 2020, Datasheet, Accessed: Aug. 2024. [Online]. Available: https://www.quark-elec.com/doc/QK-AS15_manual.pdf 5.5.1

[116] *SM1-Threaded Mount for LED*, Thorlabs, 01 2007, Datasheet, Accessed: Mar. 2023. [Online]. Available: https://www.thorlabs.com/item/S1LEDM 5.11

[117] J. Watson, *SSTCAM Simulation*, 4 2020, Software. [Online]. Available: https://github.com/sstcam/sstcam-simulation 6.4.1, 6.16

[118] J. Watson, *spefit Module*, 4 2020, Software. [Online]. Available: https://pypi.org/project/spefit/ 6.4.1

[119] M. Wahl, U. Ortmann, K. Lauritsen, and R. Erdmann, "Application of sub-ns pulsed LEDs in fluorescence lifetime spectroscopy," *Proceedings of SPIE - The International Society for Optical Engineering*, vol. 4648, 04 2002. 7

[120] Z. Li and R. Ram, "Nanosecond pulsed CMOS LED for all-silicon time-of-flight ranging," *Optics Express*, vol. 31, pp. 24 307–24 319, 07 2023. 7